Numerical modelling of crack propagation in quasi-brittle heterogeneous materials: a stochastic approach

by

Elia Gironacci

Thesis

Submitted to the University of Warwick in partial

fulfilment of the requirements for the degree of

Doctor of Philosophy

School of Engineering

August 2018

Abstract

Deformation and damage processes in brittle and quasi-brittle materials, such as rock and concrete, are strognly influenced by their heterogeneous nature, related to their formation processes. The presence of heterogeneities leads in fact to noticeable variation in material properties values: it is of extreme importance that a numerical model which aims to realistically, reliably reproduce with low computational effort deformation and damage processes is able to include the effect of laminations, micro-cracks, voids and other types of heterogeneities; this is even more important when a numerical models has to reproduce the propagation of fractures. This thesis presents the development of a numerical framework for the simulation of crack propagation in shale rocks and concrete which also looks at the optimisation problem in the sense of computational efficiency (defined as optimal computational time needed to obtain realistic and accurate results). The numerical framework for crack propagation developed in this thesis is a variational phase-field model based on a finite elements smeared approach, able to automatically and realistically capture crack initiation processes for a variety of loading conditions; this numerical framework is based on the relation between potential energy associated to body deformation and the energy released during fracture formation. Heterogeneity is considered in the model by means of a stochastic approach based on the assumption that some mechanical properties of heterogeneous brittle materials (such as fracture energy) follow a non-Gaussian Weibull distribution. To guarantee adequate convergence of the results, Monte Carlo Simulation (MCS) method has been used in combination with the developed stochastic methodology. A non-linear dimensionality reduction technique has been developed and incorporated in the algorithm to reduce the computational effort required for the generation of sample realisations. The methodology has been validated using experimental results from both laboratory tests on shale rocks and literature on fracture in concrete. Results show that the developed algorithm is capable of realistically reproducing the mechanical behaviour of the chosen case studies, showing an applicability to problems where cracks propagate in mode-I, mode-II and mixed-mode I and II, guaranteeing a fast generation of sampling realisations of realistic stochastic fields and convergence of results after a maximum of 130 MCS analyses. This methodology can be applied to materials with random spatially-distributed variations of mechanical properties and to those showing laminar natural formations.

Acknowledgments

It's finally time to conclude this experience, which let me grow as a person and as academic.

I would like to express my gratitude to my PhD supervisor (and current colleauge) Dr Mohaddeseh Mousavi Nezhad, for her constant understanding, help, scientific support and for encouraging my academic and personal development: her constant supervision has been essential for completion of my PhD, our discussions have been constructive and let me understand how scientific research needs to be conducted.

I would like to thank my second supervisor and one of my current line managers Professor James Toby Mottram, for being always available to provide valuable and useful advices and support for becoming a successful early stage academic. Thank you also to Dr Georgia Kremmyda, my other current line manager, for being supportive and understanding when my current job has overlapped with the final part of my PhD. Thank you to my examiners Dr Curiel-Sosa and Dr Seyedi for the constructive feedback on my work and thank you to Dr Zivanovic for being my internal advisor, making sure that everything went smoothly and for her advices in preparation to my Viva.

I would love to thank all my beloveds, for their constant encouragement and for believing in me since day one of this incredible path.

First of all, I would like to thank all my family, my mother, my father, my sisters and their families. Despite the distance, I've always felt their vicinity and support. They've always believed in me: if I achieved this results is also thanks to their constant encouragement, and I am sure they are as happy as me for this achievement.

Thank you to all my Italian friends, and to those people I met here. Sharing my

experiences with them gave me the force and the stamina to carry on even when seemed impossible to continue. Feeling lonely when difficulties happen can be devastating, but fortunately this has never been the case.

And finally, a big thank you to Roberto. I am so blessed I have found him on my path, there are no words able to describe his role in this achievement: willing to constantly listen, understand and help, no matter what. Any words I may use to describe his role wouldn't probably be enough, he has been (and is) just irreplaceable. Thank you.

Elia Gironacci

Contents

List of Tables

List of Figures

List of Publications

The publications listed here were completed during the author's period of registration to the higher degree program.

Referred Journals

Gironacci E, Mousavi Nezhad M, Rezania M, Lancioni G (2017). A nonlocal probabilistic method for modelling of crack propagation. International Journal of Mechanical Sciences, Accepted (In press).

Mousavi Nezhad M, **Gironacci E**, Rezania M, Khalili N (2018). Stochastic modelling of crack propagation in materials with random properties using isometric mapping for dimensionality reduction of nonlinear data sets. International Journal of Numerical Methods in Engineering,113(4),656-680.

Mousavi Nezhad M, Fisher Q, **Gironacci E**, Rezania M (2018). Experimental study and numerical modeling of fracture propagation in shale rocks during Brazilian disc test. Rock Mechanics and Rock Engineering. Accepted (In press).

Referred Conferences

Gironacci E, Mousavi Nezhad M, Rezania M (2015). Modelling of crack propagation in brittle heterogeneous materials. The 23rd Annual Conference on Computational Mechanics, Swansea, UK.

Mousavi Nezhad M, **Gironacci E**, Rezania M, Fisher Q (2015). Computational modelling of crack propagation in shale-gas reservoir rocks. The 23rd Annual Conference on Computational Mechanics, Swansea, UK.

Gironacci E, Mousavi Nezhad M, Mottram JT (2015). Modelling of crack propagation of brittle heterogeneous materials. Young Researchers Forum, The Institution of Structural Engineers, London, UK.

Gironacci E, Mousavi Nezhad M (2017). Non-linear dimensionality reduction technique of random fields applied on fracture mechanics problems. 2nd ECCOMAS Thematic Conference on International Conference on Uncertainty Quantification in Computational Sciences and Engineering UNCECOMP, Rhodes Island, Greece.

List of Symbols

Mechanics fundamentals

a	Crack length
$\mathbf{e}_i$	Vector component direction
$\mathbf{f}$	Body deformation
$\mathbf{f}_i$	Body deformation at time step i
f_{ij}^{I}	Mode-I angular variation function
f_{ij}^{II}	Mode-II angular variation function
$\mathbf{n}$	Normal direction to area
$\mathbf{p}_0$	Body force per unit volume (undeformed)
$\mathbf{p}$	Body force per unit volume (deformed)
r	Polar coordinate (distance)
t	Brazilian disc test: specimen thickness
$\mathbf{t}$	Real stress vector
$\mathbf{u}$	Displacement vector
x_0	Eulerian coordinate in stress-free configuration
x_i	Eulerian coordinate
$\mathbf{C}$	Right Cauchy-Green tensor
E	Modulus of elasticity
$\mathbf{E}$	Lagrangian strain tensor
E_G	Energy released from the propagation of a crack
$\mathbf{F}$	Deformation gradient
G	Fracture energy
$\mathbf{I}$	Identity tensor
J	Jacobian of the deformation gradient matrix
K_I	Mode-I stress intensity factor
K_{II}	Mode-II stress intensity factor
K_{III}	Mode-III stress intensity factor

K_{Ic}	Fracture toughness
P_{max}	Brazilian disc test: maximum (peak) load
P_{min}	Brazilian disc test: minimum (residual) load
R	Brazilian disc specimen radius
R_c	Brazilian disc test: distance of a point from disc centre
$\mathbf{S}$	First Piola-Kirchoff stress tensor
T	T-stress
$\mathbf{X}$	Position vector (undeformed configuration)
X_i	Lagrangian coordinate
Y_i	Dimensionless shape stress intensity factor
$\delta\mathbf{d}$	Virtual rate of deformation
$\delta\mathbf{v}$	Arbitrary virtual velocity
δW	First variation of the work W
φ	Deformation function
λ	Lame first parameter
μ	Lame second parameter
σ_{ij}	Cauchy stress tensor component
σ_{ij}^0	Finite stress at crack tip
σ_∞	Infinite stress at crack tip
$\sigma_{\theta\theta}$	Tangential stress field around crack tip
σ_t	Brazilian disc test: tensile strength
ϑ	Polar coordinate (angle)
Δa	Small element area
$\Delta\mathbf{p}$	Resultant force vector

Phase field model

b	Stiffness matrix coefficient
c	Normalisation constant
$\mathbb{c}$	Cauchy stress tensor
d	Mass matrix coefficient
g	Force vector coefficient
k_ε	Positive regularisation parameter
$\mathbb{k}$	Assembled stiffness matrix for smeared crack approach framework
ℓ	Power of the norm of the function defined in the SBV space
s	Damage parameter

s_i	Damage parameter at time step i
v	Perturbation for deformation as minimisation variable
w	Perturbation for damage as minimisation variable
$\mathcal{D}$	Domain of functions belonging to a GSBV space
$\mathbb{E}$	Material elasticity tensor
$\mathcal{E}$	Total energy of a body
$F_{i,j}^{(e)}$	Force vector component for element Ω_e
$\mathcal{F}$	Total energy of a two-dimensional body
$\mathcal{H}$	Hausdroff measure
K	Fractured zone
$K_{i,j}^{(e)}$	Stiffness matrix component for element Ω_e
L	Space of functions having integrable power of the absolute value
$M_{i,j}^{(e)}$	Mass matrix component for element Ω_e
S_f	Discontinuity points set
W	Stored energy function
W^+	Stored energy function part with positive Jacobian
W^-	Stored energy function part with negative Jacobian
X	Metric space
$\partial_i\Omega$	i-th portion of the boundary of Ω
ε	Material length scale parameter
ϕ	Weight function for FE discretisation
∇_0	Gradient with respect to x_0
Ψ	Extension of the stored energy function for neo-Hookean materials to the compressible range
Ω	Physical domain (undeformed body)
Ω'	Logical domain
Ω_0	Physical domain in stress-free configuration
Ω'_0	Logical domain in stress-free configuration
Ω_e	Element of FE discretisation
Ω_i	Physical domain at time step i

Configurational force method

g_c	Critical limit of energy release per unit area of Γ
$\mathbf{w}$	Displacement field in spatial domain

$\mathbf{x}$	Position vector
$\mathbf{y}$	Physical displacements
$\mathbf{z}$	Position vector in spatial domain
$\dot{A}_\Gamma$	Change of crack surface area
$\mathbf{A}_{\partial\Gamma}$	Orientation of the current crack front
$\mathcal{B}_t$	Material domain
$\mathbf{G}_{\partial\Gamma}$	Configurational force at crack front
$\mathcal{P}$	Power of external work on body
$\mathbf{S}_\mathbf{D}$	First Piola-Kirchoff stress tensor
$\dot{\mathcal{U}}$	Variation of internal energy
$\dot{\mathcal{U}}_\Gamma$	Variation of internal crack energy
$\dot{\mathcal{U}}_{\mathcal{B}_t}$	Variation of internal body energy
$\mathbf{W}$	Displacement field in material domain
$\mathbf{Z}$	Position vector in material domain
γ	Surface energy
$\partial\mathcal{B}_t$	Material domain boundary
$\mathbf{\Sigma}_\mathbf{D}$	Eshelbey stress tensor

Modelling of uncertainties

d_r	Reduced-order random field size
$d_E(i,j)$	Distance (Euclidean) between barycentres of elements i and j
$d_M(i,j)$	Distance (Geodesic) between barycentres of elements i and j
$\bar{f}$	Mean of the stochastic field
$\hat{f}^{(i)}$	Fluctuating part of the random field
$h(\mathbf{x})$	Zero-mean homogeneous Gaussian field
$g(\mathbf{x})$	Zero-mean homogeneous non-Gaussian field
k_r	Neighbourhood size for dimensionality reduction
$k^{(e)}$	Stochastic stiffness matrix (one element)
$k_0^{(e)}$	Deterministic part of $k^{(e)}$
l_c	Correlation length
l_m	Micro-scale dimension
l_M	Macro-scale dimension
m	Weibull shape parameter
$\hat{m}$	Estimated Weibull shape parameter
$p(x)$	Probability Density Function

t	Traction force applied at macroscale
u_i	Uniformly distributed random variable
x	Observed value of a random variable
x_M	Spatial coordinate at macrospace
x_N	Normally distributed random variable
x_{iN}	Normally distributed random variable (multivariate case)
A_n	Oscillation amplitude of the fluctuating function
$\mathbf{C}$	Cholesky decomposition of covariance matrix
$\mathbf{C}_{ff}$	Autocovariance function
$\mathfrak{C}$	Centered distance matrix
D	Random field size (prior to dimensionality reduction)
$\mathbf{D}_{\mathbf{M}}$	Matrix of shortest path distances
$E[\cdot]$	Expectation
Ev	Event
G	Cumulative distribution function of g(x)
G_{FE}	Fracture energy applied to finite element
$\mathcal{G}$	Neighbourhood graph
$\mathbf{H}$	Centering matrix
$\mathbf{K}_0$	Assembled deterministic stiffness matrix
L	Likelihood function
$P(x)$	Cumulative Density Function
Pr	Probability
Q^2	Q-Q estimation coefficient
S	Sample space
S_{ff}	Spectral density function
V	Variance
X	Random variable
$\bar{X}$	Sample mean value
Z	Normally distributed random variable with zero-mean
$\delta_n^{(i)}$	Independent random phase angle
δ_{ij}	Kronecker delta
ϵ_m	Microscopic strain vector
ϵ_M	Macroscopic strain vector
ι_i	Solutions for graphical resolution of K-L expansion equations
λ	Weibull scale parameter

$\hat{\lambda}$	Estimated Weibull scale parameter
λ_d	Eigenvalues of centered distance matrix
λ_n	Eigenvalues of the autocovariance function
μ	Mean value
μ_{LN}	Mean value (lognormal distribution)
ϕ_n	Eigenfunctions of the autocovariance function
κ_i	Cut-off number (active region of S_{ff})
ρ	Correlation coefficient
σ	Standard deviation
$\bar{\sigma}$	Sample standard deviation
σ_{LN}	Standard deviation (lognormal distribution)
σ_m	Microscopic stress
σ_M	Macroscopic stress
θ	Probability statistics
$\hat{\theta}$	Likelihood function maximiser
ξ_n	Set of uncorrelated random variables
ζ	Weibull distributed random variable
ζ_{iW}	Weibull distributed random variable (multivariate case)
ζ_0	Weibull scale parameter
$\hat{\zeta}_0$	Estimated Weibull scale parameter
$\Delta k^{(e)}$	Fluctuating part of $k^{(e)}$
$\Delta\mathbf{K}$	Assembled fluctuating part of $\mathbf{K}$
Γ	Gamma function
Φ	CDF of standard normal random variable
$\mathbf{\Sigma}$	Covariance matrix
Ω_m	RVE surface (2D) or volume (3D)

Abbreviations

BVP	**B**oundary **V**alue **P**roblem
CDF	**C**umulative **D**ensity **F**unction
DEM	**D**iscrete **E**lement **M**ethod
EOLE	**E**xpansion **O**ptimal **L**inear **E**stimation
FE	**F**inite **E**element
FEM	**F**inite **E**element **M**ethod
GMTS	**G**eneralised **M**aximum **T**ensile **S**tress
GSBV	**G**eneralised **S**o**B**ole**V** Space
IGA	Iso**G**eometrical **A**nalysis
IsoMap	**Iso**metric **Map**ping
KL	**K**arhunen **L**oeve
LEFM	**L**inear **E**lastic **F**racture **M**echanics
LHS	**L**atin **H**ypercube **S**ampling
MCS	**M**onte **C**arlo **S**imulation
MLE	**M**aximum **L**ikelyhood **E**stimation
MOAB	**M**esh **O**rientated dat**AB**ase
MOR	**M**odel **O**rder **R**eduction
NORTA	**Nor**mal **T**o **A**nithing
OLE	**O**ptimal **L**inear **E**stimation
PCA	**P**rincipal **C**omponent **A**nalysis
PDE	**P**artial **D**ifferential **E**quation
PDF	**P**robability **D**ensity **F**unction
PETSc	**P**ortable, **E**xtensible **T**oolkit for **Sc**ientific Computation

RF	**R**andom **F**ield
RVE	**R**epresentative **V**olume **E**lement
SBV	**S**o**B**ole**V** Space
SDF	**S**pectral **D**ensity **F**unction
SENS	**S**ingle **E**dge **N**otched **S**hear
SFEM	**S**tochastic **F**inite **E**element **M**ethod
SIF	**S**tress **I**ntensity **F**unction
TBM	**T**urning **B**ands **M**ethod
UQ	**U**ncertainty **Q**uantification
XFEM	e**X**tented **F**inite **E**element **M**ethod

Chapter 1

Introduction

1.1 Motivation

As alternative to experimental investigations and analytical solutions, numerical modelling has become an always more important tool for engineering applications. A numerical modelling tool must be computationally efficient and sufficiently reliable. Nowadays, a huge amount of commercial softwares are available, but improvements are always needed in order to quickly produce realistic results. In fact, very often the complexity of algorithms and numerical strategies developed for solving engineering problems can be an obstacle to their applicability, as the computational tools available, even if in continuos growth, cannot always support the computational cost required by them. For this reason, the computational efficiency of algorithms must be taken into account during the development and implementation of numerical models whenever possible and without losing accuracy.

One of the topics in continuum mechanics which deals with complex numerical frameworks is fracture mechanics, field which studies the propagation of cracks in materials. It uses principles of classical continuum mechanics for the identification of cracks and methodologies of experimental solid mechanics to characterise and quantify the resistance of materials to cracking. Macroscopically, damage evolution is identified as gradual loss of stiffness in the mechanical response of materials, while on a micro-scale, damage is described by nucleation, growth and coalescence of micro-cracks leading to failure (Bouchard, 2005).

Understanding how a crack propagates in the materials is essential for the design and construction of engineering structural components, such as beams and columns, and for expensive and dangerous operations such as gas extraction from gas reservoirs. Several approaches for the modelling of the crack propagation in homogeneous materials have been developed and applied to classical or newer computational strategies based on Finite Element Method (FEM) (Swedlow et al., 1966), Discrete Element Method (DEM) (Jirásek and Bažant, 1995) and peridynamic theory (Silling et al., 2003). For all of them, the modelling of crack advancement requires a modification in the classical formulations of the Partial Differential Equations (PDEs) describing the equilibrium problems, due to the incorporation of material discontinuities and the creation of new domain boundaries.

In the context of the FEM, crack propagation has been considered with several approaches, and the majority of them can be grouped in two main categories: discrete or smeared. The discrete approach, introduced by Saouma and Ingraffea (1981), identifies the new crack as localised new boundaries of the material volume, while the smeared approach, introduced by Rashid (1968) looks at fracture by incorporating strain or displacement discontinuities into FE discretisation variables (Rena et al., 2008). Simulating the propagation of cracks using traditional finite element methods results however particularly challenging mainly due to the topology of the domain, which changes continuously during the simulations (Richardson et al., 2011).

Nevertheless, in reality, materials are disordered and crack paths are strongly influenced by material heterogeneities. A computational framework for modelling of crack propagation must therefore be able to provide a numerical setting to include randomness in material properties and accurately resolve realistic crack patterns (Figure 1.1).

Multiscale modelling is a very robust and elegant approach widely used to incorpo-

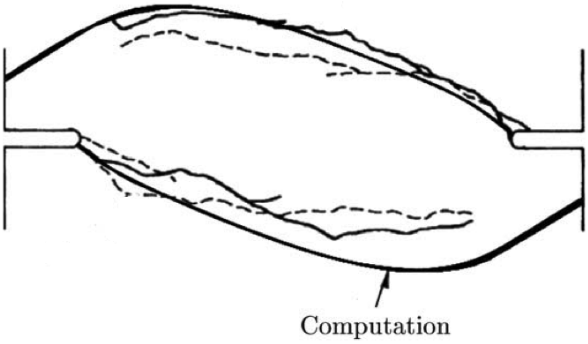

Figure 1.1: Crack path from homogeneous-based numerical model (smooth solid line) and comparison with experiments (tortuous lines) (Gasser and Holzapfel, 2006).

rate effect of heterogeneity in numerical models; nevertheless, materials with a very high degree of heterogeneity would require a certain degree of precision in the definition of the material to be modelled; the a priori knowledge of the material micro- and macrostructure are important especially for the correct definition of the micro- and, consequently, macroscale parameters (Weinan et al., 2007). Furthermore, when the problem under investigation needs knowledge of mechanical properties in space of materials located in areas reachable with difficulty, values for mechanical properties cannot be directly measured and therefore can only be defined using probability theory principles. Stochastic FEM (SFEM) is therefore developed, as standard FE methods are coupled with stochastic approaches, allowing the incorporation of material heterogeneity in standard FEM without the need of a detailed knowledge of material heterogeneity of each point in space.

1.2 Aims and Objectives

The aim of this research is to develop a novel theoretical and computationally efficient numerical framework for modelling of crack propagation in heterogeneous materials. Advanced SFEM models are developed to incorporate the effect of the material heterogeneity on crack paths. The framework is implemented into an existing computational codes that initially was developed for modelling of crack propagation in homogeneous materials. These implementations will allow:

1. predicting reliably crack paths and real mechanical behaviour of fracturing bodies;
2. extending the applicability of the existing code to a wider rang of engineering materials.

Objectives to achieve the project aim are:

1. to conduct an appropriate literature review, to investigate ability of the current approaches and software for modelling of the crack propagation in heterogeneous materials and identify the drawbacks of these approaches;
2. to highlight critical aspects of different approaches used to incorporate the effect of heterogeneity in numerical models;
3. to develop a novel stochastic modelling framework to include the effects of material heterogeneities on the crack paths and mechanical response;
4. to implement the modelling framework into an existing finite element code;

5. to optimise the computational efficiency of the developed methodologies;
6. to verify, validate the computational implementation and revise it in accordance with the results of the verification and validation phase.

1.3 Thesis outline

After this introduction, the thesis is organised as follows: in the second chapter a comprehensive review of the main methodologies for incorporation of material heterogeneity in numerical and computational frameworks for modelling of fractures is presented. The third chapter provides a comparison of two computational frameworks for modelling of crack propagation, (i) one based on a phase-field smeared-based approach which uses a scalar field to describe damage evolution in a body until its rupture and (ii) one based on a configurational force method which includes new fractures as new boundaries in the domain using a discrete approach; the chapter aims to explore and compare advantages and drawbacks of each approach and to choose which one will be implemented by incorporating the effect of materials' heterogeneity. The fourth chapter summarises the concepts of statistics used in this work to develop the stochastic methodology for modelling crack propagation in this thesis. The stochastic methodologies developed for optimal incorporation of material heterogeneity are detailed in chapters five and six. In the seventh chapter the results from numerical simulations and comparison with experimental data are presented. Concluding remarks and future works are presented in chapter eight.

Part I

Literature Review and Fundamental Concepts

Chapter 2

Literature Review

2.1 Introduction

The uncertainty assessment of engineering structures and materials has progressively become a significant topic of interest in engineering communities. Engineering practice has in fact revealed that uncertainties are very often found in the loading conditions, in the material and geometric properties of structures and components. Modelling of propagation of cracks involves safety, reliability and integrity assessment of structures; most of civil and environmental engineering materials, like concrete and rock, exhibit a heterogeneous nature due to their composition or natural formation processes. Fractures tend to propagate along the paths of least resistance, showing tortuous patterns: uncertainty in the location of the crack initiation point, flaws and possible manufacturing defects confer a non-deterministic nature to materials mechanical behaviour. In this sense, homogeneous-based numerical frameworks developed for modelling of crack propagation may lead to unrealistic and unreliable results, such as smooth crack paths and unrealistic and inaccurate values of material resistance.

Multiscale modelling method is one of the most powerful approaches used to incorporate effect of heterogeneity in computational models (due to its capability of including in the macroscopic governing equations the effect of local microstructures), for which, however, a detailed knowledge is required to model with this technique materials with a very high degree of heterogeneity; furthermore, when a full knowledge about the spatial distributions of heterogeneities is not available, values for mechanical properties essential to run a numerical model cannot be directly quantified and, therefore, can only be defined probabilistically. Stochastic approaches provide numerous advantages over multi-scale approaches, as the logical quantification of the uncertainties is conducted using probability theory. In this context, Stochastic Finite Element Method (SFEM) is an extension of the classical FEM, which solves problems for properties which are random (Zhou and Molinari, 2004). Both multiscale methods and stochastic approaches have been successfully applied to fracture mechanics problems, but, in conclusion, stochastic approaches provide suitable and satisfactory approximations where a full knowledge at fine scales is not available.

The aim of this chapter is to review the existing methodologies developed for modelling crack propagation on brittle materials of heterogeneous nature. More specifically, in the first part of this chapter the most relevant theory and literature about fracture mechanics will be reported, followed by a detailed description and comparison of two models for simulation the propagation of cracks in brittle materials. Following, a section reporting the two most important methodologies developed for including heterogeneity in numerical models will be presented. Finally a review of the existing models available for modelling crack propagation in heterogeneous materials will be produced, with a final focus on how damage in heterogeneous rock-like materials has been modelled.

2.2 Mechanics fundamentals

The mechanical formulations needed for a full comprehension of this work are presented in this section.

2.2.1 Continuum formulation: kinematics

For a body Ω in the reference (undeformed) configuration, $\mathbf{X}$ position vector is defined as

$$\mathbf{X} = X_i \mathbf{e}_i = X_1 \mathbf{e}_1 + X_2 \mathbf{e}_2 + X_3 \mathbf{e}_3 \tag{2.1}$$

where X_i are defined as Lagrangian coordinates and $\mathbf{e}_i$ represents the vector components directions. In the current (deformed) configuration the position vector $\mathbf{x}$ takes the form

$$\mathbf{x} = x_i \mathbf{e}_i = x_1 \mathbf{e}_1 + x_2 \mathbf{e}_2 + x_3 \mathbf{e}_3 \tag{2.2}$$

where x_i are the Eulerian coordinates.

A point from the reference to the current configuration is transformed (see Figure

2.1) using the function

$$\mathbf{x}(\mathbf{X}) = \varphi(\mathbf{X}) \tag{2.3}$$

and the change of position of a point of Ω due to the application of φ is defined using the displacement vector

$$\mathbf{u}(\mathbf{X}) = \mathbf{x}(\mathbf{X}) - \mathbf{X}. \tag{2.4}$$

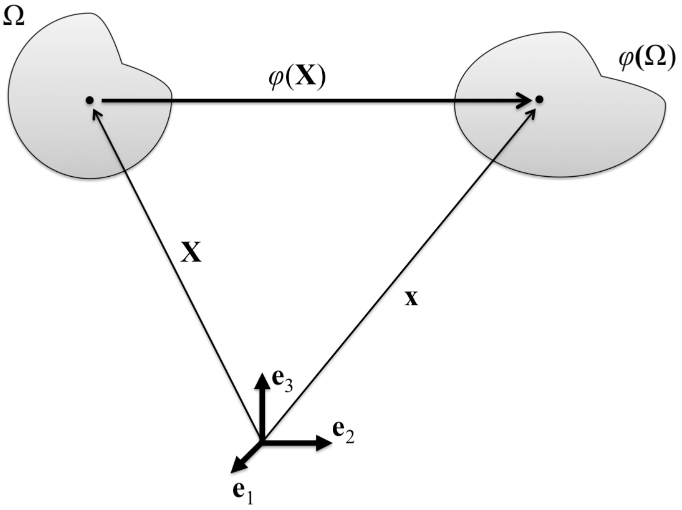

Figure 2.1: Point in reference and current configurations.

For a differential line element $d\mathbf{x}$, the transformation described above is defined by the deformation gradiend $\mathbf{F}$

$$\mathbf{F} = \frac{\partial \varphi(\mathbf{X})}{\partial \mathbf{X}} = \frac{\partial \mathbf{x}}{\partial \mathbf{X}} \tag{2.5}$$

.

2.2.2 Strain measures

As a measure of deformation, the variation in the scalar product of two elemental vectors $d\mathbf{X}_1$ and $d\mathbf{X}_2$ is considered. Knowing that

$$d\mathbf{x}_i = \mathbf{F} d\mathbf{X}_i \tag{2.6}$$

the scalar product $d\mathbf{x}_1 \cdot d\mathbf{x}_2$ is expressed via the vectors $d\mathbf{X}_1$ and $d\mathbf{X}_2$ as

$$d\mathbf{x}_1 \cdot d\mathbf{x}_2 = d\mathbf{X}_1 \cdot \mathbf{C} d\mathbf{X}_2 \tag{2.7}$$

where $\mathbf{C}$ is the right Cauchy-Green deformation tensor

$$\mathbf{C} = \mathbf{F}^T \mathbf{F}. \tag{2.8}$$

The variation in the scalar product (absolute elongation) can now be expressed in terms of the vectors $d\mathbf{X}_1$ and $d\mathbf{X}_2$ as

$$\frac{1}{2}(d\mathbf{x}_1 \cdot d\mathbf{x}_2 - d\mathbf{X}_1 \cdot d\mathbf{X}_2) = d\mathbf{X}_1 \cdot \mathbf{E} d\mathbf{X}_2 \tag{2.9}$$

where $\mathbf{E}$ in the Lagrangian strain tensor defined as

$$\mathbf{E} = \frac{1}{2}(\mathbf{C} - \mathbf{I}) \tag{2.10}$$

and where $\mathbf{I}$ is the identity tensor.

2.2.3 Equilibrium and stress measures

Let's now consider a point in the body in its deformed configuration where is found the real stress vector $\mathbf{t}$ being $\Delta\mathbf{p}$ the force resultant and Δa a small element of area of the body

$$\mathbf{t}(\mathbf{n}) = \lim_{\Delta a \to 0} \frac{\Delta\mathbf{p}}{\Delta a} \tag{2.11}$$

where $\mathbf{n}$ is the direction normal to Δa. In order to define what is called *stress tensor* the three components of $\mathbf{t}$ are expresses as a function of the three directions

$$\mathbf{t}(\mathbf{e}_1) = \sigma_{11}\mathbf{e}_1 + \sigma_{21}\mathbf{e}_2 + \sigma_{31}\mathbf{e}_3 \tag{2.12a}$$

$$\mathbf{t}(\mathbf{e}_2) = \sigma_{12}\mathbf{e}_1 + \sigma_{22}\mathbf{e}_2 + \sigma_{32}\mathbf{e}_3 \tag{2.12b}$$

$$\mathbf{t}(\mathbf{e}_3) = \sigma_{13}\mathbf{e}_1 + \sigma_{23}\mathbf{e}_2 + \sigma_{33}\mathbf{e}_3 \tag{2.12c}$$

where σ_{ij} are the components of the *Cauchy stress tensor.* In Figure 2.2 the decomposition of $\mathbf{t}(\mathbf{e}_i)$ according to σ_{ij} is shown on a small element. In general form, the stress $\mathbf{t}$ can be written as a function of σ and $\mathbf{n}$ as

$$\mathbf{t}(\mathbf{n}) = \sigma\mathbf{n}. \tag{2.13}$$

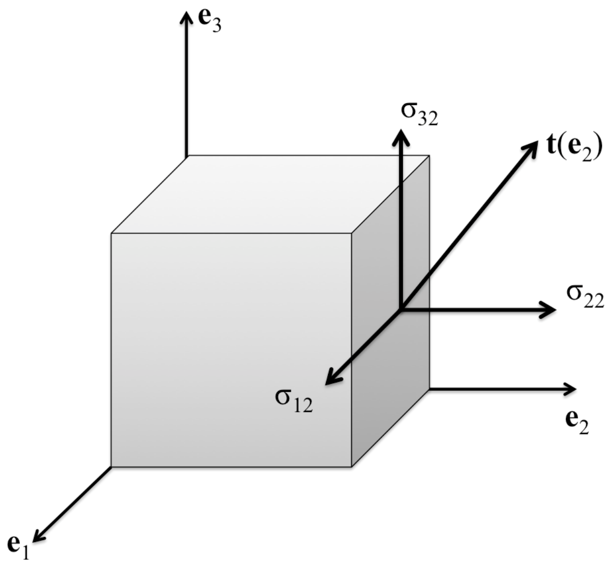

Figure 2.2: Cauchy stress components.

The body forces (per unit volume) acting on the body and surface forces (per unit area) acting on its boundaries have to satisfy the following condition of equilibrium

$$\int_{\Omega} \mathbf{p} \, \mathrm{d}\Omega + \int_{\partial\Omega} \mathbf{t} \, \mathrm{d}\partial\Omega = 0, \tag{2.14}$$

which, by using Eq. 2.13 can be written as

$$\int_{\Omega} \mathbf{p} \, \mathrm{d}\Omega + \int_{\partial\Omega} \sigma \mathbf{n} \, \mathrm{d}\partial\Omega = 0. \tag{2.15}$$

Using Gauss theorem, the second term of the left hand side of Eq. 2.15 can be rewritten and has the form

$$\int_{\Omega} \mathrm{div}(\sigma) + \mathbf{p} \, \mathrm{d}\Omega = 0 \tag{2.16}$$

which, if applied to an enclosed portion of the considered body is expresses by

$$\mathrm{div}(\sigma) + \mathbf{p} = 0 \tag{2.17}$$

known as *local spatial equilibrium equation.*
The stress tensor which is the energetic conjugate of the deformation gradient $\mathbf{F}$ is

the first Piola-Kirchoff stress tensor $\mathbf{S}$ given as

$$\mathbf{S} = J\sigma\mathbf{F}^{-T} \tag{2.18}$$

where $J = \det\mathbf{F}$ is the Jacobian of the deformation gradient matrix. The equilibrium Equation 2.17 can be therefore rewritten in the form

$$\mathrm{DIV}(\mathbf{S}) + \mathbf{p}_0 = 0 \tag{2.19}$$

where $\mathrm{DIV}(\mathbf{S})$ is the divergence of $\mathbf{S}$ with respect to the initial configuration and $\mathbf{p}_0 = J\mathbf{p}$ represents the body force per unit volume (undeformed).

2.2.4 Finite Element fundamentals and variational formulation

Eq. 2.17 represents the basic differential equation describing the equilibrium of a body subjected to a system of forces. Together with the boundary conditions, it is the starting point for the finite element formulation, which is one of the most known methods for solving differential equations in engineering practice.

Normally, Eq. 2.17 is used to obtain the weak formulation of the problem together with the principle of virtual work. An arbitrary virtual velocity (or perturbation) $\delta\mathbf{v}$ from the current configuration of the body is considered, and multiplied by Eq. 2.17. This formulation if then integrated over the volume of the body to obtain the variational formulation defined as

$$\delta W = \int_\Omega (\mathrm{div}(\sigma) + \mathbf{p}) \cdot \delta\mathbf{v}\, \mathrm{d}\Omega = 0 \tag{2.20}$$

which, after applying the Gauss theorem, expressing the equation terms as follows (Bonet and Wood, 1997)

$$\mathrm{div}(\sigma\delta\mathbf{v}) = (\mathrm{div}(\sigma)) \cdot \delta\mathbf{v} + \sigma \colon \nabla\delta\mathbf{v} \tag{2.21a}$$

$$\mathbf{n} \cdot \sigma\delta\mathbf{v} = \delta\mathbf{v} \cdot \mathbf{t} \tag{2.21b}$$

and rewriting $\nabla\delta\mathbf{v}$ in terms of $\delta\mathbf{d}$, symmetric virtual rate of deformation, the *spatial virtual work equation* is obtained as (Bonet and Wood, 1997)

$$\delta W = \int_\Omega \sigma \colon \delta\mathbf{d}\, \mathrm{d}\Omega - \int_\Omega \mathbf{p}\delta\mathbf{v}\, \mathrm{d}\Omega - \int_{\partial\Omega} \mathbf{t} \cdot \delta\mathbf{v}\, \mathrm{d}\partial\Omega = 0. \tag{2.22}$$

Eq. 2.22 is the fundamental equation describing the equilibrium state of a deformable body, basis for the finite element discretisation.

The main steps for solving a problem by means of FEM can be summarised as follows (Fish and Belytschko, 2007):

1. definition of the PDEs describing the physical problem and of the relative mechanical properties (e.g. modulus of elasticity);
2. definition of the problem domain and boundary conditions;
3. discretisation of the domain with elements, having unknown variables (e.g. displacements) allocated to each node with opportune degrees of freedom (e.g. 2 translational and 1 rotational in case of two-dimensional problems);
4. definition of suitable *weight functions* used to represent the distribution of the unknowns of the problem on each element;
5. definition of the stiffness matrix for each element and final assembly for the final linear problem and application of the boundary conditions (as values of problem unknowns which are given and assigned to selected nodes);
6. linear problem resolution.

2.3 Fracture Mechanics

In recent years, a growing number of researchers have focused on the problem of modelling heterogeneous materials containing discontinuities. In fact, practice reveals that the presence of heterogeneous structure, enclosed joints, micro-cracks, natural discontinuities and laminations can significantly affect the strength and failure mechanism of materials.

From a macroscopic standpoint, fracture is seen as the rupture separation of a structural component into two or more parts due to the propagation of cracks. The process involves the nucleation, increase and coalescence of micro-defects and voids in the material. Thus, in analysing cracks in bodies ideally researches would need to take into consideration all these aspects happening at different length scales, and the related macroscopic effects due to the loading conditions, environmental factors, and the geometric properties of the member (Erdogan, 2000).

From the standpoint of engineering applications, the theories developed from continuum mechanics and thermodynamics principles created the formulations capable of modelling and describe failure of materials. It is generally considered that the material contains imperfections which may become as fracture initiation areas and that the body is a homogeneous continuum such that the dimension of an imperfection is large if compared to the characteristic material microstructure. The problem is, therefore, to study the influence of the applied loads, flaw geometries, environmental conditions and material behaviour on the fracture process in the solid as a subject now known as fracture mechanics (Erdogan, 2000).

2.3.1 Brittle Fracture

Despite over-design approaches used for designing structures and components, unexpected failures have been happening in several events recorded in the past. A sudden failure leads furthermore to issues related to structural safety, human lives, economical losses and services disruption. Numerous episodes of catastrophic failure can be found, such as bridge failures (e.g. Montrose suspension Bridge in 1830, Husselt Bridge in 1938, Point Pleasant Bridge in 1967, Mississippi Bridge in 2007), railway accidents due to cracks in wheels and rails (in UK, there has been an average of 200 deaths per year due to railway accidents (Erdogan, 2000)) or fracture in gas transmission lines, in which typically cracks may initiate at local defects aided by corrosion phenomena. The common aspect of these failure episodes is that they are encouraged by zones of high brittleness, notches, peak loads, temperature shocks and highly corrosive environments.

The very first theories developed for fracture mechanics were based on maximum stress principles (Wieghardt, 1907). Nevertheless, the basis of the approaches developed during the last century is the theory by Griffith (1921). The starting point of his theory is the concept of equilibrium as minimisation of the potential energy of a system: the problem of the rupture of elastic bodies is solved by considering the change in potential energy during the creation of new surfaces.

Before Griffith, by means of the maximum stress principles Inglis (1913) analysed the problem of a flat plate with an elliptical hole subjected to far end stress σ as shown in Figure 2.3. The stress at the tip of the major axis is calculated as (Inglis, 1913)

$$\sigma_\infty = \sigma \left(1 + \frac{2a}{b} \right). \tag{2.23}$$

where a and b represent half of the length of the major and minor axis, respectively. If b is very small as shown in Figure 2.3 and, consequently, $a >> b$, the stress at the crack tip tends to ∞. The mathematical difficulty of this approach can be indeed observed in the case of perfectly sharp crack, where b goes to zero, leading therefore the stress to go to infinity at the crack tip. This solution is physically incorrect (Erdogan, 2000), because the predicted results would show that materials have near-zero strength: the stress near crack tip would go to infinite also for small loads, generating the rupture of the internal bonds. In his theory, Griffith developed a model for a cracked system in terms of a reversible thermodynamic process. Through his experiments on glass specimens, he assumed that pre-existing defects propagate under the influence of an applied stress due to a variation of the energy in the system. Therefore he considered fracture in bodies as physical process that needs energy to create or extend new crack surfaces (Griffith, 1921).

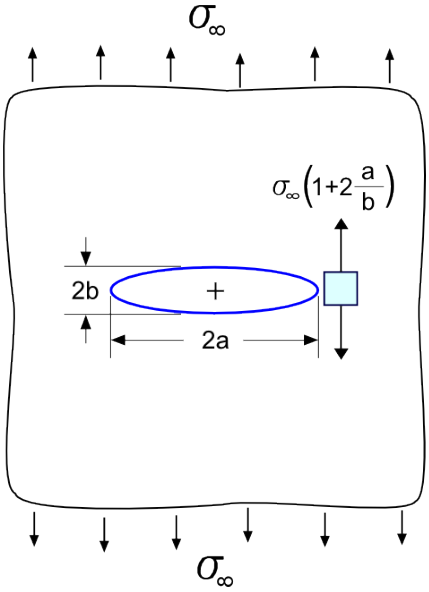

Figure 2.3: Stress distribution according to Inglis' solution: plate with elliptical hole subjected to uniform tension (McGinty, 2017).

Thereby, Griffith's theory is not directly concerned about crack tip processes or the micro-mechanisms of crack advancement, but based his research on the fact that "there is a simple energy balance consisting of a decrease in potential energy (energy accumulated during the deformation process) within the stressed body due to crack extension and this decrease is balanced by increase in surface energy due to increased crack surface" (Griffith, 1921).

Calling E_G the energy released from the propagation of the micro-crack, the stability condition, under a loading P, is expressed by $E_G(P) < G$. G is a characteristic of the material called *fracture energy* and represents the energy related to its resistance against the extension of the cracks; G is calculated as the ratio between the energy required for the formation of a new crack and the fracture surface (Griffith, 1921). From Griffith's theory, it is worth highlighting that brittle fracture can not initiate unless defects (or any other features such as notches, sharp edges or similar) already exist.

Starting from Inglis' solution of Eq. 2.23, Griffith quantified the increase in deformation energy due to applied loads and boundary conditions and, from the energy balance, he calculated the amount of stress corresponding to fracture as

$$\sigma = \sqrt{\frac{2GE^*}{\pi a}} \tag{2.24}$$

where $E^* = E$ for plane stress and $E^* = E/(1-\nu^2)$ for plane strain conditions [1] and a is the half crack length. In this way Griffith resolved the infinite stress paradox and proved that fracture stress depends on the flaw size.

2.3.2 Irwin's contribution: crack tip transition zone and Linear Elastic Fracture Mechanics (LEFM)

Griffith's theory, largely ignored until 1950's, has been the basis for further contributions. The most relevant to report at this stage is the theory of Irwin (1957), who extended Griffith's theory studying the crack propagation phenomenon in ductile materials and considered the role of the plastic zone created in proximity of a crack tip, as Griffith in his work did not account for any inelastic deformation around the crack front. According to Irwin if the size of the plastic zone in proximity of the crack tip is small compared to the dimension of the fracture, the energy going in the cracked area can be thought as coming from the body deformation and, as a consequence, its dependency on the stress state in proximity of the crack tip can be neglected. Therefore, the stresses values in the solid won't be in contraddiction with a solution of a crack purely elastic (Erdogan, 2000).

In addition to his study on ductile fracture, Irwin (1957) provided a method for the calculation of the amount of energy necessary for fracture in terms of stress field. The definition in this context involves a parameter called *Stress Intensity Factor* (SIF). SIF is defined, according to each of the three basic modes of crack deformations shown in Figure 2.4, as the stress field around the crack tip, considering crack

---

[1] Plane stress is the state of stress in which the normal stress σ_z and the shear stresses σ_{xz} and σ_{yz} directed perpendicular to the $x-y$ plane are assumed to be zero. Plane strain is the state of strain in which the strain normal to the $x-y$ plane, ε_z and the shear strain γ_{xz} and γ_{yz} are assumed to be zero.

length a, applied stress σ_N and a shape factor Y_i:

$$K_I = Y_I \sigma_I \sqrt{a} \tag{2.25a}$$

$$K_{II} = Y_{II} \sigma_{II} \sqrt{a} \tag{2.25b}$$

$$K_{III} = Y_{III} \sigma_{III} \sqrt{a} \tag{2.25c}$$

For each of these modes, crack extension may only take place in the direction of the original orientation of the crack. It is very common to find a mixed-mode opening situation, where a superposition of two (plane stress) or three modes is observed; the individual contributions to a given stress component are in fact additive. Considering the problem of a cracked plate in plane stress condition (ignoring mode III failure), total stress σ_{ij} is given by

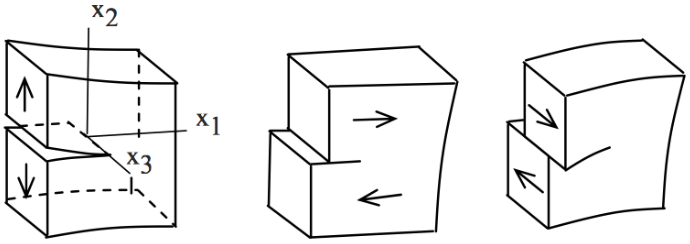

Figure 2.4: Fracture modes: Mode I Opening (left); Mode II In-Plane Shear (middle); Mode III Out-Of-Plane Shear (right) (Bui, 2007).

$$\sigma_{ij}(r, \vartheta) = \frac{K_I}{\sqrt{2\pi r}} f_{ij}^{I}(\vartheta) + \frac{K_{II}}{\sqrt{2\pi r}} f_{ij}^{II}(\vartheta) + \sigma_{ij}^{0} + O(\sqrt{r}) \tag{2.26}$$

where r and ϑ represent the polar coordinates of each point of the domain with respect to the crack tip, $i, j = x, y$ and σ_{ij}^0 indicates the finite stress at the crack tip. $f_{ij}^{I}(\vartheta)$ and $f_{ij}^{II}(\vartheta)$ represent the angular variation functions for mode I and II respectively, and are given by

$$f_{xx}^{I}(\vartheta) = \cos\left(\frac{1}{2}\vartheta\right)\left(1 - \sin\left(\frac{1}{2}\vartheta\right)\sin\left(\frac{3}{2}\vartheta\right)\right) \tag{2.27a}$$

$$f_{yy}^{I}(\vartheta) = \cos\left(\frac{1}{2}\vartheta\right)\left(1 + \sin\left(\frac{1}{2}\vartheta\right)\sin\left(\frac{3}{2}\vartheta\right)\right) \tag{2.27b}$$

$$f_{xy}^{I}(\vartheta) = \cos\left(\frac{1}{2}\vartheta\right)\sin\left(\frac{1}{2}\vartheta\right)\sin\left(\frac{3}{2}\vartheta\right) \tag{2.27c}$$

$$f_{xx}^{II}(\vartheta) = -\sin(\frac{1}{2}\vartheta)\left(2 + \cos(\frac{1}{2}\vartheta)\cos(\frac{3}{2}\vartheta)\right) \tag{2.27d}$$

$$f_{yy}^{II}(\vartheta) = \cos(\frac{1}{2}\vartheta)\sin(\frac{1}{2}\vartheta)\sin(\frac{3}{2}\vartheta) \tag{2.27e}$$

$$f_{xy}^{II}(\vartheta) = \cos(\frac{1}{2}\vartheta)\left(1 - \sin(\frac{1}{2}\vartheta)\sin(\frac{3}{2}\vartheta)\right), \tag{2.27f}$$

equations defined with the concept of linear elastic fracture mechanics (LEFM), according to which material's structure follows Hooke's law, global behaviour is linear elastic and any local small-scale crack tip plasticity is neglected. The formulas above allow thereby the characterisation of stress fields in proximity of the crack tip.

Let's now consider the example of a plate with a pre-existent crack. As fracture criteria, it is considered the stress state around the crack tip, characterised by K_I. Crack growth will happen when K_I reaches its value of critical SIF or *fracture toughness* K_{Ic}:

$$K_I = K_{Ic}. \tag{2.28}$$

Then, Irwin evaluated the amount of energy released from K_I and the elastic modulus E, as

$$G = \frac{K_I}{E^*}. \tag{2.29}$$

Typical values of fracture toughness of some materials are shown in Table 2.1.

Table 2.1: Typical values of K_{Ic} for some common materials.

Material	K_{Ic} (MN/m$^{3/2}$)
Mild Steel	140
Titanium alloys	55 - 120
High carbon steel	30
Nickel, copper	>100
Concrete (steel reinforced)	10 - 15
Concrete (unreinforced)	0.2
Glasses, rocks	1
Ceramics (Allumina, SiC)	3 - 5
Nylon	3
Polyester	0.5

2.4 Smeared and discrete approaches for FE modelling of fracture

The basic concepts of fracture mechanics provided in the previous paragraph are the theoretical basis of all the modelling approaches developed in the last century. Finite element (FE) frameworks for fracture analysis have been historically categorised in two groups of approaches: discrete and smeared. The first group of methods relies on a discrete and explicit representation of a crack in a FE discretisation. This approach has been introduced by Saouma and Ingraffea (1981) and identifies the new crack as localised new boundaries of the body. With a discrete crack model, in order to obtain realistic crack patterns, a method for adaptating the discretised domain to accommodate varying crack directions and to properly take into consideration remeshing near the crack tip must be adopted. The second group of approaches, introduced by Rashid (1968), looks at fracture by including displacement jumps into standard FE approximations (Rena et al., 2008). Numerical simulation of propagation of cracks via smeared FEM presents several challenges related, for example, to the topology of the domain, which continuously changes with the simulations (Richardson et al., 2011). If suitable strategies (such as mesh refinement) are not incorporated, is likely that classical smeared models exhibit mesh sensitivity and incorrect failure modes. Even when mesh refinement techniques are included to achieve model convergence, extreme mesh refinements at crack tip may introduce bias for the direction of crack propagation (Bazant and Lin, 1988).

A few comparative studies between smeared and discrete approaches in FEM have been carried out (Steinke et al., 2016; May et al., 2016; Mosler and Meschke, 2004; Latha and Garaga, 2012; Brighenti et al., 2013) for problems with loads applied in both quasi-static and dynamic conditions. These (and more) studies showed how both approaches present their own advantages and disadvantages, and that the choice of one method over the other mainly depends on the considered case study (Jendele et al., 2001): discrete crack models are generally more appropriate for modelling cases in which one or more crack are dominant and where the type of failure and crack geometry are well known and predictable; smeared crack models can better simulate the diffuse cracking patterns that appear due to the heterogeneity of materials and the presence of reinforcements. Furthermore, if neither the initiation mechanism nor the crack initiation point are known a priori, smeared crack models are usually more suitable for modelling the propagation of fractures (Noghabai, 1999).

Comparisons between smeared and discrete approaches have been carried out also for multi-physics problems (Sahimi, 2011). For example by studying hydro-fracture phenomena, even if a problem morphology is well-known, because of the irregularity in the solid-fluid interface in typical porous media, solving such a problem with a continuum approach can be practically and computationally unfeasible, as the determination of solid-fluid boundaries is particularly challenging, especially for large-scale porous media. The boundaries where one would have to solve the systems of PDEs can be so tortuous that the problem may become mathematically unmanageable. Discrete models are free of the limitations described above for continuum models; they seem to be more suitable for the description of phenomena at the microscopic level and have been extended to describe a number of phenomena at macroscopic scales. Their main disadvantage is the large computational effort required for a realistic modelling of the porous media (Sahimi, 2011). In fact, (and this aspect does not apply to multi-physics problems only), experience showed that discrete models are usually more computationally demanding, mainly because of the adaptive re-meshing techniques required to account for progressive failure.

A number of authors coupled smeared and discrete FEM approaches in order to combine the advantages from both approaches. A combined smeared-discrete approach has been used by Einsfeld et al. (1997) to study concrete structures, where the transition from smeared to discrete approaches is achieved in locations where strains localisation is observed. Gui et al. (2016) implemented a cohesive smeared-discrete FE framework for dynamic fracturing in rocks able to reproduce well compression, tension and shear failure behaviours. de Borst et al. (2004) showed how different advantages between smeared and discrete approaches can be summed up together by mean of "cohesive segments" method. In fact, the location of cohesive surfaces of finite size at random positions and in random directions in smeared finite element discretisation allows the modelling of diffuse crack paths. These cohesive segments can be extended, and a single and continuous crack can also be represented, allowing the simulation of the initiation and growth of a dominant crack. In this sense, the cohesive segments method can be seen as a connection between discrete and smeared crack models used in concrete fracture.

Nevertheless, since cohesive elements can only be located at the element boundaries, by using cohesive elements an a priori knowledge about the location of crack path is needed, or however cohesive surfaces must be provided between all internal continuum element borders: these aspects lead not only to an excessive increase of the degrees of freedom but also to a severe decrease of the structure stiffness (Kaliske et al., 2012).

In addition to classic Finite Element (smeared and discrete) methods, other methodologies of embedding strong discontinuities have been developed. One of the most well-known, introduced by Dolbow and Belytschko (1999), is the eXtended FE method (XFEM), in which discontinuities are included in a classical FE model by enriching the displacement field of the nodes on the basis of local partition of unity concept (Richardson et al., 2011): in this method the FE mesh is created independently from any possible crack topology, as the discretised domain doesn't have to be remeshed as the crack propagates.

Peridynamic theory is another method developed for modelling propagation of cracks (Madenci et al., 2016; Dipasquale et al., 2016). This mathematical theory extends classical continuum mechanics to incorporate discrete particles; propagation of crack is modelled considering the distance between particles to define the transition from continuous damage to fracture.

Other more recently methods developed for increasing computational efficiency and accuracy of results used also to describe fracture problems are meshless methods (Cai et al., 2016; Nguyen et al., 2016a; Belytschko et al., 1996). However, in this study, attention is focused only to classical FE methods (smeared and discrete) where the effect of heterogeneity will be included.

In the next two paragraphs, the focus will be on two numerical models, a smeared phase field approach based on a variational formulation for brittle failure (Del Piero et al., 2007) and a discrete fracture model based on the configurational-force method (Kaczmarczyk et al., 2014); both methods are representative of their respective class, and on their capability of reproducing realistic crack patterns and values of material resistance. Both methods are described: however, the incorporation of material heterogeneity will be executed on the phase field model (more details about this decision are provided in Chapter 3) and, therefore, the description of the configurational force method will be condensed to highlight its main features and formulations.

2.4.1 Phase field smeared approach: variational energy formulation

The core of the variational approach to fracture mechanics, based on the work described in Francfort and Marigo (1998), relies on association of a potential energy consisting of stored elastic energy, the work of external forces working in opposition to potential's force field, and the energy released through fracture to any crack and deformation configuration. It is considered a reference configuration $\Omega \subset \mathbb{R}^N$, $N = 2$, of a homogeneous elastic body containing a generic crack as shown in Figure 2.5. The total energy of the body is defined as

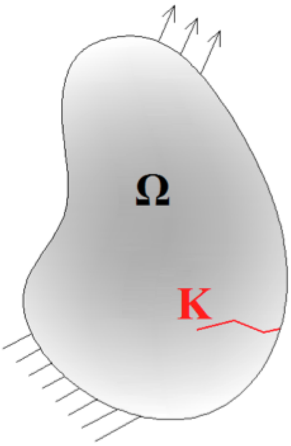

Figure 2.5: Cracked solid configuration and boundary conditions

$$\mathcal{E}(\boldsymbol{f}, K) = \int_{\Omega/K} W(\mathbf{F}(x))\,\mathrm{d}x + G\mathcal{H}^{N-1}(K) \tag{2.30}$$

where $\boldsymbol{f}$ is the body deformation, $K \subset \overline{\Omega}$ is the fractured zone, $W : \mathbb{R}^{N \times N} \to \mathbb{R}$ is the stored energy function, $\mathbf{F}$ is the deformation gradient, G is the fracture energy and $\mathcal{H}^{N-1}(K)$ is the Hausdroff measure of K which provides the measure of the length of the crack for sufficiently regular fractured zone.

In mathematics, Hausdroff measure is used to generalise lengths and areas, as it allows to measure a certain subset of $\mathbb{R}^N$. For the specific purpose of this thesis, $N-$dimensional Hausdroff measure and $N-$dimensional Lebesgue measure agree on $\mathbb{R}^N$ (Evans and Gariepy, 1992).

The first and the second terms on the right hand side of the Equation 2.30 represent bulk and surface energy of the body, respectively. Deformation of the elastic body under load increases the bulk energy. When this value reaches to a critical value in a given zone, it is energetically favourable for the system to release its energy. Therefore, crack growth is traced by consequent minimisation of energy function (i.e., Eq. 2.30) at fixed time steps.

The minimisation of the Eq. 2.30 with respect to any kinematically admissible displacement and any set of crack paths introduces a high level of complexity for the solution of the discontinuity problems, particularly due to the presence of the non-smooth values of the K parameter. Following the methodology proposed by Ambrosio and Tortorelli (1990), it is introduced K as a set of discontinuity points S_f of the function $\boldsymbol{f}$, and set the problem in a space of discontinuous functions. The formulation of the energy, by replacing the term K with a set of jump points, S_f of deformation in a Sobolev space SBV $(\Omega;\mathbb{R}^N)$, is therefore given by

$$\mathcal{E}(\boldsymbol{f}) = \int_{\Omega/K} W(\bigtriangledown \boldsymbol{f})\, \mathrm{d}x + G\mathcal{H}^{N-1}(S_f). \tag{2.31}$$

The presence of the term $\mathcal{H}^{N-1}$ (S_f) creates difficulties in the finite element discretisation of the function. To overcome such challenges, Eq. 2.31 is approximated, in the sense of Γ-convergence (Bourdin et al., 2000), using a family of numerically more tractable functionals defined over a Generalized Sobolev Space (GSBV).

Approximation via Γ-convergence

With the term *Sobolev Space* (SBV) is defined a vector space with functions having norm which is a combination of their L^q-norms (an L^q is the space of functions having integrable q^{th} power of the absolute value) and their derivatives.

Based on the regularised formulation of the energy function for brittle fracture problems presented in Bourdin et al. (2000) and Ambrosio and Tortorelli (1990), an auxiliary variable s, which is called damage parameter, is introduced. The parameter s is a regularised representation of the fractured zone defining the jump set in Equation 2.31. Therefore, a metric space X is considered, and its elements are pairs of $(\boldsymbol{f}, s)$. Then function $\mathcal{F}$: X → [0,+∞] is used, which is defined by

$$\mathcal{F}(\boldsymbol{f}, s) = \begin{cases} \mathcal{E}(\boldsymbol{f}) & \text{if } \boldsymbol{f} \in \mathcal{D},\ s \equiv 1, \\ +\infty & \text{otherwise} \end{cases} \tag{2.32}$$

where $\mathcal{D}$ is the domain of the functions belonging to GSBV. The problem of minimising $\{\mathcal{F}(f,s):(f,s) \in X\}$ to calculate the damage parameter is considered. The damage parameter provides a picture of the damage state of the body; for an undamaged and intact body, s is equal to 1 everywhere, while it goes to zero in proximity of the jump set S_f. Following Bourdin et al. (2000) the functional formulation for a generic $\ell > 1$ is expressed in the form provided by Ambrosio and Tortorelli (1990) as

$$\begin{aligned}\mathcal{F}_{\varepsilon}(\boldsymbol{f}, s) = &\int_{\Omega} (s^2(x_0) + k_{\varepsilon}) W(\boldsymbol{F}(x))\,\mathrm{d}x \\ &+ G \int_{\Omega'} \frac{\varepsilon^{\ell-1}}{\ell} |\bigtriangledown s(x)|^{\ell} + \frac{c}{\varepsilon \ell'}(1 - s(x))^{\ell}\,\mathrm{d}x\end{aligned} \tag{2.33}$$

where ℓ is the ℓ^{th} power of the norm of the function defined in the Sobolev space, $\ell' = \ell/(\ell\text{-}1)$, $c = (2\int_0^1 (1-t)^{\ell/\ell'}\,\mathrm{d}t)^{-\ell'}$ is the normalisation constant, k_{ε} is a positive regularisation parameter and ε is related to the material length scale. Bulk and surface terms are two integrations over two different domains Ω and Ω', physical domain and logical domain, respectively. Ω' is defined as open set such that

$$\Omega \subset \Omega', \qquad \partial_2\Omega \subset \partial\Omega', \qquad \mathrm{int}(\partial_1\Omega) \cap \partial\Omega' = \varnothing$$

where $\partial_1\Omega$ and $\partial_2\Omega$ are two disjoint parts of the boundary of Ω, and $\mathrm{int}(\partial_1\Omega)$ the interior of $\partial_1\Omega$ relative to $\partial\Omega$. The choice of the size of the logical domain is made on the consideration that it has to be big enough to avoid underestimation of the fracture energy when the crack reaches the boundary $\partial_1\Omega$.
For two-dimensional problem where $\ell = 2$, the total energy formulation for the body can be represented as:

$$\mathcal{F}(\boldsymbol{f}, s) = \int_{\Omega_0} (s^2 + k_{\varepsilon}) W(\bigtriangledown_0 \boldsymbol{f})\,\mathrm{d}x_0 + \frac{G}{2}\int_{\Omega_0'} (\varepsilon |\bigtriangledown_0 s|^2 + \frac{1}{\varepsilon}(1-s)^2)\,\mathrm{d}x_0 \tag{2.34}$$

where Ω_0 and Ω_0' represent initial unfractured and stress-free configuration of the body in the physical and logical domain, respectively, x_0 represents a physical point of the physical domain Ω_0 and $\bigtriangledown_0$ represents the gradient with respect to x_0.

Stored Energy formulation

Following Del Piero et al. (2007) an isotropic, compressible neo-Hookean type stored energy model is used and is defined as

$$W(\mathbf{F}) = \frac{\mu}{2}(\mathrm{tr}\mathbf{C} - 3) + \Psi(J) \tag{2.35}$$

where μ is the Lame second parameter, $\mathbf{C}$ is the right Cauchy-Green tensor and $J = \det \mathbf{F}$ is the Jacobian of the deformation gradient.
In the above equation, the first term represents the classical formulation of an incompressible neo-Hookean material and the second term is a convex function that

is defined as (Del Piero et al., 2007)

$$\Psi(J) = \begin{cases} \frac{\lambda}{2}(\ln J)^2 - \mu \ln J & 0 \leq J \leq j \\ \frac{\lambda}{2}(\ln J)^2 - \mu \ln J + (\lambda \ln J - \mu)\left(\frac{J-j}{J}\right) & J \geq j \end{cases} \tag{2.36}$$

where λ is the Lame first parameter and $j = e^{(\lambda+\mu)/\lambda}$. The Eq. 2.36 is directly related to surface deformation, as it is function of the Jacobian of the deformation gradient. As J goes to zero the stored energy function goes to infinity, penalising the extreme compression.

Numerical solution strategy

An approximation solution of minimisation of the Eq. 2.34 is achieved using an iterative procedure, shown in algorithm 1, which consists of imposing a stationary condition alternatively to one of the deformation and damage variables, while keeping the other variable fixed. For all $v \in W^{1,\ell}(\Omega, \mathbb{R}^n)$, $w \in W^{1,\ell}(\Omega_0)$, the aim is to find a deformation that satisfy the stationarity condition of

$$\delta\mathcal{F}_\varepsilon(\boldsymbol{f}_n, s_{n-1})[v, 0] = \int_{\Omega_0} (s_{n-1}^2(x_0) + k_\varepsilon) S(\triangledown_0 \boldsymbol{f}_n(x_0)) \triangledown_0 v(x_0)\, \mathrm{d}x_0 = 0 \tag{2.37}$$

and then for the scalar filed s stationary condition of

$$\delta\mathcal{F}_\varepsilon(\boldsymbol{f}_n, s_n)[0, w] = \int_{\Omega_0} 2W(\triangledown_0 \boldsymbol{f}_n) s_n w \, \mathrm{d}x_0 + G \int_{\Omega_0'} \left(\varepsilon \vartriangle s_n - \frac{1 - s_n}{\varepsilon}\right) w \, \mathrm{d}x_0 \tag{2.38}$$

where $\mathbf{S}(\mathbf{F}) = \frac{\partial}{\partial \mathbf{F}} W(\mathbf{F})$ is the first Piola-Kirchhoff stress tensor.
By taking the Updated Lagrangian formulation of Eq. 2.37 and linearisation of it the following is obtained (Del Piero et al., 2007)

$$\begin{aligned} \int_{\Omega_{n-1}} (s_{n-1}^2 + k_\varepsilon)\Big((\det \mathbf{F})^{-1}(\mathbf{I} \boxtimes \mathbf{F})[\mathbf{S}(\mathbf{F})] + \\ +(\det \mathbf{F})^{-1}(\mathbf{I} \boxtimes \mathbf{F}) \frac{\partial S(\mathbf{F})}{\partial F} (\mathbf{I} \boxtimes \mathbf{F})^T [\triangledown \bar{u}_n]\Big) \cdot \triangledown v \, \mathrm{d}x = 0 \end{aligned} \tag{2.39}$$

where $\boxtimes$ represents the conjugation product (defined, for two matrices Λ_1 and Λ_2 as $\Lambda_3(i_1, i_2, i_3, i_4) = \Lambda_1(i_1, i_3)\Lambda_2(i_2, i_4)$) (Del Piero et al., 2007), and using Eq. 2.36

$$\mathbf{S}(\mathbf{F}) = \begin{cases} \mu\mathbf{F} + (\lambda \ln J - \mu)\mathbf{F}^{-T} & 0 \leq J \leq j \\ \mu\mathbf{F} + \lambda e^{-(\lambda+\mu)/\lambda}\mathbf{F}^{-T} & J \geq j. \end{cases} \tag{2.40}$$

Applying the integration by parts, the final weak form of Eq. 2.38 is obtained

$$\int_{\Omega_0} 2W(\nabla_0 \boldsymbol{f}_n) s_n w \,\mathrm{d}x_0 - G \int_{\Omega_0'} \left(\varepsilon \, \triangle_0 \, s_n - \frac{1 - s_n}{\varepsilon} \right) w \,\mathrm{d}x_0 = 0. \tag{2.41}$$

MATLAB Partial Differential Equation Toolbox together with the Newton-Raphson iteration scheme is used to solve the above equations. The iteration stops when two consecutive pairs of solution (f_{n-1}, s_{n-1}) and (f_n, s_n) are close enough according to an identified convergence condition. In order to avoid the healing of the cracks, an approximation method was used to consider irreversibility condition for damage evolution. The methodology proposed by Del Piero et al. (2007) is followed. Based on that, irreversibility condition of $s_n(x) = s_{n-1}(x)$ if $s_n(x) > s_{n-1}(x)$ is set, and the value of damage parameter associated to each point in the body cannot exceed the one calculated at the previous time step.

Algorithm 1: Numerical solution procedure

```
Data: Model parameters, problem geometry and boundary conditions.
Initialization: set $(\boldsymbol{f}_n^0, \boldsymbol{s}_n^0) = (\boldsymbol{f}_{n-1}, \boldsymbol{s}_{n-1})$;
while $\|\boldsymbol{s}_n^j - \boldsymbol{s}_n^{j-1}\|_{L^\infty(\Omega_0)} > \boldsymbol{s}_{max}$ do
    for a given $(\boldsymbol{f}_n^{j-1}, \boldsymbol{s}_n^{j-1})$
    compute an approximate solution $\boldsymbol{f}_n^j$ for fixed $\boldsymbol{s}$
    compute $\boldsymbol{s}_n^j$ for fixed $\boldsymbol{f}$
end
Irreversibility condition: set $\boldsymbol{s}_n^j(x_0) = \boldsymbol{s}_n^0(x_0)$ at all nodal points at
    which $\boldsymbol{s}_n^0(x_0)$ becomes smaller than a given $\check{\boldsymbol{s}} > 0$
```

Furthermore, an adaptive h-refinement strategy is used to automatically refine the elements with values of s lower that given thresholds. At new nodes generated through the remeshing strategy, values of displacement and damage are calculated by linear interpolation from the existing nodes.

Matrix formulation for the FE discretisation

The two Equations 2.39 and 2.41 are solved by means of standard FEM and can be therefore written following in the basic PDE formulation

$$-\nabla(b\nabla u) + du = g \tag{2.42}$$

in a domain Ω as the classical *strong form* (with applied boundary conditions) of the problem (Fish and Belytschko, 2007). The Matlab ”pdetoolbox” package can solve PDE systems and assembling them directly for the coefficients b, d and g in the equations

$$K_{i,j}^{(e)} = \int_{\Omega_e} b \nabla \phi_j \nabla \phi_i \, \mathrm{d}x, \tag{2.43a}$$

$$M_{i,j}^{(e)} = \int_{\Omega_e} d \phi_j \phi_i \, \mathrm{d}x, \tag{2.43b}$$

$$F_{i}^{(e)} = \int_{\Omega_e} g \phi_i \, \mathrm{d}x, \tag{2.43c}$$

into the global system

$$\sum_{e=1}^{n} (\mathbf{K}^{(e)} + \mathbf{M}^{(e)}) \mathbf{u}^{(e)} = \mathbf{F}^{(e)}. \tag{2.44}$$

where n is the number of elements of the FE mesh, b, d and g represent the stiffness, mass and force coefficients respectively, ϕ are the linear weight functions used for the FE discretisation, $K_{i,j}^{(e)}$, $M_{i,j}^{(e)}$ and $F_{i}^{(e)}$ represent each component of the stiffness, mass matrices and force vector for a element Ω_e, respectively.

In order to obtain the matrix components of the linearised problem for fixed s Eq. 2.39 is considered; the section representing the constitutive model of the matrix is expressed as follows:

$$\Bbbk = (\det \mathbf{F})^{-1} (\mathbf{I} \boxtimes \mathbf{F}) [\mathbf{S}(\mathbf{F})] + (\det \mathbf{F})^{-1} (\mathbf{I} \boxtimes \mathbf{F}) \frac{\partial S(\mathbf{F})}{\partial F} (\mathbf{I} \boxtimes \mathbf{F})^T \tag{2.45}$$

From Eq. 2.45 two parts can be obtained, representing the Cauchy stress tensor, $\mathbb{c}$, and the material elasticity tensor, $\mathbb{E}$:

$$\mathbb{c}(\mathbf{F}) = (\det \mathbf{F})^{-1} (\mathbf{I} \boxtimes \mathbf{F}) [S(\mathbf{F})] \tag{2.46}$$

$$\mathbb{E}(\mathbf{F}) = (\det \mathbf{F})^{-1} (\mathbf{I} \boxtimes \mathbf{F}) \frac{\partial S}{\partial F} (\mathbf{I} \boxtimes \mathbf{F})^T \tag{2.47}$$

Using Eq. 2.40 the Piola-Kirchhoff stress tensor can be explicitly included into Eqs. 2.46 and 2.47 which can therefore take the form

$$\mathbb{c}(\mathbf{F}) = \mu J^{-1} \mathbf{F} \mathbf{F}^{-T} + J^{-1} (\lambda \log J - \mu) \mathbf{I} \tag{2.48}$$

$$\mathbb{E}(\mathbf{F}) = J^{-1} \lambda \mathbf{I} \otimes \mathbf{I} + (\mu - \lambda \log J (\mathbf{I} \boxtimes \mathbf{I} + (\mathbf{I} \boxtimes \mathbf{I})^T)) \tag{2.49}$$

In matrix form, the stiffness matrix for each element is defined as follows:

$$\hat{\mathbf{I}} \otimes \mathbb{c} = \mathbb{C} = \begin{bmatrix} \mathfrak{a} & \mathfrak{a} & \mathfrak{a} & \mathfrak{a} \\ 0 & 0 & 0 & 0 \\ 0 & 0 & 0 & 0 \\ \mathfrak{a} & \mathfrak{a} & \mathfrak{a} & \mathfrak{a} \end{bmatrix} + \begin{bmatrix} \mathfrak{b} & 0 & 0 & \mathfrak{b} \\ 0 & 0 & 0 & 0 \\ 0 & 0 & 0 & 0 \\ \mathfrak{b} & 0 & 0 & \mathfrak{b} \end{bmatrix} = \begin{bmatrix} \mathfrak{a}+\mathfrak{b} & \mathfrak{a} & \mathfrak{a} & \mathfrak{a}+\mathfrak{b} \\ 0 & 0 & 0 & 0 \\ 0 & 0 & 0 & 0 \\ \mathfrak{a}+\mathfrak{b} & \mathfrak{a} & \mathfrak{a} & \mathfrak{a}+\mathfrak{b} \end{bmatrix}$$

$$\mathbb{E} = \begin{bmatrix} \mathfrak{c} & 0 & 0 & 0 \\ 0 & \mathfrak{c} & 0 & 0 \\ 0 & 0 & \mathfrak{c} & 0 \\ 0 & 0 & 0 & \mathfrak{c} \end{bmatrix} + \begin{bmatrix} \mathfrak{d} & 0 & 0 & \mathfrak{d} \\ 0 & 0 & 0 & 0 \\ 0 & 0 & 0 & 0 \\ \mathfrak{d} & 0 & 0 & \mathfrak{d} \end{bmatrix} + \begin{bmatrix} \mathfrak{d} & 0 & 0 & 0 \\ 0 & 0 & \mathfrak{d} & 0 \\ 0 & \mathfrak{d} & 0 & 0 \\ 0 & 0 & 0 & \mathfrak{d} \end{bmatrix} = \begin{bmatrix} \mathfrak{c}+2\mathfrak{d} & 0 & 0 & \mathfrak{d} \\ 0 & \mathfrak{c} & \mathfrak{d} & 0 \\ 0 & \mathfrak{d} & \mathfrak{c} & 0 \\ \mathfrak{d} & 0 & 0 & \mathfrak{c}+2\mathfrak{d} \end{bmatrix}$$

where

$$\hat{\mathbf{I}} = \begin{bmatrix} 1 & 0 & 0 & 1 \\ 0 & 0 & 0 & 0 \\ 0 & 0 & 0 & 0 \\ 1 & 0 & 0 & 1 \end{bmatrix}$$

$$\mathfrak{a} = \mu J^{-1}\mathbf{F}\mathbf{F}^{-T}$$
$$\mathfrak{b} = -\mathfrak{d} = J^{-1}(\lambda \log J - \mu)$$
$$\mathfrak{c} = \lambda J^{-1}.$$

The final assembled stiffness matrix takes therefore the form

$$\mathbb{k} = \mathbb{C} + \mathbb{E} = \begin{bmatrix} \mathfrak{a}-\mathfrak{b}+\mathfrak{c} & \mathfrak{a} & \mathfrak{a} & \mathfrak{a} \\ 0 & \mathfrak{c} & -\mathfrak{b} & 0 \\ 0 & -\mathfrak{b} & \mathfrak{c} & 0 \\ \mathfrak{a} & \mathfrak{a} & \mathfrak{a} & \mathfrak{a}-\mathfrak{b}+\mathfrak{c} \end{bmatrix}.$$

where each component of $\mathbb{k}$ is used, in combination with the softening term $(s^2 + k_\varepsilon)$ as value for b in Eq. 2.43a (rearranged in order to meet the computational requirements of the stiffness matrix in the MATLAB subroutine). The second FE problem to be solved has the damage field as unknown and fixed $\mathbf{f}$. The formulation is more straightforward as it does not require any linearisation, being the problem already linear itself, and the values for coefficients b, d and g are given by

$$b = -\varepsilon \tag{2.50a}$$

$$d = \frac{2W}{G} + \varepsilon^{-1} \tag{2.50b}$$

$$g = \varepsilon^{-1}. \tag{2.50c}$$

2.4.2 Discrete approach: the configurational-force method

The discrete based approach considered in this study is the one proposed by Kaczmarczyk et al. (2014). This approach restricts the path of a crack to element faces, and is based on the principle of maximal energy dispassion, together with configurational forces concept. In this way forces at crack front at material and spatial equilibrium define the direction of crack propagation.

Thermodynamical equilibrium

Let's consider the thermodynamic system formed by a solid elastic body with a crack, assigned boundary conditions and applied forces which can do work on the system and develop energy in the volume. The reference material domain is related to both spatial and material domains by means of differentiable mappings, showed in Fig. 2.6 , employed to study both the deformation of material (in the physical space) and the crack evolution (in the material space). The spatial domain consists of a set of coordinates $\mathbf{z}$ related to the position of the finite element nodes in the medium, while the set of coordinates $\mathbf{Z}$ corresponds to the position of the material points. These sets are then employed for the calculation of spatial and material displacement fields ($\mathbf{w}$ and $\mathbf{W}$) relative to the reference domain χ:

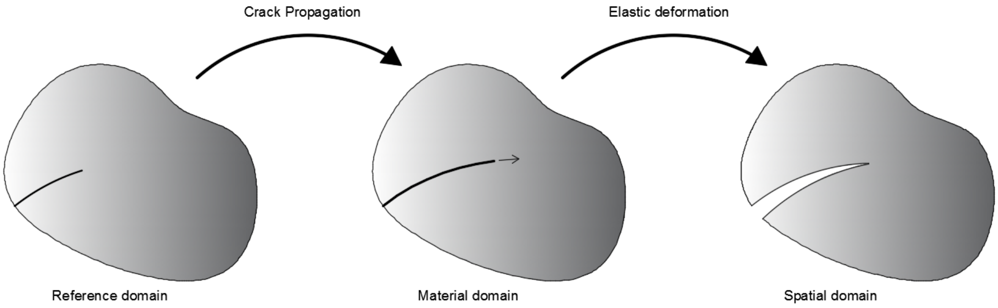

Figure 2.6: Deformation and topological change of a body with a crack.

$$\mathbf{w} = \mathbf{z} - \chi \tag{2.51}$$

$$\mathbf{W} = \mathbf{Z} - \chi, \tag{2.52}$$

and the physical displacements are then calculated as

$$\mathbf{y} = \mathbf{w} - \mathbf{W}. \tag{2.53}$$

From the energetic point of view, the crack front is considered to be the only area where there is exchange of energy between crack surface and the exterior. The power of external work on the body is expressed as

$$\mathcal{P} := \int_{\partial \mathcal{B}_t} \dot{\mathbf{y}} \cdot \mathbf{t} \, \mathrm{d}S = \int_{\partial \mathcal{B}_t} \{\dot{\mathbf{w}} \cdot \mathbf{t} - \dot{\mathbf{W}} \cdot \mathbf{F^T t}\} \, \mathrm{d}S \tag{2.54}$$

where $\mathcal{B}_t$ represents the material space and $\partial\mathcal{B}_t$ its boundary, $\dot{\mathbf{y}}$ is the velocity of a material point $\mathbf{X}$, $\mathbf{t}$ is the external traction vector, $\dot{\mathbf{w}}$ and $\dot{\mathbf{W}}$ are the spatial and material velocity fileds and $\mathbf{F}$ is the deformation gradient.
The amount of variation of internal energy of the system can be considered as the sum of two contributions:

$$\dot{\mathcal{U}} = \dot{\mathcal{U}}_\Gamma + \dot{\mathcal{U}}_{\mathcal{B}_t} \tag{2.55}$$

where the first term of the right hand side of the equation represents the change of internal crack energy (Γ represents the crack surface) and the second represents the change of internal body energy. The former is expresses as (Kaczmarczyk et al., 2014)

$$\dot{\mathcal{U}}_\Gamma := \frac{d}{\mathrm{d}t}\mathcal{U}_\Gamma = \gamma \dot{A}_\Gamma = \gamma \int_{\partial\Gamma} \mathbf{A}_{\partial\Gamma} \cdot \dot{\mathbf{W}} \, \mathrm{d}L \tag{2.56}$$

where γ is the surface energy, $\partial\Gamma$ in the crack surface boundary and $\dot{A}_\Gamma$ represents the change in the crack surface area. The second term of 2.55 is expressed as (Kaczmarczyk et al., 2014)

$$\dot{\mathcal{U}}_{\mathcal{B}_t} = \int_{\mathcal{B}_t} \{\mathbf{S_D} : \nabla_{\mathbf{Z}} \dot{\mathbf{w}} + \mathbf{\Sigma_D} : \nabla_{\mathbf{Z}} \dot{\mathbf{W}}\} \, \mathrm{d}V \tag{2.57}$$

where $\mathbf{S_D}$ is the first Piola-Kirchhoff stress tensor and $\mathbf{\Sigma_D}$ is the Eshelby stress tensor, defined, for a specific free energy function Υ as

$$\mathbf{S_D} = \frac{\partial \Upsilon(\mathbf{F})}{\partial \mathbf{F}} \tag{2.58}$$

$$\mathbf{\Sigma_D} = \Upsilon(\mathbf{F})\mathbf{I} - \mathbf{F}^T \mathbf{S_D} \tag{2.59}$$

In this way the first law of thermodynamics can be expressed as

$$\mathcal{P} = \int_{\mathcal{B}_t} \{\mathbf{S}_{\mathbf{D}} : \nabla_{\mathbf{Z}} \dot{\mathbf{w}} + \boldsymbol{\Sigma} : \nabla_{\mathbf{Z}} \dot{\mathbf{W}}\} \, \mathrm{d}V + \gamma \int_{\partial\Gamma} \mathbf{A}_{\partial\Gamma} \cdot \dot{\mathbf{W}} \, \mathrm{d}L. \tag{2.60}$$

The free energy of the body can be converted into work at the crack front, but any mechanical work of the body can be created from energy stored on the crack surface:

$$\mathcal{C} := \gamma \dot{\mathbf{W}} \cdot \mathbf{A}_{\partial\Gamma} \geq 0 \tag{2.61}$$

beign $\mathcal{C}$ the energy dissipation per unit length of the crack front. The entity described in 2.61 is equivalent to the change of the crack surface internal energy. It can be physically described as a positive growth in the crack surface, excluding other phenomena such as healing.

Material resistance

Based on Griffith's work, crack advancement happens for

$$\mathbf{G}_{\partial\Gamma} \cdot \mathbf{A}_{\partial\Gamma} > g_c/2 \tag{2.62}$$

being g_c the critical limit of energy release per unit area of the crack surface Γ and being $\mathbf{G}_{\partial\Gamma}$ the configurational force at front of the fracture.
The principle of maximum dissipation allows to determine, by means of configurational force, the crack propagation direction. Representing $\dot{\kappa}$ a length measure of the kinematic state variable for a point on the crack front, which can identify as

$$\dot{A}_{\partial\Gamma} \equiv \int_{\partial\Gamma} \dot{\kappa} \, \mathrm{d}L \geq 0 \tag{2.63}$$

which is consistent with 2.61. It is worth noting that for the purpose of this work the force is applied quasi-statically, condition that allows to have stable crack propagation. Algorithm 2 provides the full numerical solution strategy.

Spatial and material discretisation

The domain is discretised by means of tetrahedral finite elements; this approximation is applied to both material and physical domains. Higher-order basis functions are applied for displacements in the spatial configuration, while for displacements in material space linear approximation is used.

Mesh quality control

Mesh quality may deteriorate due to the adaption of the mesh when resolving the propagating crack. The quality of the finite elements has to be controlled to assure good matrix conditioning where iterative solvers are needed for solving large problems. A measure for the quality of the elements is then introduced to achieve mesh improvement by adding to $\mathbf{r}_m$ a term which considers a pseudo-stress at level of each element as a counterpart to the first Piola-Kirchoff stress. This term has impact only on the stability of the solution and not on the crack propagation criterion (Kaczmarczyk et al., 2014).

Algorithm 2: Numerical solution procedure (Kaczmarczyk et al., 2014)

```
Data: Model parameters, problem geometry and boundary conditions.
Initialization: load step $n$;
while body not fully cracked do
    for nodes at crack front do
        if crack propagation criterion is met then
            Crack direction determination;
            Faces alignment according to direction of crack;
            Crack front extension by splitting element faces;
        end
    end
    initialisation iteration $i$;
    reference configuration update;
    while convergence not achieved do
        residuals computation and problem solution
    end
    save data at load step $n$;
    load step $n \leftarrow n + 1$;
end
```

2.5 Material heterogeneity: multi scale modelling and stochastic approach

The methods mainly employed to consider material heterogeneity can be categorised in two main groups (Pindra et al., 2010): multiscale modelling and stochastic approaches.

In the following section a description of both methods is provided. It is worth mentioning that, despite both of them present some intrinsic drawbacks, both of them provide results very satisfactory when compared to experimental measurements (Liu et al., 2004).

2.5.1 Multiscale modelling

In computational modelling, multiscale modelling (or multiscale mathematics) solves problems which have important and relevant features at multiple scales of time and/or space. Generally speaking, two length scales can be identified in heterogeneous materials: macro-scale (of dimension l_M) and micro-scale (of dimension $l_m << l_M$). The principle of separation of scales states that micro- and macro-scales are distinguished when the dimension of the first (l_m) is much smaller than the dimension of the second (l_M) (Geers et al., 2010). It is important to distinguish between scales, because it has been proved that phenomena visible at a macro-scale are linked to mechanisms of a related microstructure (Nguyen et al., 2011b); in the non-linear range of large strains this influence of micro-effects on the macroscopic response is even more evident, as can be seen in Fig. 2.7 (Miehe and Bayreuther, 2007).

Babuška (1976) originally introduced the homogenisation concept in material sci-

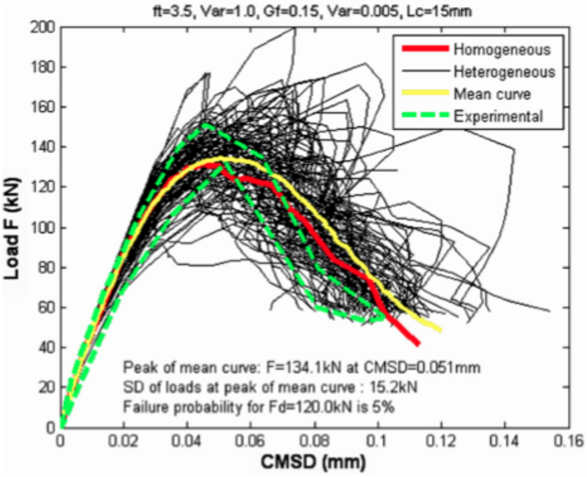

(b) CMSD-load curves

Figure 2.7: Effect of microheterogeneity on the Load-CMSD (crack mouth sliding displacement) curve of a beam subjected to bending: in the elastic range, the differences between numerical and experimental results are negligible, while in the post-peak area the responses vary significantly (Yang and Xu, 2008).

ences (Matouš et al., 2017). The main idea of this method, showed in Figure 2.8, is defined by Nguyen et al. (2011b) as a method used to "determine the apparent or overall properties of a heterogeneous material thereby allowing one to substitute this material with an equivalent homogeneous material".

A material, in comparison with the macrostructure, can be therefore seen as the repetition of periodic microstructures. An equivalent continuum is so defined, in a way that has the same average mechanical response as the heterogeneous material but, locally, it has fluctuations, which influence the mechanical response. The small microscopic cell in homogenisation theory in called Representative Volume Element (RVE), material volume with known mechanical properties representative of the surrounding material. The size of a RVE depends on sought for effective properties, loading conditions, boundary conditions and whether strain localizations occur.

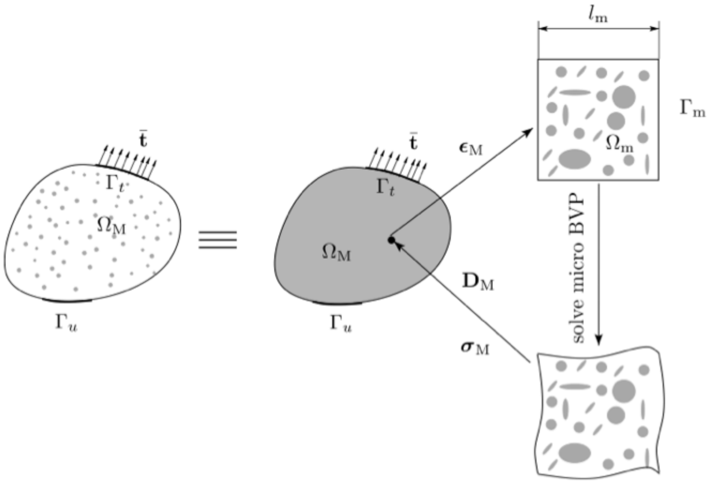

Figure 2.8: Homogenization procedure (Nguyen et al., 2011b)

Computational homogenisation can be summarised as follows (Geers et al., 2010):

1. Macro-to-Micro transition (or downscaling) in which the macroscopic strain vector ϵ_M is transferred to the RVE as boundary condition:

$$\epsilon_M(x_M, t) = \frac{1}{|\Omega_m|} \int_{\Omega_m} \epsilon_m(x_m, t)\, d\Omega; \tag{2.64}$$

   where Ω_m is the RVE surface (2D) or volume (3D) and ϵ_m is the microscopic strain tensor. This is called strain averaging theorem, as at any point of the solid the strain is defined as the average volume of the microscopic strain ϵ_m over the RVE related to that point.

2. The Boundary Value Problem (BVP) of each RVE is solved, in order to capture the effect of the surrounding medium;
3. Micro-to-Macro transition (or upscaling) in which the microscopic stresses σ_m are upscaled to the macroscale: the macroscopic stresses σ_M is thus obtained. This passage is achieved according to the Hill-Mandel principle: the macroscopic stress power must be equal to the average volume of the microscopic stress power over the RVE. At any state of the RVE characterised by a stress field σ_m in equilibrium, the equation

$$\sigma_M : \dot{\epsilon}_M = \frac{1}{|\Omega_m|} \int_{\Omega_m} \sigma_m : \dot{\epsilon}_m \, \mathrm{d}\Omega; \tag{2.65}$$

   must be hold for any $\dot{\epsilon}_m$ which is the derivative of ϵ_m with respect to the time of x). By substituting a specific boundary condition fulfilling the strain averaging theorem 2.64,

$$\sigma_M(x_M, t) = \frac{1}{|\Omega_m|} \int_{\Omega_m} \sigma_m(x_m, t) \, \mathrm{d}\Omega; \tag{2.66}$$

   is obtained. Equation 2.66 states that the macroscopic stress tensor is the average volume of the microscopic stress tensor.

As main drawback of this methodology, which has been widely proved to work efficiently, it is worth highlighting that it requires a precise definition of local material properties. In relation to the case to model, it is not always possible such a precise definition for example when, studying progressive failure in heterogeneous soil slope, the simulation of the parameters defines a rock placed in deep unattainable sites (Pathak et al., 2008). In this case, a wide range of the research community that deals with the inclusion of heterogeneity in numerical models employes statistical tools for *uncertainty quantification* to overcome this difficulty.

2.5.2 Stochastic approach: uncertainty quantification

Uncertainty quantification (UQ) is that field of science that aims to describe, quantify and possibly reduce the uncertainties involved in real world and numerical problems (Stefanou, 2009). With the term *uncertainty* is called any kind of property defined in a non-deterministic way. In the majority of UQ methods, uncertainties are treated by means of probability theory and statistics which, if implemented in standard FE methods, lead to the creation of SFEM, one of the most used and powerful tools to solve systems of stochastic partial differential equations (such as, the equation describing the equilibrium of a body subjected to a system of forces). Has always been recognised that the biggest drawback of SFEM is its computational effort (Falsone and Impollonia, 2002); however, the growth of power of computational tools and the implementations of optimisation algorithms rendered possible a good efficiency of such problems. Nevertheless, continuous improvements for the optimisation of stochastic algorithms are still needed.

Figure 2.9 summarises the general procedure followed by SFEM combined with Monte Carlo Simulation (MCS) method:

1. the first step concerns the realistic representation of the input system, in which the mechanical problem (geometry, FE discretisation, boundary conditions) and the stochastic inputs describing mechanical properties with random nature (e.g. modulus of elasticity, fracture energy) are defined and used for the generation of opportune probability distributions;

2. in the second step, probability distributions are used for the generation of different sample realisations for the mechanical properties showing random nature (the necessity of generating a certain number of samples is related to the impossibility of having accurate information about mechanical properties at each point of a domain (Shinozuka, 1972));

3. each sample realisation is used as input for the PDE describing the physical problem to be resolved, and numerical solution is obtained (following MCS principle, analyses are conducted until an acceptable convergence of the results is reached);

4. numerical solutions from each simulation are then used for the calculation of the final output in terms of mean value and standard deviations of the outputs (Stefanou, 2009).

Representation of stochastic process and field

The first step in the analysis of systems with uncertainties is the representation of the input of the system itself, usually related to variability of mechanical and geometric properties (elastic modulus, fracture toughness, section dimensions) and to the load applied. The way most widely employed to model these uncertainties is the implementation of stochastic processes together with their correlation structures and probability distributions, usually defined via experimental data. Nevertheless,

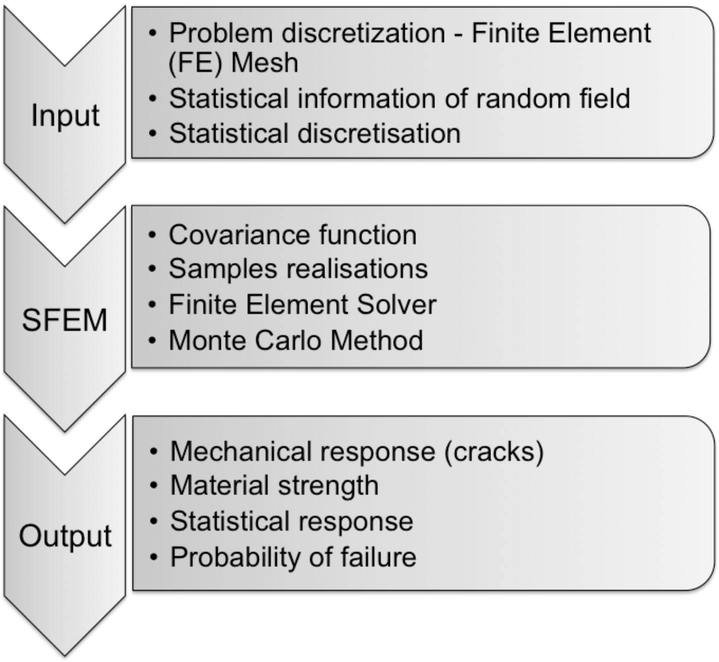

Figure 2.9: SFEM procedure

due to possible limited availability of these experimental measurements, assumptions and approximations are made with regards to uncertainty quantification.

Two main categories of stochastic processes can be defined based on probabilistic distribution used for their representation: Gaussian and non-Gaussian. The former is often used because of its simplicity and in case of lack of satisfactory experimental data. Nevertheless, non-Gaussian random fields appear to provide more suitable description of random fields of heterogeneous brittle materials (Stefanou, 2009). The Weibull distribution is one of the most widely employed distributions for brittle materials, as it describes experimental data most accurately than Gaussian distributions. (Gorjan and Ambrožič, 2012). Espinosa and Zavattieri (2003a) proved, both experimentally and numerically, that Gaussian distribution is more suitable for describing the behaviour of ductile materials.

Gaussian stochastic processes

For the simulation of Gaussian fields, the two main methods employed in applications are the spectral representation method and the Karhunen-Loeve expansion.

The spectral representation method (Shinozuka and Deodatis, 1991) expands the stochastic field $f(x)$ as the sum of trigonometric functions with randomly distributed amplitudes and phase angles. In most application the only random parameter is the angle phase. The fluctuating part of a random field is expressed as

$$\hat{f}^{(i)}(x) = \sum_{n=0}^{N-1} A_n \cos\left(\kappa_n x + \varsigma_n^{(i)}\right) \tag{2.67}$$

where $A_n = \sqrt{2S_{ff}(\kappa_n \Delta\kappa)}$, with $\kappa_n = n\Delta\kappa, \Delta\kappa = \kappa_u/N$ and $n = 0, 1, 2, ..., N-1$ and

- N is the number of intervals used to divide the wave number axes;
- A_n is the oscillation amplitude;
- S_{ff} is the spectral density function (SDF) of the stochastic field;
- κ_u is a cut-off number defining the active region of S_{ff};
- $\varsigma_n^{(i)}$ are independent random phase angles between 0 and 2π.

Since this method is based on the generation of sample functions of Gaussian fields for variables which have physical constrains (elastic modulus, for example, cannot assume negative values), there is non-zero probability that a violation of these conditions might occur in an actual MC simulation. The violation of the physical limits is due to large negative realisations of the stochastic fields, with subsequent possibility of having non-positive definite stiffness matrices (Stefanou and Papadrakakis, 2004).

The K-L expansion method considers orthogonal functions given by the eigenfunctions of a Fredholm integral equation with kernel autocovariance function. With the K-L expansion method, the stochastic field is expressed as:

$$\hat{f}(x) = \bar{f}(x) + \sum_{n=1}^{N} \sqrt{\gamma_n}\xi_n \delta_n(x) \tag{2.68}$$

$$\int_D \mathbf{C}_{ff}(x_1, x_2)\delta_n(x_1)\,\mathrm{d}x_1 = \gamma_n \delta_n(x_2), \tag{2.69}$$

where

- $\bar{f}(x)$ is the mean of the stochastic field, which usually is equal to zero;
- $\mathbf{C}_{ff}(x_1, x_2)$ is the autocovariance function;
- γ_n represent the eigenvaules of $\mathbf{C}_{ff}(x_1, x_2)$;
- $\delta_n(x)$ are the eigenfunctions of $\mathbf{C}_{ff}(x_1, x_2)$;
- ξ_n is a set of uncorrelated random variables;
- N is the number of K-L terms.

This method results to be particularly suitable in case of highly correlated stochastic fields. The biggest drawback of this method is related to the resolution of the Fredholm integral, especially is the covariance function assumes trivial formulations. The two above mentioned methods are able to adequately represent a stochastic field, but the second seems to be more powerful in case of strongly correlated stochastic fields with smooth autocovariance function. In particular, a lower number of N terms are needed to capture most of the random nature of the field (Stefanou, 2009).

In addition to these two methods, some other methods for representing Gaussian stochastic fields have been proposed. Here we briefly mention the most popular:

- Turning Bands Method (TBM): can be used for simulating random fields in more than one dimension by using one dimensional fields represented as linear-based functions going through the domain. This method provides good results only if a large number of lines are employed, making this method computationally expensive (Fenton, 1994).
- Optimal Linear Estimation method (OLE): is based on the optimal linear estimation theory. This method uses optimal shape functions depending on the prescribed correlation function, in a way that the error variance is minimal. Its expansion, called Expansion Optimal Linear Estimation method (EOLE) employes a spectral representation of the vector of nodal variables (Li and Der Kiureghian, 1993).

Sudret and Der Kiureghian (2000) compared the method mentioned above. According to their research, despite the K-L maximal error is not always less than, for example, the EOLE error, the K-L expansion method provides the lowest mean error over the domain.

Non-Gaussian stochastic processes

The task of simulating non-Gaussian stochastic fields has more and more grown in importance, as quite a few quantities in engineering practice present non-Gaussian probabilistic nature. Methods for generation non-Gaussian stochastic fields can be more challenging compared to those which use Gaussian stochastic fields: however, research has showed that this group of methods can be preferred over the Gaussian methods, mainly due to their non-uniqueness of the probability distribution in correspondence of their tails. In fact, different marginal probability distributions with almost identical mean and variance, but different tails, will bring to big differences between different realisations (Popescu et al., 1998).

In the second group of methods, the most widely used is the *translation field* method (or correlation distortion method), which aims to generate a zero-mean homogeneous non-Gaussian field via transformation of an underlying zero-mean Gaussian field:

$$g(\mathbf{x}) = G^{-1} \cdot \phi[h(\mathbf{x})] \tag{2.70}$$

where ϕ is the standard Gaussian cumulative distribution function and G is the non-Gaussian CDF of $g(\mathbf{x})$. The choice of the correlation structure, in this case, is strongly related to the choice of $g(\mathbf{x})$.

As further reading, more comprehensive reviews of the representation of stochastic processes and fields can be found in Stefanou (2009) and Elishakoff and Ren (2003).

The Stochastic Finite Element Method (SFEM)

Usually, SFEM is combined with MCS method in order to achieve convergence of results by solving a problem a large number of times, until a preset convergence criteria is achieved, and calculating the response variability by mean of simple relationships of statistics.

The first step of SFEM is the discretisation of the stochastic field, which means replacing the continuous stochastic field (defined with the methodologies shown in the previous paragraph or similar) by a number of random variables. The final random variables are then assigned to specific points of the domain (i.e. finite elements, nodes, integration points). Due to this, another important issue for sample realisations is the choice of the stochastic mesh employed for discretising the stochastic field (Yang and Xu, 2008). Its size is related to the correlation length, parameter connected to the variability of the random field, and can be different from the size of the FE mesh. In case of strongly correlated fields, in fact, the stochastic mesh has usually a bigger size compared to the size of the FE mesh, leading, furthermore, to a reduction of the dimension of the stochastic problem. Der Kiureghian and Ke (1988) and, later, Allaix and Carbone (2009) accurately studied what should be the optimal size of the stochastic mesh. They suggested a size for the stochastic mesh between a quarter and a half of the correlation length; furthermore, they concluded that the accuracy of the discretisation doesn't improve significantly if the size of the stochastic mesh is smaller than this range.

Once the stochastic field has been defined, the stochastic stiffness matrix has to be determined. The formulation of the stochastic matrix of one element takes the form

$$k^{(e)} = k_0^{(e)} + \Delta k^{(e)} \tag{2.71}$$

where $k_0^{(e)}$ and $\Delta k^{(e)}$ represent the deterministic (based on the mean value) and fluctuating parts of the stochastic finite element matrix. As consequence, the global stochastic matrix of the system takes the form

$$\mathbf{K} = \sum_{e=1}^{Ne} k^{(e)} = \mathbf{K}_0 + \Delta \mathbf{K} \tag{2.72}$$

where N_e is the number of finite elements.

2.6 Fracture propagation on heterogeneous materials

Experiments performed on heterogeneous ceramics shows how the microscopic defects significantly influence both the strength and failure mode of the material (Zhou and Molinari, 2004). Computer simulations cannot reproduce this behaviour unless micro-structure information and defects are supplied by the user; nevertheless materials such as concrete and rocks present a distribution of heterogeneity which is usually unknown a priori because of the complex and inherently random microstructure of the material. Therefore, an approach to predict the accumulating damage process accurately accounting for all uncertainties involved is essential. In this way, realistic crack patterns and reliable values of material strength can be obtained from computational simulations.

One very valid way used to obtain information about the material heterogeneity of samples is the use of experimental tools and techniques such as X-ray tomographic projections (Nguyen et al., 2016d,c; Li et al., 2014) or image-based methods (Sun and Li, 2015; Vemaganti and Oden, 2001). However, these methods are limited to applications where a suitable number of laboratory-scaled samples can be collected and analysed to extract the information needed and where suitable (and sometimes expensive) tools are available.

As already stated, In computational mechanics both multi-scale and stochastic approaches have been successfully applied to fracture mechanics problems. One of the first work that applied a multi-scale approach to a damage problem is the one by Fish and Yu (2001), who applied a two-scale model to reproduce damage phenomena in ceramic composite materials. After this work, multi-scale methods have been successively implemented and applied (to FEM and other methods such as DEM and cohesive elements methods) by a high number of authors (Liang et al., 2004; Rong et al., 2006; Nguyen et al., 2011a; Prechtel et al., 2011; Nguyen et al., 2012b; Lloberas-Valls et al., 2012; Nguyen et al., 2012a; Karamnejad et al., 2013; Rinaldi, 2013; Sparks and Oskay, 2016; Fu et al., 2017; Putar et al., 2017). From all these works, it is worth mentioning Liang et al. (2004), who applied a multi-scale method to study the progressive damage of rock-like materials, and concluded that incorporation of heterogeneity in numerical models can reproduce non-linear deformability of materials even when a purely linear elastic and brittle constitutive law is used; a similar conclusion has been obtained by Nguyen et al. (2012a) and Patinet et al. (2013).

Despite multi-scale method has been widely used and showed to provide very good results also when applied to fracture mechanics problems, its application is limited to those cases where a detailed knowledge of the material is available. For this reason, the power of the computational tools available has grown together with the number of works where stochastic approach are applied to reproduce materials heterogeneity in fracture mechanics problems.

From a review conducted on a wide number of researches where stochastic approaches were implemented to numerical methods for reproducing the evolution of damage and cracks, it can be observed that the majority of these works adopted linear elastic fracture mechanics principles. These works can be divided between those that applied Gaussian (Dimas et al., 2014; Pawar, 2011; Berthelot et al., 2008) and non-Gaussian (Dimas et al., 2016; Li and Salah, 2014; Khasin, 2014; Berthelot and Fatmi, 2004; Wang et al., 2012; Guy et al., 2012) processes to describe heterogeneity's distribution. Despite both provide good results, the use of non-Gaussian distributions is still preferred by most of the more recent literature because of its capability of better representing the mechanical response of heterogeneous materials and avoiding negative and physically meaningless sampled values.

By modelling material properties as probabilistic random fields, Most (2005) and Yang and Xu (2008) employed MCS method to asses the structural reliability. This method has however the drawback of the computational cost associated with generating a large number of finite element meshes, and the use of a method for sampling that leads to a quicker convergence is therefore a primary concern.

One of the first studies using a stochastic approach to model material heterogeneity is the one carried out by Carmeliet and Hens (1994). They combined nonlocal continuum damage mechanics, MCS method and random field theory to model stochastic damage behaviour of a strain-softening material with random field properties, introducing two different parameters in their cohesive model: the characteristic length of the nonlocal damage model and the correlation distance for the random field. To obtain the probabilistic formulation of the damage evolution, the authors considered as random parameter the initial damage threshold and the ultimate strain of the material. Despite the questionable choice of a uniform correlation coefficient function and the employment of a linear-elastic linear-softening behaviour at a local scale, a non-linear response for the probabilistic nonlocal damage model is observed, which is consistent with experimental observation.

Gutiérrez and de Borst (1999) performed deterministic and stochastic analyses considering material strength as random variable. With their method, the authors have been able to evaluate probability of failure, but also to identify the most critical configurations leading to failure, studying the so-called *size effect* and its influence on material failure. Their results show how damage evolution is dependent on both size effect and random nature of material, comparing numerical results from a notched specimen and a traction test with experimental observations.

Further studies on the size effect combined with effect of heterogeneity have been also carried by Vořechovskỳ (2007). He performed numerical simulations of the random response of tensile tests with dog-bone samples; randomness is considered here via material strength. He highlighted how the bigger the specimen is, the lower the material strength is and the higher is the influence of heterogeneity in material failure process. Size effect is clearly observable for both deterministic and stochastic analyses, but the incorporation of heterogeneity leads to numerical results which are closer to experimental data.

A three-dimensional micro-cracking cohesive model with statistical distribution of internal defects has been developed by Zhou and Molinari (2004). The brittle structures are considered as bodies containing initial defects modelled as the facets shared by two neighbouring ordinary cohesive elements. Each of these facets has a specified strength assigned on the basis of a Weibull distribution. Authors demonstrated that the failure strength of the analysed specimens increases with the Weibull modulus of the microscopic strength, that is the case of a more homogeneous material.

A micro mechanical cohesive FE model within explicit resolution of arbitrary crack paths and morphologies has been proposed by Tomar and Zhou (2005). They observed that micro structural morphology is strongly related to the changes in fracture response when material properties have stochastic nature. The method proposed involves the superposition of a perturbation analysis together with a cohesive FEM. While the deterministic analysis explicitly shows crack propagation, the perturbation analysis focuses on the statistical distribution material properties (both bulk properties and interfacial properties). The effect of property variations on the variation of crack length, energy dispersion and damage is provided, and is shown that a microstructure less prone to fracture displays higher variations in fracture response when compared to the one which gives least resistance to fracture advancement.

Multiple cracking phenomena in plain and reinforced concrete structures have been studied by Most (2005), who showed how that this phenomenon is highly influenced also by the effect of material heterogeneity. Meshless methods have been employed to describe the propagation of crack surfaces. The cracking process of concrete has been modelled using a cohesive crack model able to reproduce the failure mechanisms under different crack opening modes. This crack growth algorithm was implemented with the aim of representing the fluctuations of the concrete properties by expanding the one-parameter random field concept for multiple material properties with cross-correlation. The random field concept was used in order to model the fluctuations of Young's modulus, tensile strength and Mode-I fracture energy.
Two methodologies for the sampling phase of random values have been adopted. First, a log-normally distributed random filed with exponential correlation has been used, where the stochastic analyses have been carried out by analysing the material response curves of 10000 MCS of 30 random variables. Successively, analyses was performed by using Latin Hypercube Sampling method (LHS[2]) with different numbers of samples. Results obtained with only 70 LHS samples are in excellent agreement with the MCS curves. This result shows that LHS method can be applied to crack propagation problems to obtain the statistical properties of the structural response with a small number of samples.
Furthermore, in one of the examples presented in his work, the author proved that

---

[2] In LHS method the variables are 'stratified' in different *classes*. This methods relies on the use of uniform and normal distributions.

the numerical crack pattern is in good agreement with the experimental patterns, but the detailed crack path with branches observed in the experiment and, according to the author, developed by the local inhomogeneity, is not represented in the numerical model.

A cohesive model for the study of microcrack initiation and evolution in brittle specimens of allumina has been proposed by Espinosa and Zavattieri (2003a,b). A RVE of a microstructure subjected to multi-axial loads has been considered, and an elastic-anisotropic model of the grains, incorporating grain anisotropy by randomly generating principal material directions, is included. Furthermore, for accounting of material heterogeneity, SiC particles and glass pockets have been modelled and introduced in the interfaces between RVEs of allumina, as it is believed to lead to the consideration of a statistical variation in the interfacial strength dependent on the grain disorientation. Furthermore, the cohesive strength between interfaces of elements and fracture toughness have been described by a Weibull distribution applied to describe the distribution of fracture toughness and local material strength. Following these assumptions for their numerical analyses, the authors concluded that fracture toughness influences damage evolution more than local material strength, and that initial defects introduced in the model only affect the cases for which the interface strength is higher the applied stress.

Another important issue when modelling materials failure using FEM is the *mesh sensitivity*. In fact, performing simulations considering a homogeneous distribution of material properties, very often provides incorrect and unrealistic crack patterns are observed together with load-displacement curves wrongly obtained due to strong mesh-dependance. Carmeliet and Hens (1994) showed that heterogeneous models are capable of predicting realistic and complex fracture processes with a smaller mesh dependance. In their work possible fractures are included by pre-including cohesive elements with constitutive laws with softening, modelled by means of Weibull distributions.
Furthermore, Zhou and Molinari (2004) proved in their work that brittleness of heterogeneous materials tends to degrade the mesh dependence of the problem. More recent developments in the field, however, have found suitable ways to overcome mesh sensitivity issues, by allowing the FE mesh to realign the element facets according to the direction of the force on the crack tip (Kaczmarczyk et al., 2014).

It is worth mentioning that both multiscale and stochastic approached have

been successfully applied to the Discrete Element Method (Pisarenko and Gland, 2001; Fu et al., 2017; Groh et al., 2011), XFEM (Patil et al., 2017), meshless methods (Zhou and Bi, 2016; Zhou et al., 2015; Douillet-Grellier et al., 2016) and IsoGeometrical Analysis (IGA) method (Bhardwaj et al., 2015).
Furthermore, different problems studied by means of either stochastic or multi-scale approaches include crack propagation on ductile materials (Lauschmann, 1987; Bieler et al., 2009) and dynamic fracture problems (Sun and Li, 2015).

Advantages of multi-scale and stochastic approach have been also coupled together: as an example, an adaptive stochastic multi-scale method is developed by Sencu et al. (2016)for cohesive fracture modelling of quasi-brittle heterogeneous materials under uniaxial tension. The methodology developed by the authors is able to predict crack paths and material strength with results very close to those obtained using a multiscale methodology; however these results highly depend on the distribution of the volume fractions, unknown a priori and therefore to be properly determined.

A number of works, on the other hand, tried to reproduce the heterogeneous nature of materials with methods which cannot be strictly categorised as either multi-scale modelling approaches or stochastic approaches.
For example, Alkhateb et al. (2009) studied the behaviour of heterogeneous materials by means of the spring network method introducing inclusions randomly distributed in a homogeneous domain. Similar approach has been followed by Schicker and Pfuff (2006), who developed a weak-link law applied to the interface between the homogeneous material matrix and the randomly-orientated fibres contained in the material.

2.7 Shale gas reservoir rocks: anisotropy and natural beddings

In the last years, interest of research has massively moved in direction of shale rock characterisation. This is due to the fact that gas extraction procedures from shale rock reservoirs are extremely expensive, and therefore accurate prediction of induced-fractures propagation is indispensable.
Considerable effort has been put in analysing results from laboratory tests, for shale mechanic and physical characterization (Bobko and Ulm, 2008; Veytskin et al., 2017). These tests are crucial to understand the effect of material composition

and local heterogeneities on the mechanical response of rocks, which, because of their natural genesis, significantly differ the one from the other. Hou et al. (2016), in fact, recently compared the behaviour of shale, coal and sandstone specimens subjected to high-pressure fluid-driven fracturing, and observed how the different microscopic composition of these materials leads to important differences in the measured values of mechanical properties, strains and crack patterns. Kim et al. (2012) also performed a comparative study between shale, gneiss and schist rocks samples, analysing, for each of them, the influence of their composition and direction of bedding planes on their thermo-mechanical properties.

Angle between directions of bedding plane and maximum stresses applied can be considered to be a noticeable source of influence on crack morphologies, failure mode and material strength. Tests conducted on Brazilian discs specimens (traditionally used to indirectly calculate rock's tensile strength) showed the high influence of laminations inclination on materials mechanical response (Wang et al., 2016; Mokhtari and Tutuncu, 2016). Zhong et al. (2015) also studied the effect of damage at micro-scale on the macroscopic overall response of shale samples subjected to triaxial compression, and highlighted that the effect of both bedding inclinations and different confining pressures induce highly-varying values of compressive strength and elastic modulus and considerably affect crack morphology and opening mode. Holt et al. (2015) also studied the effect of local heterogeneities on material response and rock brittleness, while Mahanta et al. (2016) studied the importance of understanding the effect of the load applied on shale specimens and how, for varying strain rate, fracture toughness and, consequently, the energy required for fracturing the material changes.

Observations from experimental studies highlight a general anisotropic response for shale: this means that numerical frameworks (usually used where laboratory or site tests result in a prohibitive cost), to realistically reproduce the mechanical response of the rock, cannot just consider an isotropic and homogeneous model. Duan and Kwok (2015) and Zhou et al. (2016) modelled the Brazilian disc problem and a fluid-driven fracture problem, respectively, in shale using the Discrete Element Method (DEM). However, the main issue with DEM model is the computational cost, which becomes prohibitive if lagrer-scale problems need to be analysed. Classic Finite Element Method (FEM) (Dokhani et al., 2016; Zeng and Wei, 2017) and eXtended FEM (Sun et al., 2016) have been successfully applied to fracture propagation and fracking simulations on shale rocks. Anisotropy has been included in all above numerical models by decreasing the values of mechanical properties, such as elastic modulus, cohesion coefficients or fracture toughness, in precise locations in the domain in order to create weak layers which affect fracture extents and shapes. However, only the introduction of weak bands may not be able to entirely reproduce the real composition of shale rocks as they are composed by laminations, but also local heterogeneities, inclusions (i.e. quartz, calcite and dolomite (Chen et al., 2016)), voids and micro-fractures, which, in order to be captured, require an in-depth knowledge and more sophisticated and comprehensive numerical implementations (Nguyen et al., 2016b).

An attempt to use stochastic approaches for modelling layered materials has been proposed by Bossi et al. (2016), in which the authors modelled a simplified slope made up by clay with horizontal gravel layers. A probabilistic technique has been used to assign the same deterministic value of gravel's cohesion and friction angle to randomly selected elements forming the domain. This inclusions influence the results of the analyses, but mechanical properties have been deterministically defined, which may lead to an unrealistic representation of the problem. Borghi et al. (2015) also used a stochastic approach for modelling layering effect on fracture propagation problems: also in this study the stochastic approach is not applied for the creation of a stochastic set of input data describing mechanical properties, but is used to randomly introduce in the model fractures with random dimensions and locations to reproduce possible orientations of geological structures. A noteworthy approach has been recently outlined by Li et al. (2016b) where material heterogeneity has been considered through a combined stochastic methodology accounting for different type of natural materials on a soil profile. Although this approach looks very promising, it does not account for material microstructures, which is well known to appreciably affect the macroscopic behaviour (Bobko and Ulm, 2008).

More recently Na et al. (2017) reported an experimental and numerical study (using a phase field approach, FEM) on the effect of the heterogeneous and anisotropic nature of Mancos Shale specimens in Brazilian tests. They tested a set of layered specimens, varying the relative angle between loading and bedding direction. From experimental investigations, they confirmed findings from previous investigations (Li and Wong, 2013) where the role of maximum strains for the failure in Brazilian disc tests is revealed to be crucial, leading to material failure starting not from the centre of the disc, but from a point located in vicinity of the loading point. Furthermore, the numerical investigations highlighted that the best results are achieved in the problem is simulated using an anisotropic constitutive model combined with an alternation of soft and stiff layers; if only the soft - stiff alternation is used with an isotropic model, results are still satisfying, while the use of the only anisotropic constitutive model leads to too smooth crack patterns.

He and Afolagboye (2017) executed both experimental and numerical investigations. The experimental investigations showed that the material strength is lower for vertical layers and higher for horizontal layering, and crack patterns are different as well as the inclination changes. The authors used the Discrete Element Method to simulate the problem, and studied how the variation of the inter-granular bonding force between particles influences both material resistance and crack path, more significantly when the bonding force between particles is lower.

Figueiredo et al. (2017) performed numerical investigations in order to understand the effect on fractures induced by hydraulic pressure of several factors. The authors checked the efficiency of using a continuum model to reproduce the propagation of cracks considering the influence of complex geological settings and the changes in pore pressure and permeability produced by the interaction between fractures and geological configurations. The hydraulic fracture problem has been also studied by Haddad et al. (2015) by means of the XFEM combined with cohesive elements approach.

Crawford et al. (2014) investigated the potential for considering shales as bilaminate materials and used a FE model with variably inclined layers to reproduce results from laboratory testing. Resultant strength anisotropy exhibits many of the features observed from laboratory testing of orientated shale samples and suggests that strength reduction due to the activation of weak bedding laminations should be expectable from information on the bulk trans-laminar strength without the use of time-consuming laboratory testing.

2.8 Conclusions

From the review conducted above, the following conclusions can be drawn:
- a wide number of techniques and methodologies for modelling of crack propagation have been proposed and implemented; however the majority of them have been developed considering mainly fully linear and brittle models. Literature has

shown that heterogeneous materials show strong non-linear behaviour that, therefore, needs to be carefully reproduced numerically;
- stochastic approaches provide a significant contribution to the inclusion of heterogeneity in numerical and computational models and a number of advantages over multi-scale modelling techniques. However, the most noticeable drawback of stochastic approaches is the computational cost, due to the generation of sample realisations and to the number of analyses needed to achieve an acceptable convergence of the mechanical response results; for this reason a suitable technique able to reduce the computational cost related to the implementation of such stochastic approaches is essential;
- the interest of research in studying shale-gas rocks is in continuous growth. Both the mechanical characterisation of materials through lab tests and full field simulations. Shale rocks are heterogeneous and layered materials, and their mechanical response is highly dependent on the orientation of the bedding. The anisotropic nature of shales has been modelled using only a few methodologies, and further research is needed in this direction.

Chapter 3

Smeared and discrete crack approaches: a preliminary comparison

3.1 Introduction

In this chapter, the numerical results of three cases study analysed using the two numerical models, one based on a smeared representation of cracks (Del Piero et al., 2007) and the other on a discrete approach (Kaczmarczyk et al., 2014), described in the previous chapter are presented. In particular, the aim of this chapter is to understand how the two models capture the initiation and propagation of cracks and the damage evolution in quasi-brittle materials. The capability of the two models in automatically capturing different crack-opening modes is analysed. Furthermore, the mesh convergence techniques adopted for these two approaches, that is on the mesh refinement procedure for smeared and mesh adaptivity for discrete approach, are also studied.

3.2 Application of the models to fracture on quasi-brittle materials

The behaviour of three types of concrete specimens using the two aforementioned models is studied in order to evaluate their relative performance against several different specimen geometries and load conditions. Numerical results are then compared with the relative experimental tests results.

For the discrete approach, all problems are discretised using tetrahedral elements. An adaptive mesh refinement strategy, including both h- and p- refinement, is adopted. For the solution approach for this method open-sources libraries have been employed. A mesh-oriented database (MOAB) (Tautges et al., 2004) is used to store input and output processes and information regarding mesh topology. For resolving linear systems of equations, algebraic operations and parallel matrix and vector calculation the Portable, Extensible Toolkit for Scientific Computing (PETSc) (Balay et al., 2012) is employed.

On the other hand, the two-dimensional numerical code based on the smeared approach incorporates a mesh refinement technique, which automatically splits those elements where the values of damage parameter s become smaller than a given threshold. Simple linear interpolation is used to obtain values of damage and displacements for the new nodes.

It has to be highlighted that, in order for the results to be comparable, it is necessary to run 2-dimensional (or equivalent) simulations also with the 3-dimensional code based on a discrete crack approach. For different reasons, 2-dimensional simulations have been run using 3-dimensional based codes in past works (Brunet et al., 1998; Pardo et al., 2008). Brunet et al. (1998) performed numerical analyses using a combined 2D and 3D based FEM computational framework to study the roll-forming procedures of metal sheets. In terms of finite element approximation, this study allowed to include a purely 2D mesh with linear shape functions and two degrees of freedom on each node, and analyses have been performed in plane strain conditions (due to the third dimension of the metal sheet being much higher that the two others). The 3D smeared crack based numerical framework employed here does not allow this approximation, as domain discretisation needs to be performed using three-dimensional tetrahedral elements (Kaczmarczyk et al., 2014). For this reason, the three problems analysed in the next three sections have been first modelled using a three-dimensional domain, keeping the third dimension (in the direction of the thickness of the specimens) much smaller compared to the other two (1 and 2 mm). However, this approximation has lead to numerical instabilities which made the numerical framework not capable of predicting any crack pattern. Therefore, the thickness of each specimen has been increased to a dimension able to avoid any numerical instabilities, but still significantly smaller compared to the two other dimensions. The first two examples analysed in the next three sections have been therefore modelled with a thickness of 20 mm, while the third example has been modelled considering a thickness of 5 mm.

This simplification is similar to those that, mainly for computational efficiency purposes, execute numerical analyses only on portions of larger domains by imposing opportune additional boundary and symmetry conditions (Kaczmarczyk et al., 2014; Duan et al., 2009; Areias and Belytschko, 2005; Gasser and Holzapfel, 2005). However, additional analyses (but not reported in this thesis) on the specimens inclusive of the real thickness have been performed to check the correctness of the results obtained with the reduced-thickness domains.

3.3 Case study 1: Single-Edge Nothced Shear Beam

The first example used in this study is the four-point single-edge notched shear beam (SENS) studied experimentally by Arrea (1982). This benchmark is one of the most widely used to validate numerical models for simulating mixed-mode crack propagation in concrete. Specimen geometry, boundary conditions and material properties about this benchmark are shown in Figure 3.1 and Table 3.1. Load is applied in quasi-static regime and in displacements-controlled mode.

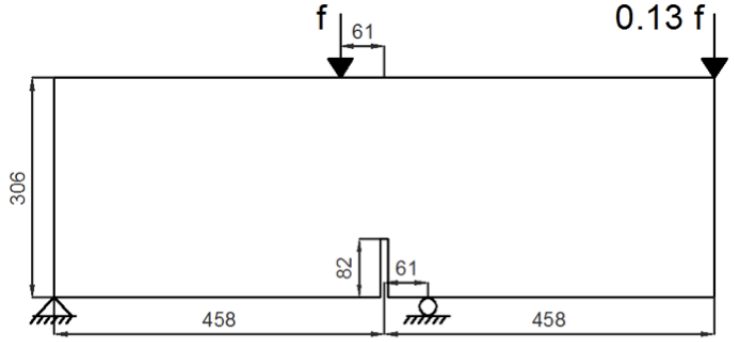

Figure 3.1: Experimental set up for the SENS concrete specimen (units: mm)

Table 3.1: Material characterisation for the SENS specimen

Parameters	
Modulus of elasticity	24.8 GPa
Poisson ratio	0.18
Fracture Energy	0.15 N/mm

Figure 3.2 shows the discretised problem for the two different approaches. Table 3.2 summarises the information about the two different discretisations and about the computational effort needed for obtaining a full crack path. For the

smeared approach, a mesh composed of 690 nodes, 1256 3-nodes linear triangles has been generated. A value of $\varepsilon = 8$ mm is selected, while the size of the mesh is chosen to be equal to 5 mm. The value for ε is chosen, following the considerations listed in Lancioni and Royer-Carfagni (2009), on the basis of the average size of the material constituents: in particular ε is typically 2-3 times the characteristic material length scale. As concrete is formed by constituents of different sizes, an average dimension of 4-5 mm is here considered and, consequently, the value of 8 mm for ε is selected. The discretisation used for the discrete approach consists of 4660 nodes and 19784 tetrahedrons. In proximity of the crack front, the spatial node positions are discretised using higher-order approximations. (Kaczmarczyk et al., 2014). For zones far from crack patter mesh size is bigger compared to the area where the crack is likely to propagate, in order to reduce the computational effort and, at the same time, keep the accuracy of the model.

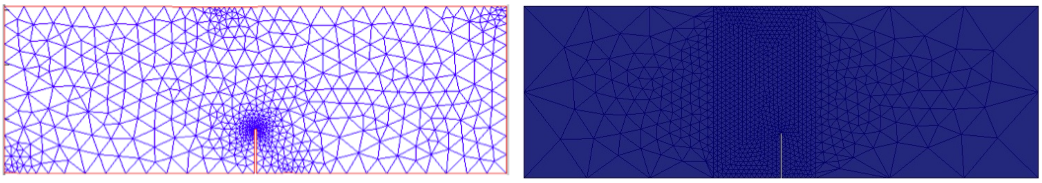

Figure 3.2: Finite Element discretisation: smeared (left) and discrete (right) approach.

Table 3.2: Models characterisation for the SENS specimen.

Smeared		***Discrete***
1256	**Number of elements**	19784
690	**Number of nodes**	4660
12 hours	**CPU time**	34 hours

The results in terms of damage distribution obtained using the smeared approach are shown in Figure 3.3. As can be observed, the damage is localised in proximity of the supports. This result is not correct if compared with both the experimental investigations (Arrea, 1982) and numerical results (Yang and Xu, 2008). In fact, damage is expected to begin at the tip of the notch, where the crack will initiate to propagate then in the direction of the main loading point. This results suggest that this numerical framework is not capable of predicting mixed-mode crack opening conditions.

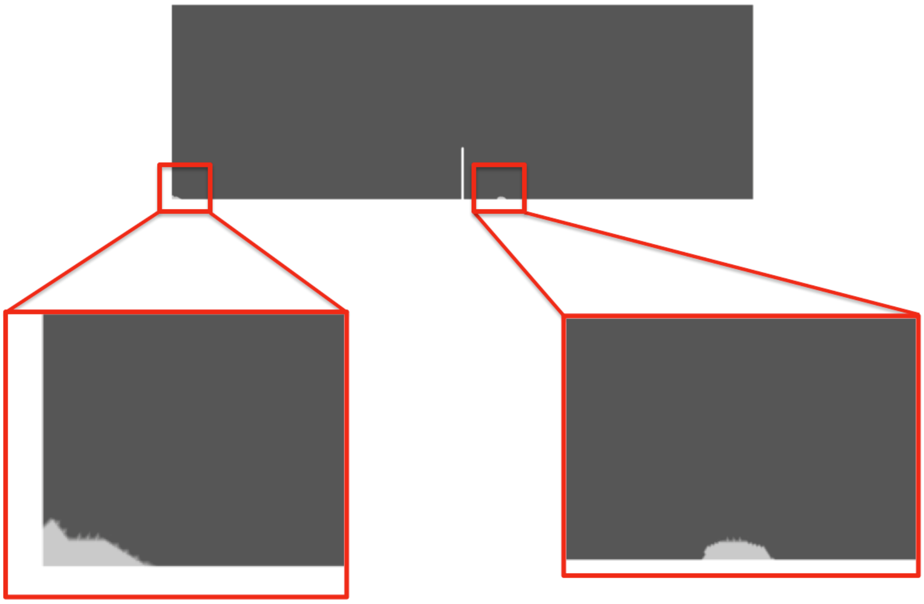

Figure 3.3: Damage distribution obtained with the smeared approach model: the damage doesn't start from the initial notch, as it would be expected, but is localised in the supports.

In order to make the model capable of capturing the correct crack pattern, an implementation able to differentiate the mechanical response between elements in tension and compression has been introduced: to account for this tension-compression asymmetry of damage behaviour of material, a methodology similar to the one proposed by Li et al. (2016a) is included, and the energy function is decomposed into two parts, a positive part which is considered to contribute to damage, and a negative part that resists to damage:

$$W(F) = W^{+} + W^{-} \tag{3.1}$$

where

$$W^{+} = (s^{2} + k_{\varepsilon})W|_{J>1} \tag{3.2}$$

$$W^{-} = (1 + k_{\varepsilon})W|_{J<1} \tag{3.3}$$

In the above equations, it can be noticed that the damage parameter appears only in the positive part of the energy function, the part associated to the elements that increase in surface (i.e., in the elements with $J > 1$), the value for damage in the elements is kept as calculated. The elements that decrease in surface (i.e., the elements with $J < 1$), do not contribute in damage. In this way, different behaviours for tension and compression are explicitly taken into account.

Figure 3.4 shows and compares the crack patterns obtained with the discrete and the implemented smeared- based models: cracks are predicted in both cases, especially for the area next to the crack initiation point. As the analysis proceeds the crack paths obtained using the smeared approach deviates from the experimental scatter. The evolution showed in Figure 3.5 highlights this aspect for the smeared approach, showing how the accuracy decreases for the last steps of the simulation. On the other hand, the crack path obtained using a discrete approach is perfectly predicted and included within the experimental scatter. The capability of the methodology based on the configurational forces approach is therefore fully capable of automatically identifying the crack opening mode on the basis of the direction of maximum energy dissipation.

Analysing the load-displacement curve shown in Figure 3.6, it can be observed how in both cases realistic results are obtained. Nevertheless, the variational approach seems to provide a peak load for larger displacements compared to the configurational force method. However, the discrete approach provides a load-deflection curve close to the experimental one especially in the post-peak range.

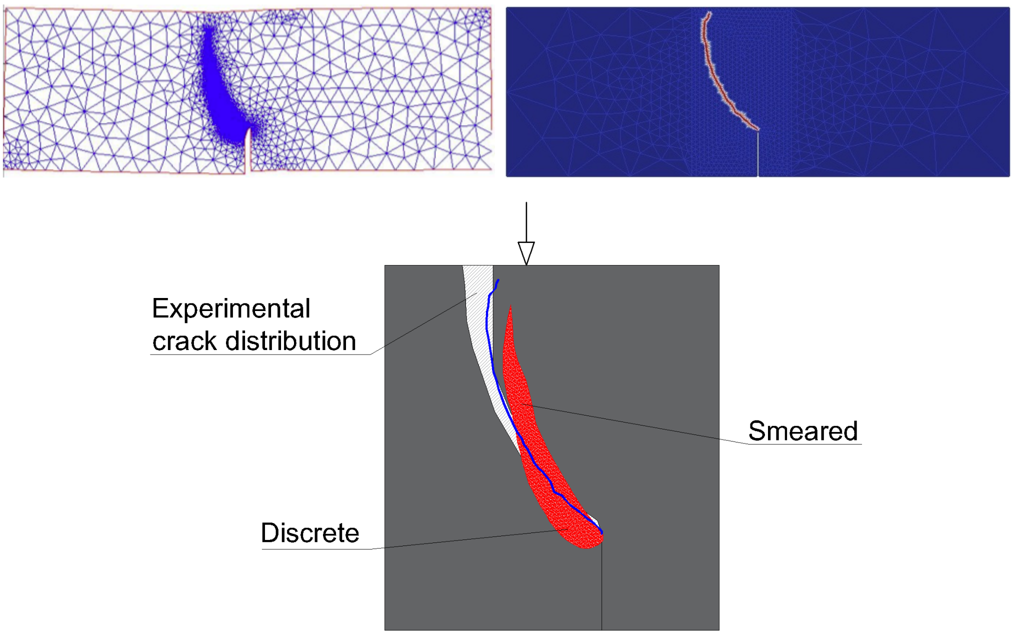

Figure 3.4: Crack patterns obtained with smeared (top left) and discrete (top right) models; comparison with experimental scatter (bottom).

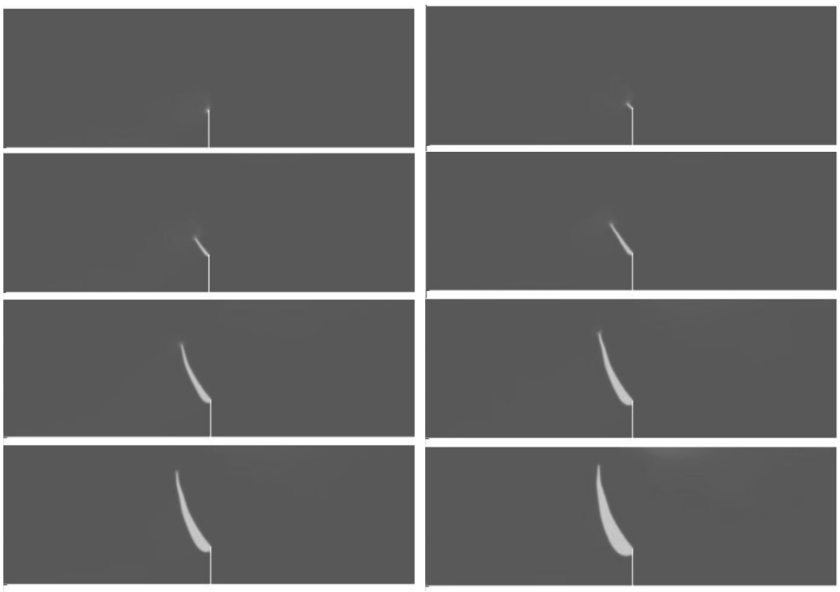

Figure 3.5: Damage evolution for model solved with the smeared approach.

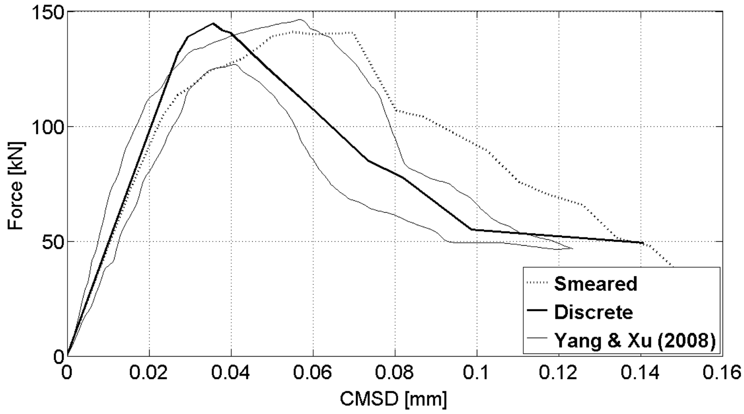

Figure 3.6: Load-Displacement plot for the SENS beam specimen: comparison of smeared and discrete approach results with experimental data from Yang and Xu (2008).

3.4 Case study 2: L-Shaped fibre reinforced concrete

The second example contemplated in this study is the L-Shaped specimen test performed in a quasi-static loading regime and displacement-controlled conditions. This case study has been investigated experimentally in Winkler (2001) to study and examine curved crack patterns. The size of the specimen and the set up of the panel are shown in Figure 3.7. The characterisation of concrete is provided in Table 3.3.

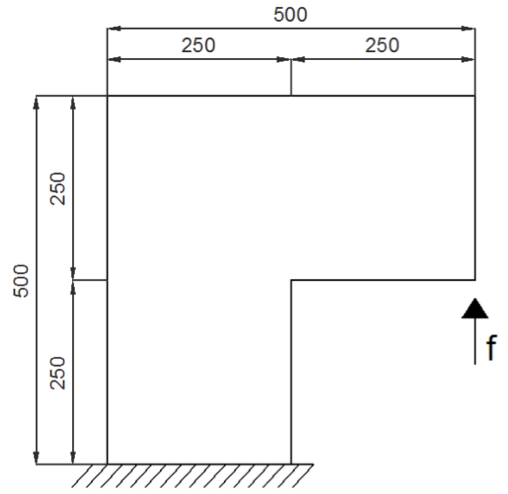

Figure 3.7: Experimental set up for the L-Shaped fibre-reinforced concrete specimen (units: mm).

Table 3.3: Material characterisation for the L-Shaped specimen.

Parameters	
Modulus of elasticity	26 GPa
Poisson ratio	0.18
Fracture Energy	90 N/m

Figure 3.8 shows the problem discretised for the two different approaches. Table 3.4 provides the information on the two different discretisations, also including the duration needed to complete a whole simulation and obtain a full crack path. For smeared approach, a mesh formed by 386 nodes and 697 3-nodes linear triangles is used. The mesh size was chosen based on the average size of the aggregates and following the considerations listed for the previous example. The discretisation mesh used for the discrete approach consists of 2524 nodes and 9881 tetrahedrons. As in the previous example, locally the mesh is automatically refined during the propagation of the crack. For further details about the type of approximation it is suggested Kaczmarczyk et al. (2014) for further reading. In order to reduce the computational effort and, at the same time, keep the accuracy of the model, initial mesh size is smaller in the area where the crack will propagate and of a bigger size elsewhere.

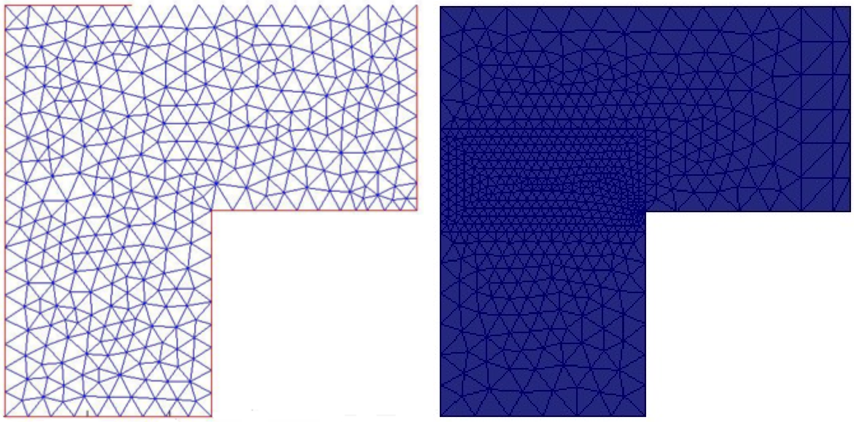

Figure 3.8: Models employed for analysing the problem with smeared (left) and discrete (right) approach.

Table 3.4: Models characterisation for the L-Shaped specimen.

Smeared		***Discrete***
697	**Number of elements**	9881
386	**Number of nodes**	2524
6 hours	**CPU time**	31 hours

Figure 3.9 shows the numerical results in terms of crack paths. The crack pattern is predicted by both methods. However, the smeared approach shows some discrepancies when compared to the experimental results. In fact, besides the zone next to the crack initiation point, crack path curves downwards, overstepping the experimental limit (probably due to the heterogeneous nature of material, which for this example can therefore be an essential feature that needs to be considered), while the crack path obtained using a discrete approach is in a better agreement with the experimental results, as it is fully included in the experimental crack range. Figure 3.10 shows the evolution of damage with the smeared model. For the first steps of analysis, damage localisation and crack path are clearly identified, but for further steps of the analysis, the damage is spread over a wider area. From this point of view and for problems in which a single crack path is usually identified, discrete model seems to be more suitable. This aspect is congruent with the conclusions in de Borst et al. (2004).

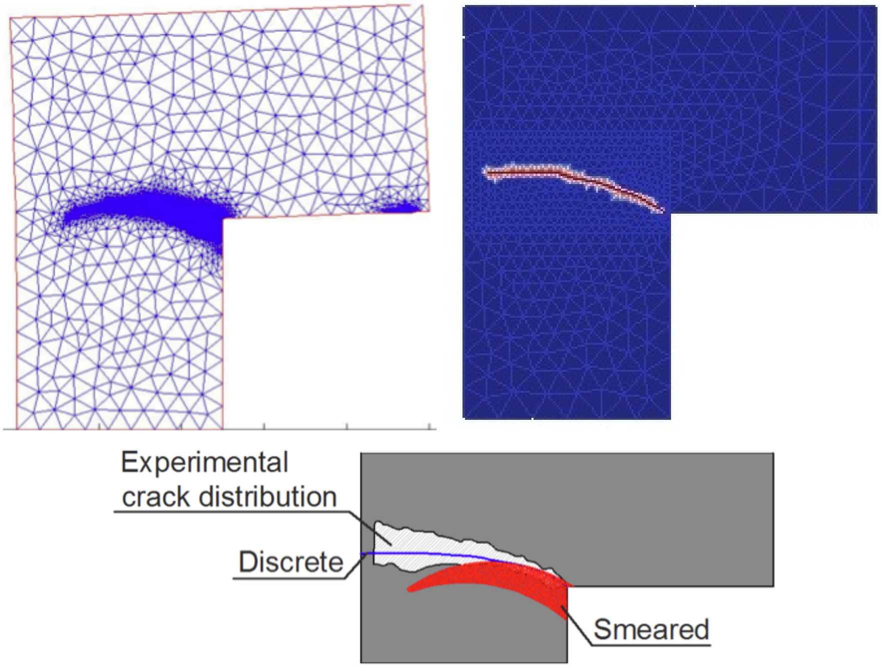

Figure 3.9: Crack patterns obtained with smeared (top left) and discrete (top right) models; comparison with experimental scatter (bottom).

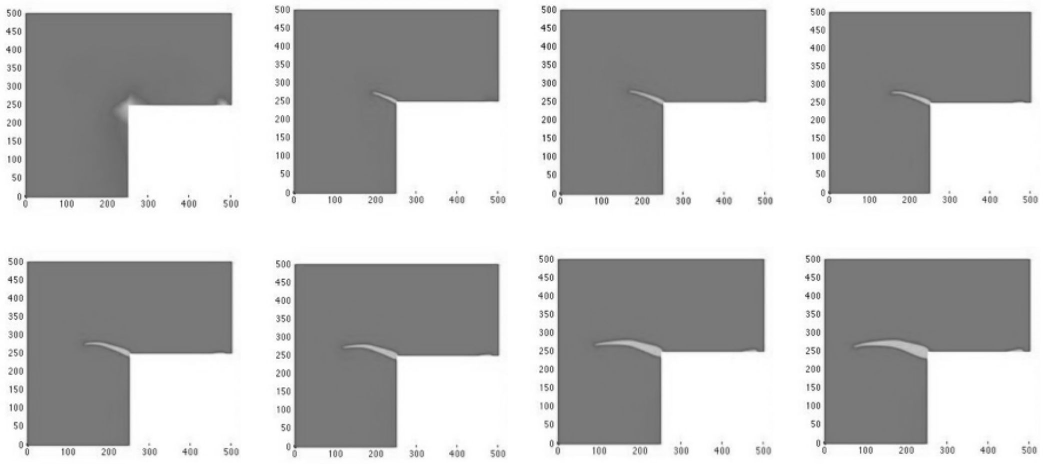

Figure 3.10: Damage evolution for model solved with the smeared approach.

Analysing the computational cost required for each analysis, it is clearly observed that, in accordance with other comparative studies, the smeared model requires much less effort than the discrete model: the computational framework based on the discrete approach is definitely more demanding, due to the number of nodes and elements and, above all, to the type of implementations included to guarantee mesh convergence: in fact, while for the smeared approach, mesh convergence is guaranteed by just splitting the elements until the desired new mesh size is obtained, for the discrete approach the mesh convergence criteria involves a realignment of the FE nodes, in a 3D setting, according to the direction of the configurational force, procedure more computationally demanding.

Analysing the load-displacement curve shown in Figure 3.11, it can be noticed how the two models provide similar results within the pre-peak range, with a slight overestimation in the value of the peak load for the discrete approach. Furthermore a discordance in the post-peak behaviour can be observed in the results for both methodologies: the reason can be attributed (i) to the non-consideration of heterogeneities in the numerical frameworks and (ii) to the fact that both models have been developed for fully brittle materials, materials which have no residual load after the peak load.

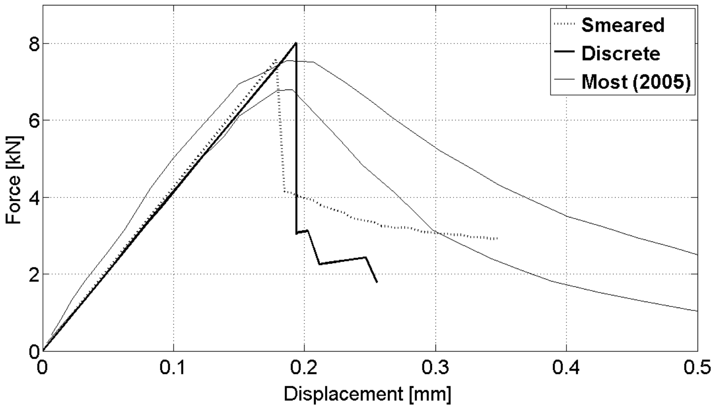

Figure 3.11: Load-Displacement plot for the L-Shaped specimen: comparison between smeared and discrete approach and comparison with experimental data.

3.5 Dog-Bone specimen

The third configuration studied here is the test on a Dog Bone shaped concrete specimen subjected to traction performed in a quasi-static loading regime. This case study has been experimentally investigated inVan Vliet (2000). The description of the specimen is shown in in Figure 3.12. The characterisation of the concrete is provided in Table 3.5.

Figure 3.13 shows the problem discretised for the two different approaches, in Table 3.6 the information about the two different discretisations are reported. For the smeared-based approach, the problem is discretised with 240 nodes and 421 elements. For the discrete approach the domain has been discretised using 2432 nodes and 11392 elements.

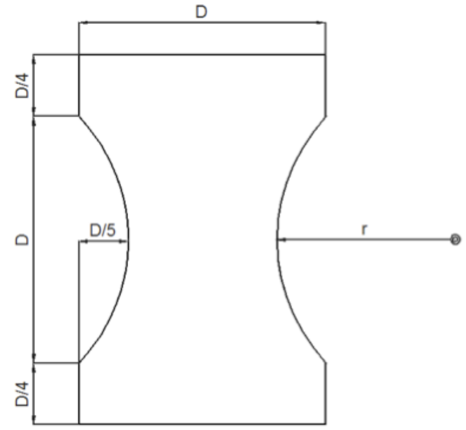

Figure 3.12: Geometry description for the Dog Bone specimen, with D = 50 mm and r = 36.35 mm.

Table 3.5: Material characterization for the Dog Bone specimen

Parameters	
Modulus of elasticity	26 GPa
Poisson ratio	0.18
Fracture Energy	90 N/m

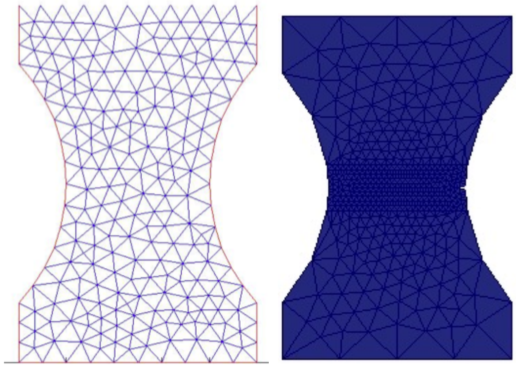

Figure 3.13: Models employed for a analysing the problem with smeared (left) and discrete (right) approach.

Table 3.6: Models characterization for the Dog Bone specimen.

Smeared		*Discrete*
421	**Number of elements**	11392
240	**Number of nodes**	2432
3 hours	**CPU time**	13 hours

Vořechovskỳ (2007) proved that for this example a single crack path is hardly identified. In fact, mainly due to the size effect and effect of material heterogeneity, damage in the real specimen and crack initiation points can be detected in different areas. Figure 3.14 shows the crack patterns obtained from the two models. With the discrete approach an initial defect needs to be manually identified, from which a single crack starts to propagate. The smeared approach allows the identification of the initiation area when the specimen is progressively damaging. For a homogeneous model, crack path is then created in the same location of the model studied with the discrete approach. In fact, in absence of other factors, damage is localised where the cross-section area is minimum, therefore in the middle of the specimen. Figure 3.15 clearly shows how damage starts spreading all over the specimen, concentrating then in the middle due to its geometry.
From the load-deflection curves plotted in Figure 3.16, it can observed how both models are capable of capturing the linear behaviour and predicting an appropriate peak load, but, similarly for what observed is the previous example, the post-failure behaviour is totally missing due to the crack modelling methodologies, developed to reproduce the behaviour of brittle materials.

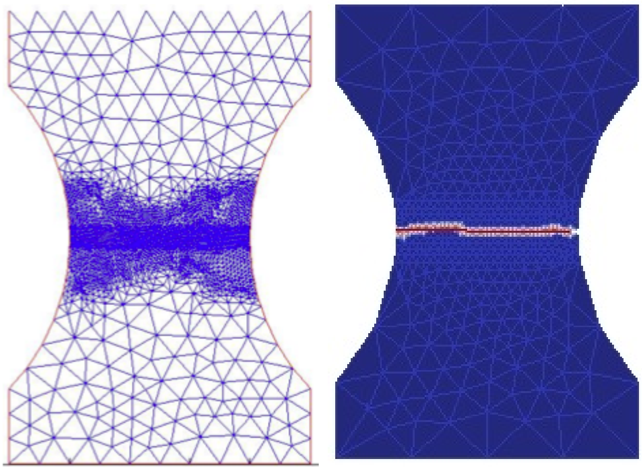

Figure 3.14: Crack patterns obtained with smeared (left) and discrete (right) models.

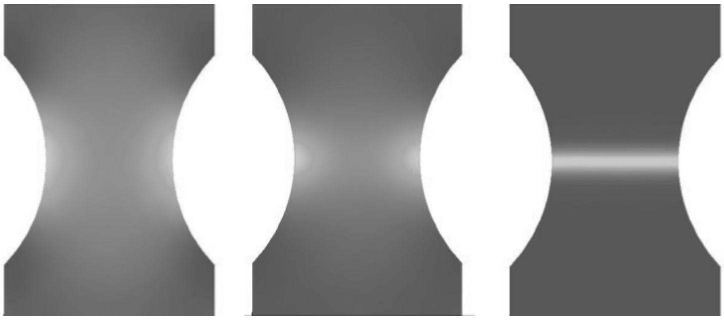

Figure 3.15: Damage state evolution with smeared model.

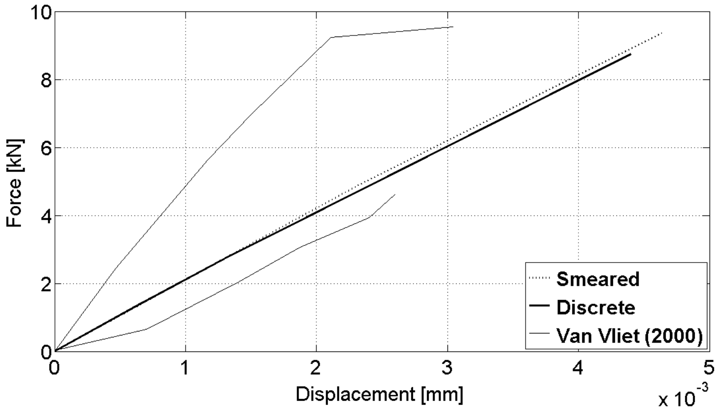

Figure 3.16: Load-Displacement plot for the Dog Bone specimen: comparison between smeared and discrete approach and comparison with experimental data.

To further validate the capability of the smeared approach to predict crack initiation point as a function of both geometrical and material properties, as shown in Figure 3.17 a layer with lower resistance (lower elastic modulus and fracture energy both decreased of 30%) is introduced in a random location. Where the effect of spatially varying material properties is analysed in terms of damage localisation, local damage and crack initiation point vary according to the material properties distribution (Vořechovskỳ, 2007). A weak zone is more likely to be the zone where damage is going to localise and a crack is going to propagate or, however, its presence is going to influence the extend and the direction of a crack. Figure 3.18 shows how the damage spreads within the specimen and can be clearly observed how effectively the presence of the weak layer influences the damage evolution. In fact, damage starts in proximity of both the middle of the specimen, where the area of the section is minimum, and in the weak zone. Damage localises in the upper part of the

specimen and then crack is formed there.
Looking at the computational cost required for each analysis, also for this example, the considerable difference between the two methods is noted, due to the differences in the methodologies used for guaranteeing mesh convergence.

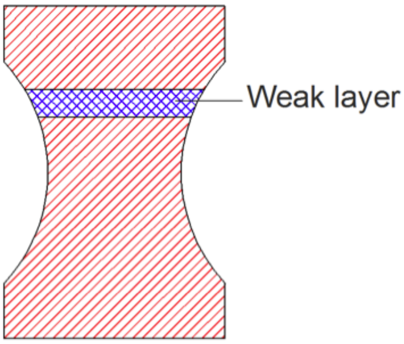

Figure 3.17: Dog Bone specimen with weak layer.

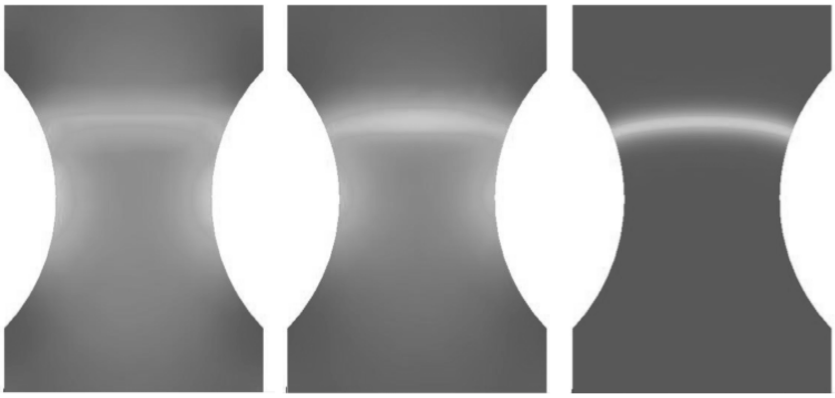

Figure 3.18: Damage state evolution with smeared model with weak layer.

3.6 Error estimators and results quality

In order to check the capabilities of the numerical codes to provide accurate results, error estimators and convergence criteria for the two numerical frameworks are described.
For the numerical framework based on the configurational force method residuals are provided at each iteration for all the nodes belonging to the crack front. One of the main focuses of the work from Kaczmarczyk et al. (2014) is on the improve-

ment of the quality and the stability of numerical solutions; in the calculation of the material force residuals, in fact, additional consideration has been put to take into account the quality of the elements at the crack front, as they change their shape as crack propagates due to the mesh alignment technique incorporated. Also, it should be reminded that an adaptive hp-refinement strategy is included, which also contributes to provide more accurate numerical solutions. For all the three examples analysed in this chapter, 95% of the residuals calculated are in the order of 10^{-5}, and the maximum value observed for the residual is in the order of 10^{-2}. Furthermore, these values for residuals are considered in the calculation of convergence of the Newton-Raphson, as the iterative procedure continues until the residuals have norms smaller than a given tolerance (Kaczmarczyk et al., 2014).

For the numerical framework based on the smeared approach, the resolution of the numerical problem described by the two different PDEs is directly solved by means of the function "assempde" which does not explicitly provide values for residuals of the FE discretisation and problem resolution. However, the mesh h-refinement strategy adopted (Del Piero et al., 2007) aims to minimise the error fro those elements where damage develops; furthermore it is still possible to check the accuracy of results in terms or Newton-Raphson convergence. In fact, an iterative procedure able to give accurate results is incorporated in the model, and lets the iterative procedure continue until the norm of the difference between two consecutive iterations doesn't become less that a fixed value (Del Piero et al., 2007), that for all simulations has been selected to be equal to 0.01.

3.7 Conclusions

In this chapter two distinct crack modelling approaches for brittle materials are compared. In one approach, the focus is on a discrete model that represents cracks by predicting the direction and extend of fractures on the basis of the principle of energy minimisation together with a node-based Griffith-like crack criterion. The second methodology is the variational model that studies fracture within a continuous framework, in which energy minimisation of a functional considering bulk and fracture energy leads to equilibrium configuration of bodies.

In order to compare the two methodologies, three examples have been selected: the SNES beam, the L-Shaped specimen and the Dog Bone specimen. These examples have been selected as they have different failure modes and, therefore, they have the capability to highlight different aspects of failure in quasi-brittle materials.

For the first example, both models provide results in good agreement in terms of both material resistance and crack pattern, with results from the discrete-based approach closer to experimental investigations.
For the second example, it is observed that both models can localise the crack path, but, as observed also in the previous example, by using a discrete approach crack is more precisely identified and closer to experimental results. In fact, the discrete approach appears more suitable when a single crack is dominant. Furthermore, this model is capable of predicting true crack pattern without the need to define the crack opening mode, thanks to the configurational forces acting on the crack front and of the remeshing technique.
On the other hand, by studying the Dog Bone specimen, the smeared model is capable of capturing the progressive damage over the specimen itself. Damage is localised in the middle of the specimen because of the cross section area of the specimen in that location is smaller compared to the rest of the sample; if other factors were included in the model (e.g. heterogeneity) damage localisation would have happened in other locations of the specimen (for example, in zones with lower value of fracture energy). The discrete approach is capable of defining a realistic crack path, but its localisation is more of all related to the location of an initial notch, manually introduced in the sample modelled numerically.

On the basis of the considerations shown above, it is decided that the methodology for heterogeneity that will be shown in Chapters 5 and 6 will be applied to the numerical framework developed using a smeared approach. The main reasons are:

1. the capability of the smeared-based framework to capture both crack initiation and propagation of material without the need of introducing initial notches;
2. the computational cost required for each analysis, as the methodology (explained in Chapter 5) includes the employment of Monte Carlo method, which itself increases significantly the overall computational effort;
3. the not-full capability of the smeared-based methodology to reproduce a fully-realistic crack pattern, especially for mixed-mode crack opening conditions, compared to the results obtained by using the discrete-based methodology which, without the inclusion of heterogeneity, is able to provide crack patterns in excellent agreement with experimental results;
4. the possibility of observing differential damage distributions in the specimens when the effect of heterogeneity is incorporated in the numerical framework;

5. for the discrete model, the need of a extremely sophisticated algorithm able to accurately compute the (eventual) new values of random mechanical properties assigned to those nodes which change their position.

Chapter 4

Probability theory

4.1 Introduction

Probability theory involves the development of mathematical frameworks able to treat random phenomena. A random phenomenon is defined as a repeated experiment with a set of possible results. If the experiment is performed several times, with all conditions maintained as identical and precise as possible, and the measured results are also identical, then the item which is measured is said to be deterministic. Otherwise, the item is said to be random.

A real number, connected to each of the results in the second scenario, is defined probability of the event. It seems reasonable that: (i) the probability is related to the expected frequency of occurrence of the event in a long series of experiments, (ii) it should lie between 0 and 1, and (iii) the sum of probabilities of all possible events in an experiment should be equal to unity (Kleiber and Hien, 1992).

The aim of this chapter is to provide an overview of the main concepts of probability and the probability distributions used in this thesis.

4.2 Probability

An experiment can be defined *random* when its outcome can not be predicted with certainty. If this random experiment is repeated, it would be likely that the outcome would change. These changes can be due to different factors, such as errors in measurements and readings, differences in the geometric properties of the object or local variations in mechanical properties of materials. A statistical model, in order to be defined efficient, must be able to model and analyse these possible scenarios. In practice, some examples of experiments with random nature are:

- the CPU time needed to execute a computational analyses, which may vary according to the amount of processors available in the machine at a specific moment;
- the material resistance of concrete (heterogeneous material) tested for the same mixture on different specimens, depending on the internal distribution of aggregates, sand, water and cement.

To represent the outcomes from random experiments, an uppercase variable, such as X is usually used. X is called *random variable*. Its value depends on the intrinsic uncertainty nature of the experiment, and can take different values, based on its probability distribution. The observed value of the random variable X is denoted by a lowercase x. (Martinez and Martinez, 2007)
Random variables are divided into two main categories: discrete and continuous. A *discrete* random variable can take on values from a countable set of numbers. A *continuous* random variable gets its values from an interval of real numbers (Martinez and Martinez, 2007).
A subset of outcomes in the sample space is called *event*. If two events can not occur simultaneously of jointly they are called *mutually exclusive events*. This definition can be extended to any number of events by considering all pairs of events. Every pair of events must be mutually exclusive for all of them to be mutually exclusive (Martinez and Martinez, 2007).

Probability can be defined as the measure of the likelihood at which certain events will happen. It is also a way to estimate the likelihood that an observed random variable will have on values within a specified range of values. Probabilities are always included between 0 and 1. A probability distribution of a random variable defines the probabilities connected to every value of the variable.
The most common way to find the desired probability that an event occurs is to use a probability density function (PDF) when continuous random variables (or a probability mass function in the case of discrete random variables) are given. In this thesis, $p(x)$ is used to represent the probability density function for continuous random variables.
To find the probability that a continuous random variable falls in a particular interval of real numbers, the area under the curve of $p(x)$ has to be considered. The integral of $p(x)$ over the interval of random variables corresponding to the event of interest has to be therefore evaluated. This is represented by (Martinez and Martinez, 2007)

$$P(a \leq X \leq b) = \int_a^b p(x)\,\mathrm{d}x. \tag{4.1}$$

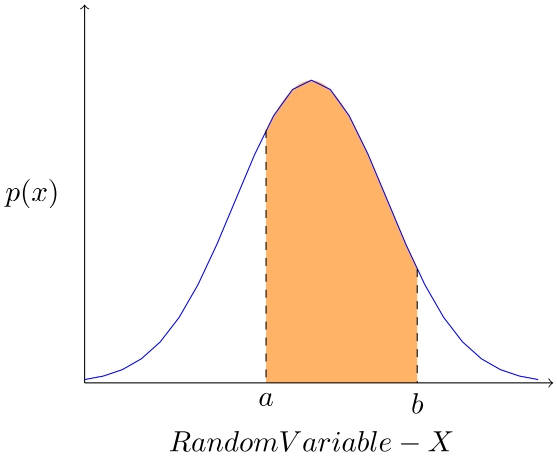

Figure 4.1: The area under the curve of $p(x)$ between a and b is the same as the probability that an observed value of the random variable will assume a value in the same interval.

The area under the curve of $p(x)$ between a and b represents the probability that an observed value of the random variable X will assume a value between a and b. This concept is illustrated in Figure 4.1 where the shaded area represents the desired probability.

The cumulative distribution function (CDF) $P(x)$ is defined as the probability that the random variable X assumes a value less than or equal to a given x. This is calculated from the probability density function, as follows (Martinez and Martinez, 2007)

$$P(x) = Pr(X \leq x) = \int_{-\infty}^{x} p(t)\,\mathrm{d}t. \tag{4.2}$$

It is trivial that the cumulative distribution function takes on values between 0 and 1, so $0 \leq P(x) \leq 1$. A probability density function, along with its associated cumulative distribution function are illustrated in Figure 4.2.

For a discrete random variable X, that can take on values x_1, x_2, ... , the probability mass function is given by

$$p(x_i) = Pr(X = x_i); \qquad i = 1, 2, ... \tag{4.3}$$

and the cumulative distribution function is

$$P(a) = \sum_{x_i \leq a} p(x_i); \qquad i = 1, 2, ... \tag{4.4}$$

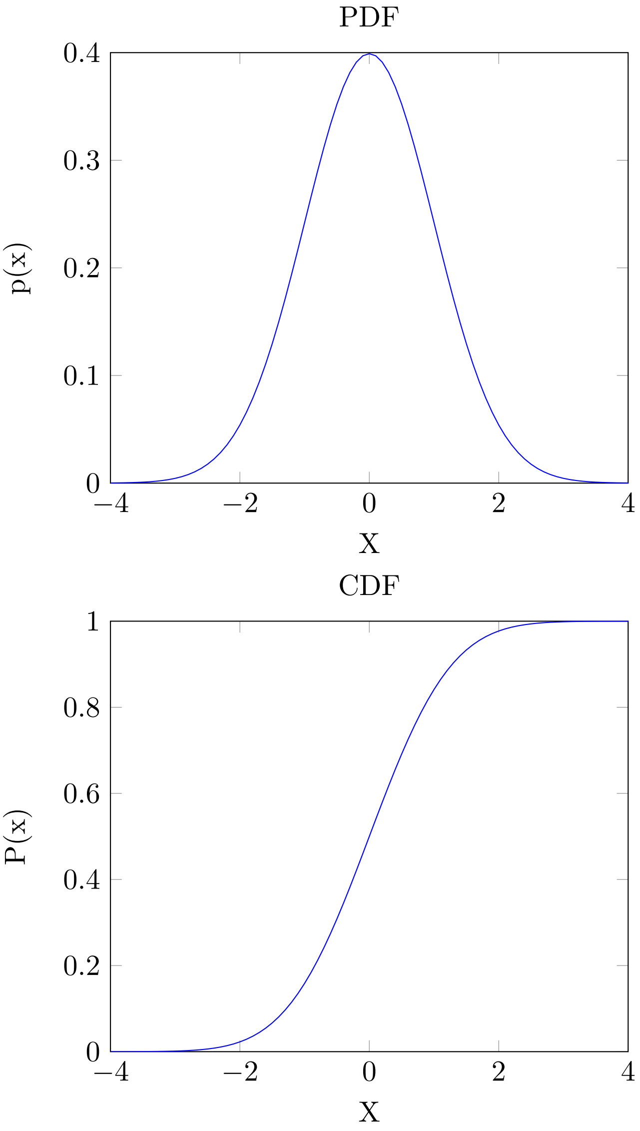

Figure 4.2: This shows the probability density function on the left with the associated cumulative distribution function on the right. Notice that the cumulative distribution function takes on values between 0 and 1.

4.3 Axioms of probability

Probabilities follow certain axioms that can be useful in computational statistics. S represent the sample space of an experiment and Ev represent some event that is a subset of S (Martinez and Martinez, 2007).

"AXIOM 1
The probability of event Ev must be between 0 and 1:

$$0 \leq Pr(Ev) \leq 1.$$

AXIOM 2
An outcome from one experiment must occur, and the probability that the outcome is in the sample space is 1:

$$Pr(S) = 1.$$

AXIOM 3
For mutually exclusive events, $Ev_1, Ev_2, ..., Ev_k$

$$Pr(Ev_1 \cup Ev_2 \cup ... \cup Ev_i) = \sum_{i=1}^{k} Pr(Ev_i)''.$$

4.4 Expectations: mean value and variance

Mean (or expected) values and variances are fundamental concepts in statistics. They are employed to describe distributions, to evaluate the performance of estimators, to obtain test statistics in hypothesis testing, and in many other applications. The *mean value* of a random variable is defined using the PDF and gives a measure of central tendency of the distribution. If several values of the random variable are observed and the average of them in taken, that value is expected to be close to the mean. The mean value is defined below for the discrete case:

$$\mu = E[X] = \sum_{i=1}^{\infty} x_i p(x_i). \tag{4.5}$$

The expected value is a sum of all possible values of the random variable where each one is multiplied by the probability that X will take on that value.

The *variance* of a discrete random variable is given, for $\mu < \infty$ by the following definition:

$$\sigma^2 = V(X) = E[(X - \mu)^2] = \sum_{i=1}^{\infty}(x_i - \mu)^2 p(x_i). \tag{4.6}$$

From Eq. 4.6, can be seen that the variance is the addition of the squared distances, each calibrated by the probability that $X = x_i$. Variance measures the dispersion in the probability distribution. When the variance of a random variable is large, then is more probable that each value of the variable is far from μ. The square root of the variance is defined as standard deviation σ.

The mean and variance for continuous random variables are similarly described, with the sum being substituted by an integral. The mean of a (continuous) random variable is given as (Martinez and Martinez, 2007):

$$\mu = E[X] = \int_{-\infty}^{+\infty} xp(x)\,\mathrm{d}x. \tag{4.7}$$

The variance of a continuous random variable is given below for $\mu < \infty$:

$$\sigma^2 = V(X) = E[(X - \mu)^2] = \int_{-\infty}^{+\infty} (x - \mu)^2 p(x)\,\mathrm{d}x. \tag{4.8}$$

Eq. 4.8 can be also written as

$$V(X) = E[X^2] - \mu^2 = E[X^2] - (E[X])^2. \tag{4.9}$$

4.5 Sampling

In this section, the main concepts related to random sampling and the sampling distribution of statistics are covered and some of the most used methods for deriving estimators, such as the maximum likelihood estimation method, will be described.

4.5.1 Sampling concepts

An experiment is performed to collect data needed to provide information about the phenomena of interest. These data are used to generalise from that specific experiment to the class of all similar experiment. This concept is the basis of *inferential statistics*: the degree of uncertainty in the results can be estimated and managed. Inferential statistics is an assortment of techniques and tools able to use the information obtained from experiments to make statements about the entire population of objects of interest (Martinez and Martinez, 2007).

The *target population* is defined as the whole collection of objects about which it is needed to get information. It must be well defined in terms of which characteristics the user wants to be measured. Realistically speaking, most of the times it is not feasible to observe the entire population; so only one part of the target population, called *sample* is considered. If inferences about the population are made using the information obtained from a sample, then it is important that the sample be representative of the population. This can usually be accomplished by selecting a simple random sample, where all possible samples are equally likely to be selected.
A sample of size n is called independent and identically distributed (iid) when the random variables $X_1, X_2, ..., X_n$ each have a common PDF $p(x)$. Additionally, when they are both iid, the joint PDF is given by

$$p(x_1, ..., x_n) = p(x_1)\text{x}...\text{x}p(x_n),$$

which is the product of the individual densities evaluated at each sample point.
Inferential statistics can employ the sample to estimate population parameters. It is needed to remember that a parameter is a quantitative measure for a population or a distribution of random variables. Clear examples of such parameters are the mean (μ), the standard deviation (σ) and correlation parameters. (Martinez and Martinez, 2007)

4.5.2 Statistics

A *statistic* is a function of the observed variables from a random sample and has no unknown population parameters. Often it is employed for the following cases:
- as a point estimate for a population parameter;
- to obtain a confidence interval estimate;
- as a test statistic in hypothesis testing.

In most cases, it is assumed that a random sample, $X_1, ..., X_n$ is representative of iid random variables.
A familiar statistic is the sample mean given by

$$\bar{X} = \frac{1}{n} \sum_{i=1}^{n} X_i. \tag{4.10}$$

Another statistic that will be needed is the sample variance, calculated from

$$\bar{\sigma}^2 = \frac{1}{n-1}\sum_{i=1}^{n}(X_i - \hat{X})^2 = \frac{1}{n(n-1)}\left(n\sum_{i=1}^{n}X_i^2 - \left(\sum_{i=1}^{n}X_i\right)^2\right) \tag{4.11}$$

4.5.3 Sampling distributions

Considering that most of the times sample are employed instead of an entire population, errors in the estimate can be easily incorporated. In order to control the error in the estimate, the *sampling distribution* for the statistic needs to be available.
The sampling distributions for many common statistics are available and well-known. For example, when a random variable is obtained from a Gaussian distribution, then it is known how the mean is distributed. Once the sampling distribution of the statistic is known, statistical hypothesis tests can be done and confidence intervals estimated. If the distribution of a statistic is not known, then Monte Carlo simulation techniques or bootstrap methods should be employed to estimate the needed distribution (Martinez and Martinez, 2007).
To illustrate the concept of a distribution, the sampling distribution for X that follows a distribution given by $p(x)$ is analysed. The distribution for the sample mean can be obtained using the Central Limit Theorem (Martinez and Martinez, 2007).

CENTRAL LIMIT THEOREM
"Let $p(x)$ represent a probability density with finite variance σ^2 and mean μ. Also, let X be the sample mean for a random sample of size n drawn from this distribution. For large n, the distribution of X is approximately normally distributed with mean μ and variance given by $\frac{\sigma^2}{n}$" (Martinez and Martinez, 2007).

The Central Limit Theorem says that as the sample size gets bigger, the distribution of the mean gets closer to the normal distribution independently on how X is distributed. However, if a normal population is used for sampling, then the distribution of the sample mean is exactly normally distributed with mean μ and variance $\frac{\sigma^2}{n}$.

4.5.4 Parameter estimation

One of the first tasks a statistician undertakes when facing some data is to try to summarise or describe quantitatively them. Some of the statistics can be used as quantitative description for a sample. In this section, one of the methods to derive and to evaluate estimates of population parameters is described.

There are several methods available in literature for obtaining parameter estimates, but in this thesis the maximum likelihood estimation (MLE) method is used, specifically for calculating shape and scale parameter of the Weibull distribution (which will be described in detail in the next section) from the corresponding normal distribution.
A MLE is that value of the parameter (or parameters) that maximises the likelihood function of the sample. The likelihood function of a random sample of size n from density function $p(x;\theta)$ is the joint probability density function, denoted by

$$L(\theta; x_1, ..., x_n) = p(x_1, ..., x_n; \theta). \tag{4.12}$$

Equation 4.12 gives the likelihood that the random variables take on a particular value $x_1, ..., x_n$. Given a random sample (iid random variables), the likelihood function can be expressed as (Bhattacharya, 2011)

$$L(\theta) = L(\theta; x_1, ..., x_n) = p(x_1; \theta)\text{x...x}p(x_n; \theta) = \prod_{i=1}^{n} p_{x_i}(x_i; \theta). \tag{4.13}$$

which is the product of the individual density functions evaluated at each x_i or sample point. In most cases, to find the value $\hat{\theta}$ that maximises the likelihood function, the derivative of L is taken, set it equal to 0 and solved for θ (Bhattacharya, 2011):

$$\frac{d}{d\theta} L(\theta) = 0. \tag{4.14}$$

It can be shown that the likelihood function, $L(\theta)$, and logarithm of the likelihood function, $\ln L(\theta)$, have their maximum values at the same value of θ. Many times can be easier to find the maximum of $\log L(\theta)$, when, for example, exponential function are involved. However, it is needed to keep in mind that a solution to the above problem might also be a minimum. It is therefore essential that the user is sure he found a maximum and not a minimum.
If a distribution has two or more parameters, the likelihood function depends on the parameters related to the distribution. If this is the case, the MLEs are calculated by considering the partial derivatives of L or $\log(L)$, equaling them to zero, and calculating the results of the system of equations. Results are defined as joint MLEs.

4.6 Probability distributions

In this section, a review of some useful probability distributions is provided and some applications to modelling data are very briefly described. Most of these distributions are used in later in this thesis, so it is opportune to define them and to fix notations.
There are many distributions available, used according to the specific application. The most important and common discrete distributions are the binomial and the Poisson distributions. These are followed by several continuous distributions, i.e. the uniform, the normal, the exponential, the gamma, the chi- square, the Weibull, the beta and the multivariate normal.
In the next section the focus will be only on some on the continuous distributions that will be used it this thesis: the normal, lognormal, Weibull and multivariate.

4.6.1 Normal distribution

One of the most employed and known distribution in statistics is the normal (or Gaussian) distribution. Its PDF is formulated as (Martinez and Martinez, 2007)

$$p_{norm}(x;\mu,\sigma^2) = \frac{1}{\sigma\sqrt{2\pi}} \exp\{-\frac{(x-\mu)^2}{2\sigma^2}\}, \tag{4.15}$$

where $-\infty < x < \infty; -\infty < \mu < \infty; \sigma^2 > 0$. This distribution is completely defined by its parameters μ and σ^2, which, furthermore, are the expected value and variance for a normal random variable. The notation $X \backsim \mathcal{N}(\mu, \sigma^2)$ is used to indicate that a random variable X is normally distributed with mean μ and variance σ^2. Several normal distributions with different parameters are shown in Figure 4.3.
The special case of a standard normal random variable is one whose mean is zero ($\mu = 0$) and variance is equal to unity ($\sigma^2 = 1$). If X is normally distributed, then

$$Z = \frac{X - \mu}{\sigma} \tag{4.16}$$

is a standard normal random variable.

The CDF of a standard normal random variable is denoted by

$$\Phi(z) = \frac{1}{\sqrt{2\pi}} \int_{-\infty}^{z} \{-\frac{y^2}{2}\} \, \mathrm{d}y. \tag{4.17}$$

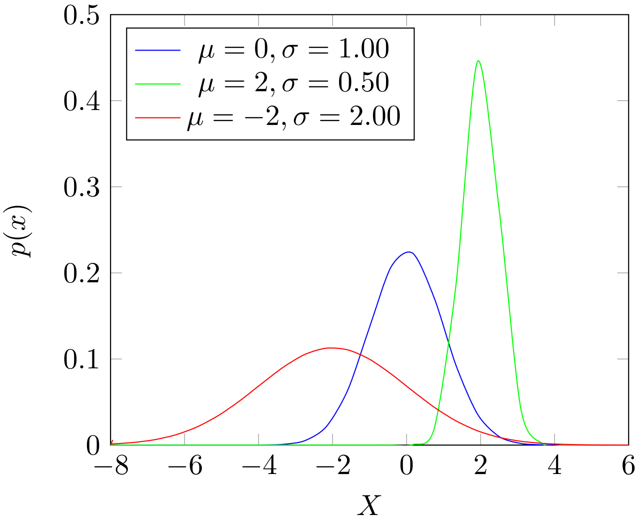

Figure 4.3: Examples of probability density functions for normally distributed random variables. Note that as the variance increases, the height of the probability density function at the mean decreases..

In statistics, the *error function* $\operatorname{erf}(x)$ is defined as the probability of a random variable with normal distribution of mean 0 and variance 0.5 to fall in the range $[-x, x]$:

$$\operatorname{erf} x = \frac{1}{\sqrt{\pi}} \int_{-x}^{x} e^{-t^2}\, \mathrm{d}x. \tag{4.18}$$

Equations 4.17 and 4.18 are closely related, namely

$$\Phi(x) = \frac{1}{2}\left[1 + \operatorname{erf} \frac{x}{\sqrt{2}}\right] \tag{4.19}$$

and therefore the CDF takes the final form of

$$P_{norm}(x) = \Phi\Big(\frac{x-\mu}{\sigma}\Big) = \frac{1}{2}\left[1 + \operatorname{erf} \frac{x-\mu}{\sigma\sqrt{2}}\right]. \tag{4.20}$$

4.6.2 Log-Normal Distribution

The Log-Normal distribution is another type of continuous probability distribution largely employed in numerous fields. A random variable X which follows a log-normal distribution has its logarithm normally distributed: if X is log-normally distributed, consequently $\ln X$ is normally distributed. An extremely important property of this distribution, especially if related to engineering applications, is that a random variable which is log-normally distributed takes only positive real values.

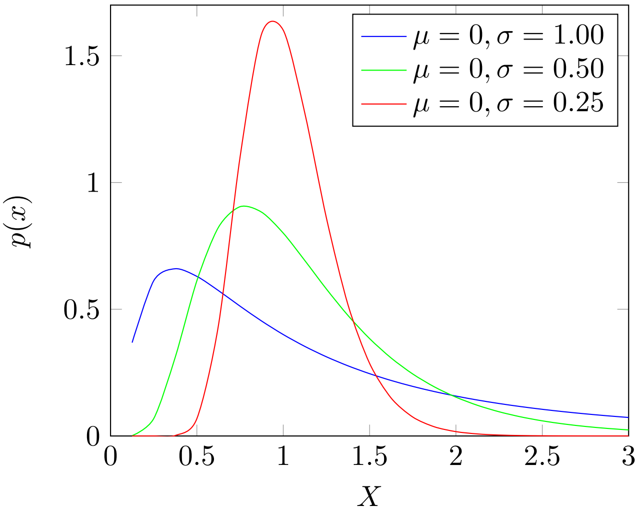

Figure 4.4: Examples of probability density functions for log-normally distributed random variables. Note that as the variance increases, the height of the probability density function at the mean decreases.

The probability density distribution for this case takes the form

$$p_{logn}(\ln x, \mu, \sigma^2) = \frac{1}{\sigma\sqrt{2\pi}} \exp\left(-\frac{(\ln x - \mu)^2}{2\sigma^2}\right), \tag{4.21}$$

where $-\infty < x < \infty; -\infty < \mu < \infty; \sigma^2 > 0$. As for the normal distribution, also the log-normal distribution is fully defined by its parameters μ and σ^2. The notation $\ln X \backsim \mathcal{N}(\mu, \sigma^2)$ indicates that when $\ln X$ follows a normal distribution, then X follows a log-normal distribution with mean μ and variance σ^2. Several log-normal distributions with different values for μ and σ^2 are shown in Figure 4.4.

The CDF of a lognormally distributed random variable is given by

$$\int_0^x \ln \mathcal{N}(x; \mu, \sigma)\, \mathrm{d}\xi = \frac{1}{2}\left[1 + \operatorname{erf} \frac{\ln x - \mu}{\sigma\sqrt{2}}\right] = \Phi\left(\frac{\ln x - \mu}{\sigma}\right) \tag{4.22}$$

where Φ is the CDF for the standard normal distribution.

4.6.3 Weibull distribution

In engineering practice, the Weibull distribution is one of the most widely used, in particular in reliability analyses. The probability density function of a random variable from Weibull distribution is given by (Martinez and Martinez, 2007)

$$p_{Weib}(\zeta; m, \zeta_0) = \begin{cases} \frac{m}{\zeta_0}\left(\frac{\zeta}{\zeta_0}\right)^{m-1} e^{-(\zeta/\zeta_0)^m} & \zeta \geq 0, \\ 0 & \zeta < 0, \end{cases} \tag{4.23}$$

where $m > 0$ is the *shape parameter* and $\zeta_0 > 0$ is the *scale parameter*. The shape of the density function is strongly affected by the value of its parameters as can be noted in Fig. 4.5. If $0 < m < 1$, the density function tends to ∞ as ζ approaches zero from above and is strictly decreasing. For values of m equal to unity, the probability density function goes to $1/\zeta_0$. For $m > 1$, the density function tends to zero as ζ approaches zero from above, increases until its mode and decreases after it. The cumulative density function takes the form

$$P_{weib}(\zeta; m, \zeta_0) = 1 - e^{-(\zeta/\zeta_0)^m}. \tag{4.24}$$

The mean and the variance of a Weibull random variable can be expressed as

$$E(X) = \zeta_0 \Gamma\left(1 + \frac{1}{m}\right) \tag{4.25}$$

and

$$\sigma^2(X) = \lambda^2\left[\Gamma\left(1 + \frac{2}{m}\right) - \left(\Gamma\left(1 + \frac{1}{m}\right)\right)^2\right] \tag{4.26}$$

In order to apply the MLE described in section 4.5.4 to estimate shape and scale parameters for Weibull distribution, Equation 4.23 can be put into 4.13 and apply 4.14 (Bhattacharya, 2011). Detailed calculations on this method will be provided in Chapter 5.

4.6.4 Multivariate normal distribution

Until this point, univariate distributions for continuous variables have been described. In this section the multivariate normal distribution is described. Given (at least) two random variables $X_i, i = 2, ...\infty$ defined on a probability space, the *joint probability distribution* is the probability distribution that gives the probability that each of X_i falls in any particular range.

In case of d-variate normal distribution, the univariate normal distribution becomes

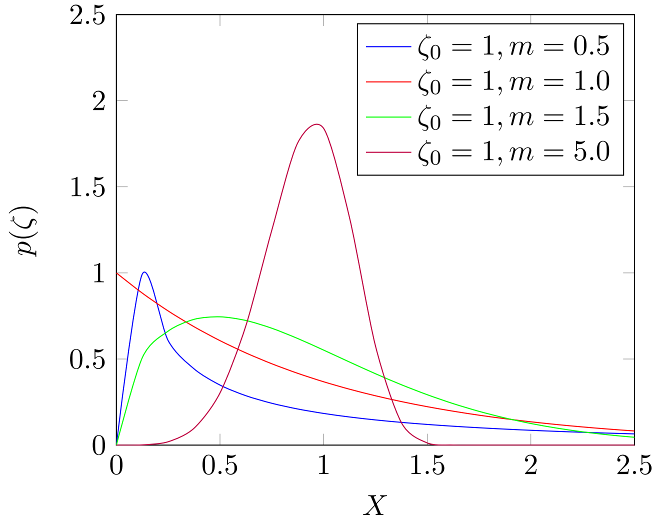

Figure 4.5: Examples of probability density functions for random variables distributed according Weibull distributions. Note that as the variance increases, the height of the probability density function at the mean decreases.

(Martinez and Martinez, 2007)

$$p_{MVN}(\mathbf{x}) = \frac{1}{(2\pi)^{d/2}|\mathbf{\Sigma}|^{0.5}} \exp -\frac{1}{2}(\mathbf{x}-\mu)^T \mathbf{\Sigma}^{-1}(\mathbf{x}-\mu) \tag{4.27}$$

where random variables are related to each other by $\mathbf{\Sigma}$, called *covariance matrix*. In case of bivariate probability function random variables are two with X_1 and X_2 being the two random variables with their own mean values $\mu(X_1), \mu(X_2)$ and variances $Var(X_1), Var(X_2)$. The covariance of X_1 and X_2 is defined to be

$$Cov(X_1, X_2) := E[X_1, X_2] - E[X_1]E[X_2] \tag{4.28}$$

and the correlation of X_1 and X_2 is then defined to be

$$Corr(X_1, X_2) = \rho(X_1, X_2) = \frac{Cov(X_1, X_2)}{\sqrt{Var(X_1)Var(X_1)}} \tag{4.29}$$

The quantity ρ, called correlation coefficient, measures the strength and the relationship between two variables. The value of ρ is such that $-1 \leq \rho \leq 1$:
- if the two variables have a strong positive linear correlation, ρ is close to $+1$. Positive values indicate a relationship such that as values for X_1 increase, values for X_2 also increase;
- if the two variables have a strong negative linear correlation, ρ is close to -1. Neg-

ative values indicate a relationship where if values for X_1 increase, values for X_2 decrease;
- if there is no linear correlation, ρ is equal to 0.
Given the value for ρ, is then possible to generate $\mathbf{\Sigma}$.
The $(i,j)^{th}$ element of $\mathbf{\Sigma}$ is given by $\mathbf{\Sigma}_{i,j} = Cov(X_i, X_j)$. In the case of two correlated random variables, the covariance matrix takes the form

$$\mathbf{\Sigma} = \begin{bmatrix} Var^2(X_1) & \rho Var(X_1)Var(X_2) \\ \rho Var(X_1)Var(X_2) & Var^2(X_1) \end{bmatrix} \tag{4.30}$$

This covariance matrix:
- is symmetric;
- has the diagonal elements that satisfy $\mathbf{\Sigma}_{i,j} \geq 0$;
- it is positive semi-definite[1].
Such a correlation structure, allows to create a Multivariate Probabilistic Distribution for sampling correlated random values for the mechanical properties of interest. In this work the aim is to study the behaviour for three different probabilistic distributions described above.

Once the covariance matrix has been defined, the problem is the generation a vector $\mathbf{X} = (X_1, ..., X_n)$ where $\mathbf{X}$ follows the multivariate normal distribution. Suppose $Z_i \backsim \mathrm{N}(0,1)$, iid for $i = 1, ..., n$. Then

$$c_1 Z_1 + ... + c_n Z_n \backsim \mathrm{N}(0, \sigma^2)$$

where $\sigma^2 = c_1^2 + ... + c_n^2$. The linear combination of normal random variables is normal itself.
More generally, let $\mathbf{C}$ be a $(n\text{x}m)$ matrix and let $\mathbf{Z}= (Z_1 Z_2 ... Z_N)^T$. Then

$$\mathbf{C}^T\mathbf{Z} \backsim \mathrm{MN}(0, \mathbf{C}^T\mathbf{C})$$

so the problem clearly reduces to finding $\mathbf{C}$ such that

$$\mathbf{C}^T\mathbf{C} = \mathbf{\Sigma}$$

It is possible to calculate the Cholesky decomposition of a symmetric positive-definite matrix in MatLab using the `chol` command.
Let $\mathbf{C}$ be the Cholesky decomposition of the covariance matrix. If $\mathbf{X} \backsim \mathrm{MN}(0, \mathbf{\Sigma})$

---

[1] Given a non-zero column vector $\mathbf{v}$, a matrix $\mathbf{M}$ is defined positive semi-definite if the scalar $\mathbf{v}^T\mathbf{M}\mathbf{v}$ in non-negative.

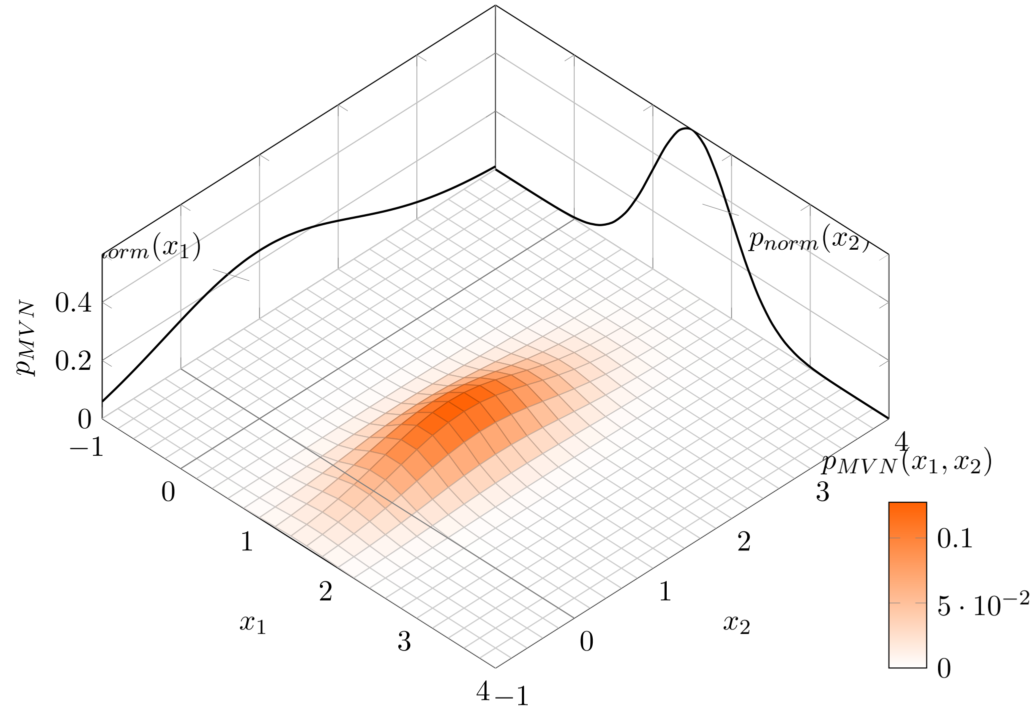

Figure 4.6: Bivariate normal density from two normal distributions with $\mu_1 = 1.5$, $\mu_2 = 1$, $\sigma_1 = 0.5$, $\sigma_2 = 1.2$.

then random samples of $\mathbf{X}$ can be generated as follows:

```
>> Input : CorrMat
>> C = chol(CorrMat)
>> Z = randn(s1, s2)
>> X = C^T * Z
```

where `randn` is the Matlab built-in function for the generation of normally distributed s_1 random vectors of dimension s_2.

For the generation of lognormal correlated random variables the procedure to follow is the same showed for normal random variables. The only difference is in the generation of the random vector Z to be multiplied by $\mathbf{C}^T$.

4.7 Conclusions

Notions and theory introduced in this chapter are the theoretical basis for a full understanding of the concepts showed and the methodologies developed in the next chapter, used to implement the smeared-based numerical framework for modelling of crack propagation using stochastic approaches.

Part II

Methodology

Chapter 5

The stochastic finite element method: continuum damage model implementation

5.1 Introduction

In Part I, the numerical frameworks considered in this work have been described and, on the basis of the comparative study reported in Chapter 3 on three different examples, the model considered and implemented is finally chosen. Implementations for modelling material heterogeneity have been done on the continuum damage mechanics model (based, therefore, on a smeared approach).

The process for solving stochastic problems using SFEM can be divided in two parts:

1. quantitative description of the stochastic fields of a heterogeneous system (by means of probability theory);
2. application of the uncertainty in properties of the system to be analysed and estimation of its stochastic response.

With regards to the first point, uncertainties can be included in a system by defining mechanical properties (i.e. modulus of elasticity, fracture toughness, ultimate strength) as spatially-distributed random variables, geometric properties (i.e. specimen cross section, defects, voids) or load (Stefanou, 2009). Probability distributions and correlation structures used for sampling[1] procedures (described and compared in chapters 2 and 4) result to be therefore the most convenient way to describe

---

[1] In statistics, the term *sampling* refers to the selection of a series of data, from a given population, which is fully representative of the characheristics of the population itself.

heterogeneities, mainly because of possible lack of data for comprehensive systems characterisation (Stefanou, 2009).

With regards to the second point, it must be specified that SFEM includes three main steps: (i) discretisation and representation of the stochastic field, (ii) stochastic matrices formulation and assembly, (iii) calculation of the response variability.

This chapter aims to describe the incorporation of heterogeneity into the variational approach method, in order to study its effect on the response of the system (i.e. crack patterns and material resistance to failure).

Heterogeneity has been modelled by using non-Gaussian Weibull distribution: the possibility of using non-Gaussian stochastic processes has received an increasing attention in the scientific community because (i) they provide only positive values, while Gaussian field may lead to negative (and therefore physically meaningless) values of mechanical properties, and (ii) several common quantities in engineering practice show non-Gaussian probabilistic characteristics (Stefanou, 2009; Gorjan and Ambrožič, 2012). The methodology proposed in this work generates samples compatible to probabilistic information (mean value, standard deviation, correlations) obtained from either literature or experimental data.

The results obtained using a non-Gaussian Weibull process is then compared to those obtained using a Gaussian process, the Karhunen-Loeve (K-L) expansion method described in Chapter 2. This method is one of the most widely used for the representation of stochastic fields: however its implementation in numerical models is often difficult especially for complex geometries and correlation structures. More details with regards to this point will be accurately described in the following paragraphs. The problem of sampling one and two correlated random variables is also presented and described. While for the K-L expansion method this problem has been already faced by several authors, in case of bivariate Weibull distribution this problem becomes more challenging: in this thesis an optimal algorithm for the generation of two-dimensional samples from bi-variate Weibull distribution has been developed and implemented, and details about the code can be found in Appendix A. It is worth mentioning that only few bivariate Weibull distributions have been proposed in the literature and applied to engineering problems, but none of them has been explicitly applied to fracture mechanics problems.

For the calculation of the response variability, Monte Carlo Simulation (MCS) method is chosen. With this method, a N_{sim} number of simulation analyses are performed until an acceptable convergence of the results is achieved (i.e. when the variation between the results is less than 10%). Despite this method provides realistic results in agreement with experimental observations, the computational cost increases noticeably.

In fact, one of the key aspects to be taken into account in this context is the computational cost required for generating samples of random values of the selected mechanical property, which can be prohibitive if the size of the sample vector (which is the vector, where each element stores the value for the mechanical property for each element of the discretised domain) is extremely high. This issue will be solved in the next chapter, where a novel methodology for reducing the size of the stochastic problem and saving a considerable amount of computational time will be presented.

5.2 Variational model implementation

For analysis with only one random variable, fracture energy is the mechanical parameter showing heterogeneous nature, while in case of two random variables both fracture energy and modulus of elasticity are the mechanical parameters where heterogeneity is considered.

Let's recall the regularised formulation of the total energy expressed as per Eq. 2.34 in Chapter 2:

$$\begin{aligned}\mathcal{F}(\boldsymbol{f}, s) = &\int_{\Omega_0} (s^2(x_0) + k_\varepsilon) W(\triangledown_0 \boldsymbol{f}(x_0)) \, \mathrm{d}x_0 \\ &+ \frac{G}{2} \int_{\Omega_0'} (\varepsilon | \triangledown_0 \, s(x_0)|^2 + \frac{1}{\varepsilon}(1 - s(x_0))^2) \, \mathrm{d}x_0.\end{aligned} \tag{5.1}$$

As shown in the Literature Review of Chapter 2, Eq. 2.34 is minimised according to the two variables $\boldsymbol{f}$, representing the deformation of a body, and s, representing the damage state of the same body. The two minimised equations are then solved by means of standard FEM and, therefore, can be expressed in the basic PDE formulation

$$-\nabla(b \nabla u) + du = g. \tag{5.2}$$

5.2.1 Fracture energy as random process

If fracture energy is considered as the mechanical parameter where heterogeneity is considered it can be expressed as $G(\mathbf{x}, \theta)$ (where θ defines the random nature of the variable), and the functional of Eq. 5.1 can be therefore rewritten as

$$\begin{aligned}\mathcal{F}(\boldsymbol{f}, s) = &\int_{\Omega_0} (s^2(x_0) + k_\varepsilon) W(\triangledown_0 \boldsymbol{f}(x_0)) \, \mathrm{d}x_0 \\ &+ \frac{G(\mathbf{x}, \theta)}{2} \int_{\Omega_0'} (\varepsilon | \triangledown_0 \, s(x_0)|^2 + \frac{1}{\varepsilon}(1 - s(x_0))^2) \, \mathrm{d}x_0.\end{aligned} \tag{5.3}$$

It should be observed that, when Eq. 5.3 is minimised with respect to the variable $\boldsymbol{f}$, deformation of the domain, the second term of the RHS of the equation, and therefore also $G(\mathbf{x}, \theta)$ vanishes; however, the effect of the heterogeneous nature of the fracture energy is still taken into account by the model by reintroducing in the model at each time-step the output values for s obtained as result of the minimisation of the energy functional according to the damage variable (keeping the stationarity condition for fixed $\boldsymbol{f}$). In fact, when Eq. 5.3 is minimised with respect to s, the coefficients b, d and g are expressed as

$$b = -\varepsilon \tag{5.4}$$

$$d = \frac{2W|_{J>1}}{G(\mathbf{x}, \theta)} + \varepsilon^{-1} \tag{5.5}$$

$$g = \varepsilon^{-1}. \tag{5.6}$$

where ε, W and J are as per Chapter 2. The heterogeneous nature of the material is therefore considered to influence both the damage distribution in the body and the mechanical response of the material (in terms of deformation).

5.2.2 Modulus of elasticity as random process

The formulation of coefficients b, d and g of Eq. 5.2 is provided below, where the spatial variability of the material is incorporated considering the modulus of elasticity $E(\mathbf{x}, \theta)$ as heterogeneous mechanical parameter:

$$b = f(J, s(J), k_\varepsilon, \hat{\lambda}(\mathbf{x}, \theta), \hat{\mu}(\mathbf{x}, \theta)) \tag{5.7a}$$

$$d = 0 \tag{5.7b}$$

$$g = f(x, x_0) \tag{5.7c}$$

where $\hat{\lambda}(\mathbf{x}, \theta)$ and $\hat{\mu}(\mathbf{x}, \theta)$ are the random Lame coefficients calculated from random $E(\mathbf{x}, \theta)$

$$\hat{\lambda}(\mathbf{x}, \theta) = \frac{\nu E(\mathbf{x}, \theta)}{(1+\nu)(1-2\nu)} = \alpha E(\mathbf{x}, \theta) \tag{5.8a}$$

$$\hat{\mu}(\mathbf{x}, \theta) = \frac{E(\mathbf{x}, \theta)}{2(1+\nu)} = \beta E(\mathbf{x}, \theta) \tag{5.8b}$$

with ν being the Poisson's coefficient and

$$\alpha = \frac{\nu}{(1+\nu)(1-2\nu)} \tag{5.9a}$$

$$\beta = \frac{1}{2(1+\nu)}. \tag{5.9b}$$

The Cauchy stress tensor $\mathbb{c}$ and material elasticity tensor $\mathbb{E}$ defined in Part I can be finally rewritten as function of the random Lame coefficients as

$$\mathbb{c} = \hat{\mu} J^{-1}\mathbf{F}\mathbf{F}^{-T} + J^{-1}(\hat{\lambda}\log J - \hat{\mu}) \tag{5.10}$$

$$\mathbb{E}(\mathbf{F}) = J^{-1}\hat{\lambda}\mathbf{I}\otimes\mathbf{I} + (\hat{\mu} - \hat{\lambda}\log J(\mathbf{I}\boxtimes\mathbf{I} + (\mathbf{I}\boxtimes\mathbf{I})^T)). \tag{5.11}$$

For the damage problem (stationarity condition for fixed $\mathbf{f}$), the coefficients b, d and g of Eq. 5.1 take the form

$$b = -\varepsilon \tag{5.12}$$

$$d = \frac{2W(\mathbf{F},\theta)|_{J>1}}{G} + \varepsilon^{-1} \tag{5.13}$$

$$g = \varepsilon^{-1} \tag{5.14}$$

where

$$W(\mathbf{F},\theta)|_{J>1} = \frac{\hat{\mu}}{2}(\mathrm{tr}\mathbf{C} - 3) + \frac{\hat{\lambda}}{2}(\log J^+)^2 - \hat{\mu}\log J^+. \tag{5.15}$$

is called *stochastic stored energy function*.

Therefore, the functional of the Eq. 5.1 can be rewritten as

$$\begin{aligned}\mathcal{F}(\boldsymbol{f}, s) = &\int_{\Omega_0} (s^2(x_0) + k_\varepsilon) W(\triangledown_0 \boldsymbol{f}(x_0), \theta)\,\mathrm{d}x_0 \\ &+ \frac{G}{2}\int_{\Omega_0'} (\varepsilon|\triangledown_0\, s(x_0)|^2 + \frac{1}{\varepsilon}(1 - s(x_0))^2)\,\mathrm{d}x_0.\end{aligned} \tag{5.16}$$

5.2.3 Fracture energy and modulus of elasticity as random process

When the heterogeneous nature of the material is considered by incorporating spatially variability in both fracture energy and modulus of elasticity, in the energy functional 5.1 both W and G are function of θ:

$$\begin{aligned}\mathcal{F}(\boldsymbol{f}, s) = &\int_{\Omega_0} (s^2(x_0) + k_\varepsilon) W(\triangledown_0 \boldsymbol{f}(x_0), \theta)\,\mathrm{d}x_0 \\ &+ \frac{G(\mathbf{x},\theta)}{2}\int_{\Omega_0'} (\varepsilon|\triangledown_0\, s(x_0)|^2 + \frac{1}{\varepsilon}(1 - s(x_0))^2)\,\mathrm{d}x_0.\end{aligned} \tag{5.17}$$

Values of b, d and g, for the deformation problem, take the form

$$b = f(J, s(J), k_\varepsilon, \hat{\lambda}, \hat{\mu}) \tag{5.18}$$

$$d = 0 \tag{5.19}$$

$$g = f(x, x_0) \tag{5.20}$$

while for the damage problem take the form

$$b = -\varepsilon \tag{5.21}$$

$$d = \frac{2W(\mathbf{x}, \theta)|_{J>1}}{G(\mathbf{x}, \theta)} + \varepsilon^{-1} \tag{5.22}$$

$$g = \varepsilon^{-1}. \tag{5.23}$$

5.3 Spatial autocorrelation function

For both Gaussian and non-Gaussian processes that will be described later in this chapter, the same spatial autocorrelation function will be considered. Let consider a FE mesh with np nodes and nt triangular elements, used to discretise the problem. Let $X(\mathbf{x}, \theta)$ be a random field with zero mean and specified variance, chosen according to the degree of heterogeneity of a material. The correlation function for a random field is chosen as

$$\rho(\mathbf{x}_1, \mathbf{x}_2) = \exp\left[-\frac{\pi|\mathbf{x}_1 - \mathbf{x}_2|}{l_{c^2}}\right] \tag{5.24}$$

where l_c is the correlation length. It is generally used to indicate the characteristic length of a heterogeneous medium.

In the computational framework developed for modelling of crack propagation, material properties are assigned at each element (for the case of domain discretised using FE models). The correlation function is created for each of this element, forming a symmetric and definite positive correlation matrix with nt rows and nt columns. This matrix relates each FE element to each other. All the elements in the main diagonal have unit value as they refer to the correlation between the value of mechanical properties in the same elements:

$$\mathbf{C}_{ff} = \sigma^2 \begin{bmatrix} 1 & \rho_{1,2} & \cdots & \rho_{1,nt} \\ & 1 & \cdots & \rho_{2,nt} \\ Sym & \vdots & \ddots & \vdots \\ & & \cdots & 1 \end{bmatrix} \tag{5.25}$$

where σ represents the standard deviation of the stochastic field.

5.4 Gaussian process: the Karhunen-Loeve expansion

5.4.1 Monovariate Gaussian process

The K-L expansion can be considered as a variant of the orthogonal series expansion. In this method, the orthogonal function are the eigenfunctions of the Fredholm integral equation with the spatial autocorrelation function as kernel (Stefanou, 2009):

$$\hat{f} = \bar{f}(x) + \sum_{n=1}^{N} \sqrt{\gamma_n}\xi_n\delta_n(x) \tag{5.26}$$

$$\int_D \mathbf{C}_{ff}(x_1, x_2)\delta_n(x_1)\,\mathrm{d}x_1 = \gamma_n\delta_n(x_2) \tag{5.27}$$

where the parameters of Eq. 5.26 and 5.27 are defined as per Eq. 2.68 and 2.69.
The use and implementation of K-L expansion method can be often difficult because of the complexities related to the resolution of the Fredholm integral of Eq. 5.27 (Stefanou, 2009). In fact, analytical solutions for this equation are available for simple geometries and simple covariance functions. For more complex problems and covariance functions, special numerical treatments are necessary. The level of accuracy in the calculation of γ_n and δ_n affects significantly the performance of the K-L expansion.
In this study, $\mathbf{C}_{ff}(x_1, x_2)$ will follow the formulation of Eq. 5.25. For this formulation, the analytical solution has been studied and developed by Oliveira (2012), and it provides the exact eigenvalues and eigenfunction associated with $\mathbf{C}_{ff}$ as

$$\gamma_n = \frac{2\sigma l_c}{l_c^2\iota_i^2 + 1} \tag{5.28}$$

$$\delta_n = \frac{l_c\iota_i\cos(\iota_i x) + \sin(\iota_i x)}{\sqrt{(l_c^2\iota_i^2 + 1)/2 + l_c}} \tag{5.29}$$

where ι_1, ι_2, ... are solutions of the equation

$$(l_c^2\iota^2 - 1)\sin(\iota) = 2l_c\iota\cos(\iota). \tag{5.30}$$

Fracture energy decomposed by means of the K-L expansion can be written as

$$G(\mathbf{x}, \theta) = \bar{G}(\mathbf{x}) + \sum_{i=1}^{\infty} \sqrt{\gamma_i}\xi_i(\theta)\delta_i(\mathbf{x}). \tag{5.31}$$

where $\bar{G}$ represents the mean value of G.

Modulus of elasticity decomposed by means of the K-L expansion can be written as

$$E(\mathbf{x},\theta) = \bar{E}(\mathbf{x}) + \sum_{i=1}^{\infty} \sqrt{\gamma_i}\xi_i(\theta)\delta_i(\mathbf{x}). \tag{5.32}$$

where $\bar{E}$ represents the mean value of E.

5.4.2 Bivariate Gaussian process

Let's now consider the case in which two random variables are introduced in the system. Let $\mathbf{X}(x,\theta) = (X_1, X_2, ..., X_{\mathfrak{d}})$ be a vector containing $\mathfrak{d}$ stochastic processes (if, for example, only one variable of the system has random nature, $\mathfrak{d} = 1$); in this study, a maximum of two stochastic processes will be considered and, therefore $\mathfrak{d}_{max} = 2$.

The multivariate K-L expansion can be expressed as (Wang, 2008):

$$\mathbf{X}(x,\theta) = \begin{bmatrix} X_1 \\ X_2 \\ ... \\ X_{\mathfrak{d}} \end{bmatrix} = \sum_{i=1}^{N} \sqrt{\gamma_i}\delta_i\xi_i = \sum_{i\geq 1} \sqrt{\gamma_i} \begin{bmatrix} \delta_i^{(1)} \\ \delta_i^{(2)} \\ ... \\ \delta_i^{(\mathfrak{d})} \end{bmatrix} \xi_i \tag{5.33}$$

where ξ_i is a two-dimensional vector sampled from a bivariate normal distribution, γ_i, $\delta_i^{(1)}$ and $\delta_i^{(2)}$ are obtained from the Fredholm integral of Eq. 5.27.

For the case of bivariate gaussian distribution, the KL expansion takes the form

$$\begin{bmatrix} X_1 \\ X_2 \end{bmatrix} = \sum_{i=1}^{N} \sqrt{\gamma_i}\delta_i\xi_i = \sum_{i\geq 1} \sqrt{\gamma_i} \begin{bmatrix} \delta_i^{(1)} \\ \delta_i^{(2)} \end{bmatrix} \xi_i. \tag{5.34}$$

5.5 Non-Gaussian process: Weibull distribution

The main method used in this study to sample random values of fracture energy and modulus of elasticity considers heterogeneity using a non-Gaussian Weibull process. The non-Gaussian Weibull distribution used in sampling phase has been chosen due to its capability in realistically describing the mechanical properties of brittle materials such as ceramics and rocks (Gorjan and Ambrožič, 2012; Stefanou, 2009; Yang and Xu, 2008). Similarly to what has been described for the K-L expansion method in the previous paragraph, in this section the descriptions of both monovariate and bivariate Weibull distribution are provided.

5.5.1 Monovariate Weibull process

For the simulation with only one random field , Cumulative Density Function (CDF), denoted by $P(.)$, and Probability Density Function (PDF), denoted by $p(.)$, for Weibull distribution, take the form of

$$P(\zeta) = 1 - \exp\Big(- \Big(\frac{\zeta}{\zeta_0}\Big)^m\Big) \tag{5.35}$$

$$p_s(\zeta) = \frac{\mathrm{d}P(\zeta)}{\mathrm{d}\zeta} = \frac{m}{\zeta_0}\Big(\frac{\zeta}{\zeta_0}\Big)^{m-1} \exp\Big(- \Big(\frac{\zeta}{\zeta_0}\Big)^m\Big) \tag{5.36}$$

where ζ is the random parameter following the Weibull distribution, m is shape parameter and ζ_0 is scale parameter.
Maximum Likelihood Estimator (MLE), briefly described in the previous chapter, is used to define both the shape and the scale parameters. Let $\zeta_1, \zeta_2, ..., \zeta_n$ be a set of hypothetical data which is randomly generated. It is plausible to fit a Weibull distribution to this hypothetical data (Devroye, 1986). In other words, it is assumed that $\zeta_1, \zeta_2, ..., \zeta_n$ constitute a sample of size n taken from a Weibull distribution with PDF given in Eq. 5.36 where the $p_{\zeta_i}(\zeta_i, m, \zeta_0)$ and m are unknown parameters. These parameters can be estimated using the MLE method. For the hypothetical sample $\zeta_1, \zeta_2, ..., \zeta_n$ taken from $p_{\zeta_i}(\zeta|m, \zeta_0)$, the likelihood function $L(\zeta_0, m, \zeta_1, ..., \zeta_n)$ which is the joint density function of the n random variables is defined as

$$L(\zeta_0, m, \zeta_1, ..., \zeta_n) = p(\zeta_1, \zeta_2, ..., \zeta_n|\zeta_0, m) = \prod_{i=1}^{n} p_{\zeta_i}(\zeta_i|\zeta_0, m). \tag{5.37}$$

where $\prod_{i=1}^{n}$ represents the product of a series of n terms. The MLEs of (ζ_0, m) are derived by maximising the likelihood function L given in Eq. 5.37 with respect to (ζ_0, m). This can be done by simultaneously solving the following equations:

$$\frac{\mathrm{d}Log(L)}{\mathrm{d}m} = 0; \qquad \frac{\mathrm{d}Log(L)}{\mathrm{d}\zeta_0} = 0. \tag{5.38}$$

In order to obtain the MLEs of the Weibull parameters, Eq. 5.36 is substituted into Eq. 5.37 and then Eq. 5.38 is solved to achieve the following system of equations:

$$\frac{\sum_{i=1}^{n} \ln(\zeta_i)\zeta_i^m}{\sum_{i=1}^{n} \zeta_i^m} - \frac{1}{n}\sum_{i=1}^{n} \ln(\zeta_i) - \frac{1}{m} = 0 \tag{5.39a}$$

$$\zeta_0 = \left(\frac{\sum_{i=1}^{n} \zeta_i^m}{n}\right). \tag{5.39b}$$

Unfortunately, this system of equations cannot be analytically evaluated and an iterative numerical algorithm should be used to solve it. Newton-Raphson algorithm is first applied on Eq. 5.39a to present m in terms of ζ_0, the details of Newton-Raphson algorithm to obtain the estimation of m are as follows:

$$m_{n+1} = m_n - \frac{f(m_n)}{f'(m_n)} \tag{5.40}$$

where

$$f(m_n) = \frac{\sum_{i=1}^{n} \zeta_i^m \ln \zeta_i}{\sum_{i=1}^{n} \zeta_i^m - \frac{1}{m} - \frac{1}{n}\sum_{i=1}^{n} \ln \zeta_i} \tag{5.41}$$

$$f'(m_n) = \sum_{i=1}^{n} \zeta_i^m (\ln \zeta_i)^2 - \frac{1}{m^2}\sum_{i=1}^{n} \zeta_i^m (m \ln \zeta_i - 1) - \Big(\frac{1}{n}\sum_{i=1}^{n} \ln \zeta_i\Big)\Big(\frac{1}{n}\sum_{i=1}^{n} \zeta_i^m \ln \zeta_i\Big). \tag{5.42}$$

The estimated value of m, denoted by $\hat{m}$, is then substituted into Eq. 5.39b to obtain the estimation of scale parameter ζ_0 denoted by $\hat{\zeta}_0$ and finally define the Weibull distribution function. Given the estimated parameters $(\hat{m}, \hat{\zeta}_0)$ uncorrelated random realisations can be generated from the Weibull distribution over the simulation domain using the inverse method (Devroye, 1986). In this method, a sample $u_1, u_2, ..., u_n$ is drawn from a uniform distribution defined over $(0, 1)$, and the corresponding sample taken from Weibull distribution can be then obtained by solving the following equation

$$\zeta_i = P^{-1}(u_i) - \hat{\zeta}_0 \sqrt[\hat{m}]{\ln(1 - u_i)}, \qquad i = 1, ..., n. \tag{5.43}$$

5.6 Inclusion of spatial autocorrelation function into the monovariate Weibull distribution

In order to include the spatial autocorrelation matrix 5.25, the following algorithm has been implemented:

1. Generate a hypothetical data set according to probabilistic characteristics of the heterogeneous material (mean value, standard deviation and correlation function)

2. Given the hypothetical data spatially distributed according the autocorrelation matrix, the parameters of the monovariate Weibull distribution are estimated using the ML method, denoted by $(\hat{m}, \hat{\zeta})$

3. The values distributed according the Weibull distribution can be obtained transforming the values sampled in point 2 using the formulation (Villanueva et al., 2013; Faraz et al., 2015)

$$\zeta_i = \left[-\log\left(\frac{1-\mathrm{erf}(\frac{x_N}{\sqrt{2}})}{2} \right) \right]^{m^{-1}} \tag{5.44}$$

being x_N the variable representing the vector sampled in point 2 of the algorithm.

5.6.1 Bivariate Weibull process

For the generation of a two-dimensional random field, the use of a multivariate Weibull PDF and CDF is needed. The approach used in this work, known as Normal-to-anything (NORTA), is to obtain the multivariate Weibull PDF from the multivariate Standard Normal PDF applying the change of variable. The details of formulation of the bivariate Weibull distribution considered is developed on the basis of Villanueva et al. (2013) and the transformation function between Gaussian to any other non-Gaussian is also explicitly expressed by Faraz et al. (2015). Here it is presented the methodology to generate correlated samples from the bivariate Weibull distribution derived from its relationship to the bivariate Standard Normal distribution. The Bivariate standard normal PDF i given as

$$f(x_{1N}, x_{2N}|\rho) = \frac{1}{2\pi\sqrt{1-\rho^2}} \exp\left(-\frac{1}{2(1-\rho^2)}(x_{1N}^2 + x_{2N}^2 - 2\rho x_{1N}x_{2N}) \right) \tag{5.45}$$

where ρ is the correlation coefficient between hypothetical random variables generated by the normal distribution (Villanueva et al., 2013) and is calculated by the exponential correlation function proposed by Yang and Xu (2008).
The bivariate Weibull distribution can be then obtained from the following equation

$$p_w(\zeta_{1W}, \zeta_{2W}|\zeta_{01}, \zeta_{02}, m_1, m_2, \rho) = f(x_{1N}, x_{2N}|\rho) \begin{vmatrix} \frac{\partial \zeta_{1W}}{\partial x_{1N}} & \frac{\partial \zeta_{1W}}{\partial x_{2N}} \\ \frac{\partial \zeta_{2W}}{\partial x_{1N}} & \frac{\partial \zeta_{2W}}{\partial x_{2N}} \end{vmatrix}^{-1}. \tag{5.46}$$

By substituting Eq. 5.45 into Eq. 5.46 the bivariate Weibull distribution depending on five parameters (2 shape parameters, 2 scale parameters and the correlation coefficient ρ) takes the following form

$$p_w(\zeta_{1W}, \zeta_{2W} | \zeta_{01}, \zeta_{02}, m_1, m_2, \rho) =$$

$$\frac{1}{4\sqrt{1-\rho^2}} \frac{e^{\left(-\frac{1}{2(1-\rho^2)}(x_{1N}^2 + x_{2N}^2 - 2\rho x_{1N} x_{2N})\right)}}{\left| \prod_{i=1}^{2} \frac{\zeta_{0i}}{m_i} \frac{e^{(-\frac{x_{iN}^2}{2})}}{1-\text{erf}\,\frac{x_{iN}}{\sqrt{2}}} \left(-\log\left(\frac{\left(1-\text{erf}(\frac{x_i}{\sqrt{2}})\right)}{2}\right)\right)^{m_i^{-1}-1} \right|}. \tag{5.47}$$

Eq. 5.47 can be then fully represented in terms of (ζ_{1W}, ζ_{2W}) using the relationship between normally-distributed variables and the Weibull distributed ones as expressed by Villanueva et al. (2013) and Faraz et al. (2015) and given below

$$x_{iN} = \frac{\sqrt{2}}{\text{erf}\,1 - 2\exp\left(-(\frac{\zeta_{iW}}{\zeta_{0i}})^{m_i}\right)}. \tag{5.48}$$

The inverse of the Eq. 5.48 used to generate samples from bivariate Weibull distribution in terms of the samples taken from the bivariate standard normal distribution is given in the formulation below:

$$\zeta_{iW} = \zeta_{0i} = \left[-\log\left(\frac{1-\text{erf}\left(\frac{x_{iN}}{\sqrt{2}}\right)}{2}\right)\right]^{m_i^{-1}}. \tag{5.49}$$

Algorithms for the generation a random set of variables sampled from bivariate lognormal distributions have been developed by some authors (Thomopoulos, 2012), but to the best knowledge of the authors no explicit algorithms have been provided for bivariate Weibull distribution. The algorithm for generating realisations from a bivariate Weibull-distributed random field is therefore expressed as follows:

1. Generate a hypothetical data according to probabilistic characteristics of the heterogeneous material
2. Given the hypothetical data, the parameters of the bivariate Weibull distribution are estimated using ML method, denoted by $(\hat{m}_1, \hat{m}_2, \hat{\zeta}_{01}, \hat{\zeta}_{02}, \rho)$
3. A sample of desired size can be easily drawn from a bivariate standard normal distribution with the estimated correlation coefficient $\hat{\rho}$. This bivariate sample is illustrated as $\left\{\left(x_{1N}^{(i)}, x_{2N}^{(i)}\right), i = 1, 2, ..., n\right\}$
4. By replacing the sample generated in Step 3 into Eq. 5.49 a bivariate sample $\left\{\left(x_{1W}^{(i)}, x_{2W}^{(i)}\right), i = 1, 2, ..., n\right\}$ can be generated from the bivariate Weibull distribution with the estimated parameters $\hat{m}_1, \hat{m}_2, \hat{\zeta}_{01}, \hat{\zeta}_{02}, \rho$.

Figure 5.1 shows three different bivariate Weibull distributions with three different coefficients of correlation. It is interesting to notice that for a low value of correlation the shape of the PDF has a more scattered nature, while for an increasing value of correlation, it is observed a higher correspondence leads to a stronger relation between values sampled for two random fields. Figures 5.2 shows an example of three samples (normalised according to their mean value) generated using the algorithm shown above and considering three different values of cross correlation representative of null, partial and total cross-correlation. Figure 5.3 shows the same scenario of Figure 5.2, for different values of correlation coefficient ρ, but using the bivariate normal distribution.

The most interesting facts to highlight between Figures 5.2 and 5.3 are related to the applicability of the two distributions used for the generation of the three samples to engineering problems where values of mechanical properties generated have to be realistic and physically meaningful:

1. both Figures 5.2 and 5.3 show the realistic sensitivity of the results for different values of ρ: for samples generated using null correlation, with both methods it can be seen that there is no observed correspondence between values sampled for the same Finite Element; the correspondence between values increases as the correlation between variables increases, until a complete correspondence between values is found when full correlation between the two random fields is taken into account;

2. in both Figures 5.2 and 5.3 two different standard deviations for the generation of the samples is considered: it can be noted that the two samples generated using the novel bivariate Weibull distribution are capable to keep the same difference observed in the samples generated using the classical bivariate normal distribution;

3. all the samples of Figure 5.3, generated therefore using a bivariate normal distribution, have positive and negative values, while all the samples presented in Figure 5.2 have only positive values.

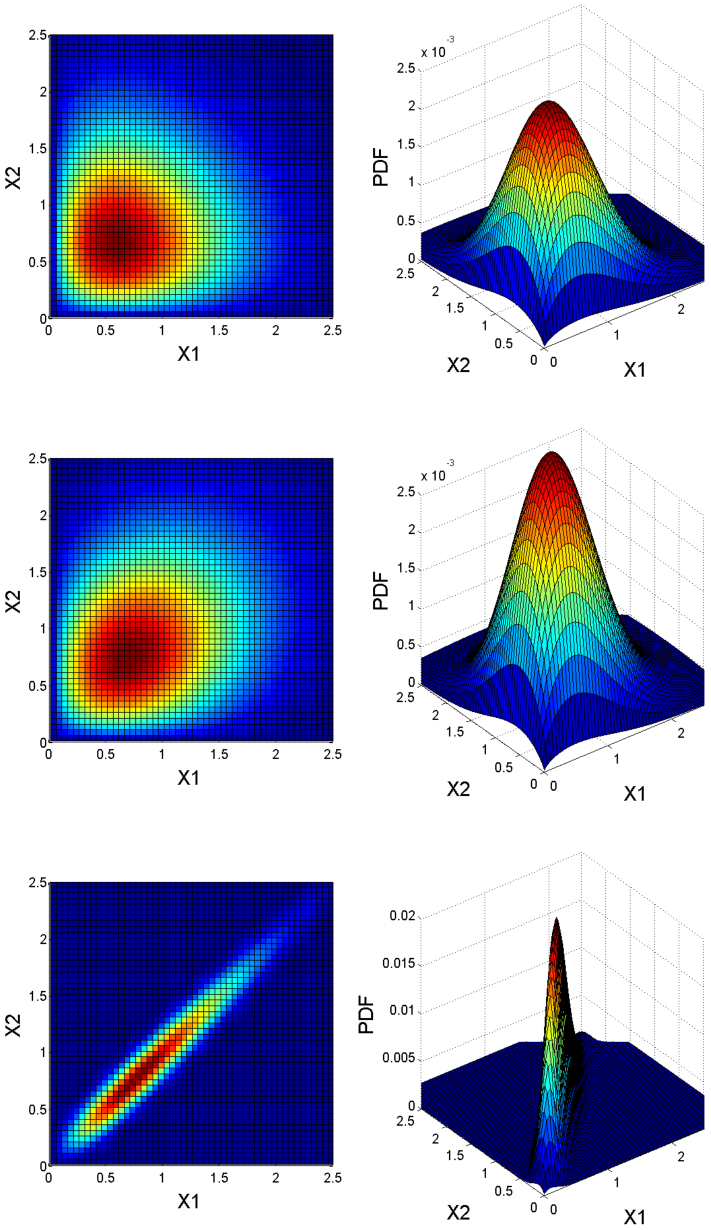

Figure 5.1: Bivariate Weibull distributions with null correlation (top); partial correlation (middle); full correlation (bottom).

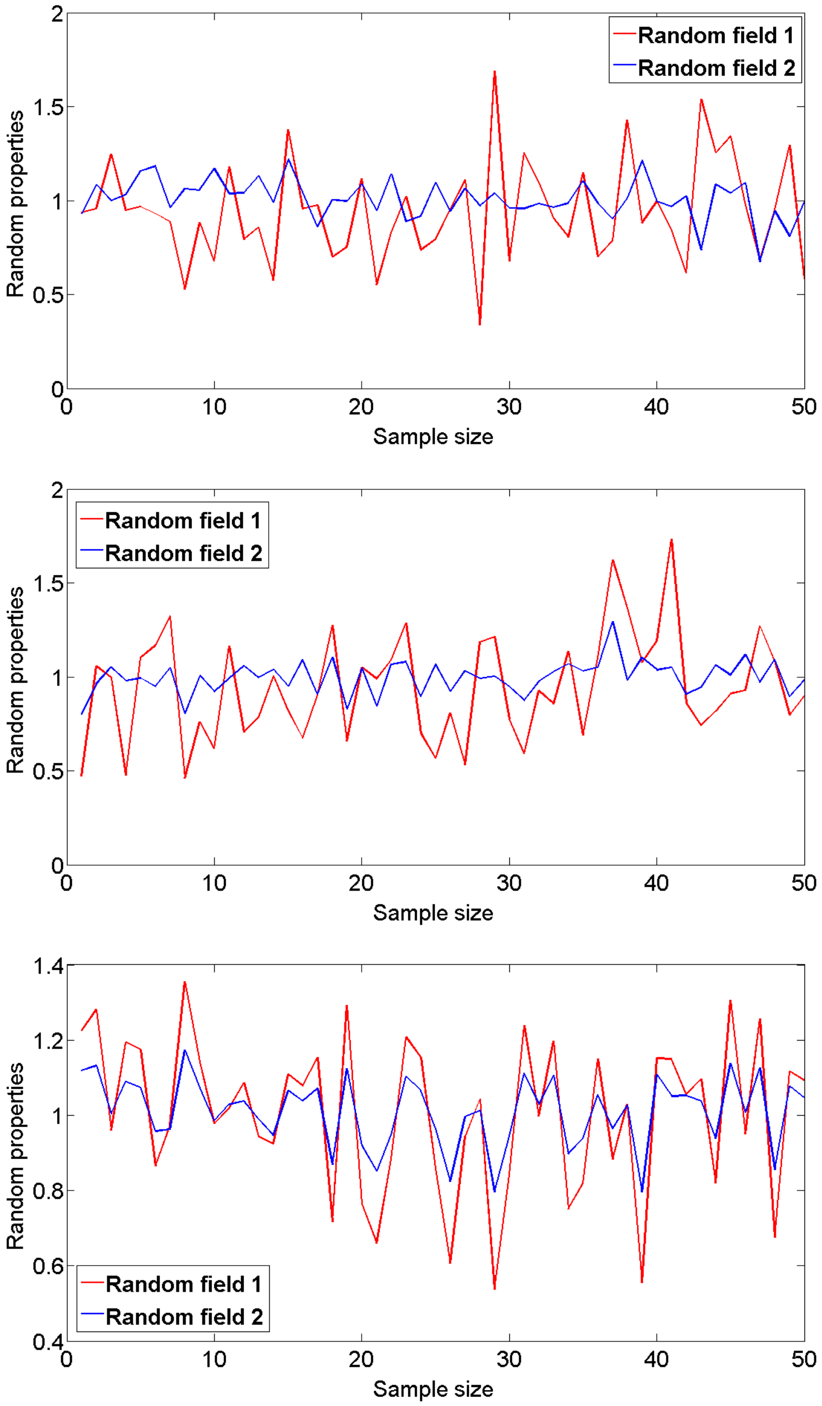

Figure 5.2: Bivariate Weibull distributions with null correlation (top); partial correlation (middle); full correlation (bottom). In this work, the term 'sample size' refers to the number of Finite Elements discretising the domain, which is equal to the size of the sample vector.

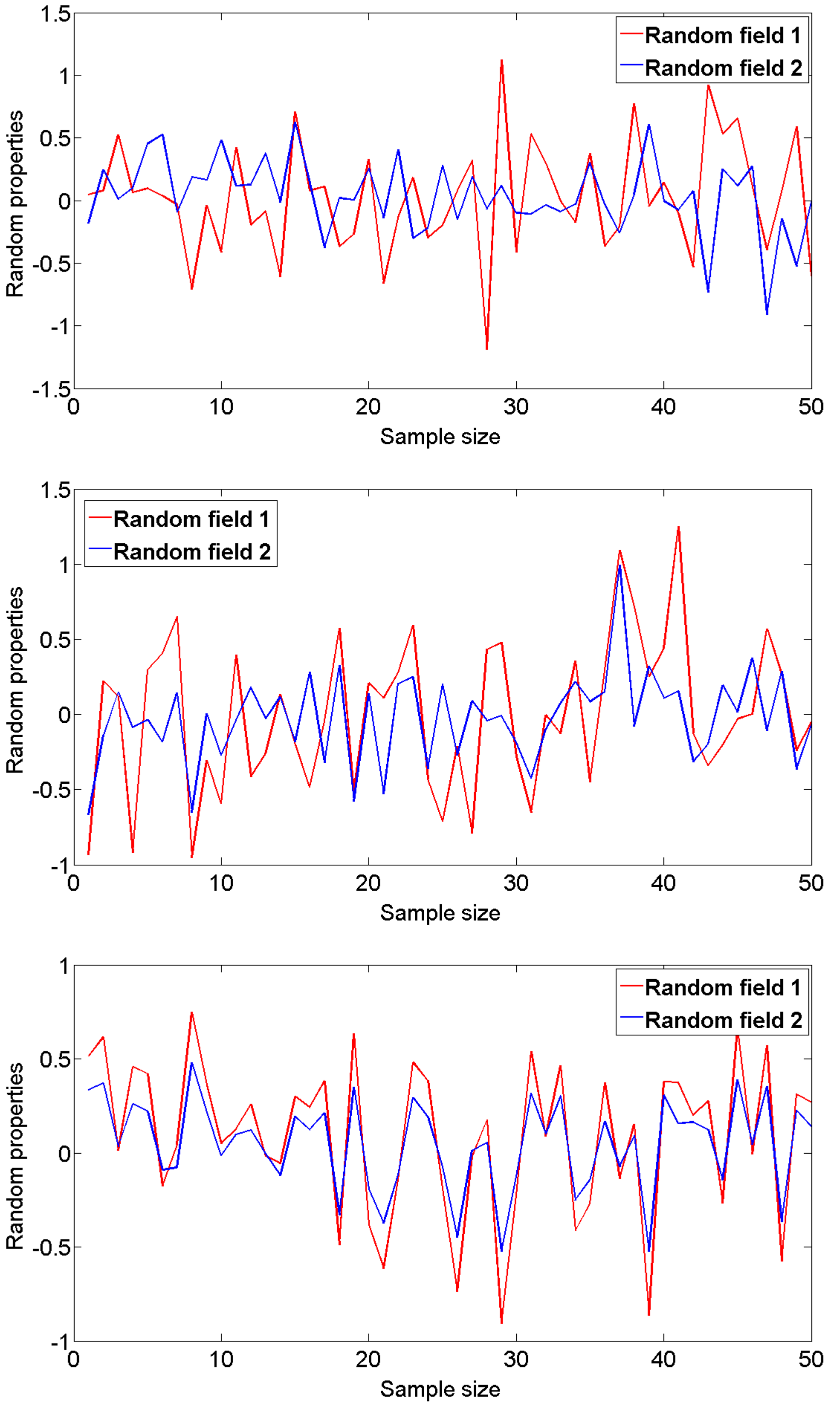

Figure 5.3: Correlated normally distributed random samples with null correlation (top); partial correlation (middle); full correlation (bottom). In this work, the term 'sample size' refers to the number of Finite Elements discretising the domain, which is equal to the size of the sample vector.

5.7 Model verification

5.7.1 Spatial autocorrelation application

The spatial correlation function aims to define the spatial variation of the mechanical properties in a domain and depends on the material length scale l_c: a low value of l_c denotes a more scattered distribution of the heterogeneity, while a higher value of l_c denotes a more homogeneously-distributed random field (Georgioudakis et al., 2014). Figure 5.4 shows how the methodology described above is capable to reproduce this behaviour on a simple rectangular domain and compares the result obtained with results achieved with a spectral method used by Georgioudakis et al. (2014).

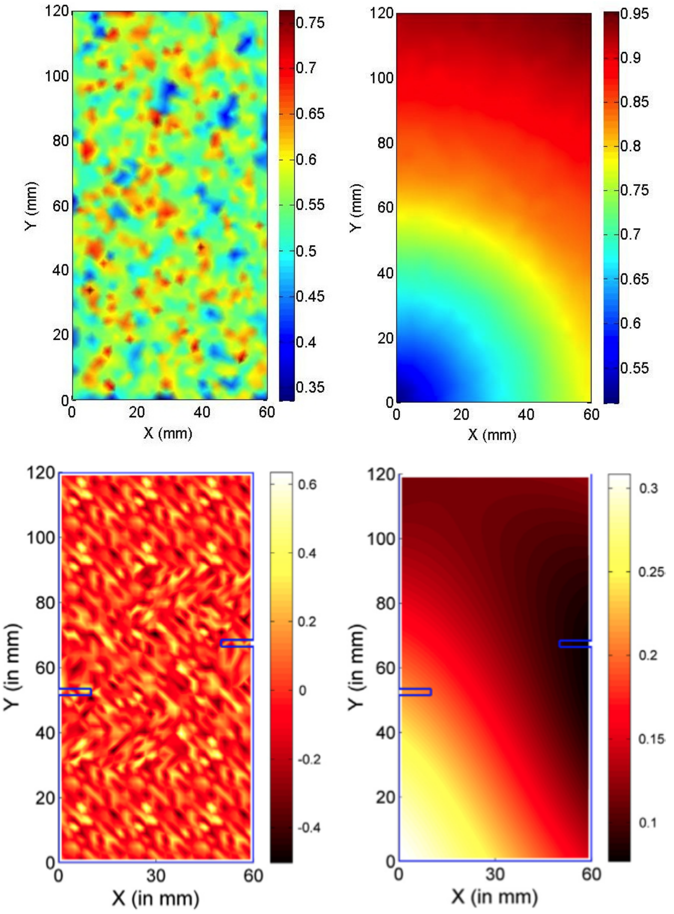

Figure 5.4: Rectangular domain: realisations of a Weibull field for fixed standard deviation and $l_c = 1.2$ (top left) and $l_c = 120$ (top right) and comparison with the results obtained by Georgioudakis et al. (2014) with the spectral method for $l_c = 1.2$ (top left) and $l_c = 120$ (top right). Similar trends are obtained between the two methods.

It can be observed in both figures that the effect of the variation of l_c is taken into account properly: for a low value of l_c, the spatial distribution of heterogeneity is appears to be more scattered, while for a higher value of l_c the values of the random field sampled have a distribution more homogeneously distributed in the domain.

5.7.2 Weibull and lognormal distributions

This paragraph aims to show that the method proposed in this chapter is capable to generate the PDF of a Weibull distribution which is similar to the relative log The mean value μ_{LN} and standard deviation σ_{LN} of a lognormal random variable are functions of the Gaussian mean value μ and standard deviation σ. These quantities can be calculated with the Matlab *lognstat* function, and mathematically they are expressed as:

$$\mu_{LN} = \mu_{LN} \exp\left(\frac{\sigma_{LN}^2}{2}\right) \tag{5.50}$$

$$\sigma_{LN}^2 = \exp\left(2\mu + \sigma^2\right)\left(\exp(\sigma_{LN}^2) - 1\right) \tag{5.51}$$

respectively. For the Weibull distribution, shape and scale parameters needs to be estimated in order to create the desired sample of random values. Using MLE method described above in this chapter, and given a vector containing a set of random values $(x_1, ..., x_N)$, the formulation for m and s is obtained using the Matlab function *mle*.

Afterwards, a vector containing random values following Weibull distribution can be computed. Let's assume a system with two correlated parameters with a random nature (e.g. fracture energy and modulus of elasticity) with given normal mean values and standard deviations. Lognormal mean value and standard deviation and shape and scale parameters for Weibull distribution are calculated as described above in this paragraph and are summarised for two Random Fields (RF) in Table 5.1.

Table 5.1: Parameters estimation for Normal, Lognormal and Weibull distributions using the Maximum Likelihood Method

		Normal	**Lognormal**	**Weibull**	
Random Field 1	Mean Value	0	1.03	Shape	15.4
	Std Deviation	0.25	0.07	Scale	2.91
Random Field 2	Mean Value	0	1.13	Shape	2.99
	Std Deviation	0.5	0.36	Scale	3.48

Figure 5.5 shows the correspondence between lognormal distribution and Weibull distribution with shape and scale parameters obtained from MLE method. Two lognormal and two Weibull distributions are generated using two normal distribution with same mean value (equal to 0) and two different standard deviations (one equal to 0.25, the other equal to 0.5). It can be observed that the method proposed for the generation of the Weibull distribution provides a result very close to the lognormal distribution generated from the correspondent Gaussian distribution, but some small differences can be noticed. Despite these differences looks small, they significantly influence the generation of a sample. In order to prove this, result from studies that analysed what is the best probabilistic distribution aimed to reproduce the behaviour of brittle materials is reported.

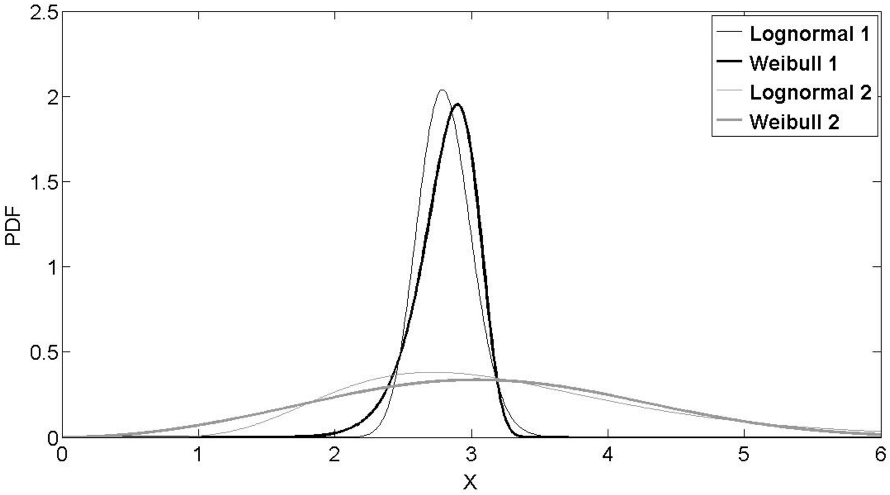

Figure 5.5: Comparison between LogNormal and its correspondent Weibull distribution

The first study is the one conducted by Gorjan and Ambrožič (2012). In their work, the authors evaluated the statistical distribution that better describes the response of 5100 experimental values of material bend strength of alumina specimens. The authors compared four different distributions, including the normal, lognormal and Weibull distributions. Comparisons between experimental observations and the probability distribution for each of the function considered have been conducted using the 'Q-Q' plots shown in Figure 5.6. Using a Q-Q plot, each experimental value σ_i corresponds to the coordinate on the vertical axis and the theoretically expected strength $\sigma_{i,th}$ corresponds to the coordinate on the horizontal axis. The closer the points are to the oblique line of the function $y = x$, the better is the agreement between the experimental data and the theoretical distribution. From a visual analysis of the three plots, can be seen that the data points fit best to a straight line in the case of a Weibull distribution. Furthermore, the authors calculated for each distribution, a coefficient called Q^2, used to calculate analytically how close the points are to the line of $y = x$:

$$Q^2 = 1 - \frac{\sum_{i=1}^{N}(\sigma_i - \sigma_{i,th})^2}{\sum_{i=1}^{N}(\sigma_i - \langle\sigma_i\rangle)^2} \tag{5.52}$$

where $\langle\cdot\rangle$ represent the mean value. If the Value for Q^2 is equal to 1, the sample fits perfectly, but in general the closer the value for Q^2 is to 1, the better is the fit.
For the normal, lognormal and Weibull distribution the three calculated values for Q^2 are equal to 0.98, 0.94 and 0.99, which proves that Weibull distribution is the best function to describe the mechanical response of the materials.

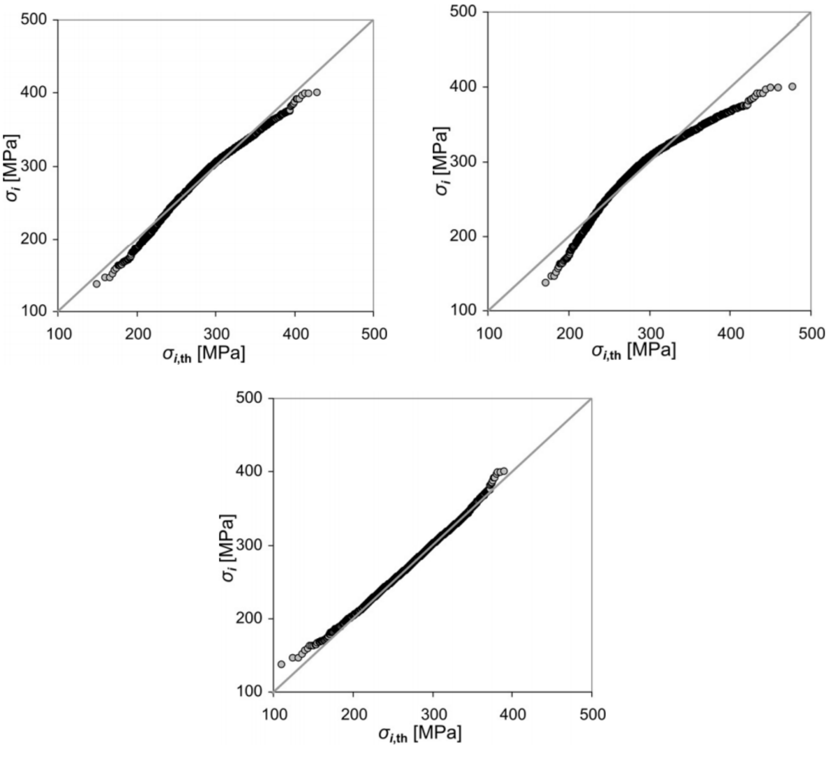

Figure 5.6: Q-Q plots of comparisons between experimental measurements on 5100 alumina specimens and theoretical values from probability distributions: comparison with normal (top left), lognormal (top right) and Weibull (bottom) distributions (Gorjan and Ambrožič, 2012)

.

Weibull distribution theory has been used to study the failure initiation process by Guy et al. (2012). More specifically, this study provides a Weibull model capable of introducing uncertainty in the crack initiation threshold for crack opening mode fractures. This model provides good results and shows how, for accurately selected material length scales and crack lengths, the scale parameter ζ_0 can be approximated by the value of the material length scale itself. For the propagation of the crack, on the other hand, a method purely based on the principles of fracture mechanics is adopted.

Another work is the one recently published by Gironacci et al. (2017). In their work, authors developed a novel numerical strategy able to predict damage evolution direction in heterogeneous materials by combining nonlocal mechanics, random field and continuum damage theories. The novelty of the proposed strategy relies on its capability to use Gaussian-distributed statistical information of crack initiation angle (generated using a spectral representation approach), defined by studying the distribution of the damage around the so-called fracture process zone developed around a crack tip, for the generation of probabilistic distributions describing the fracture toughness and fracture energy for brittle materials. The most interesting aspect of this method is its capability, by using Gaussian-related statistical information, to capture the non-Gaussian nature of the statistical distribution of the fracture toughness and fracture energy for brittle materials. Figure 5.7 shows the PDF of fracture toughness generated for one of the examples studied in the work by Gironacci et al. (2017).

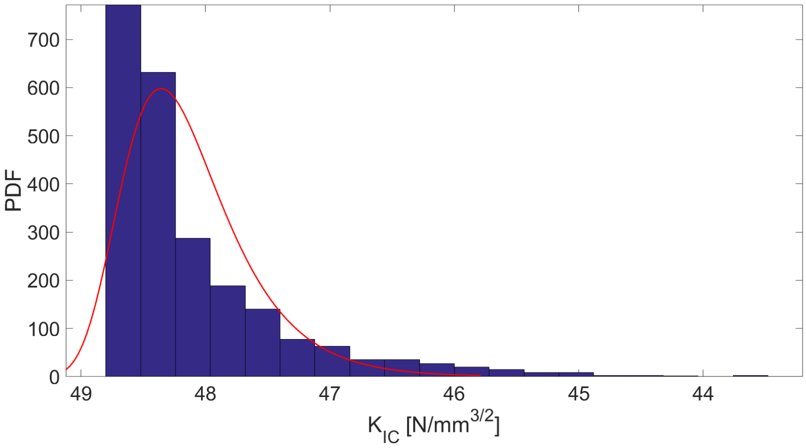

Figure 5.7: PDF obtained with the method proposed by Gironacci et al. (2017). The histogram showing the distribution of K_{Ic} is in very good agreement with the PDF of a Weibull distribution.

Chapter 6

Model Order Reduction

6.1 Introduction

In the previous chapter the methodology used for sampling random values of mechanical properties has been described.

In this chapter the focus will be on the assignment of these values to the FE mesh which is used to represent the desired problem domain and on the choice of the optimal dimension of the elements forming the so-called *random field* (RF) mesh. When FE and RF meshes do not coincide, it is said that a *dual mesh* approach is used (Shang and Yun, 2013). The size of the elements of the FE and RF meshes needs to be chosen following different criteria; the size of the elements of the FE mesh should take into account mesh convergence criteria related to the numerical model (to avoid for example numerical errors), while the size of the elements for RF mesh should be selected to adequately capture the essential features of the stochastic spatially variable properties (eg. material length scale) during the sampling phase. The size of the RF mesh element, therefore, should not be too large to cause underestimation of the spatial variability and should not be too small to prevent the numerical instability problems related to the necessity of dealing with a unfeasibly high computational cost (Li et al., 2016a). Relationships for the optimal ratio between mesh size and correlation length of random properties as a measure of heterogeneity are provided in several works (Yang and Xu, 2008). In these studies it is suggested that the size of the elements should be less than the half of the correlation length, and, more specifically, for optimal results it should be between one quarter and one half of the correlation length.

For this study the dual mesh approach introduced above is employed, and therefore two different meshes are identified: a RF mesh, containing all the information related to the material heterogeneity, and a FE one for numerical solving partial differential equations describing the fracture problem. The material length scale is used to define the size of the initial stochastic mesh. A nonlinear technique has been developed and used to reduce the dimensionality of the RF mesh. This simplifies and accelerates materials stochastic analysis process through constructing isometric low-dimensional representations of material formation variations. With the term isometric it is defined any technique that is able to preserve geometrical properties and features at all scales (Zhang et al., 2015).

6.2 Model Order Reduction

The growing demand for reliable simulations of complex systems creates big challenges for researchers working in the area of computational mechanics. Realistic simulations should in fact show only very small errors of the computational models, and a wide number of aspects must always be considered for the replication of realistic behaviours (Schilders, 2008).

The increase in computational power allowed the possibility of the creation of complex algorithms, which, nevertheless, always need to look at their efficiency. Not always is possible to simplify a priori a model realistically describing the material properties and the mechanical response of a material. In such cases, a procedure for the automatic identification of the possible approximations and simplifications able to further increase the computational efficiency and realistically describe material properties must be identified. Developing such algorithms is the aim of model order reduction (MOR) techniques (Schilders, 2008).

In fact, MOR tries to quickly and realistically capture the essential characteristics of a domain. The input consists of a physical domain, represented via RF mesh, where its size is decided taking into account the microstructure of the material. To reduce the computational cost related to the sample realisation vectors containing values of G and E for each element, the size of each RF element is increased and, consequently, the size of the sample vector reduces. At a certain moment, which is defined by the achievement of given convergence requirements, the process of reduction is stopped. At that point, all necessary properties of the original model can be captured with sufficient precision.

Despite MOR is now employed in several fields of research (e.g. vision, speech, motor control and data compression), its development started within the field of systems and control theory, to analyse properties of dynamical systems in

application for the reduction of their complexity, while preserving their input-output features as much as possible (Schilders, 2008).
Figure 6.1 schematically illustrates the concept of the MOR, demonstrating that, despite a high number of details provide an accurate description of the features of a model, less information can be enough to to describe the same model accurately enough. This example with pictures of the Stanford Bunny shows that, even only with a few facets, the rabbit of Figure 6.1 can still be identified.

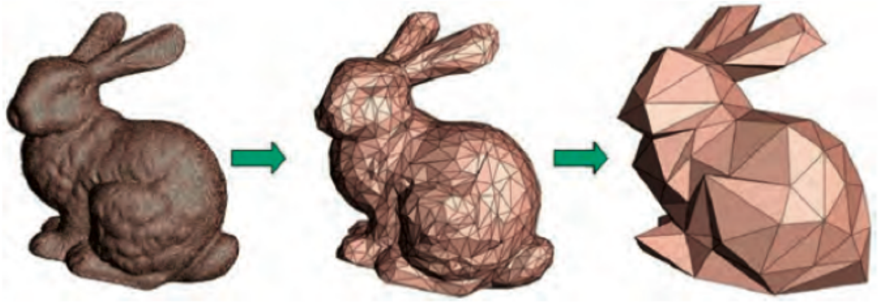

Figure 6.1: Model Order Reduction graphical illustration: the Stanford Bunny. (Schilders, 2008)

Applied to this study, MOR can be therefore seen as the task of reducing the dimension of the sampling space-dependent vector, while reserving the nature of the input-output relations. In order to provide a good approximation of the original input-output system, a number of conditions should be satisfied:
- the approximation error from original to reduced-order input is small;
- the properties of the original system are preserved;
- the reduction procedure must be computationally efficient.

6.3 Linear and non-linear MOR techniques

The fundamentals of MOR techniques started during the eighties with Moore (1981), Glover (1984) and Sirovich (1987). However, all these methods were applied to the field of systems and control theory, and only in the latter years MOR started to be applied to other fields of research.
All methods for dimensionality reduction can be grouped into two main categories: linear and non-linear methods. Linear methods, such as Principal Component Analysis (PCA), are used when the information passing through different elements of a

problem are connected sequentially, and therefore the direct, or *euclidean* distances can be considered during the dimensionality reduction process. Non-linear methods, such as IsoMap, are normally used when data elements are attached and dependent to several other data elements, in such a way that the information stored in one element is influenced by its whole surrounding (Zhang et al., 2015).

PCA is able to obtain linear structures and relations between data points in a low-dimensional space (lower compared to the size of the initial stochastic domain), in a way that the most important features characterising the RF mesh are preserved. However, this method fails to in the reconstruction of non-linear features as it bases its algorithm in the euclidean distances between nodes. PCA has however the advantages of being simply implementable and efficiently computable (Zhang et al., 2015).

One more efficient way of obtaining the optimal dimension able to realistically describe the RF domain is using geodesic distances instead of euclidean distances (Tenenbaum et al., 2000), which are able to catch the non-linear features of the domain that would remain hidden if euclidean distances were used, as can be seen in Figure 6.2.

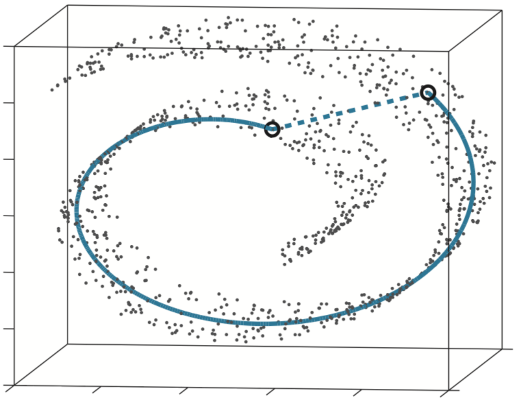

Figure 6.2: The "Swiss roll" data set, showing how IsoMap uses geodesic paths for non-linear dimensionality reduction. For two points on a domain, their Euclidean distance in the input space, represented by the length of dashed line, not necessarily reflects their intrinsic similarity, as measured by geodesic distance shown by the solid curve (Tenenbaum et al., 2000).

Table 6.1 shows the main advantages and disadvantages of the two most popular methods for dimensionality reduction. Both methods are able to provide a reduced-dimension representation of the RF, however the overestimation of the dimension of the RF domain using PCA makes the use of a non-linear MOR technique more suitable for this study.

Table 6.1: Comparison between PCA and ISOMAP (Zhang et al., 2015).

PCA (Linear method)	**IsoMap (Non-Linear method)**
-Simple to implement -Efficiently computable -Discover a realistic structure of the input space	-Correct dimensionality detection -Recover the intrinsic geometric structure
-It cannot be extended to multi-component materials -It constructs the closest linear subspace of the high-dimensional input space -It tends to overestimate the actual dimensionality of the space	-Computationally slightly more expensive than PCA

6.4 Modified IsoMap applied to SFEM

This section aims to develop the stochastic computational strategy used in this thesis by combining a stochastic damage theory with isometric mapping (IsoMap) theory in order to obtain a description of the RF mesh with an optimal and computationally efficient algorithm.

IsoMap theory was originally proposed by Tenenbaum et al. (2000) for dimensionality reduction of non-linear data sets. In this theory, every data element is connected to several other data elements using tree and graph concepts in a way to represent their inner non-linear relationships. This theory overcomes the shortcomings of traditional dimensionality reduction techniques such as PCA in preserving realistic features of realisations which are not arranged linearly in a sequential structure, as shown in Figure 6.2.

The dimension of the initial RF is set equal to D. Each realisation with D elements is considered as a point in D-dimensional space. The plan is to map each realisation to a d_r-dimensional space ($d_r << D$) while the intrinsic characteristics in the realisation will be well maintained. All the geodesic distances between all pairs of data points are computed. The geodesic distance can be understood to be the shortest distance between the sample points in the high-dimensional space and is computed by constructing a neighbourhood graph $\mathcal{G}$ in which every point is connected with its k_r nearest neighbours. After choosing the size of the neighbourhood, the distances between all pairs of elements (distances are calculated between elements barycentre) is calculated and the distance between elements as $d_E(i, j)$ is defined. Then, a line between each two neighbouring points is drawn if their distance is included within the neighbourhood size. By repeating this process for all the elements the so-called neighbourhood graph is obtained. The shortest pattern between points is calculated. The shortest path between two points in the graph forms an estimate of the geodesic distance between these two points, and can be computed by means of Floyd's algorithm (Floyd, 1962), schematically shown in Figure 6.3.

Geodesic distance d_M between two points for IsoMap is measured by summing all the distances between points within the two nodes under consideration. The distances between points are initialised to $d_M = d_E$ if two points are directly connected and, to $d_M = \infty$ otherwise. For each couple of points, the shortest path is then defined as

$$d_M(i,j) = min\{d_M(i,j), d_M(i,k) + d_M(k,j)\} \tag{6.1}$$

which is known as Floyd's algorithm (Floyd, 1962).

The matrix of shortest path distances is defined as $\mathbf{D_M} = (d_M(i,j))^2$. In the next step it is shown how to compute the matrix

$$\mathfrak{C}(\mathbf{D_M}) = \mathbf{-HD_MH/2} \tag{6.2}$$

where $\mathbf{H}$ is the centering matrix defined by Tenenbaum et al. (2000) as $H_{ij} = (\delta_{ij} - 1/D)$, with δ_{ij} being the Kronecker delta defined as

$$\delta_{ij} = \begin{cases} 0 & \text{if } i \neq j, \\ 1 & \text{if } i = j. \end{cases} \tag{6.3}$$

The eigenvalues λ_d of the matrix $\mathfrak{C}(\mathbf{D_M})$ are calculated and sorted in decreasing order. The new dimension d_r is specified by estimating a value called cumulative residual variance, a measure of the difference in the distribution of heterogeneity between the initial and the reduced spatial configuration, given by the eigenvalues λ_d. The new dimension d_r is defined as the dimension for which the convergence criteria for cumulative variance is reached. Figure 6.3 shows the procedure followed for getting the reduced order stochastic model.

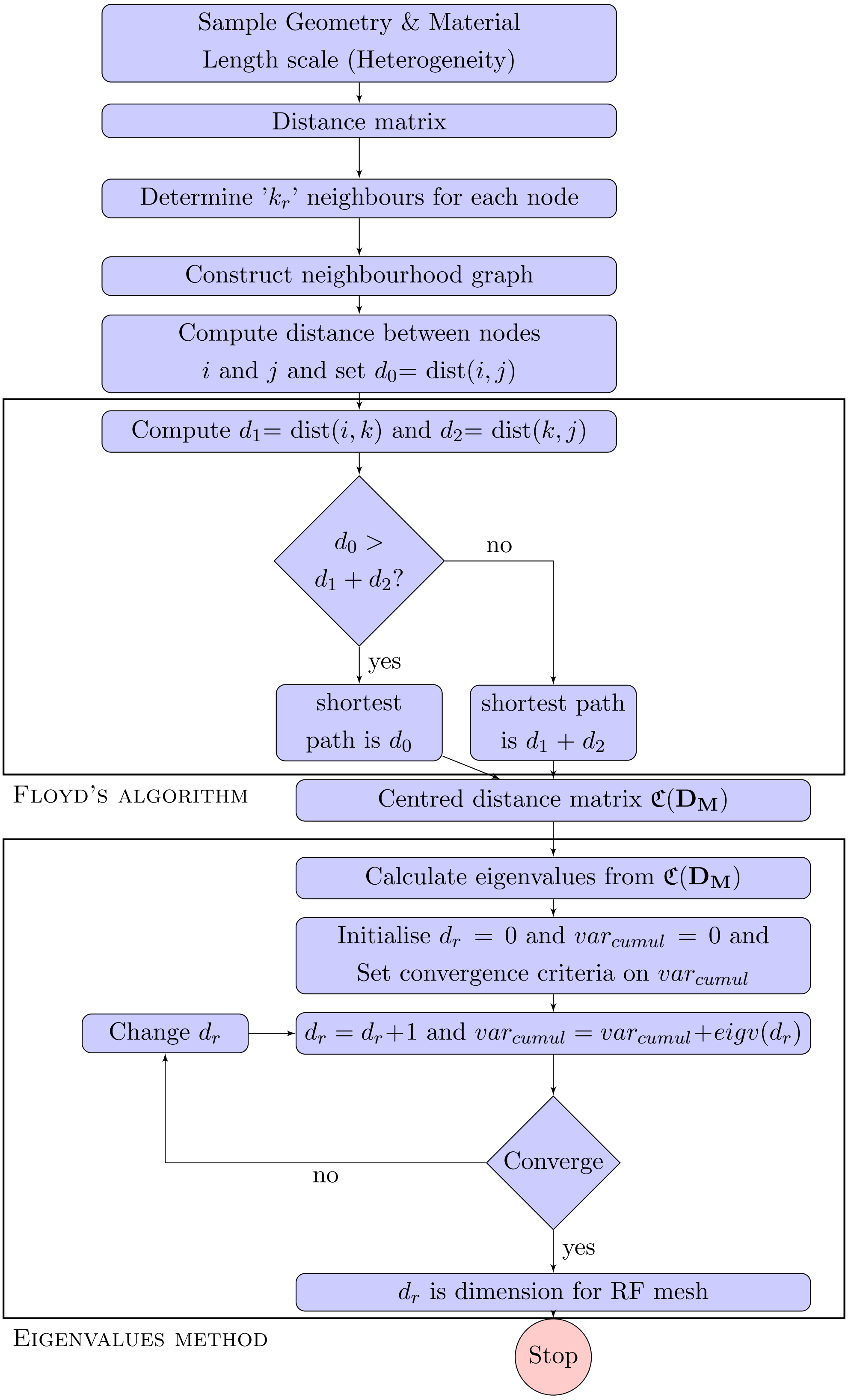

Figure 6.3: Algorithm for IsoMap

The new dimension d_r is directly connected to the size of the neighbourhood considered to obtain the new RF mesh dimension. Table 6.2 summarises how d changes for a change of k_r for a sample of stochastic realisation on a circular domain. From the table can be seen that for and increase of k_r, the values of d_r increase and, therefore, a finer RF mesh is obtained. However, the choice for the optimal value of k_r has to be done considering also the computational effort required during the sampling phase. In fact, in Figure 6.4 can be observed how the time needed for generating a sample is decreasing when the size of the stochastic mesh increases. However, the slope of the graph visibly decreases after the size of the element becomes bigger that 2 mm. The generation of a sample for a RF discretisation with mesh size equal to 1 mm required 55.4 seconds, while already for a mesh size equal to 2 mm, the CPU dropped drastically to 4.9 seconds and to 3.6 seconds for a mesh size equal to 2.5. All the analyses are computed using MATLAB installed on a MacBook Pro equipped with a 2.5 GHz Intel Core i5 processor and 8GB RAM. In conclusion, for this example the optimal values of k_r and d_r are equal to 9 and 307 respectively.

Table 6.2: Dimension and mesh size for optimal cumulative variance trend for different sizes of neighbourhood k_r

	Cumulative Variance 0.95		**Cumulative Variance 0.90**	
k_r	d_r	**Mesh size** (mm)	d_r	**Mesh size** (mm)
3	71	5.7	65	6.1
4	103	4.6	94	4.8
5	140	3.9	127	4
6	180	3.3	164	3.5
7	246	2.8	223	2.9
8	290	2.6	264	2.75
9	307	2.5	279	2.7
10	342	2.4	310	2.5
11	375	2.3	341	2.35
12	424	2.25	383	2.3
13	460	2.2	412	2.25
14	488	2.2	432	2.25
15	551	2	473	2.2
16	551	2	508	2.1
17	551	2	551	2

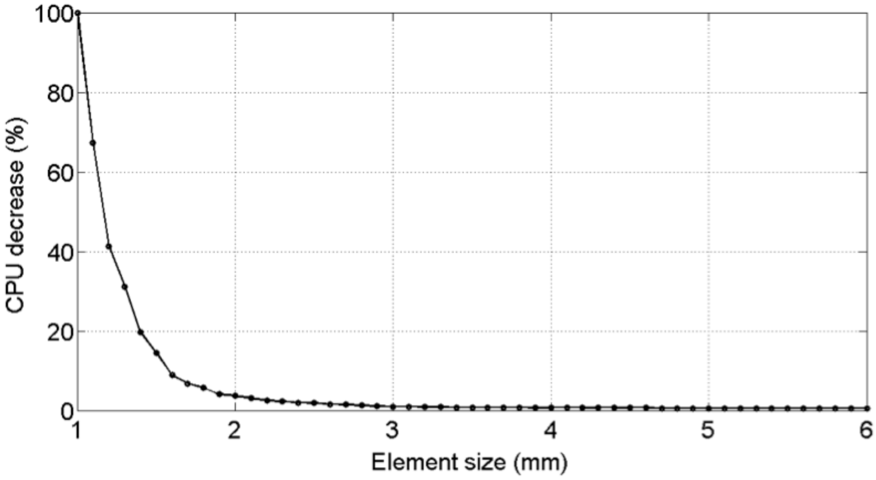

Figure 6.4: Sample generation: CPU evolution for different stochastic element sizes on the same problem. An increase in the size of the mesh leads to a reduction of the CPU time needed for the process. However, an excessive increase for the mesh size doesn't lead to any significant improvement

6.5 Mapping from RF to FE mesh

After generating the reduced order mesh, a mapping procedure for transferring values of random parameter from the stochastic mesh to the finite element mesh is implemented. This mapping is necessary, in order to maintain the same (or very similar) distribution of material properties from RF to FE mesh.

The mapping is based on a graphical method which refers to the distance between elements and based on the midpoint method. Each element of the finer mesh has a different value of fracture energy. The elements from the coarser mesh are projected, as shown in Figure 6.5, on those of the finer mesh. To assign a value of fracture energy the mapping employed here considers the values of fracture energy of those elements of the fine mesh in proximity of the single element of the coarse mesh. This procedure can be attributed to the spatial averaging method, which assigns a value obtained as an average of stochastic field values over another finite element domain (Haldar and Mahadevan, 2000). Essentially, for mapping the values of fracture energy between the two meshes, both values of fracture energy and distance between elements barycentre, representing the distance between the elements, are considered. The final value of fracture energy is assigned using

$$G_{FE} = \sum_{i=1}^{nr} \frac{G_i}{d_i} \tag{6.4}$$

where nr represents the number of element for which the relative distance between the reduced and the original barycentre is less than a given threshold which, for this work, is considered to be the size of the new mesh. In fact, as shown in Figure 6.5, the higher the distance between the elements is, the lower will be the influence of that element to the calculation of random parameter for the FE element.
If during the analysis an element is refined, the new value of fracture energy will be assigned considering the same procedure in order to keep the same local heterogeneity distribution during the whole analysis.

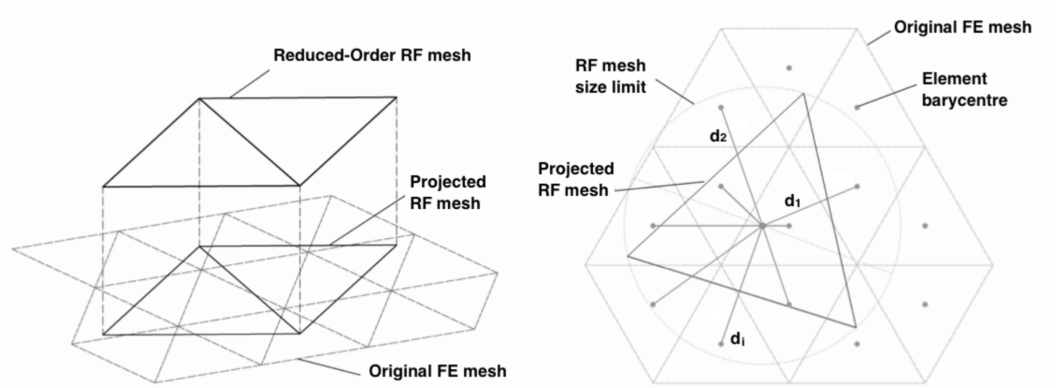

Figure 6.5: Mapping procedure from RF to FE mesh: projection of one mesh on the other (left) and calculation of the distances between barycentre (right). The new value of the random properties for the original finite element mesh is given by an average of the elements included within the projection, averaged according to the relative position between the elements' barycentres.

6.6 Conclusions

In this chapter a methodology for reducing the size of the RF mesh to reduce the computational time during sampling procedures and, at the same time, to keep a realistic distribution of mechanical properties with random nature. A version of non-linear dimensionality reduction technique adapted to FE problems has been used, as it is able to better capture all the essential heterogeneous features. Furthermore, a mapping procedure able to transfer the values of random mechanical properties from RF to FE mesh has been developed, and its application will be shown in the next chapter.

Part III

Results and discussion

Chapter 7

Numerical analyses on shale gas rocks

7.1 Introduction

The first case study investigated in this project is presented. The attention will be first on the geo-mechanical characterisation of layered heterogeneous shale gas rocks, on their anisotropic behaviour and the effects of random orientation of shale layers on the failure mechanisms. Experimental data have been collected from five specimens, using the indirect tension Brazilian disc test. Laboratory measurements on the mechanical properties of core samples of shale-gas reservoir rocks have been used. Samples have been collected from the Dove's Nest site on the east coast of North Yorkshire in England. Data on the general mechanical behaviour of these rocks are calculated to delineate the basic parameters that control propagation of cracks in rocks: elastic modulus and fracture toughness of shale samples with different microstructural formations and layering orientations are calculated.

Furthermore, numerical results are also presented and compared to the experimental measurements: the specimens are modelled considering models of homogeneous nature, with layered configuration and with randomly-distributed values of fracture energy G and modulus of elasticity E.

Afterwards, two different cases study will be also considered: one which considers material failure driven by a pure traction test (mode I failure) and the second in which cracks form and propagate due to mixed-mode failure (mode I and II) in concrete samples. The capabilities of the implemented numerical code will be verified by comparisons with experimental results. For these last two examples, heterogeneity is modelled only using the Weibull distribution.

7.2 Experimental investigations on shale rock samples

7.2.1 Experimental setup: the Brazilian test

The Brazilian tests were conducted to measure the tensile strength of cylindrical samples collected from the shale gas reservoirs in the Dove's Nest site on the east coast of North Yorkshire. Tests have been conducted in the School of Earth and Environment of the University of Leeds, and results from these tests have been recently published by Mousavi Nezhad et al. (2018). These results have the main purpose of verification of the methodology proposed in the previous chapter, together with an initial study on the effect of modelling of layered materials presented in the next paragraphs of this chapter. Figure 7.1 shows the experimental setup used to test the specimens: the equipment consists of a high-speed camera to take pictures of the fracture propagation, a strain gauge and a loading rig.

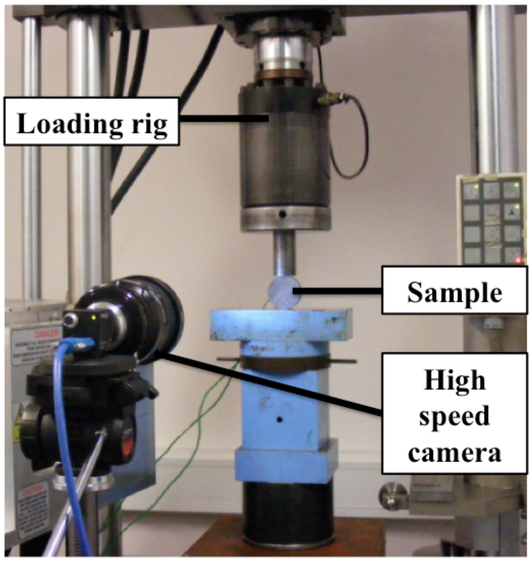

Figure 7.1: Photograph of the Brazilian test setup used in the School of Earth and Environment, University of Leeds.

For the Brazilian test, loading conditions influence significantly damage and stress distribution inside a specimen. The load can be applied to the specimens using either flat platens or curved jaws (Figure 7.2). It is worth noting that failure always initiates in an area located under loading points if flat steel plates are used, while the crack initiation point gets closer to the centre of the specimen if curved jaws are employed (see Figure 7.6) (Hobbs, 1964; Hudson et al., 1972).

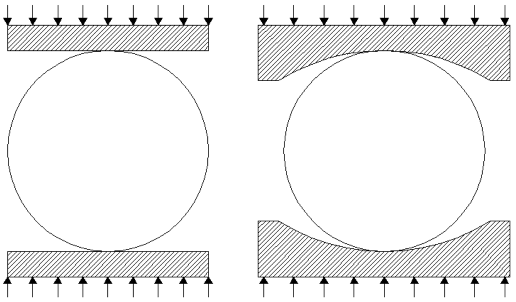

Figure 7.2: Brazilian disc experimental configurations: with flat plates (left); with curved jaws (right).

7.2.2 Experimental method and measurements

The fracture tests were carried out on samples showing different types of heterogeneity: despite in some of them the presence of randomly-distributed inclusions can be observed, all the specimens show a layered nature (in some of them more evident), and for each test angles between loading direction and bedding plane orientations varied. The mechanical strength was determined by crushing the cylinder samples between steel platens. Load, axial displacements and time data are recorded from transducers attached to the loading frame. Scenarios of the experimental sets that have been carried out to measure fracture properties of shale rock and investigate the effects of bedding orientation, are presented in Tables 7.1 and 7.2.

Table 7.1: Scenarios of experimental sets using flat steel plates

	R (mm)	t (mm)	P_{max} (KN)	P_{min} (KN)	σ_t (MPa)	E (GPa)	K_{Ic} (N/mm$^{\frac{3}{2}}$)	G (N/mm)
A	18.29	19.76	6.86	2.00	6.36	29.6	12.02	0.4 x 10^{-2}
B	18.30	20.69	9.46	4.22	8.04	18.5	22.77	2.6 x 10^{-2}

Table 7.2: Scenarios of experimental sets using flat curved jaws.

	R (mm)	t (mm)	P_{max} (KN)	P_{min} (KN)	σ_t (MPa)	E (GPa)	K_{Ic} (N/mm$^{\frac{3}{2}}$)	G (N/mm)
C	23.70	21.87	11.90	4.85	7.30	26.6	18.97	1.5 x 10^{-2}
D	27.30	22.28	22.28	5.59	10.40	20.3	22.14	2.2 x 10^{-2}
E	30.81	27.26	29.25	14.29	11.20	24.0	43.64	7.5 x 10^{-2}

For each specimen (all of them are intact), fracture toughness K_{Ic} is initially calculated using the method proposed in Guo et al. (1993). This method relies on the value of the post residual load being maintained by each fractured disc P_{min}. The modulus of elasticity E was determined by cementing an electrical resistance strain gauge at the centre of a disc to measure the lateral strain until failure.

All the tested samples are shown in Figure 7.3. All the discs were tested in the air-dried state. In this figure it can be observed that specimens A and E show a well-defined layered structure, even if in specimen E the presence of small inclusions is visible; also specimen B shows a layered structure, but less defined. On the other hand, specimens C and D show a structure more randomly distributed through the domain.

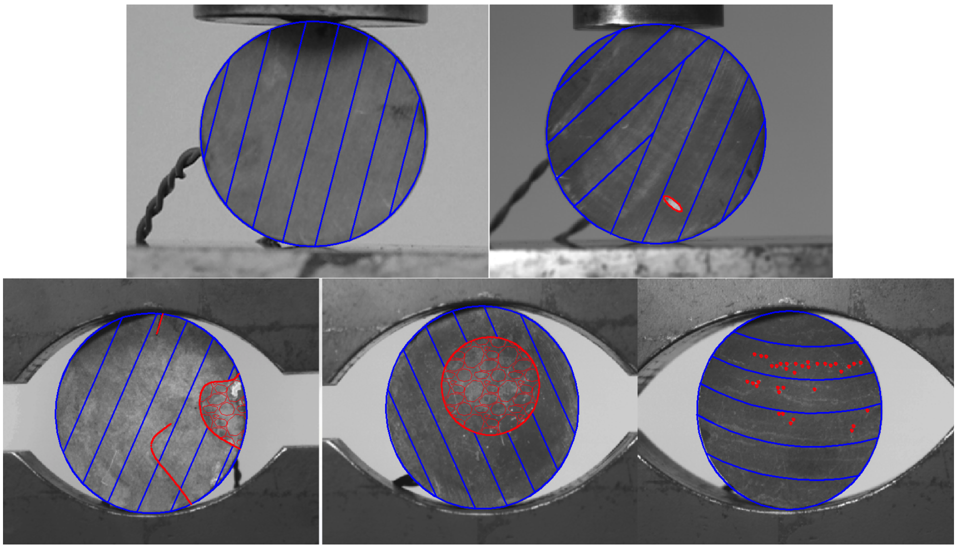

Figure 7.3: Tested shale samples: samples A (top left) and B (top right) tested using flat plates and samples C (left bottom), D (middle bottom) and E (right bottom)

The indirect tensile strength σ_t of the cylindrical samples under compression on the vertical diameter of the specimen were obtained using (ISRM, 1978; Li and Wong, 2013):

$$\sigma_t = \frac{P_{max}}{\pi R t} \tag{7.1}$$

where P_{max} is the maximum load applied to sample before failure, R the radius of the specimen and t its thickness. The tensile stress-strain curves for all the experimental sets described above are plotted in Figure 7.4. For the case of experiments conducted with flat plates, it can be observed that specimen B shows a lower stiffness, but a higher value of ultimate tensile strength and a wider post-elastic behaviour. For experiments conducted with curved jaws, it is observed that the higher value of resistance is obtained for the sample with a clear-layered structure and horizontal direction of layers. It should be observed that graphs of Samples B and C show some scattered behaviours in their plots, most probably related to the sudden movement of the strain gauges during the formation of cracks.

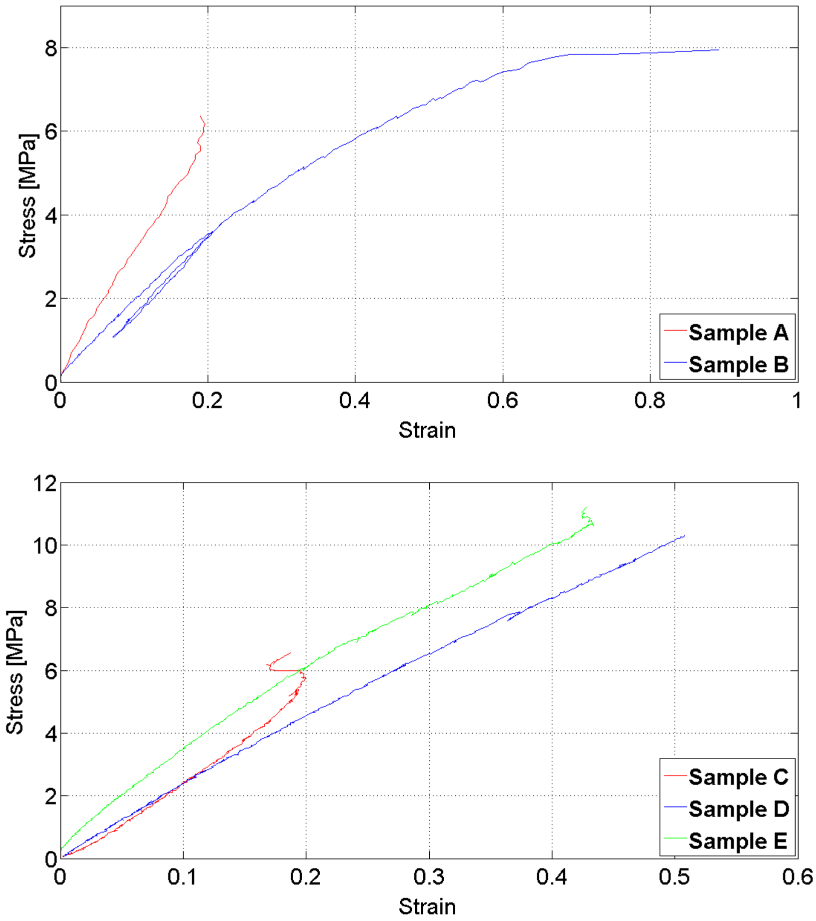

Figure 7.4: Stress-strain plots for the 5 sets of experiments performed on shale rocks: results from the specimens tested using flat plates (top) and curved jaws (bottom).

Figure 7.5 shows all crack patterns obtained from the specimens described above. Crack pattern obtained for specimen A doesn't have a very noticeable tortuous nature, probably due to the low degree of visible heterogeneity. Furthermore, specimens with a clear layered nature show a well-defined and unique crack pattern which is more curved if compared to the one in specimen A, while specimens with a less-defined layered and more scattered heterogeneous nature show multiple and more tortuous cracks.

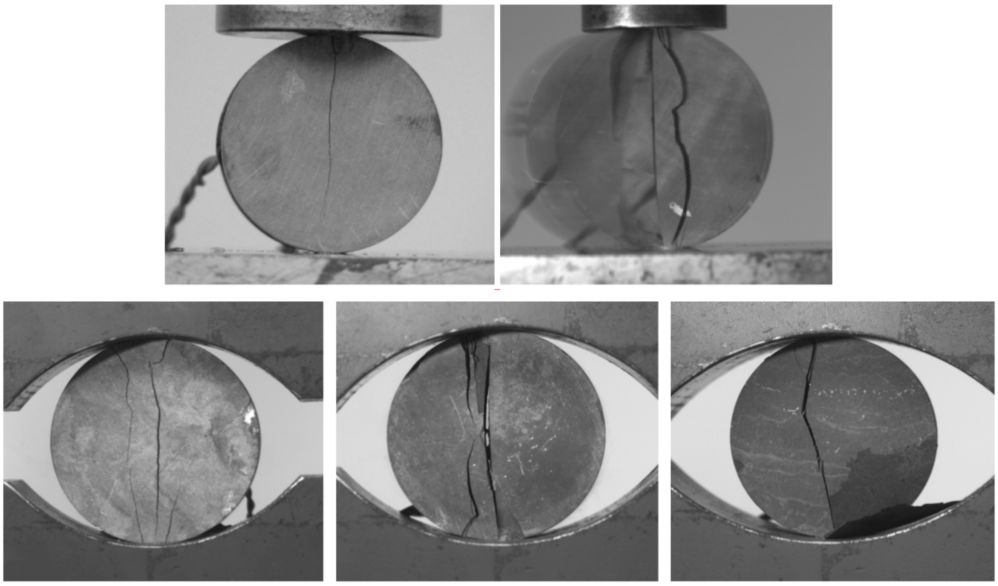

Figure 7.5: Tested shale samples: crack patterns obtained from samples A (top left), B (top right), C (left bottom), D (middle bottom) and E (right bottom)

7.3 Fracture toughness calculation for intact samples

7.3.1 Novel approach for intact specimens

As mentioned in the previous paragraph, for all the specimens presented above, K_{Ic} is calculated using the method proposed in Guo et al. (1993). However, as can be observed for specimen A, it might be necessary to use alternative methodologies to calculate fracture toughness. In fact for this specimen fracture toughness was calculated using a different methodology, because the value of P_{min} seems to be significantly low to be used for calculating an opportune value of fracture toughness with this method. Therefore, for calculating K_{Ic} for this specimen the generalised maximum tensile stress (GMTS), which describes the elastic tangential stress field distribution around the crack tip in the two-dimensional polar coordinates as a linear function of the mode-I and mode-II stress intensity factors, is considered:

$$\sigma_{\theta\theta} = \frac{1}{\sqrt{2\pi r}} \cos\frac{\vartheta}{2}\left[K_I \cos^2\frac{\vartheta}{2} - \frac{3}{2}K_{II}\sin\vartheta\right] + T\sin^2\vartheta + O(\sqrt{r}) \qquad (7.2)$$

where K_I and K_{II} are the mode I and II Stress Intensity Factors (SIF), T is the T-stress, constant and non-singular term defining the stress parallel to the crack and independent of r; the higher order term $O(\sqrt{r})$ can be neglected in proximity of the crack tip and r and ϑ are the crack tip polar coordinates.

Assuming pure Mode I failure for the Brazilian test (and therefore $\vartheta = 0$), fracture toughness can be calculated as

$$K_{Ic} = \sigma\sqrt{2\pi r_c}. \tag{7.3}$$

According to the GMTS criterion (Aliha et al., 2010) a crack initiates when along the direction ϑ_0 of maximum tangential stress $\sigma_{\theta\theta}$ and at a critical distance from the crack tip, r_c when $\sigma_{\theta\theta}$ reaches its critical value.

According to Hobbs (1964), on intact specimens tested using the Brazilian test, a crack initiates in the location of maximum tensile strain point. This point corresponds to the location of the transition zone between the local shear damage zone in proximity of the loading points and tensile failure point (Figure 7.6) . Figure 7.7 shows the location of this damaged zone in the shale specimen employed in the experiment A. This local damage has spread over a distance of about 2.9 mm, which corresponds to $R_c/R \approx 0.84$, being R_c the distance of the point from the disc centre. This is in agreement with the finding of Hudson et al. (1972) who, using experimental observation and theoretically calculations, proved the crack initiation point (i.e., maximum radial and transversal strains) are located at a point between $0.85 > R_c/R > 0.95$.

After calculation of fracture toughness K_{Ic}, fracture energy G can be calculated

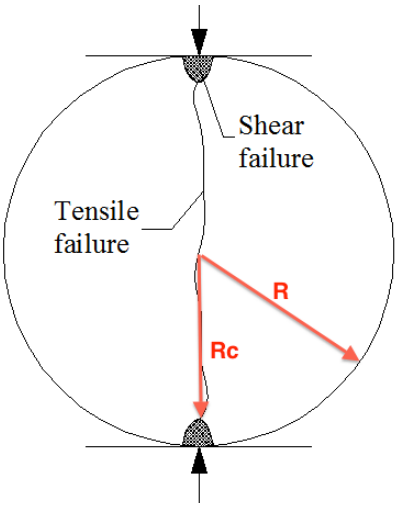

Figure 7.6: Brazilian disc test failure modes according to Hobbs (1964): transition between shear and tensile fracture zone

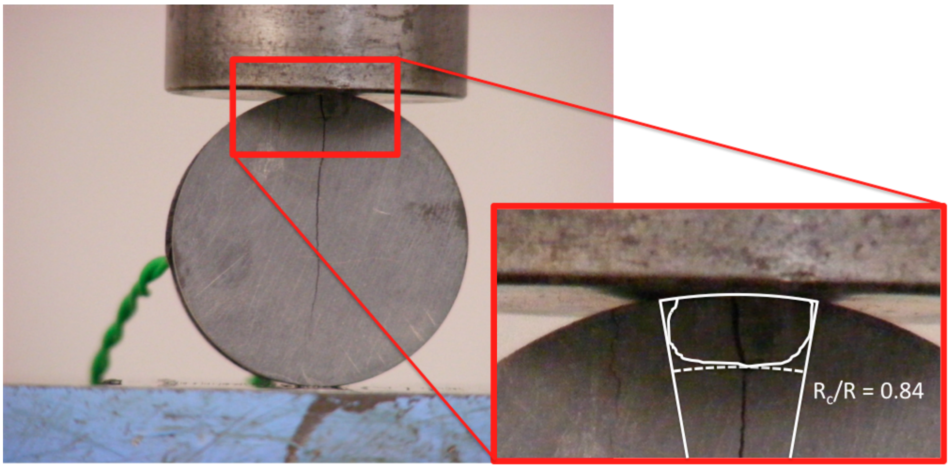

Figure 7.7: Local damage zone under loading point: damage in the specimen and distance from the centre of the disc

using (Knott and Elliott, 1979):

$$G = \frac{K_{Ic}^2}{E^*} \tag{7.4}$$

where, E^* is the modulus of elasticity in either plane strain or stress conditions, ν is Poisson ratio and K_{Ic} is the fracture toughness shown in Tables 7.1 and 7.2.

7.3.2 Fracture toughness values summary

The method presented in the previous paragraph used to calculate fracture toughness from intact Brazilian specimens is applied to all the specimens.

Specimens A and B have been both tested using flat plates. It must be recalled that, on the basis of the conclusions from Hudson et al. (1972) and Hobbs (1964), it is assumed that a crack will start at a point located between $0.85 > R_c/R > 0.95$. These two values are therefore used as minimum and maximum thresholds to calculate a range of possible values for K_{Ic}. In Table 7.3 the calculated values of K_{Ic} and G are reported and compared to the values obtained by Guo et al. (1993). Values for K_{Ic} are calculated using Eq. 7.3, while the corresponding values for G are calculated using Eq. 7.4. It is worth mentioning that these ranges of values will be considered in the section where statistical analyses will be performed, in order to estimate the different values of mean value and standard deviation for the definition of the needed PDFs.

For the specimen A it has been already discussed that this methodology has been considered because the method of Guo et al. (1993) provide a unrealistic and extremely low value for K_{Ic}. For specimen B, it can be observed that the value calculated with the two methodologies are consistent: the value calculated by Guo et al. (1993) falls within the range of values provided by the methodology proposed in this study.

Table 7.3: Values for K_{Ic} calculated with the method proposed in this study and comparison with the values calculated using the method proposed by Guo et al. (1993) for specimens loaded using flat plates.

		Sample A	**Sample B**
Guo et al. (1993)	K_{Ic} (N/mm$^{3/2}$)	12.02	22.77
	G (N/mm)	$0.4 \cdot 10^{-2}$	$2.6 \cdot 10^{-2}$
Irwin & Hobbs (1964)	K_{Icmin} (N/mm$^{3/2}$)	15.18	18.97
	G_{min} (N/mm)	$0.7 \cdot 10^{-2}$	$1.8 \cdot 10^{-2}$
	K_{Icmax} (N/mm$^{3/2}$)	26.24	33.20
	G_{max} (N/mm)	$2.5 \cdot 10^{-2}$	$5.6 \cdot 10^{-2}$

Table 7.4 summarises the values of K_{Ic} calculated with the two different methodologies for the specimens tested using curved jaws. It can be observed that, except for sample E, the minimum and the maximum values of K_{Ic} calculated for samples C and D are not consistent with the value calculated using the methodology of Guo et al. (1993). In fact, the assumption of finding the crack initiation point below the loading point is valid only when flat plates are used to load a specimen. With curved jaws, crack initiation point is in fact usually found at a point closer to the centre to the disc.

Table 7.4: Values for K_{Ic} calculated with the method proposed in this study and comparison with the values calculated using the method proposed by Guo et al. (1993) for specimens loaded using curved jaws.

		Sample C	**Sample D**	**Sample E**
Guo et al. (1993)	K_{Ic} (N/mm$^{3/2}$)	18.97	22.13	43.64
	G (N/mm)	$1.5 \cdot 10^{-2}$	$2.2 \cdot 10^{-2}$	$7.5 \cdot 10^{-2}$
Irwin & Hobbs (1964)	K_{Icmin} (N/mm$^{3/2}$)	19.6	30.35	34.78
	G_{min} (N/mm)	$1.3 \cdot 10^{-2}$	$4.2 \cdot 10^{-2}$	$4.7 \cdot 10^{-2}$
	K_{Icmax} (N/mm$^{3/2}$)	35.10	52.49	60.08
	G_{max} (N/mm)	$4.1 \cdot 10^{-2}$	$1.2 \cdot 10^{-1}$	$1.4 \cdot 10^{-1}$

7.4 Preliminary numerical simulations: homogeneous vs layered models

In this section the first numerical investigations on the 5 specimens tested experimentally are presented. For all the five specimens two types of simulations are performed:

- one simulation where the simulation domain is assumed to be homogeneous;
- one simulation which aims to reproduce the layered nature of the specimens: for each layer, a different value of G will be considered.

Comparisons in terms of damage distribution, crack patterns and stress-strain curves will be discussed in order to show how the effect of spatially-variable mechanical properties changes the mechanical response of the material.

The values for G for each layer have been selected considering a variation between different layers included in a range of 10-20% with respect to the mean value. Furthermore, for samples D and E zones containing small inclusions are numerically modelled. Inclusions in shale-gas rocks are usually made of calcite and dolomite, which are the principal constituents of marble rocks. (Shushakova et al., 2013). Experimental observations showed that the range of values for fracture energy of materials forming small inclusions can vary within a wide range of values, from a minimum of $0.2 \cdot 10^{-2}$ to a maximum of $4.5 \cdot 10^{-2}$ N/mm (Jeong et al., 2017). Further experimental studies, reporting values for fracture energy G for different types of rocks, showed how values for G for shale rocks are lower compared to values for G for rocks made of calcite and dolomite (Chandler et al., 2016). After considering these ranges of values, for samples D and E values of fracture energy for small inclusions are carefully chosen and details can be found in the following sections.

7.4.1 Models input

For each sample a different model is created. For homogeneous models, values for radius of specimens, fracture energy G, modulus of elasticity E are all reported in Tables 7.1 and 7.2, while Poisson's ratio is considered equal to 0.25 for all models. Based on the International Society of Rock Mechanics's guidelines, the experimental set up for a Brazilian test is usually designed with a 5 to 15 degrees contact arc between specimen and loading jaws (depending on the type of loading system employed). Accordingly, in order to reproduce a realistic simulation for sample A for example, the length of the section where load is applied should be between 1.5 and 3.2 mm. Therefore, a distributed displacement with a rate of 0.0005 mm/step is applied over length equal to 2 mm (always for sample A) at above and below of the disc. For samples B, C, D and E these lengths, taking into account the size of the samples and the use of either flat plates of curved jaws, the contact length between samples and loading devices are equal to 2, 4.3, 5 and 5.5 mm respectively. Figure 7.8 shows all the samples with highlighted the layered conformation considered for the numerical simulations together with the different values of G assigned to each layer. For samples D and E, it is worth highlighting the presence of small inclusions with a higher value of G (assigned following the considerations of (Shushakova et al., 2013), (Jeong et al., 2017) and (Chandler et al., 2016)) compared to those assigned to the surrounding layers. More details about the values assigned to these inclusions can be found in Figure 7.8.

7.4.2 Damage distribution, crack patterns and material strength

In this section, the results in terms of distribution of the damage parameter s are discussed for homogeneous and layered models. These results can be observed in Figure 7.9: in the homogeneous specimens, damage is symmetric and homogeneously distributed, with a higher damage in the centre of the specimen: it is worth noting that the biggest damage is found approximately at the same point where crack is assumed to begin. For the specimen with layered configuration it can be observed that the distribution of the damage follows the orientation of the layers, and in particular damage tends to spread quicker through the layers with lower value of fracture energy; this is a trivial result, but it is important to highlight as it shows that the numerical model can sensibly and realistically capture the effect of variations of mechanical properties in the domain . For samples D and E, the damage parameter gets lower values in those areas with lower G, as in the previous examples; however, the presence of harder inclusions introduces areas where the damage gets closer to unity.

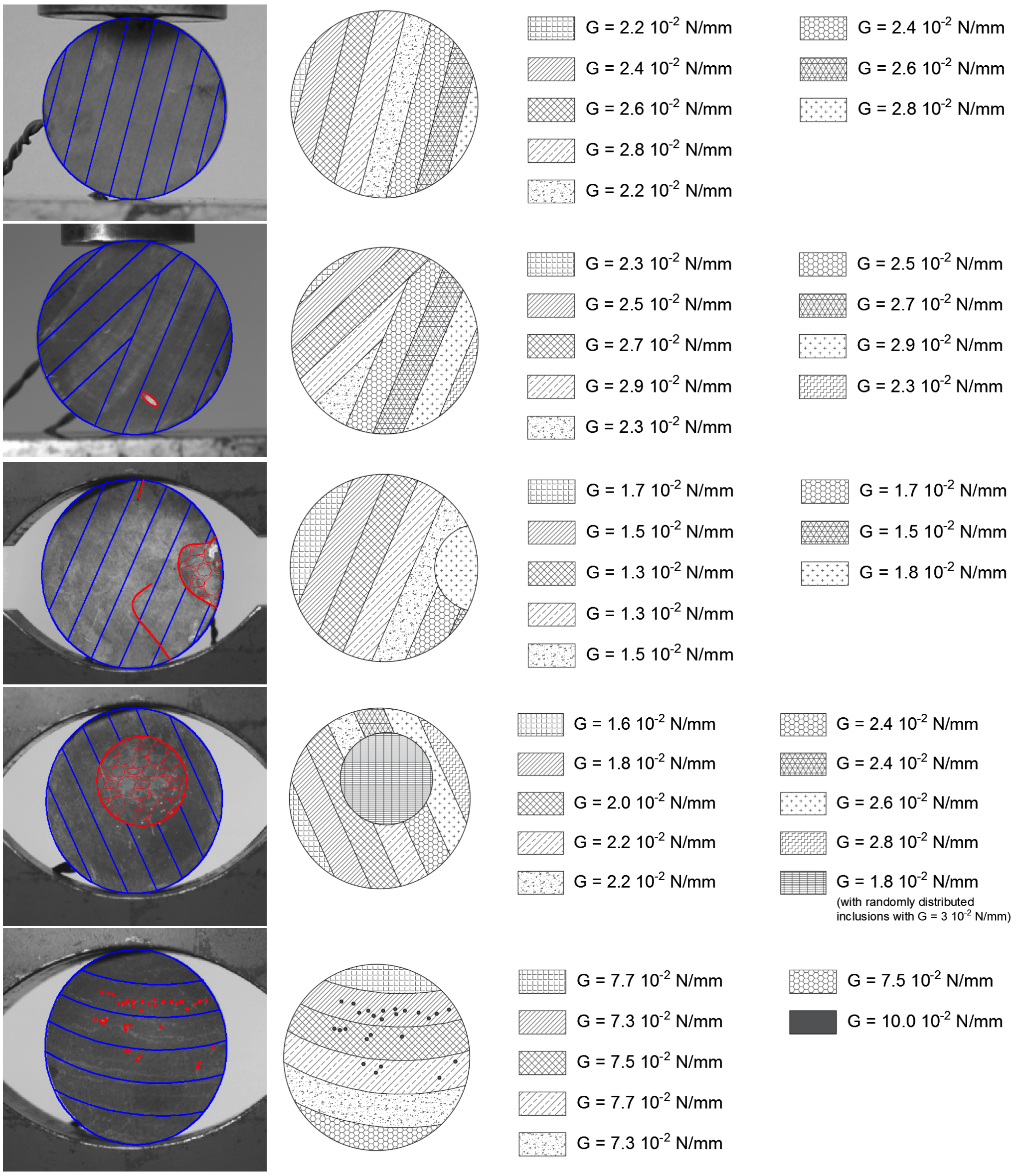

Figure 7.8: Samples simplified layered structure, with specified values of G for each subdomain.

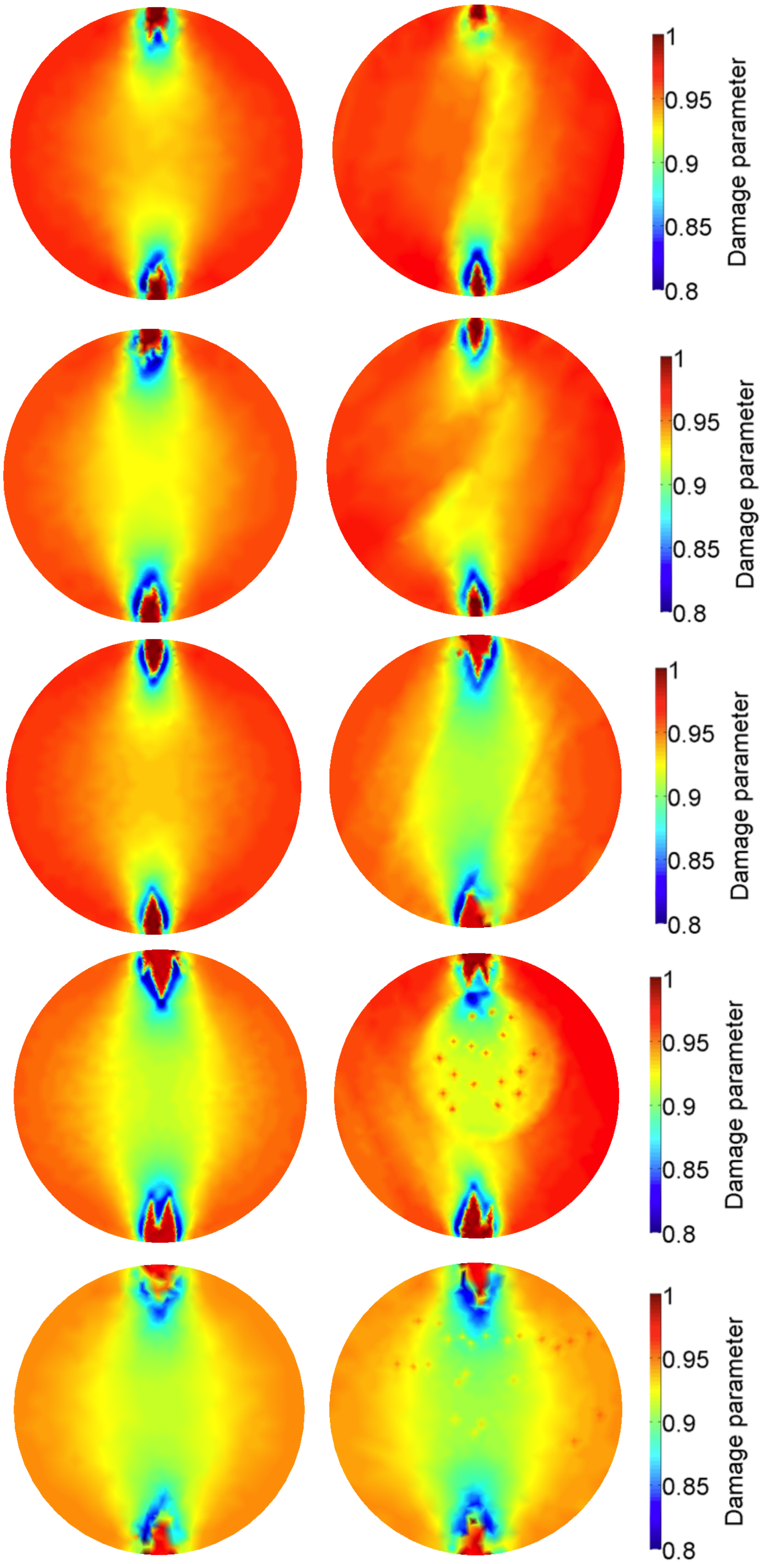

Figure 7.9: Damage distribution over the homogeneous (left) and layered (right) models of samples A (top), B, C, D and E (bottom).

These different distributions of damage through the domains influence the shape of the crack patterns obtained in the homogeneous and layered models. Figure 7.10 shows all the crack paths obtained for all the five samples modelled with both configurations. With the only exception of sample A, where the two crack patterns obtained with the two different models are very similar, in all the other samples a clear difference between patterns can be observed. Cracks obtained with the layered models are more tortuous, multiple crack are present and, especially for samples B and E, a more evident similarity with the experimental results. In addition, it must be highlighted that in samples D and E the biggest deviation it is observed in correspondence of the zones where small hard inclusions are modelled (as cracks try to spread in the area with lower G but at the sime time can not go through the inclusions themselves), proving that both layered nature of material and spatially-variable heterogeneities are factors that influence the direction and extent of cracks.

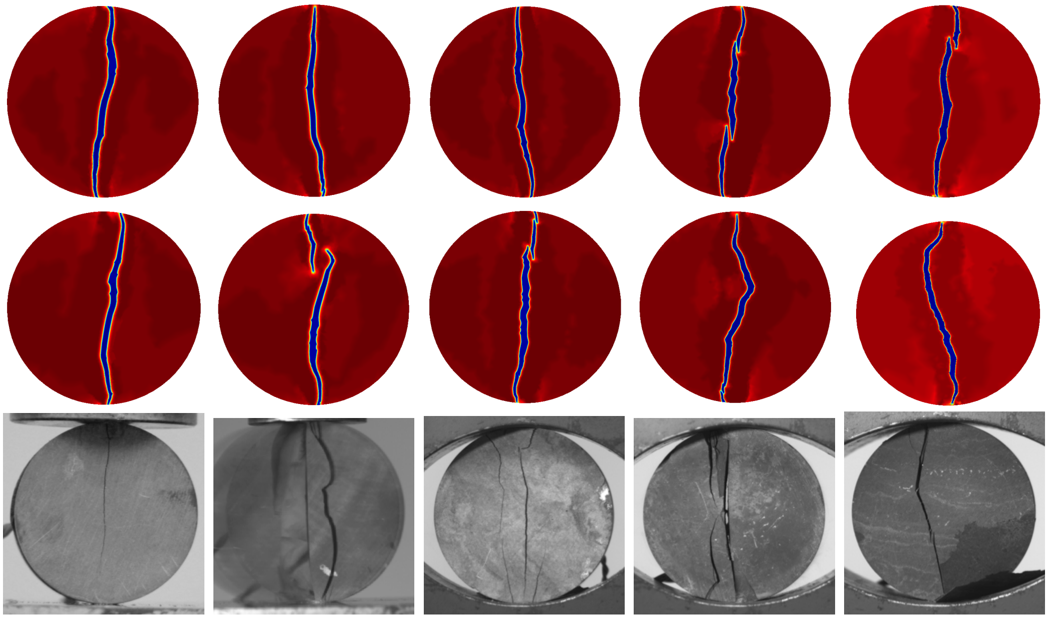

Figure 7.10: Crack paths for the homogeneous (top) and layered (middle) numerical models and comparison with the experimental (bottom) crack pattern of all the five samples.

Stress - Strain plot for sample A can be found in Figure 7.11: it can be observed that the homogeneous model can predict with good approximation the final value of material resistance but the ultimate strain is underestimated and it shows a stiffness significantly higher that the experimental measurements: the curve obtained with the layered model provides a higher value of material resistance and

overestimates the ultimate strain, but is shows a stiffness significantly closer to the one showed by the experimental data. Stress - Strain plots for sample B are shown in Figure 7.12: both the homogeneous and the layered models show a higher stiffness compared to the experimental results, even if the final value of material resistance gets closer when the layered model is considered. Therefore for this example a neither the homogeneous nor the layered models are capable of estimating the correct material stiffness. For sample C, interesting is the trend obtained in the Stress - Strain plot shown in Figure 7.13: while, in comparison with the experimental curve, the plot obtained from the homogeneous model show an overestimation of the final material resistance and stiffness, the curve obtained with the layered model shows a value of maximum tensile strength closer to the experimental one and a gradual decrease of the stiffness, leading the numerical curve closer to the experimental one. Figure 7.14 shows the Stress - Strain plots for sample D. In this case, the layered model provides a curve closer to the experimental results than the one obtained with the homogeneous model, in particular in terms of stiffness. For sample E, despite the layered model provides a crack pattern closer to the experimental results if compared to the crack path from the homogeneous model, the Stress - Strain plot of Figure 7.15 shows that the layered model cannot realistically reproduce the experimental trend, which is however better captured by the homogeneous one.
The results presented in Figures 7.11 to 7.15 are obtained by simply assigning different values of G to each layer; this scenario is still not quite close to the real one, but it shows how the model can capture the effect of variations in the values of G.

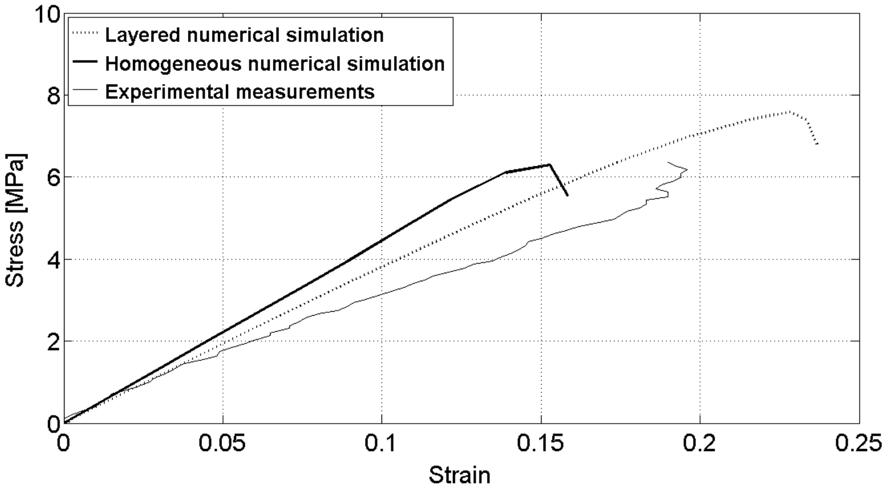

Figure 7.11: Stress - strain plots of the homogeneous and layered models and results obtained from experimental investigations on sample A.

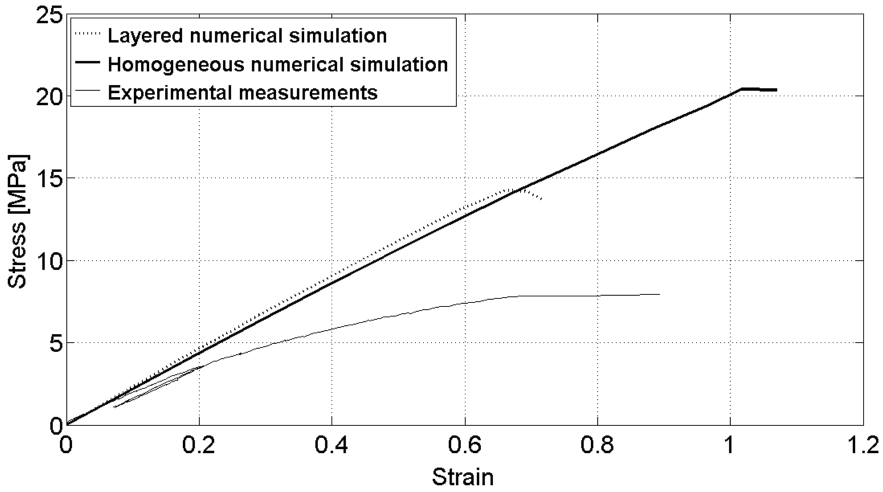

Figure 7.12: Stress - strain plots of the homogeneous and layered models and results obtained from experimental investigations on sample B.

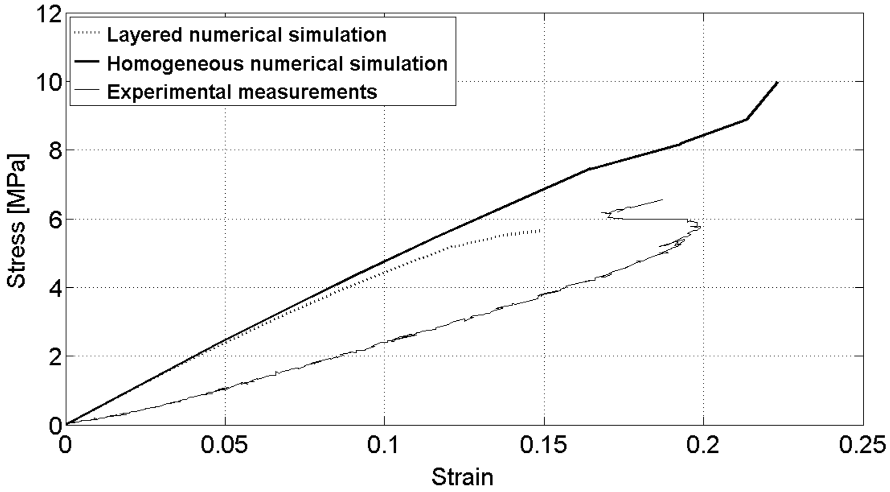

Figure 7.13: Stress - strain plots of the homogeneous and layered models and results obtained from experimental investigations on sample C.

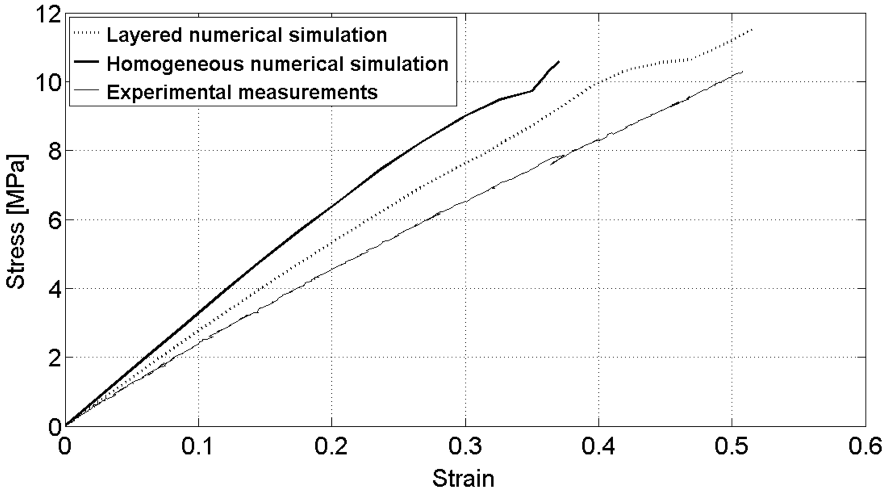

Figure 7.14: Stress - strain plots of the homogeneous and layered models and results obtained from experimental investigations on sample D.

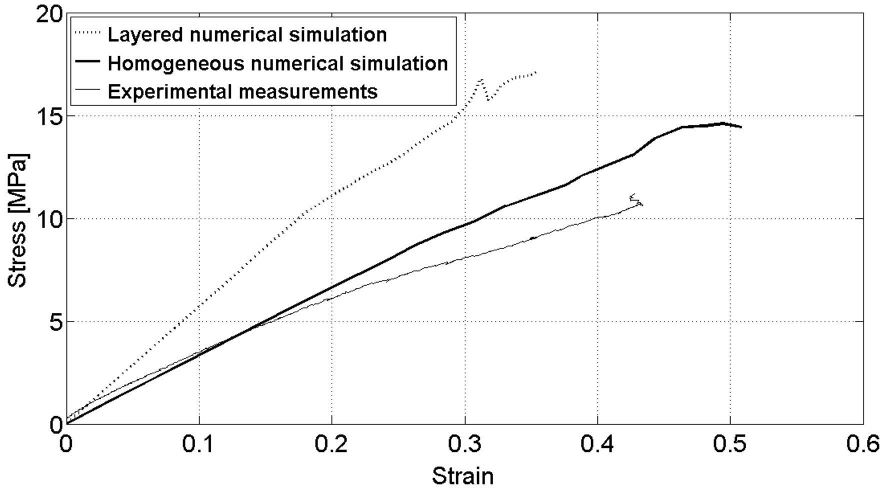

Figure 7.15: Stress - strain plots of the homogeneous and layered models and results obtained from experimental investigations on sample E.

7.5 Numerical simulations of heterogeneous shale rocks: stochastic approach applied to sample A

In the previous paragraph all the 5 samples have been numerically studied, considering both homogeneous and layered configurations by assigning different values of fracture energy G to each of the modelled domains. It has been observed that the way a problem is modelled significantly affects the results in terms of distribution of damage, crack pattern, material strength prediction and material stiffness. Furthermore, it has been observed that capturing the exact distribution of heterogeneity is not an easy task, as it would require very sophisticated analyses, such as chemical investigations or imaging processing techniques (Sun and Li, 2015).For this reason, in the following paragraph the probabilistic approach described in the methodology section is applied to the sample A.

The geometry, boundary and loading conditions of sample A are shown in Figure 7.16. The sample is discretised using triangular elements. The finite element mesh with size 2 mm consists of 1189 triangular elements and 551 nodes that is also shown in Figure 7.16. Initially, the same mesh is used for the finite element and stochastic discretisation. Thickness of the damage zone and morphology of cracks are significantly influenced by the value of the ε. A better approximation for crack patterns would be achieved with the smaller value of the epsilon. However, this would lead to a smaller mesh size and high computational costs (Amor et al., 2009; Bourdin et al., 2014). For identifying the value of the ε recommendations of Lancioni and Royer-Carfagni (2009) and Bazant and Planas (1997) are followed. Based on the experimental observations, the value of ε should be approximately 2 to 3 times the size of constituent grains, and for this case-study it is selected a value of ε of 2 mm: shale rocks are made of constituents with different scales, and an average size of constituents in the range 0.2 - 1mm is considered (Na et al., 2017)

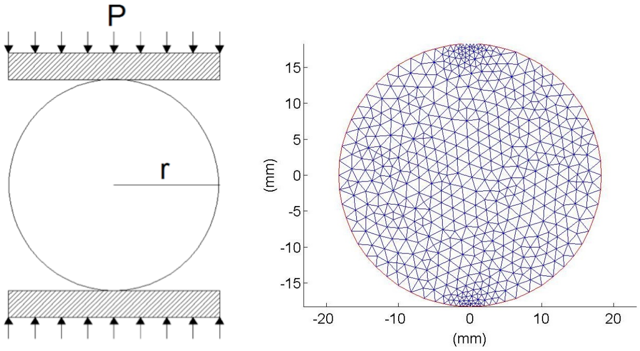

Figure 7.16: Geometry, boundary and loading conditions of the rock sample and two-dimensional finite element mesh discretisation.

In this study, a displacement-controlled condition was implemented. A distributed displacement with a rate of 0.0005 mm/step over length equal to 2 mm at above and below of the disc is applied. The residual stiffness k_ε is set equal to 0.01, to be one order of magnitude smaller than the finite element mesh size after refinement. Fracture energy is initially selected to be that property, with mean value of $2.5 \cdot 10^{-2}$ N/mm and standard deviation equal to $0.1 \cdot 10^{-3}$, $0.5 \cdot 10^{-3}$ and $1 \cdot 10^{-3}$. This value for fracture energy has been calculated from experiments following basic principles of fracture mechanics, given the geometry, the loading conditions and the modulus of elasticity. The three different standard deviations have been selected in order to study the effect of the degree of heterogeneity on the material response.

7.5.1 Numerical results

Spatial variation of fracture energy G is described by both Gaussian (KL expansion) and non-Gaussian (Weibull) distributions. Figure 7.17 shows a realisation of this property sampled according to the Weibull distribution and randomly distributed over the spatial domain. The crack path obtained for a model with this specific realisation of the fracture energy is shown in Figure 7.18 and is compared with the crack path obtained from the homogeneous model and with the crack obtained experimentally. It is observed that crack path obtained from the model considering a heterogeneous material property shows a more tortuous pattern, as crack tends to propagate towards zones of less resistance but, for this example, cracks obtained with both homogeneous and one of the heterogeneous models realistically reproduce the experimental pattern.

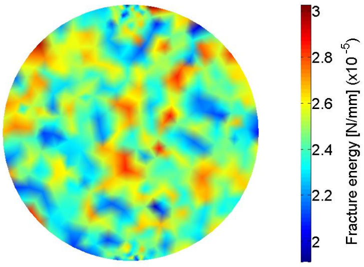

Figure 7.17: A realisation of the randomly distributed fracture energy in the cylindrical disc.

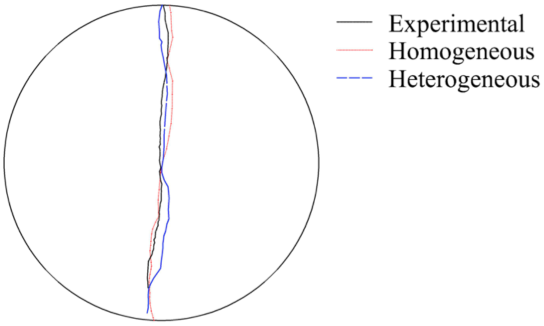

Figure 7.18: Comparison between crack paths achieved with homogeneous, one of the heterogeneous models and experiment.

Figure 7.19 shows a quick comparison for this case study highlighting the importance of calculating a suitable reduced order model reproducing the spatially-distributed heterogeneity. In fact, with a reduced-order stochastic mesh a crack path almost identical to the one obtained with the initial stochastic mesh is obtained, which is not the case if a too coarse stochastic mesh is used.

The first row of Figure 7.19 shows three different RF meshes: the original RF mesh (left), the correct reduced-order RF mesh (middle) and a too big RF mesh (right). The second row of Figure 7.19 shows the same distribution of G on the three RF meshes with three different sizes. The distribution of the optimal RF mesh must be capable to capture with sufficient accuracy the distribution of G showed in the original RF mesh. The last two rows of Figure 7.19 show the effect of the three different RF meshes on a FE mesh of constant size: despite small differences between some of the element for the first two meshes, the final crack paths are identical, with only a very small difference next to the loading points, while the crack path obtained with the coarse RF mesh provides a crack path of a completely different shape.

In Figure 7.20 the evolution of the damage state of the body for both homogeneous and heterogeneous models can be observed. It shows that heterogeneity causes a random distribution of local damage zones in the domain, which significantly affects the mechanical performance of the body. Especially during the last steps of the simulation, it is clear how heterogeneity creates zones of weakness (low values of s) that will introduce that tortuous patterns observed in the crack path. These zones of weakness are not visible for the homogeneous model, where damage is concentrated only in correspondence of the loading points. Stochastic response of the fracturing sample is computed using MC simulations.

In Figures 7.21 and 7.22, the mean value and standard deviation of the tensile strength of a set of specimens modelled using a Weibull distribution are plotted as a function of the number of MC simulations, which show that the statistical convergence is achieved after only 65 simulations.

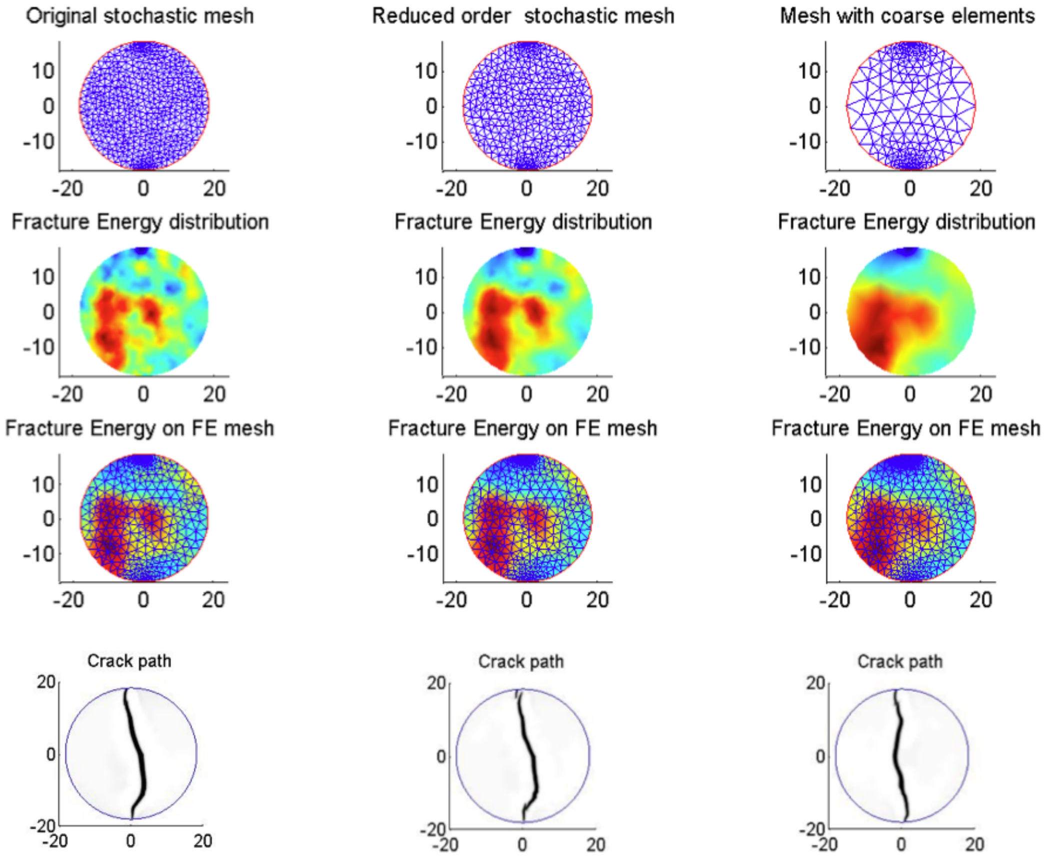

Figure 7.19: Comparison between original stochastic mesh (left column), reduced-order stochastic mesh with correct size (central column) and excessive dimension (right column). The dimension of the reduced-order stochastic mesh is related to the size of its neighbourhood. With a very small neighbourhood size, the size of the mesh increases, leading to a loss of information of the stochastic field. This causes the predicted crack path to be significantly different from the original one. With an adequate dimension of the neighbourhood, crack path is still very close to the initial one.

In Figure 7.23 all the stress-strain curves resulted from MC simulations associated to different random realisations of fracture energy sampled using the Weibull distribution together with their mean curve are plotted. The tensile strength is considered as the maximum value of stress, which occur at the centre of the disc, obtained through experiment and numerical simulations.

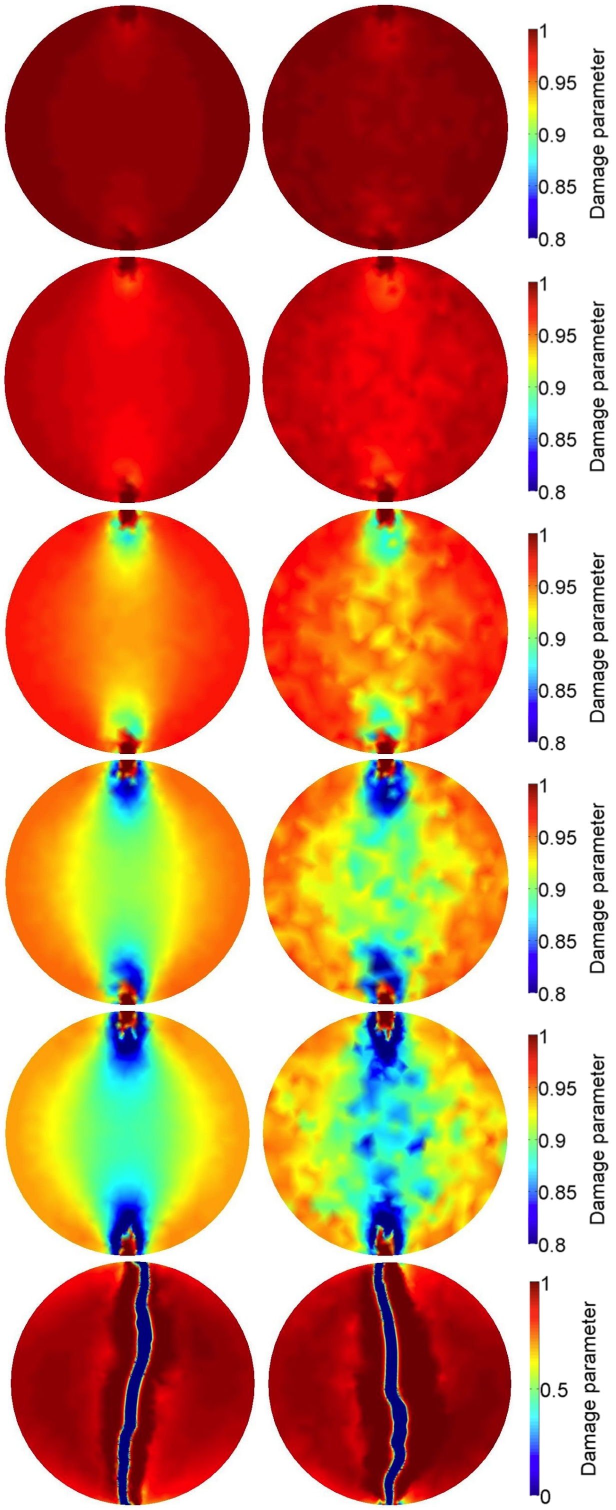

Figure 7.20: Evolution of damage state in the disc for homogeneous (left) and one of the heterogeneous models with unit standard deviation (right).

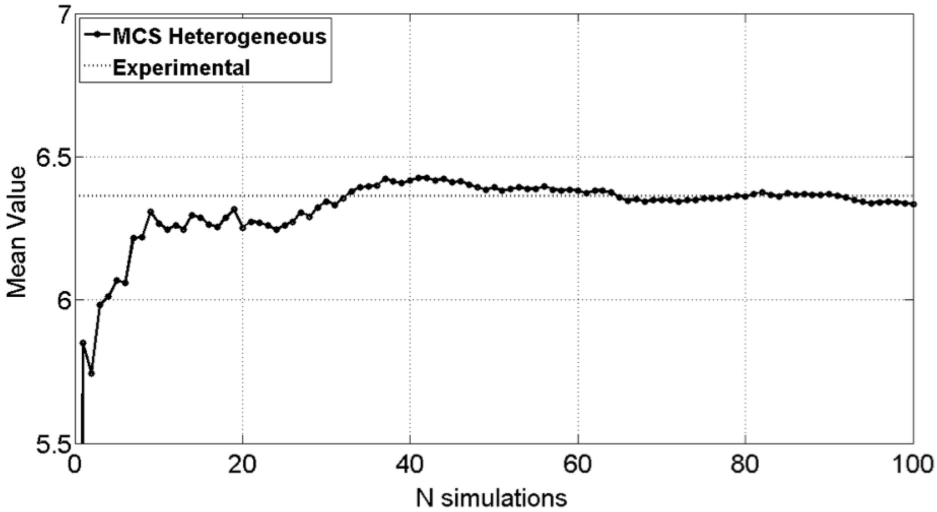

Figure 7.21: Brazilian disc test: Convergence of calculated mean value of tensile strength from simulations and comparison with tensile strength obtained from experiment for unit standard deviation.

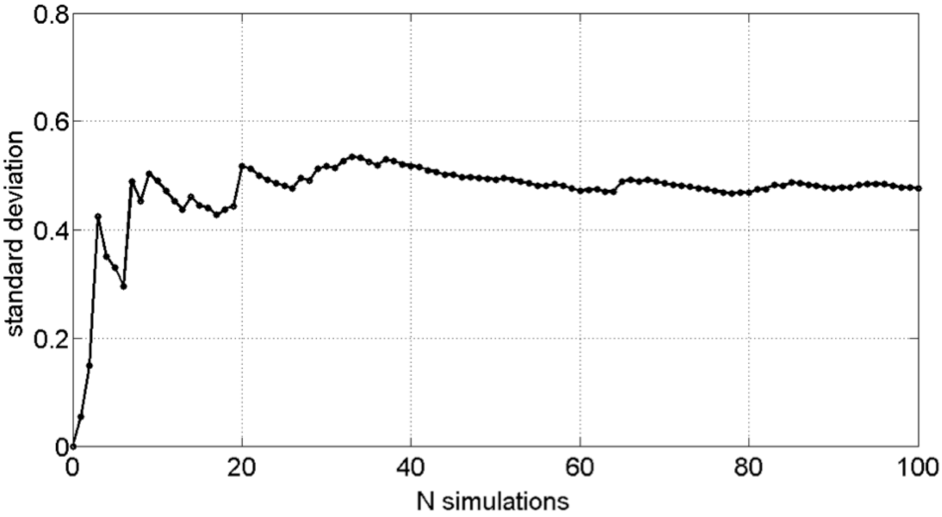

Figure 7.22: Brazilian disc test: Effect of the number of MC simulation samples on the standard deviation of the tensile strength for unit standard deviation. Standard deviation's trend gets stable after about 65 simulations.

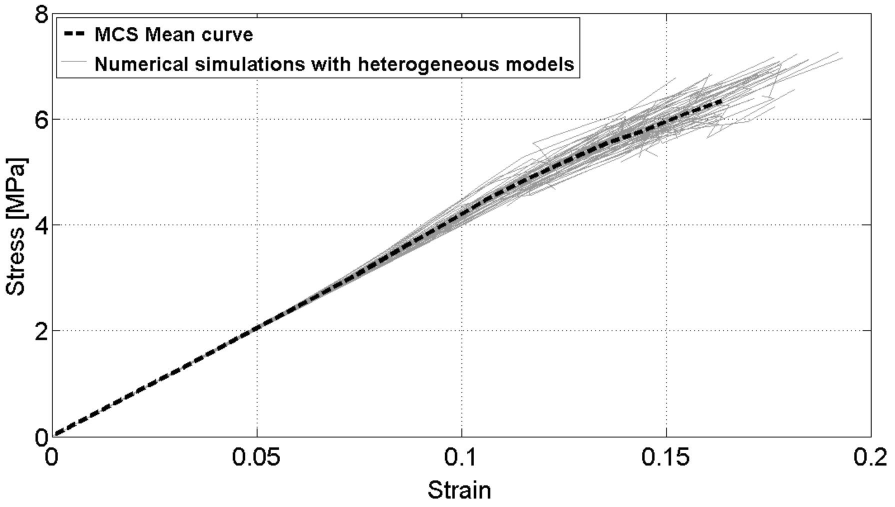

Figure 7.23: Brazilian disc test: stress-strain curves for 100 simulations and mean Stress-Strain curve.

Figure 7.24 compares stress-strain curves obtained from experimental test and numerical modelling considering simulations with both homogeneous and heterogeneous models. It is noticeable that the maximum tensile strength calculated from the stochastic based modelling is not very different from the one calculated by the homogeneous based modelling. The stochastic based modelling result shows a notably better agreement with experimental measurements, in particular in terms of ultimate strain reached before material failure. The physical interpretation of the difference between strains at failure is related to the increase of deformability for heterogeneous models, due to the higher roughness and tortuousness of cracks compared to those obtained with the homogeneous model. Furthermore, it can be observed how the local damages described above lead to a piecewise linear behaviour, in which material stiffness progressively decreases before failure, which still has brittle nature. The homogeneous model is not capable of reproducing this aspect of the sample behaviour until brittle failure occurs.

Figure 7.25 shows the stress-strain curve for the three degrees of standard deviation considered in this study with values of fracture energy modelled by means of Weibull distribution and KL expansion method. Despite the different values of standard deviation, it can be observed, for both cases and especially for the first phases of the simulations, that the simulated behaviours are very close, and differ only in the last phase, closer to failure. A higher standard deviation, i.e., index of a higher degree of heterogeneity, leads to a curve closer to the experimental plot. In both figures can be seen that for higher standard deviation the stress-strain plot gets closer to the experimental results but, overall, the results obtained with the Weibull distribution are closer to those obtained with the KL expansion.

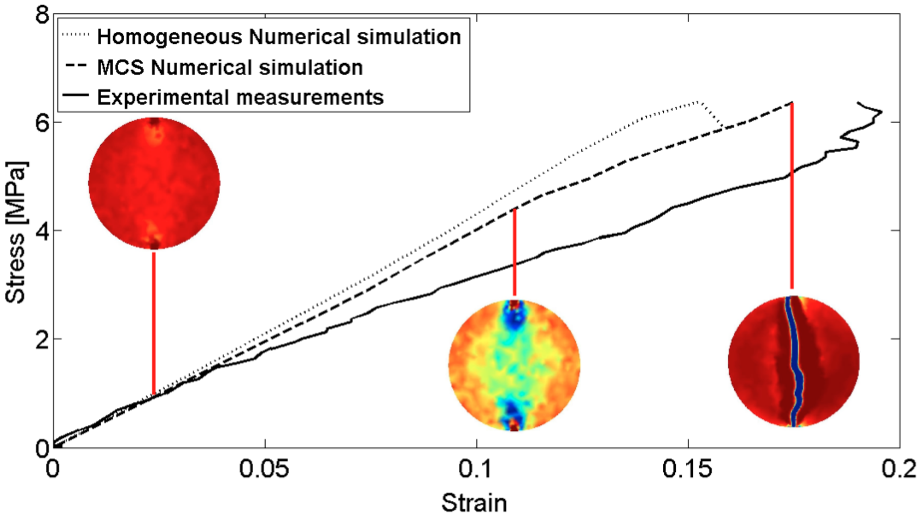

Figure 7.24: Brazilian disc test: Stress-Strain curves, comparison between experimental data and numerical results from homogeneous and heterogeneous models for unit standard deviation.

In order to study the effect of cross-correlation between random parameters on the behaviour of fracturing body, both fracture energy and modulus of elasticity are selected as random variables. A mean value of 29.1 GPa and standard deviation of 0.5 was selected for the modulus of elasticity. Three different degrees of cross-correlation are analysed, for correlation coefficient equal to 1, 0.5 and 0, representing full, partial and absence of correlation, respectively.

Figures 7.26 and 7.27 shows the stress - strain curve for the three different scenarios and the mean curve obtained from the 100 Monte Carlo simulations with values of fracture energy modelled by means of Weibull distribution and KL expansion method. Figure 7.28 compares the three mean curves with the curve obtained experimentally and with the homogeneous model, from where it can be seen that a full correlation moves the curve from the experimental plot, while a lower degree of correlation leads to more realistic results in terms of material strength. Figure 7.29 shows how convergence of the results is achieved after 60 analyses using both methods; however, it is worth noticing how, when a satisfactory convergence is reached, the mean values and standard deviations have values slightly closer to the experimental results when the Weibull distribution is used for modelling of heterogeneity in comparison to the KL expansion method.

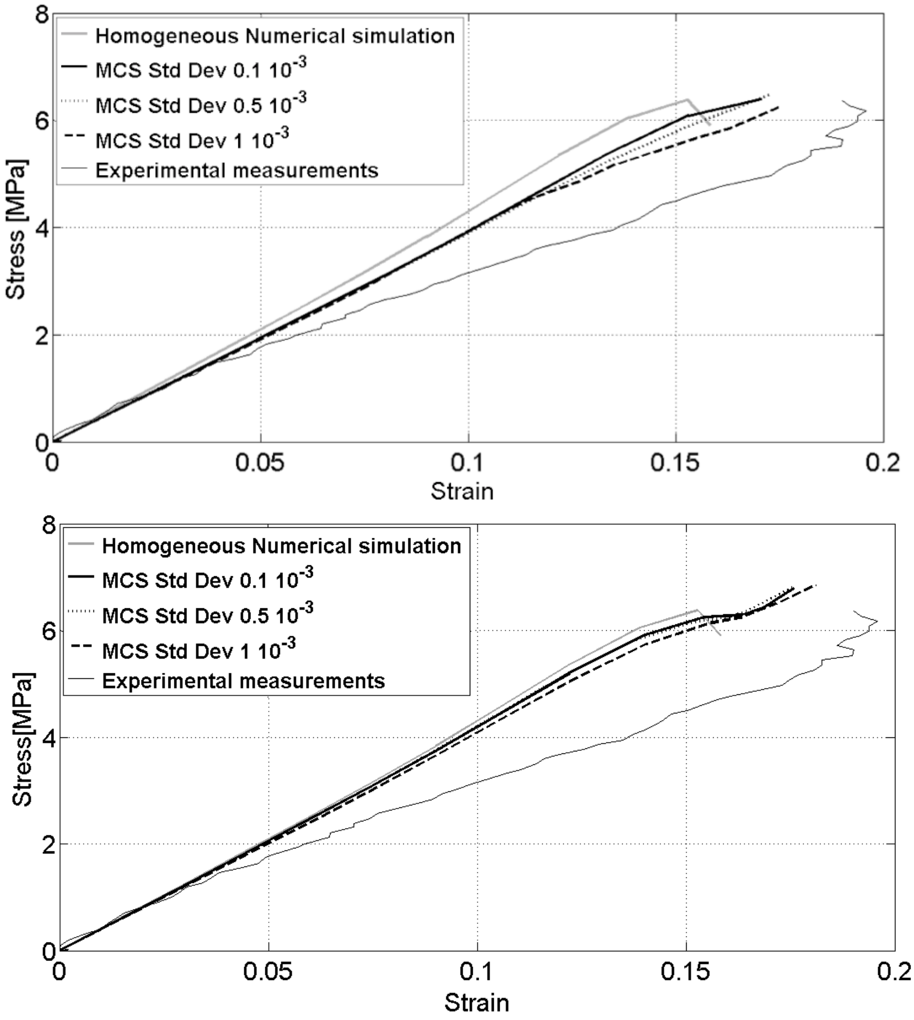

Figure 7.25: Brazilian disc test: stress-strain curves, comparison between experimental data and numerical results from homogeneous and heterogeneous models with different standard deviations. Values of fracture energy have been sampled by means of the Weibull distribution (top) and the KL expansion method (bottom).

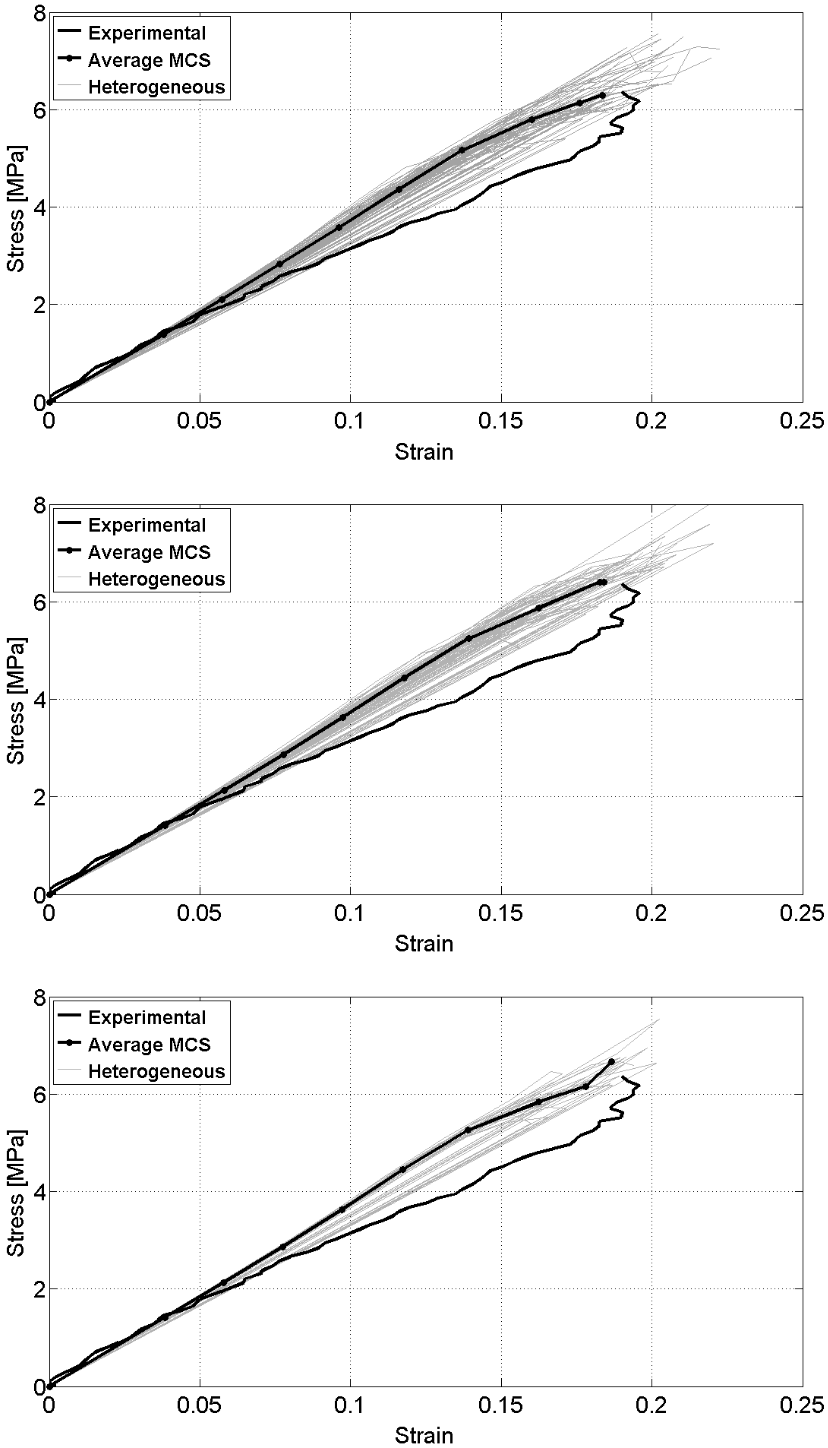

Figure 7.26: Brazilian disc test: stress - strain plots obtained from MC simulation for three different degrees of correlation. No correlation (top), partial correlation (middle) and full correlation (bottom) between fracture energy and modulus of elasticity modelled by means of the Weibull distribution.

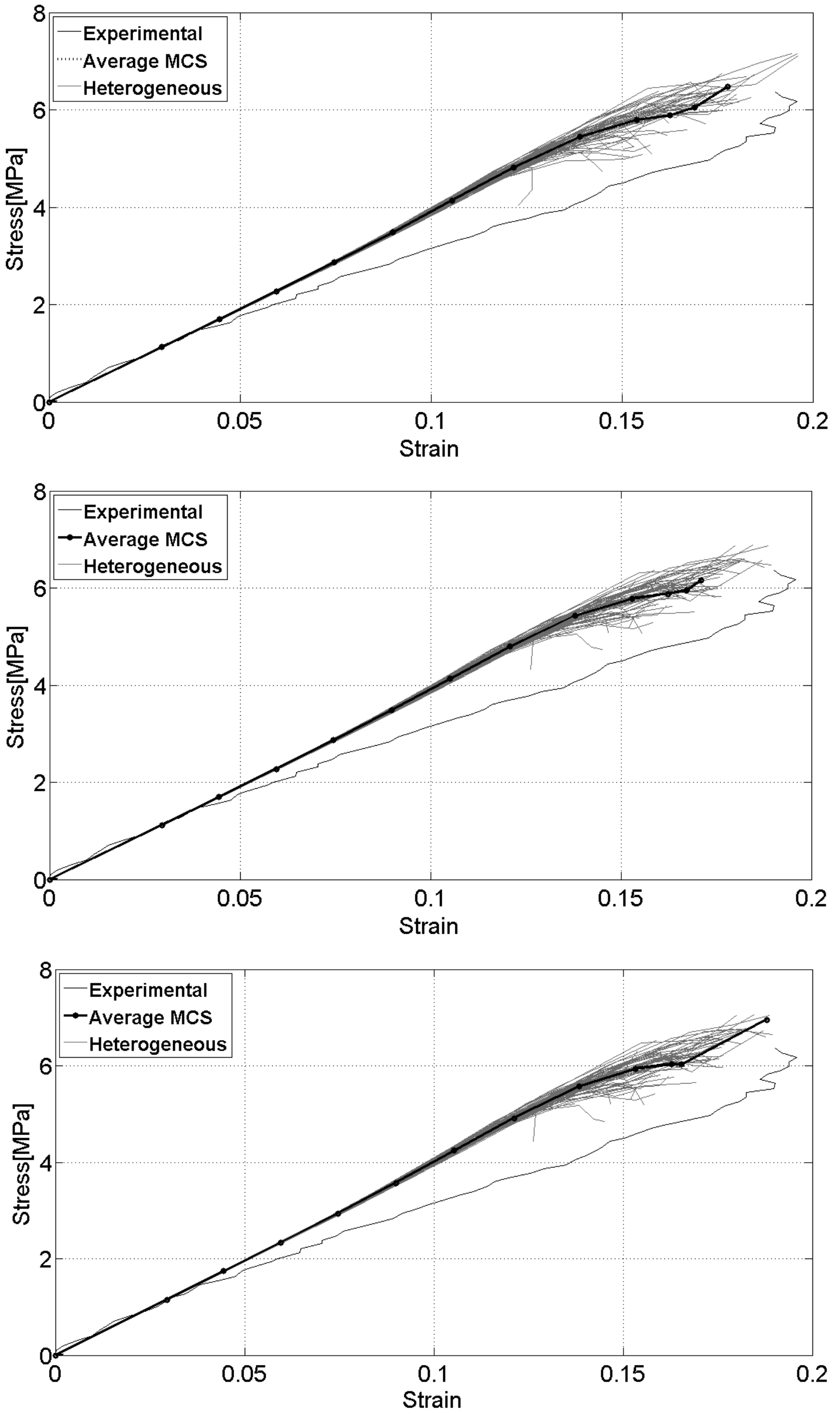

Figure 7.27: Brazilian disc test: stress - strain plots obtained from MC simulation for three different degrees of correlation. No correlation (top), partial correlation (middle) and full correlation (bottom) between fracture energy and modulus of elasticity modelled by means of the KL expansion method.

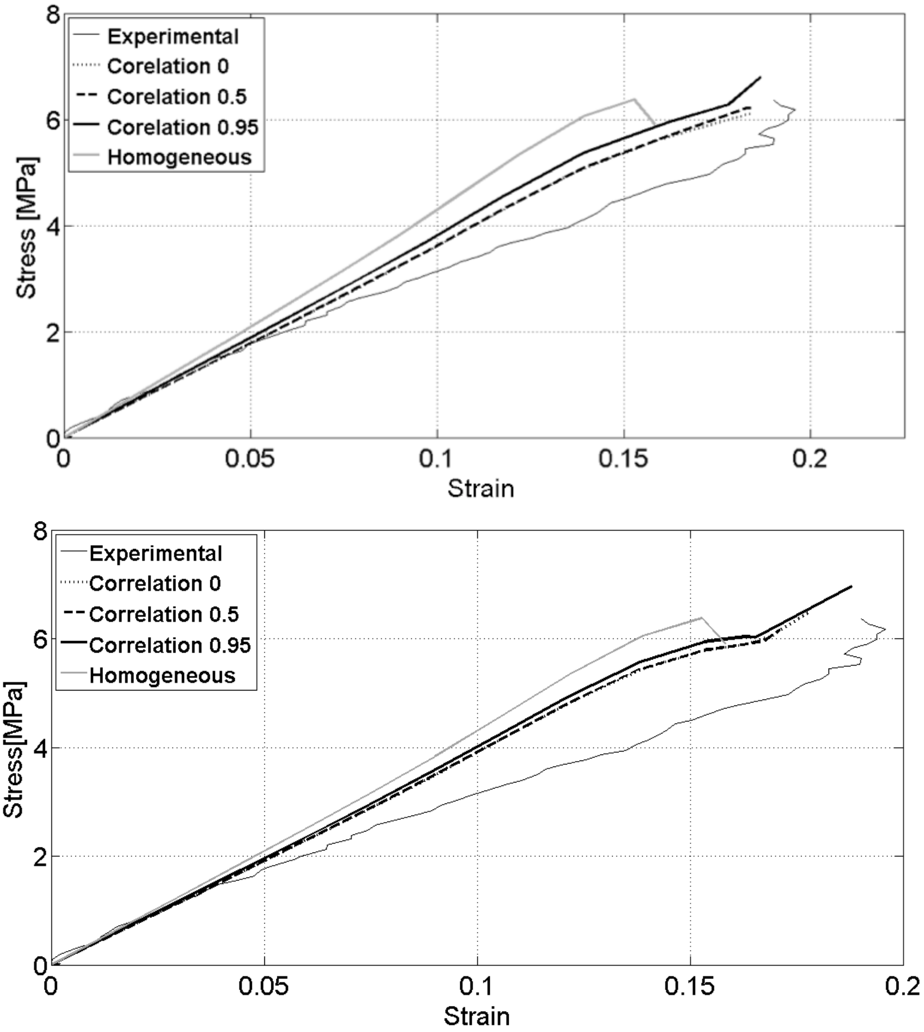

Figure 7.28: Brazilian disc test: Comparison between the stress - strain curves obtained from MC simulation for three different degrees of correlation. Values of fracture energy and modulus of elasticity sampled by means of the Weibull distribution (top) and KL expansion method (bottom).

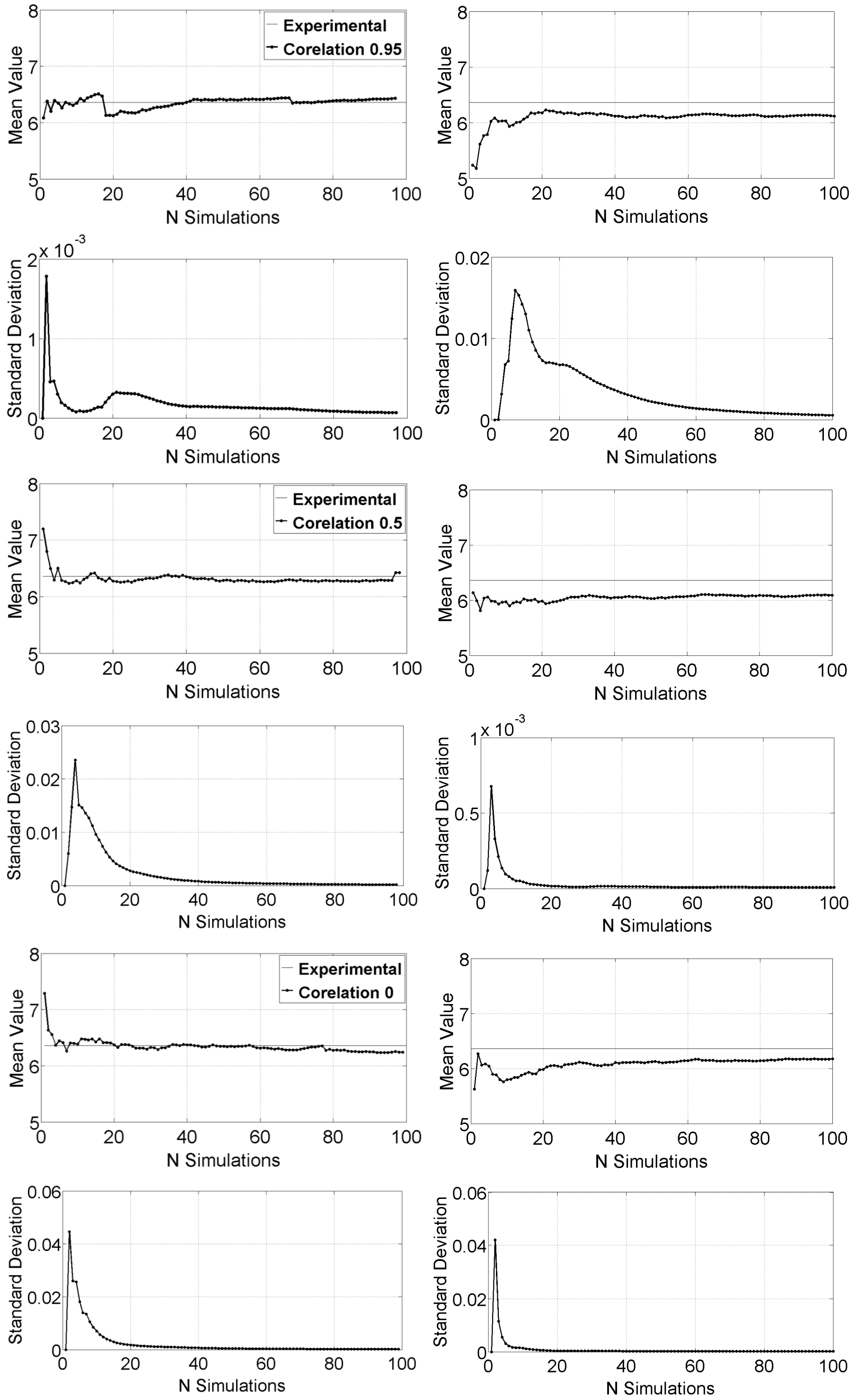

Figure 7.29: Brazilian disc test: convergence of the mean value and standard deviation obtained from simulations with (top) full, (middle) partial and (bottom) no correlation, between fracture energy and modulus of elasticity sampled with Weibull distribution (left) and KL expansion method (right).

It is worth highlighting the effect of dimensionality reduction and the overall time saved. Table 7.5 provides all the required information to appreciate the overall reduction in the time needed for sampling and, therefore, for the whole analysis. For a RF mesh of size 1mm the CPU needed for the generation of 1 sample is of 55.4 seconds, while for a reduced RF mesh of size 2.5 mm the CPU drops to 3.6 seconds. Considering that has been observed that convergence of results has been achieved after an average of 60 simulations, the overall reduction in terms of computational cost can be estimated to be approximately 52 minutes.

Table 7.5: Reduction of computational time needed for sampling due to the application of MOR technique.

RF n. el	RF mesh size	MOR n. el	MOR mesh size	FE n. el	FE mesh size	Sampling time RF	Sampling time MOR
3452	1 mm	768	2.5 mm	582	3 mm	55.4 s	3.6 s

7.6 Influence of bedding direction of shale rocks

7.6.1 Layers with fixed values of modulus of elasticity and fracture energy

Investigating the influence of the rock bedding orientation on propagation of fractures allows the determination of the optimal angle at which cracks will grow in a desired length and direction. In fact, as shown in paragraph 7.4, the anisotropic nature of the shale rock creates huge differences in results when different bedding plane directions are considered (Morgan et al., 2014).

In this section, sample A is modelled considering different orientations of the layers. Figure 7.30 shows four distinct models labelled a-d that differ by the angle between the direction of loading and the orientation of the bedding planes, which is at 0, 30, 60, and 90 degrees from the vertical axis. Different values of material properties are assigned to each layer and they are all summarised in Table 7.6. These values have been chosen in a way that their calculated mean value is equal to the single value obtained by the experimental measurements. While in pargraph 7.4 only G varied in each layer, here each domain of the models created here has different values of E, ν and G.

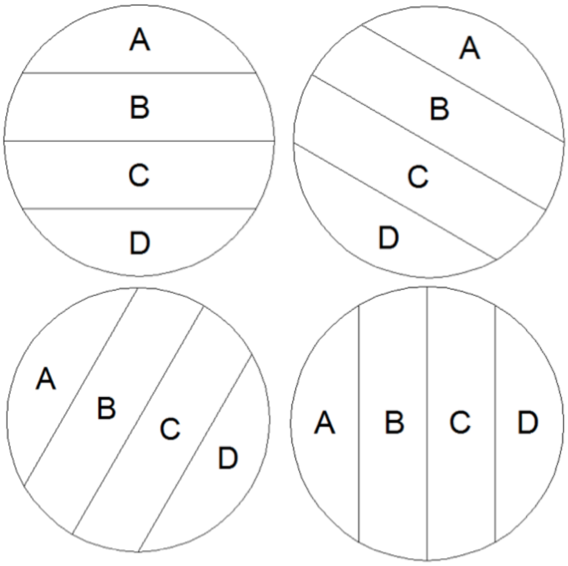

Figure 7.30: Bedding directions for Brazilian disc: bedding at (left to right, top to bottom) 90, 60, 30 and 0 degrees.

Table 7.6: Input mechanical properties for layered material models.

Layer	E (GPa)	ν (-)	G (N/mm)
A	25.1	0.22	$3.0 \cdot 10^{-2}$
B	28.1	0.24	$2.7 \cdot 10^{-2}$
C	31.1	0.26	$2.4 \cdot 10^{-2}$
D	34.1	0.28	$2.1 \cdot 10^{-2}$

Crack paths for each layered model and comparison with damage state over the specimen are shown in Figure 7.31. Crack paths are influenced in accordance to direction of bedding layers. The values for damage parameter are different in different layers, and bedding direction influences this damage localisation. In fact, variability of mechanical properties and damage state, which is not uniformly distributed over the specimen, influence the pattern of the cracks.

Figure 7.32 shows how effectively tensile strength is the function of bedding angle, and the 'u-shape' graph is in agreement with conclusions in Morgan et al. (2014), where the minimum value of tensile strength is found for bedding inclinations between 30 and 60 degrees. However, it is quite uncommon, for specimens with comparable geometrical and mechanical properties, to find a higher value of tensile strength for a specimen with vertical orientation of layers: Abbas et al. (2015), for example, reported result of indirect tensile tests on cap rock shale samples. Tests are conducted for load direction both perpendicular and parallel with bedding. For specimens with same geometry, density and collected from sites with same depths, some of the sample in which loading is applied in parallel direction with respect to the bedding. However, this seems to be one of the very few cases in literature where this phenomenon happens.

Figure 7.33, taken from Chong et al. (2017), shows what should be the expected variation of tensile strength for different anisotropy angles: the highest value is expected for horizontal layers, and decreases as the angle increases. The minimum is expected to be found for specimens loaded in the same direction of the bedding planes, unless shear effect between layers is found, which makes the specimens weaker for angles between 20-30 and 50-60 degrees.

Results reported in Figures 7.31 and 7.32 don't reproduce fully the typical behaviour reported in Figure 7.33, especially in terms of tensile strength, as they are relative to only one possible combination of values of E, ν and G for each bedding orientation. In order to further verify the capability of the model to capture the effect of the anisotropic nature of shale, further analyses have been performed for different bedding orientations and different values of mechanical properties for each layer.

Tables 7.7, 7.8 and 7.9 summarise three new scenarios considered for new simulations, where to each layer a new combination of values for E, ν and G are considered. Figure 7.34 reports all the crack patterns obtained with the three different scenarios for all the bedding directions considered in this work, while Figure 7.35 summarises all the values of tensile strength for all the scenarios (including also the one shown in Figure 7.32) together with their mean curve. The average maximum tensile strength is observed for loading perpendicular to the bedding direction, and it decreases with the bedding direction angle, consistently with the observation of Chong et al. (2017). It must be however mentioned that the values of the curve of Figure 7.35 are calculated as the mean value obtained from each scenario. For a bedding angle of 60 degree the scatter of values is noticeably big; this highlights how this implementation needs to be improved and that, for example, the inclusion of the effect of shear strength can improve the quality of the results and overcome this drawback.

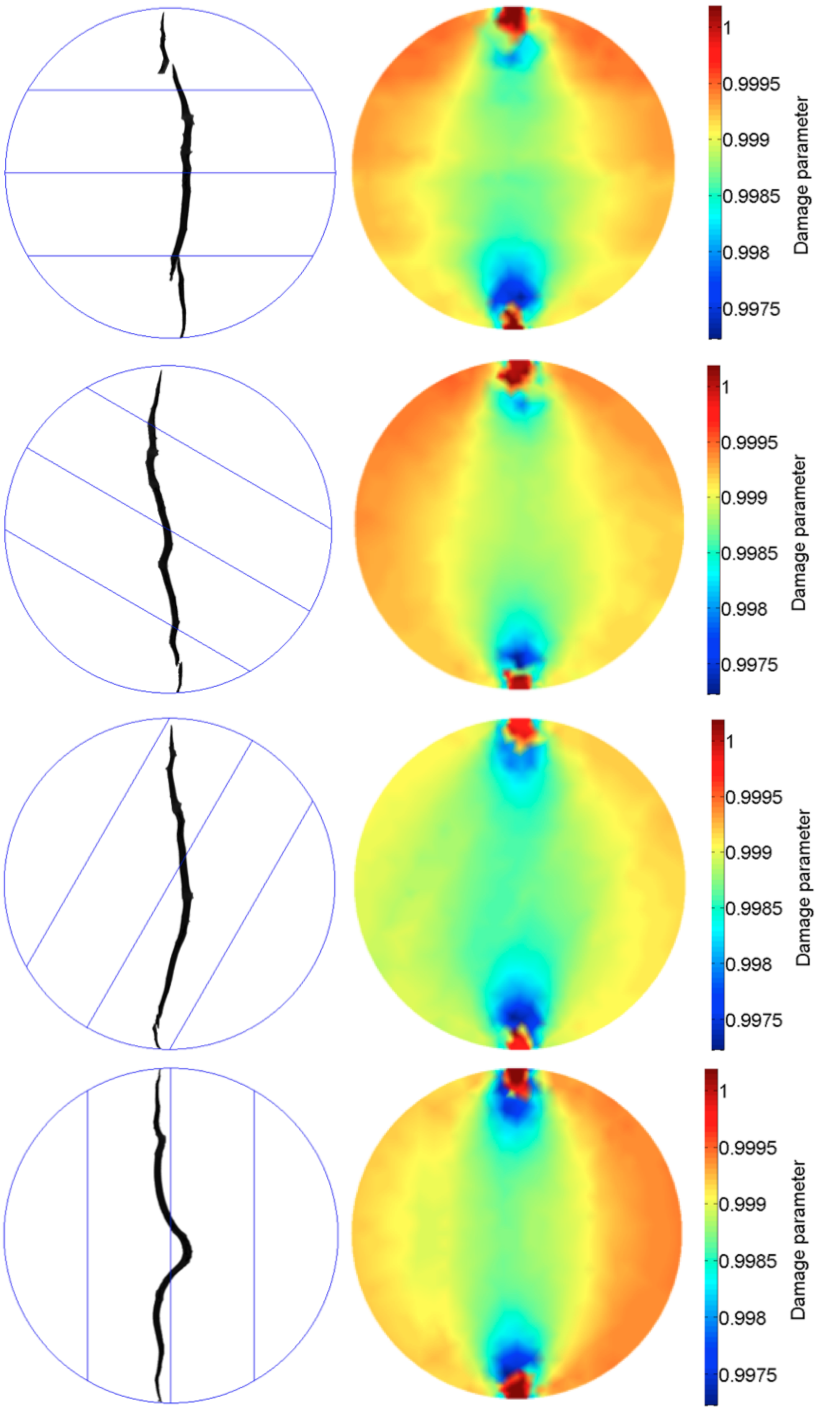

Figure 7.31: Crack paths and damage state for layered materials: bedding at (top to bottom) 90, 60, 30 and 0 degrees.

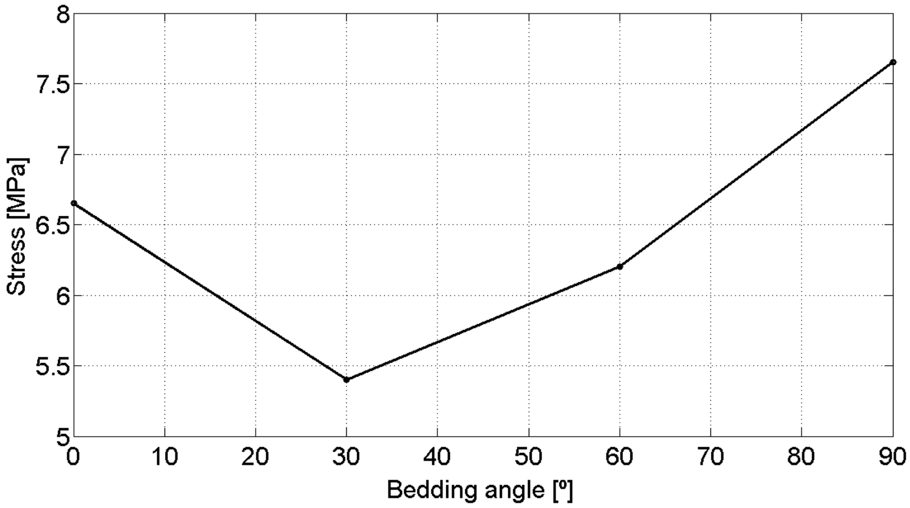

Figure 7.32: Tensile strength variation as function of bedding directions.

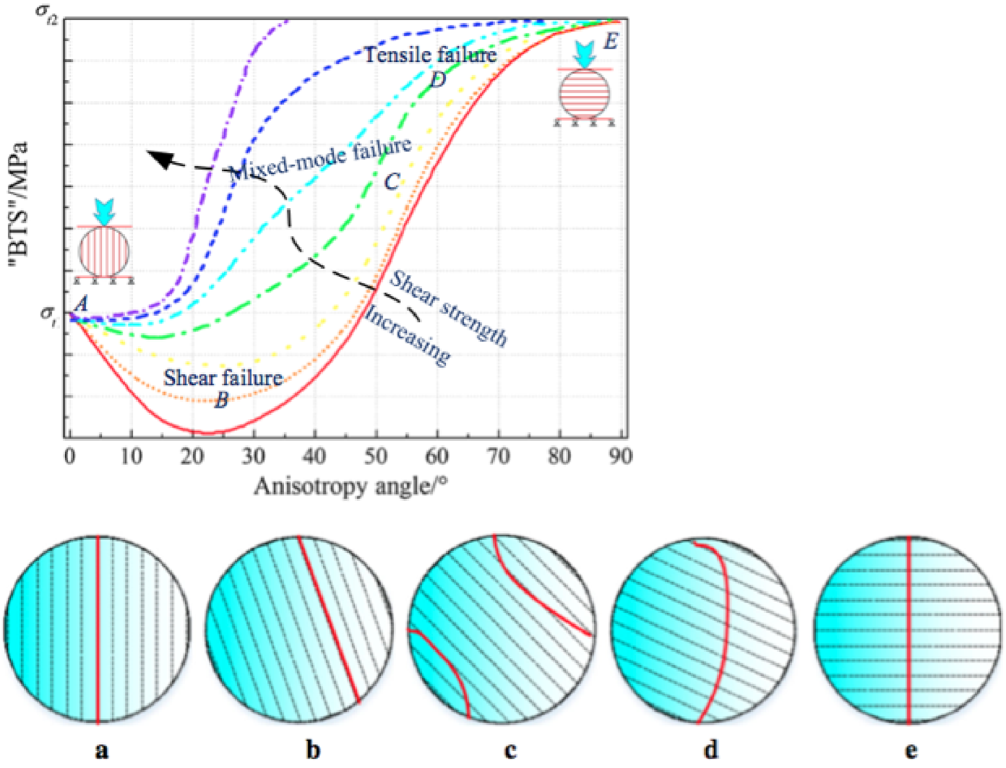

Figure 7.33: Typical behaviour observed in layered rocks tested using the Brazilian disc test (Chong et al., 2017): the final value of tensile strength and the shape of the crack path vary according to the anisotropy angle and the shear strength.

Table 7.7: Input mechanical properties for layered material models for Scenario 1.

Layer	E (GPa)	ν (-)	G (N/mm)
A	30.1	0.26	$2.6 \cdot 10^{-2}$
B	28.1	0.24	$2.4 \cdot 10^{-2}$
C	26.1	0.22	$2.2 \cdot 10^{-2}$
D	32.1	0.28	$3.0 \cdot 10^{-2}$

Table 7.8: Input mechanical properties for layered material models for Scenario 2.

Layer	E (GPa)	ν (-)	G (N/mm)
A	30.1	0.26	$2.6 \cdot 10^{-2}$
B	32.1	0.28	$3.0 \cdot 10^{-2}$
C	26.1	0.22	$2.2 \cdot 10^{-2}$
D	28.1	0.24	$2.4 \cdot 10^{-2}$

Table 7.9: Input mechanical properties for layered material models for Scenario 3.

Layer	E (GPa)	ν (-)	G (N/mm)
A	31.1	0.26	$2.4 \cdot 10^{-2}$
B	34.1	0.28	$2.1 \cdot 10^{-2}$
C	25.1	0.22	$3.0 \cdot 10^{-2}$
D	28.1	0.24	$2.7 \cdot 10^{-2}$

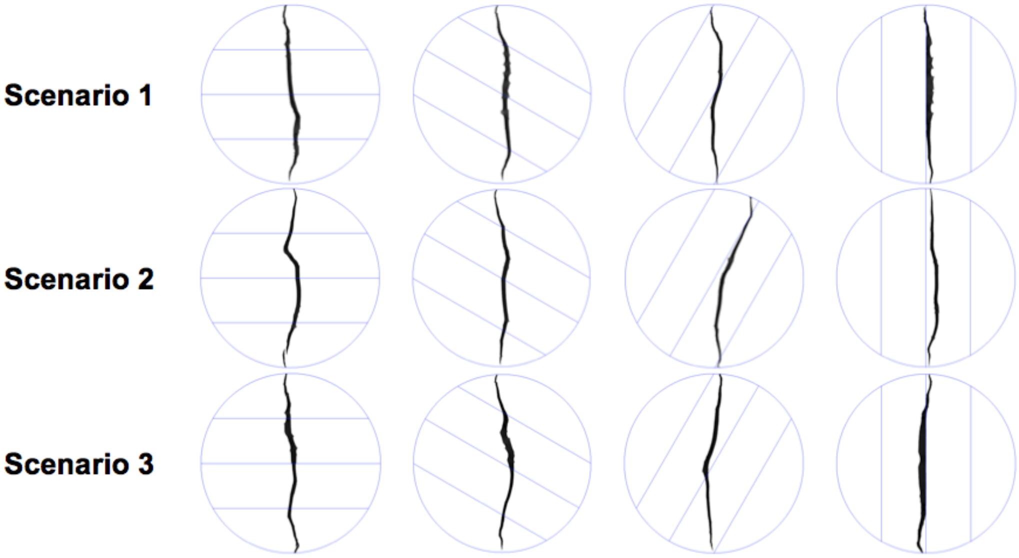

Figure 7.34: Crack patterns obtained for the new three sets of simulations performed on the simplified layered models.

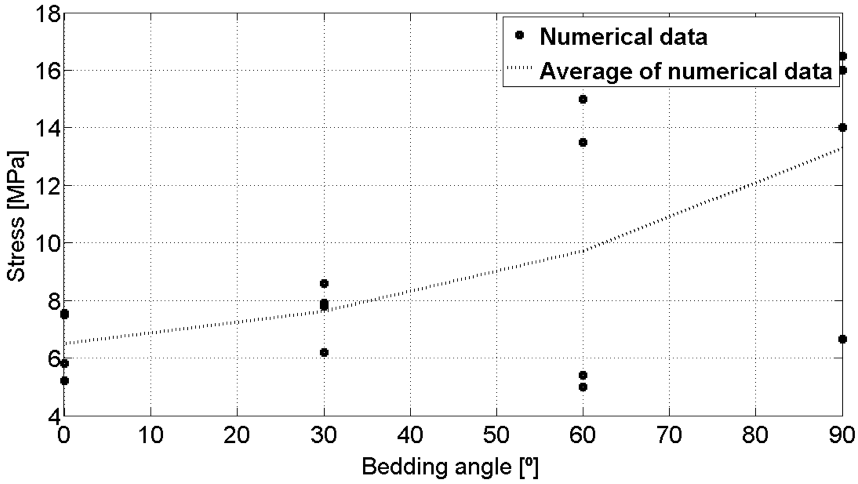

Figure 7.35: Values of tensile strength obtained, for each scenario, for varying values of bedding angle.

7.6.2 Preliminary results of layered specimens with spatial variability approach

In this paragraph the heterogeneity of the specimen is considered in a way, which can be seen as the combination of the two methods described above. In order to consider the layered nature of the material, the stochastic approach explained in the previous paragraph is applied considering correlation length related to the thickness of each layer. This criterion has been applied as the correlation length defines how much the variability is spatially distributed and, therefore, if properly applied for the case of layered materials, can provide a realistic picture of the layers forming the samples. For this example the results obtained considering a correlation length of about 10 mm and standard deviation of 10 % are presented.

Figure 7.36 shows the crack paths achieved through numerical simulation performed to demonstrate the effects of bedding directions on the direction of crack propagation. In these models fracture energy changes across the layers, resembling a heterogeneous layered formation. Figure 7.37 compares the experimental crack pattern from specimen A with the numerical crack pattern obtained for a numerical model with bedding inclination similar to specimen A. The same shape of the crack patterns can be observed. Stress-Strain curves of numerical results compared with the experimental measurement plotted in Figure 7.38 show a good agreement of the results. However, the nonlinear nature on the material (in terms of gradual reduction of the slope of the curve) is not as well captured as when heterogeneity is included by considering pure spatial variability as in section 7.4.

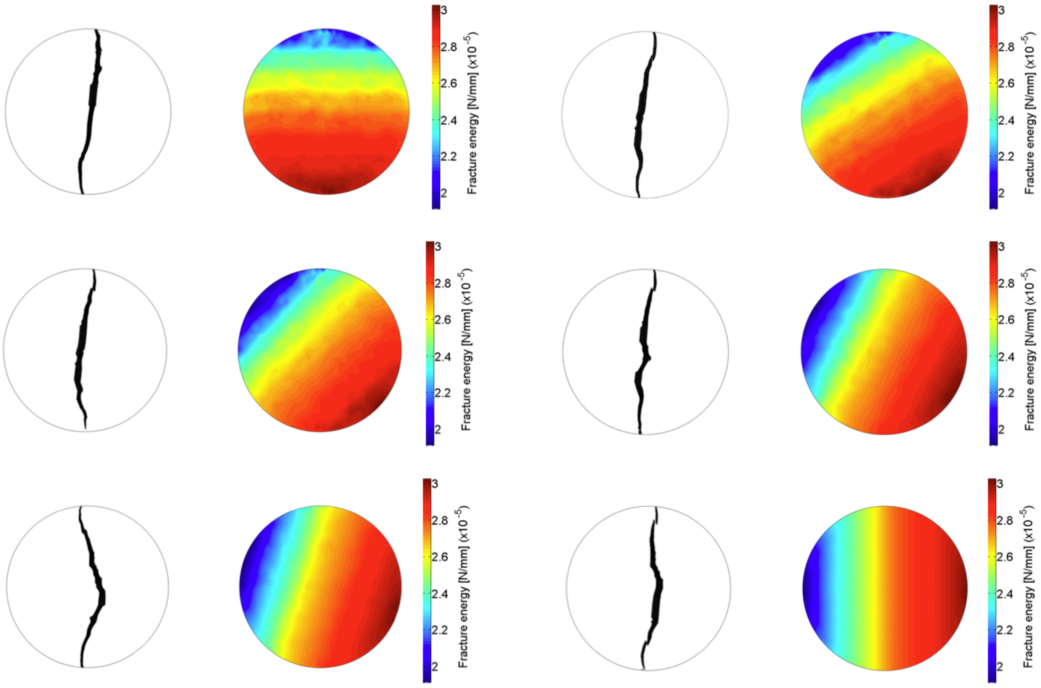

Figure 7.36: Numerical crack patterns obtained with simulations of layered materials with different layers inclinations with respect to horizontal: 0 degrees (top left), 30 degrees (top right), 45 degrees (middle left), 60 degrees (middle right), 70 degrees (bottom left), 90 degrees (bottom right).

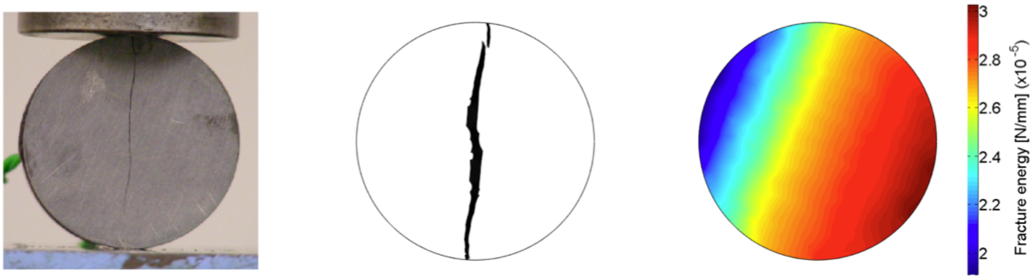

Figure 7.37: Numerical crack path obtained with simulation of layered material (67 degrees) and comparison with the experimental crack pattern.

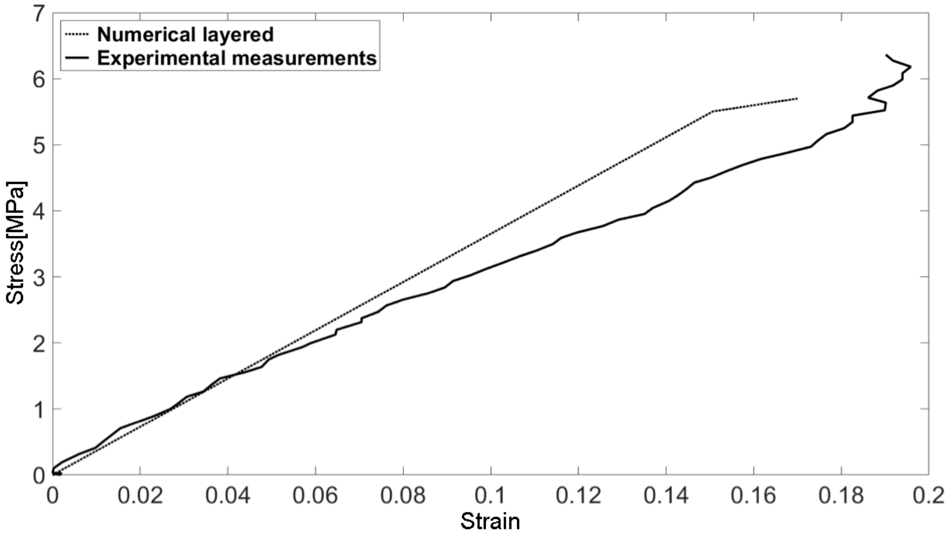

Figure 7.38: Stress-strain cures of experimental data and numerical simulation with layers inclined of 67 degrees.

7.7 Pure mode I fracture: the Dog-Bone experiment

The second case study analysed in this chapter is the case study of the dog bone specimen analysed in the chapter 3. This example has been studied experimentally by Van Vliet (2000). Information about the specimen geometry and the FE discretisation are provided in section 3.5. The problem is analysed under plane strain conditions, as the thickness (z-direction) of the problem is predominant on the other two directions The spatial fluctuation of the random parameters is described by Weibull distribution; furthermore the dimensionality reduction and the dual mesh technique are both employed for this case study.

A value of 0.4 was selected for the length scale ε for this case-study. The mean value for fracture energy, selected from literature (Van Vliet, 2000), is equal to $0.95 \cdot 10^{-1}$ N/mm, and four different values for the standard deviation, including $0.1 \cdot 10^{-2}$, $0.5 \cdot 10^{-2}$, $1 \cdot 10^{-2}$ and $5 \cdot 10^{-2}$, are considered.Two different values of correlation length ($l_c = 1.2$ and 15 mm) are used, corresponding to stochastic field of low and strong spatial autocorrelation.

In order to guarantee mesh convergence, the mesh refinement procedure for those elements subjected to high damage is incorporated for this example as well. The ratio between the correlation length of the random field and ε is kept in the range suggested by previous contributions (Yang and Xu, 2008; Vu and Stewart, 2005). The size of the refined finite element mesh is between one half and one quarter of the minimum correlation length selected for discretising the random fields (Yang and Xu, 2008).

The dimensionality reduction technique described in Chapter 6 and applied to the first case study, is also applied to this example. Figure 7.39 shows how, for a Weibull distributed stochastic field with standard deviation $0.5 \cdot 10^{-2}$ and correlation length of 1.2 mm, the original and reduced order RF meshes provide two spatial distributions of G that, when mapped into the FE mesh, are almost identical.

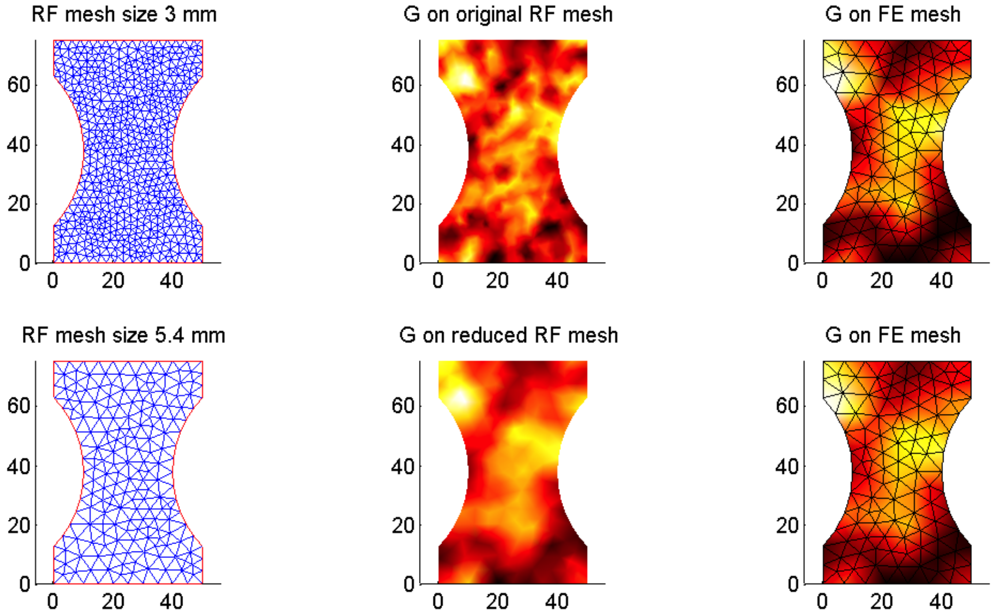

Figure 7.39: Dog bone specimen: application of the dimensionality reduction technique for the generation of a sample having standard deviation $0.5 \cdot 10^{-2}$ and correlation length of 1.2 mm: the size of the RF mesh has been increased from 3 mm to 5.4 mm (with a reduction in the number of elements from 898 to 473), leading to a considerable reduction in the computational cost needed for the generation of the desired sample.

Sample functions of a Weibull distributed stochastic field for standard deviation $5 \cdot 10^{-2}$ and l_c equal to 1.2 and 15 mm are shown in Figure 7.40. It is clear how a higher degree of heterogeneity is given not only by a higher standard deviation in input, but also by a lower correlation length, as observed in the study of Georgioudakis et al. (2014).

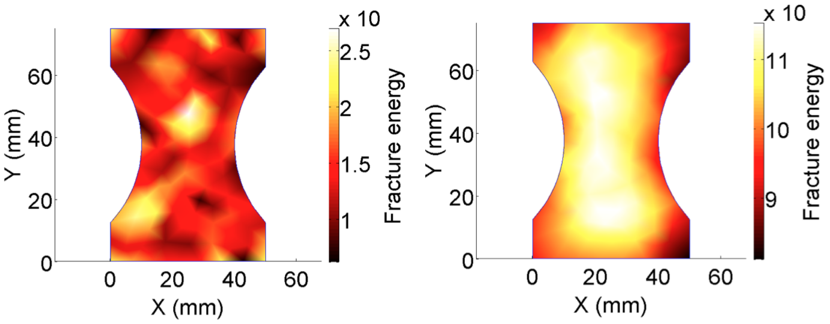

Figure 7.40: Dog bone specimen: randomly selected realisations for standard deviation $5 \cdot 10^{-2}$ and correlation length of 1.2 (left) and 15 (rigth) mm.

Figure 7.41 shows the crack patterns obtained for four realisations with two different degrees of standard deviation ($0.1 \cdot 10^{-2}$ and $5 \cdot 10^{-2}$) and two different correlation lengths (1.2 and 15 mm). It is worth noticing that in the case with higher spatial variability the crack paths show an extremely tortuous and deviated pattern compared to the others. Together with the final crack patterns, in Figure 7.42 also contour plots for damage parameter for different realisations are shown for the time step immediately before the failure.

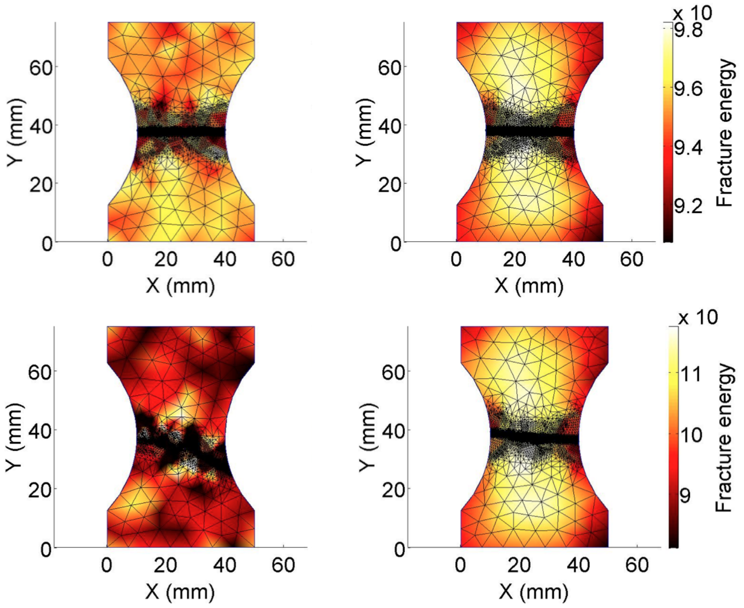

Figure 7.41: Dog bone specimen: crack paths for randomly selected realization and for different values of correlation length and standard deviation. (top left) $l_c = 1.2$, Std Dev $0.1 \cdot 10^{-2}$; (top right) $l_c = 15$, Std Dev $0.1 \cdot 10^{-2}$; (bottom left) $l_c = 1.2$, Std Dev $5 \cdot 10^{-2}$; (bottom right) $l_c = 15$, Std Dev $5 \cdot 10^{-2}$.

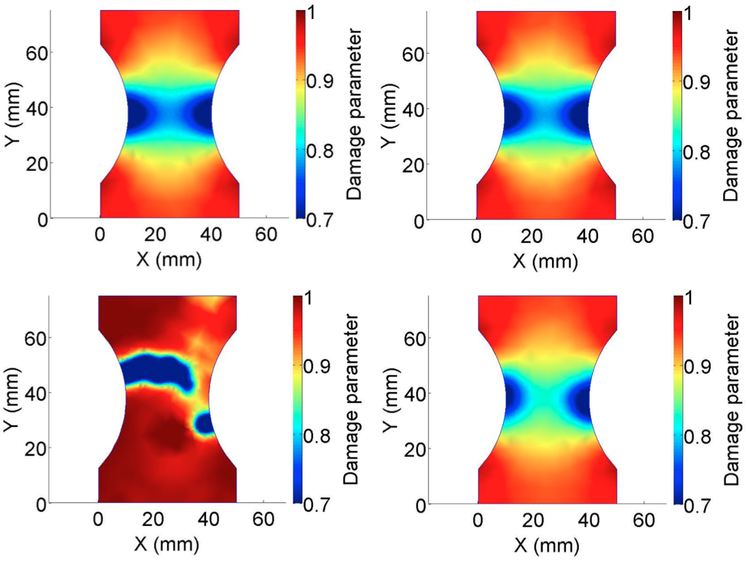

Figure 7.42: Dog bone specimen: damage distribution over the specimen for randomly selected realisation and for different values of correlation length and standard deviation. (top left) $l_c = 1.2$, Std Dev $0.1 \cdot 10^{-2}$; (top right) $l_c = 15$, Std Dev $0.1 \cdot 10^{-2}$; (bottom left) $l_c = 1.2$, Std Dev $5 \cdot 10^{-2}$; (bottom right) $l_c = 15$, Std Dev $5 \cdot 10^{-2}$.

The response variability is computed using MC simulation with sample size equal to 100. The statistical convergence achieved within this number for simulations with $l_c = 1.2$ mm and the standard deviation equal to $5 \cdot 10^{-2}$, is shown in Figure 7.43.

Mean Load-Displacement curves obtained from the MC method corresponding to four different combined values of correlation length ($lc = 1.2$ and 15 mm) and standard deviation ($0.1 \cdot 10^{-2}$ and $5 \cdot 10^{-2}$) are plotted in Figure 7.44. Comparison of the results shows that, compared to the mean curve obtained for analyses with high correlation length and low standard deviation, either the increase of standard deviation of the reduction of correlation length does not lead to a significant variation in the response of the material. However, for both low values of correlation length and high values of standard deviation (which represents the scenario of a highly heterogeneous material) a different mean curve is obtained, especially regarding the value of ultimate deformation on the elastic range.

Figure 7.45 shows different plots for the same value of correlation length ($l_c = 1.2$ mm) and the four different values of standard deviation. Again, differences in the responses of different realisations are appreciable only for high standard deviations despite the low correlation length.

Figure 7.46 shows realisation for the same simulation of both fracture energy and modulus of elasticity when different degrees of cross correlation between variables are considered (0.95, 0.5 and 0). The amount of variation for the fracture energy and modulus of elasticity is the same for the case with full correlation, while they vary randomly when cross correlation is equal to zero. Crack patterns are shown in Figure 7.47 together with the mesh topology after refinement.

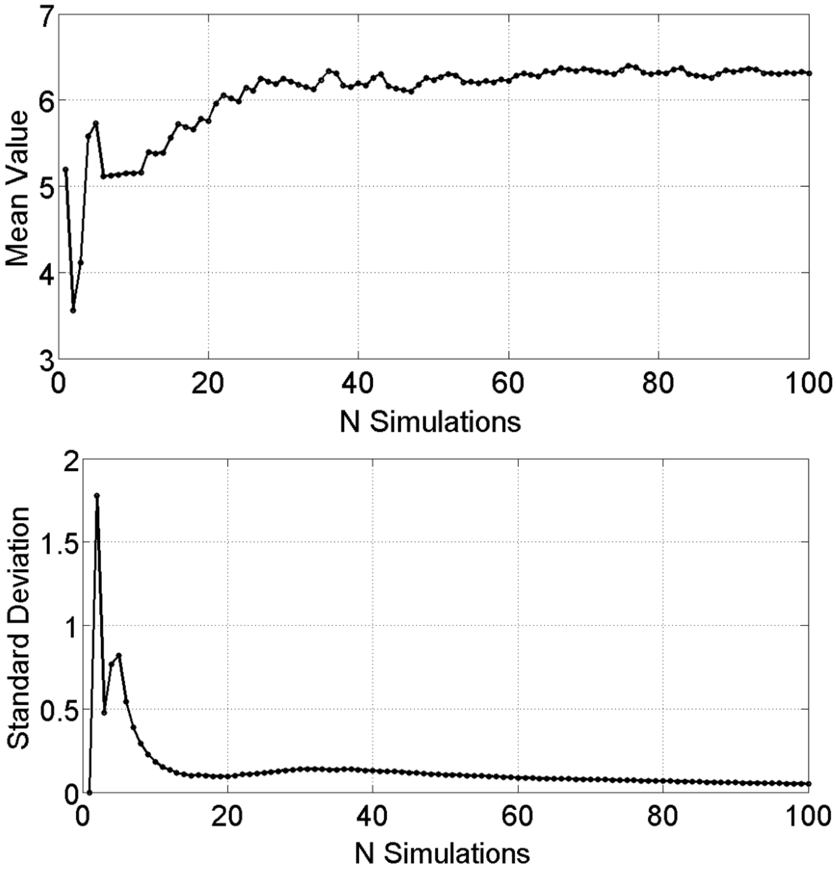

Figure 7.43: Dog bone specimen: convergence for mean (top) and standard deviation (bottom) of the peak load (stochastic fracture energy with standard deviation $5 \cdot 10^{-2}$ and $l_c = 1.2$).

The statistical convergence achieved within 100 MC simulations is illustrated for the three different values of cross correlation in Figure 7.48 where the mean value and standard deviation of the peak load are plotted. Convergence is achieved quicker when partial correlation between variables is considered.
Figure 7.49 shows the load - displacement curves obtained for different simulations with variable fracture energy and modulus of elasticity. Comparison with experi-

mental results is provided. For each case, a small different behaviour for the post peak part of the curve is observed. However, always for an intermediate value of cross correlation the results are slightly closer to the experimental measurements. This conclusion is consistent with the results obtained by Carmeliet and Hens (1994).

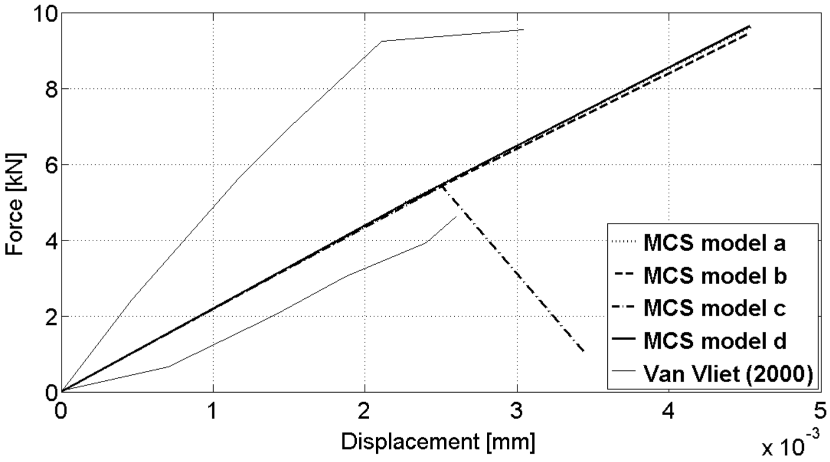

Figure 7.44: Dog bone specimen: load - displacements curves for different values of correlation length and standard deviation. (model a) l_c = 1.2, Std Dev $0.1 \cdot 10^{-2}$; (model b) l_c = 15, Std Dev $0.1 \cdot 10^{-2}$; (model c) l_c = 1.2, Std Dev $5 \cdot 10^{-2}$; (model d) l_c = 15, Std Dev $5 \cdot 10^{-2}$.

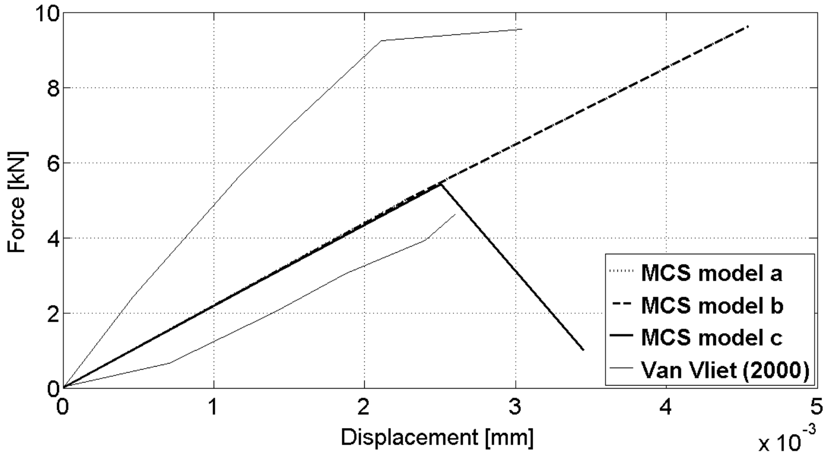

Figure 7.45: Dog bone specimen: load - displacements curves for l_c = 1.2 and different values of standard deviation: (model a) Std Dev $0.5 \cdot 10^{-2}$; (model b) Std Dev $1 \cdot 10^{-2}$; (model c) Std Dev $5 \cdot 10^{-2}$.

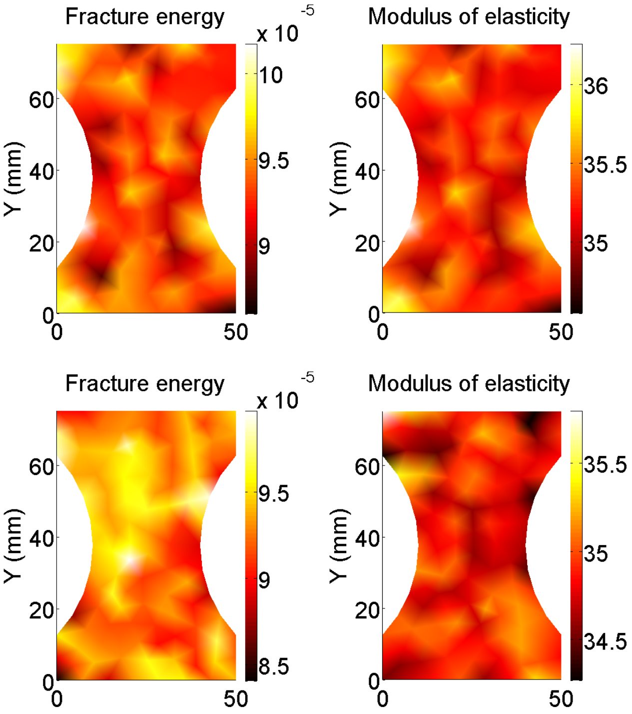

Figure 7.46: Dog bone specimen: randomly selected realisations for fracture energy and modulus of elasticity in case of full correlation (top) and no correlation (bottom) between variables.

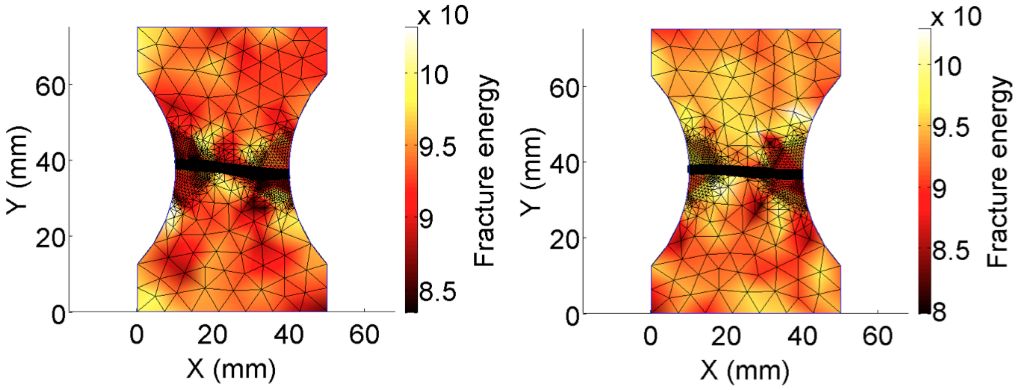

Figure 7.47: Dog bone specimen: crack paths for randomly selected realisation and for different values of cross correlation between fracture energy and modulus of elasticity. (left) Fully correlated variables; (right) uncorrelated variables.

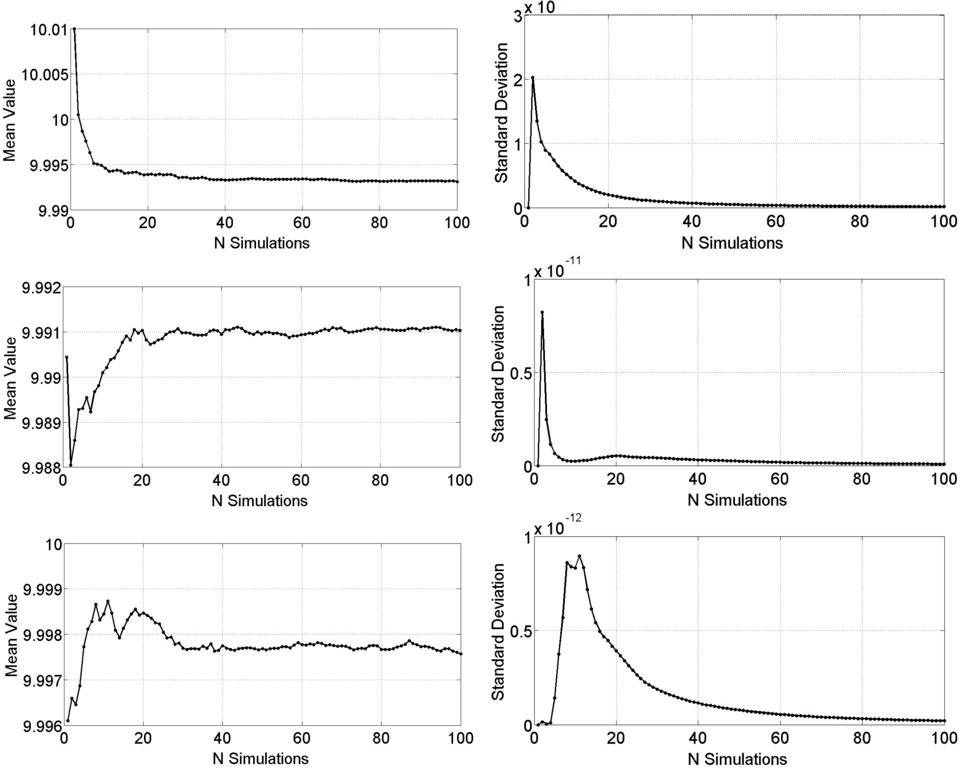

Figure 7.48: Dog bone specimen: convergence for mean (left) and standard deviation (right) of the peak load for different degrees of cross correlation. (top) Fully correlated, (middle) partially correlated and (bottom) uncorrelated variables.

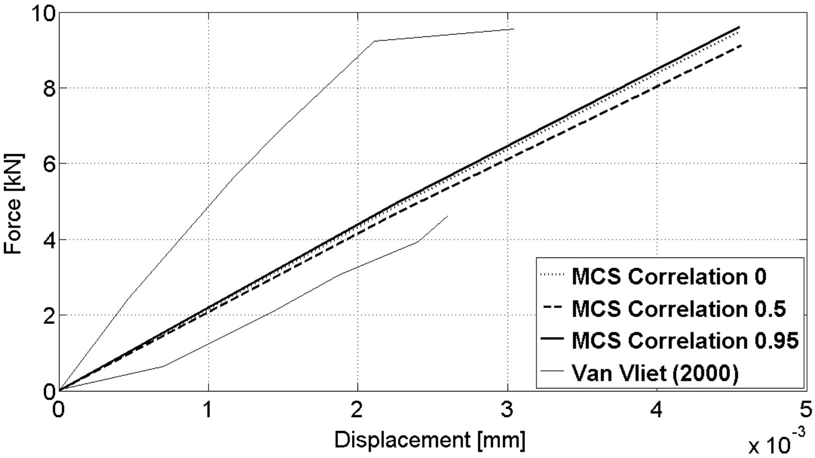

Figure 7.49: Load - displacements plot for the dog bone specimen for realisation with different values of cross-correlation.

Also for this example a summative table (Table 7.10) showing the effect of the dimensionality reduction on the computational cost needed for sampling has been provided. If for the shale specimen the reduction in computational cost has been significative, for this example the difference is still appreciable but not as effective as in the previous example. In fact, considering that the reduction in computational time reduces from 5.2 to 2.0 seconds for the generation of one single sample, if it is considered that convergence of results is achieved approximately within 70 simulations, the overall reduction in computational cost is 225 seconds, almost 4 minutes. This lower effectiveness of this MOR technique for this example may show that this method works better for materials which have finer constituents such as shale rocks.

Table 7.10: Reduction of computational time needed for sampling due to the application of MOR technique to the DogBone example.

RF n. el	RF mesh size	MOR n. el	MOR mesh size	FE n. el	FE mesh size	Sampling time RF	Sampling time MOR
1116	3 mm	346	5.4 mm	194	7.5 mm	5.2 s	2.0 s

7.8 Mixed mode I-II fracture: the Four-Point bending beam and the effect of correlation length

The third case study considered in this chapter is another of the examples analysed in the chapter where smeared and discrete approaches for modelling the propagation of cracks have been compared. The example is the Four-Point Bending SENS Beam. For this example, Yang and Xu (2008) implemented a stochastic approach to include heterogeneity in a numerical framework which considers cohesive elements for modelling of crack propagation. This case study has been chosen because the implementation introduced to realistically reproduce mixed-mode crack opening by differentiating the mechanical response in tension and compression and the implementation used to consider the effect of heterogeneity can be both considered in one example.

In this case study, standard deviation for fracture energy G in input is kept constant, while the effect of different correlation lengths on mechanical response and crack path is analysed. Information about specimen geometry and finite element discretisation are shown in detail in section 3.3. The mean value for fracture energy, selected from Yang and Xu (2008), is equal to $1.5 \cdot 10^{-1}$ N/mm, its standard deviation is equal to 5%, and two different values of correlation length l_c equal to

1.2 and 120 mm are considered (Georgioudakis et al., 2014).

In order to guarantee mesh objectivity, the mesh refinement procedure for those elements subjected to high damage (low values for s) is incorporated.

An example of the spatial distribution of two stochastic fields sampled with the two different correlation lengths is provided in Figure 7.50. Also for this example, the effect of the correlation length on the spatial distribution of the random fracture energy is noticeable. For $l_c = 1.2$ the values for G are more scattered, while values for G in case of $l_c = 120$ are more homogeneously distributed. It has to be mentioned that these represent a range of minimum and maximum values that can be used to clearly show the effect of variation of values for l_c, but in reality values of 120 mm are not usually considered for concrete.

Figure 7.51 shows the crack pattern obtained with the homogeneous model. This crack pattern is used as reference to compare crack patterns obtained with the models in which heterogeneity has been included. In fact, the crack pattern of Figure 7.51 is very smooth and without sharp deviations, which is what is expected to find in fractured concrete.

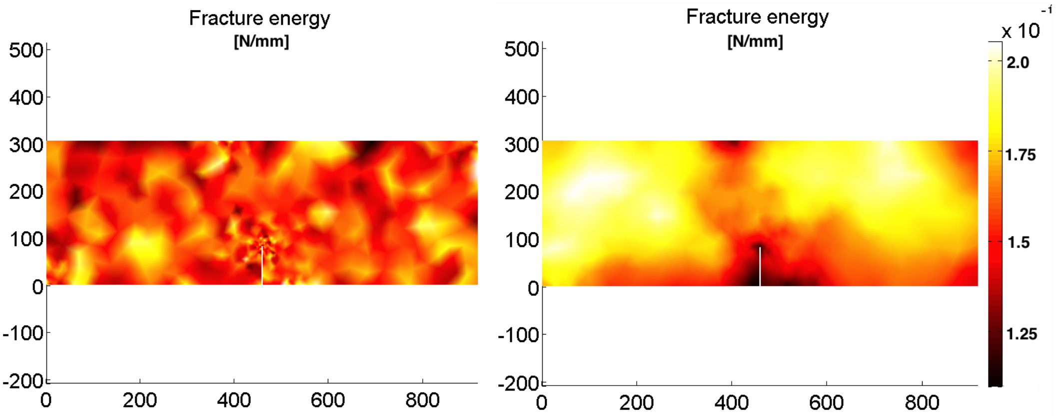

Figure 7.50: Fracture energy distribution over the model: low (left) and high (right) correlation length.

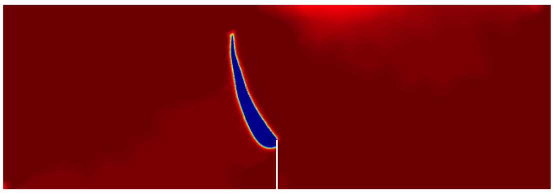

Figure 7.51: Damage zone obtained with analysis performed with the homogeneous model.

Figure 7.52 shows the crack paths obtained from 6 of the models in which l_c=120. The crack patterns obtained differ the one from the other and are slightly more tortuous if compared to the crack path of Figure 7.51, but with small appreciable differences in terms of shape and extent. Fig. 7.53, on the other hand, shows four eight different crack patterns obtained from 8 of the 150 simulations run for the case with $l_c = 1.2$. The crack patterns obtained have more tortuous nature if compared to the one shown in Figures 7.51 and 7.52. Fractures obtained vary in shape, inclination and curvature.

A comparison between crack patterns obtained with the homogeneous model, one of the heterogeneous with lower correlation length and the range of cracks obtained experimentally is provided on the left of Figure 7.54. Here is evident how the effect of heterogeneity for this case study provides a more realistic picture in terms of direction and extent of cracks. Furthermore, on the right of Figure 7.54 a small branch (for some of the crack patterns obtained) when low correlation length is considered can be observed. This is an interesting phenomenon to highlight. In fact, in literature crack branching is recognised to happen for problems in which a dynamic load is applied to the system, while in the simulations carried in this study load is applied in quasi-static conditions. It is in fact well recognised that the classical Griffith theory does not include the possibility of crack branching for problems with load applied in quasi-static conditions, but it is also known that the application of Γ-Convergence theory to approximate fractures by means of scalar fields makes the variational model capable of reproducing crack branching phenomena (Nguyen et al., 2015). This, in combination with the inclusion of heterogeneity in the model, generates two branches. The phenomenon can be indeed attributed to the possibility that crack advancement criterion can be satisfied at the same step of analysis at two different points (due to the presence of weak local zones). For small lengths, therefore, crack may advance in two different paths, but the final crack obtained has no branches.

In Figure 7.55 the load - CMSD (Crack Mouth Slide Displacements) curve for homogeneous and heterogeneous models are plotted and compared to the experimental results. The curve with the highest value of force recorded is the one calculated from the homogeneous model. For the two curves obtained with the MCS method it can be observed that for both of them a lower value of peak load is recorded and, despite the different values of l_c, the overall average peak load is approximately the same. This behaviour is in accordance with what has been reported by Yang et al. (2009), where for the same standard deviation and different values of l_c haven't been recorded significant differences in terms of peak load.

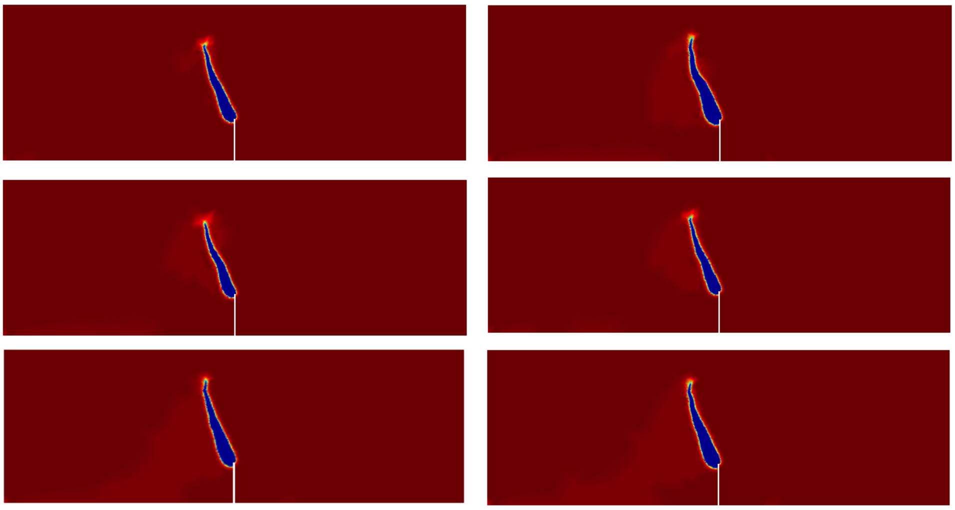

Figure 7.52: Damage zone obtained with 6 of the heterogeneous models with a high correlation length.

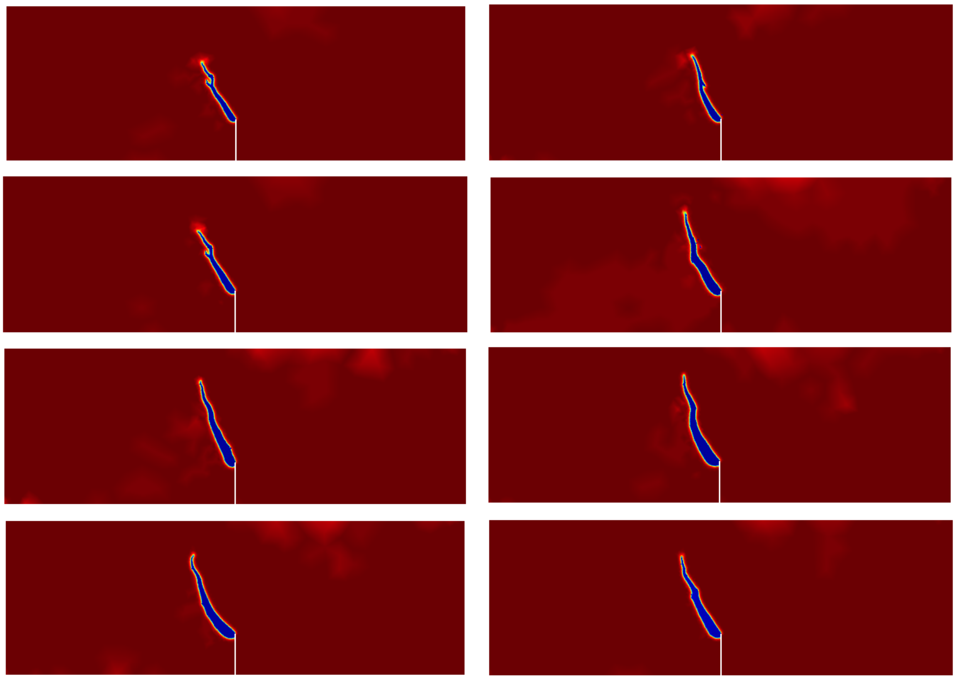

Figure 7.53: Damage zone obtained with 8 of the heterogeneous models with a low correlation length.

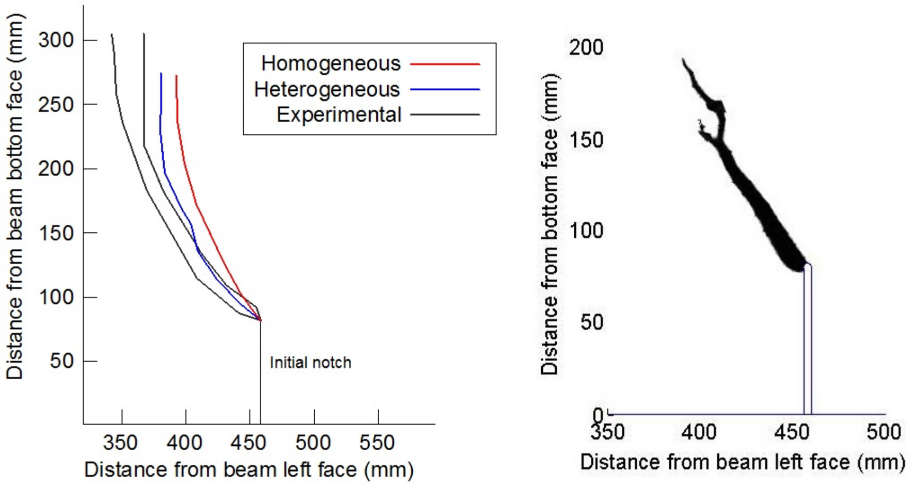

Figure 7.54: Comparison between crack paths obtained with homogeneous and one of the heterogeneous models and final comparison with the experimental scatter (left). Crack pattern obtained for one of the heterogeneous models with low correlation length: crack branching phenomena are recorded, due to the high heterogeneity of the specimen (right).

However, as for the previous case study, it is worth noting that the model seems to be more capable of realistically reproducing the behaviour recorded by the experimental measurements in the elastic region of the plot; further discussions about the mechanical response in peak and post-peak phase are needed after more analyses with different values of standard deviation and correlation length.

For the homogeneous model, it can be observed that the peak value is realistically estimated, but the maximum elastic strains are overestimated. This behaviour is slightly improved for $l_c = 1.2$ mm, while is significantly improved for $l_c = 120$ mm. For what the post-peak behaviour is concerned, none of the three curves are capable of fully reproduce this section. As for the previous example, this is related to the fact that the variational model employed in this work and the formulation of the stored energy function W are able to reproduce the behaviour of fully brittle materials, while concrete is usually considered and quasi-brittle material. However, a slight improvement can be observed is the curve obtained with $l_c = 1.2$ mm.

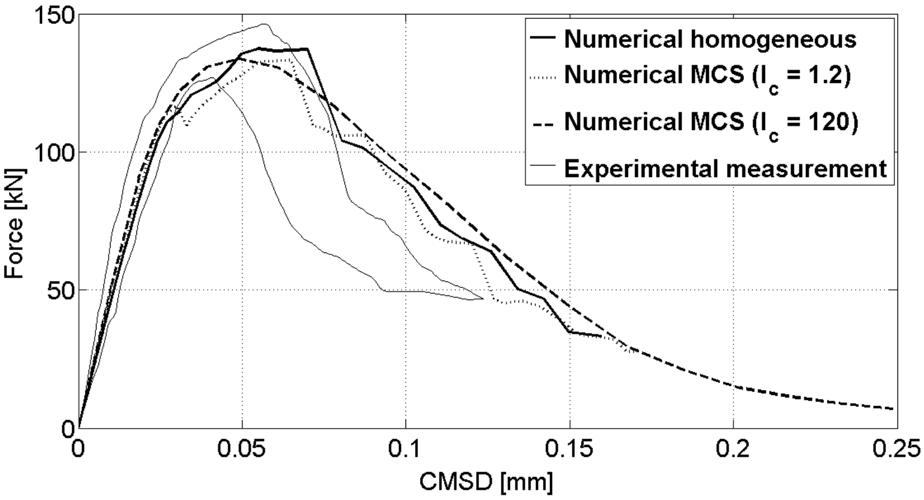

Figure 7.55: Load-CMSD curves: comparison with the experimental measurements between curves obtained from the homogeneous model and the mean curve obtained from the MCS analyses of the two heterogeneous models.

Also for this case convergence of the results has been studied and analysed for the mean value of the peak load, as shown in Figure 7.56. It can be noted that for $l_c = 120$ acceptable convergence is achieved after 60 to 65 simulations. Furthermore, for smaller correlation lengths ($l_c = 1.2$ mm) in order to achieve an acceptable convergence more simulations are required. The mean value of the peak load stabilises after approximately 120 simulations. Again, this behaviour is the same recorded by Yang et al. (2009): the authors showed that for the same standard deviation and different l_c, convergence of results is achieved faster for higher values of l_c.

In Figure 7.57 convergence of results in terms of variance of the peak load is reported. It can be observed that, as expected, convergence is achieved faster for $l_c = 120$ mm. This response makes the methodology employed in this study capable to capture the real mechanical behaviour of concrete. Again, this behaviour is consistent with the results reported by Yang et al. (2009), where convergence is achieved faster for higher values of l_c.

For this example, convergence in terms of variance of the displacements recorded at the loading point at the peak load is calculated and reported in Figure 7.58.

It can be observed that for both low and high values of l_c convergence is achieved, but for the case with $l_c = 120$ convergence is achieved quicker, after approximately 20 simulations.

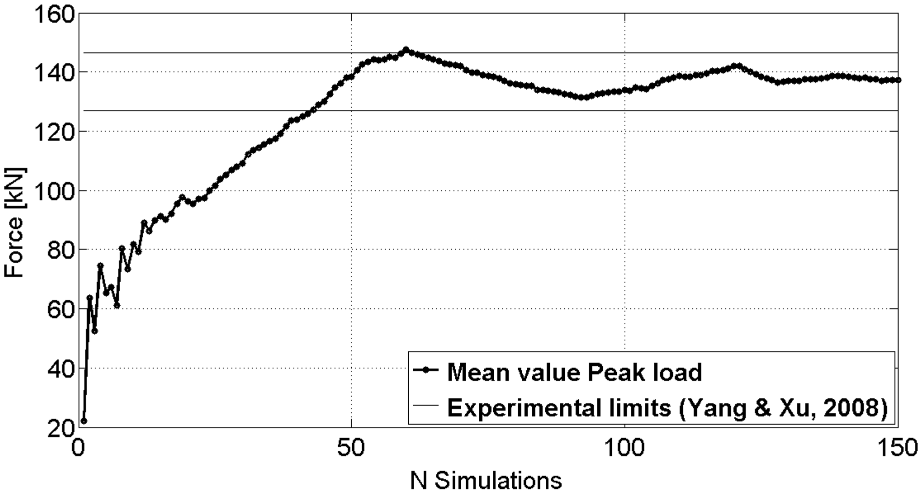

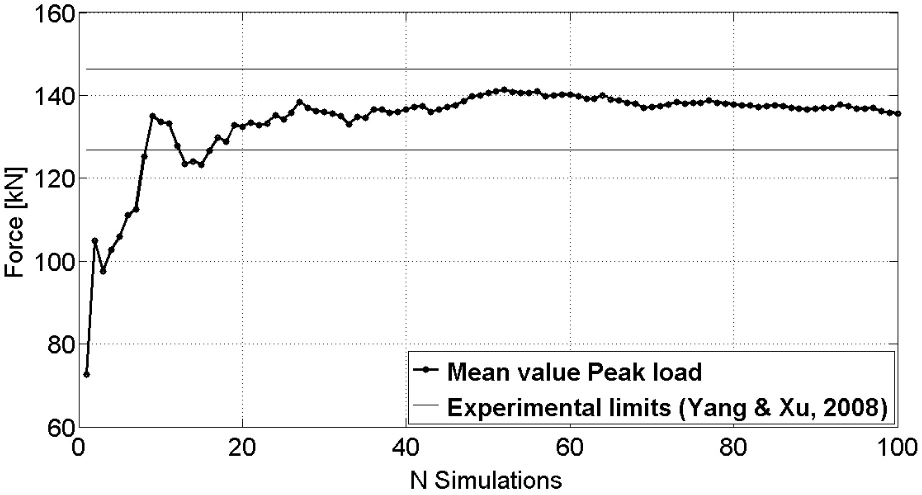

Figure 7.56: Convergence of the mean value of the peak load for the heterogeneous models with: (top) $l_c = 1.2$ mm and $l_c = 120$ mm (bottom).

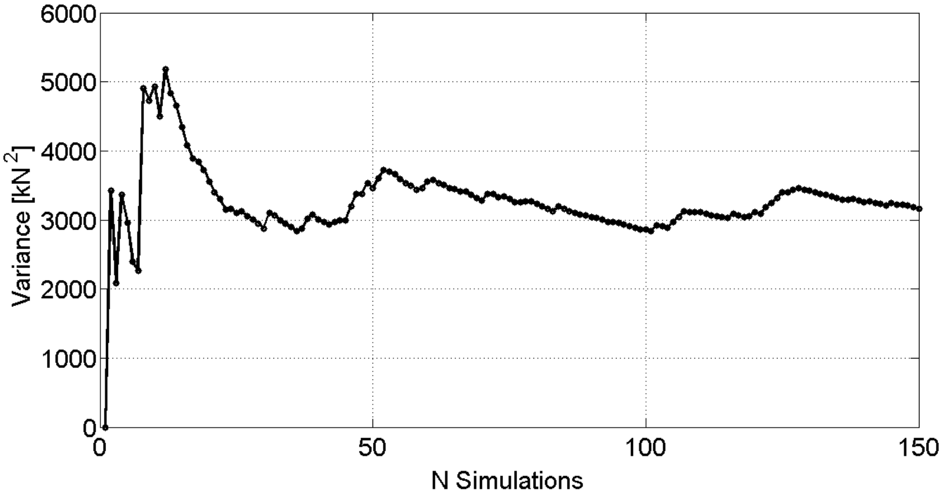

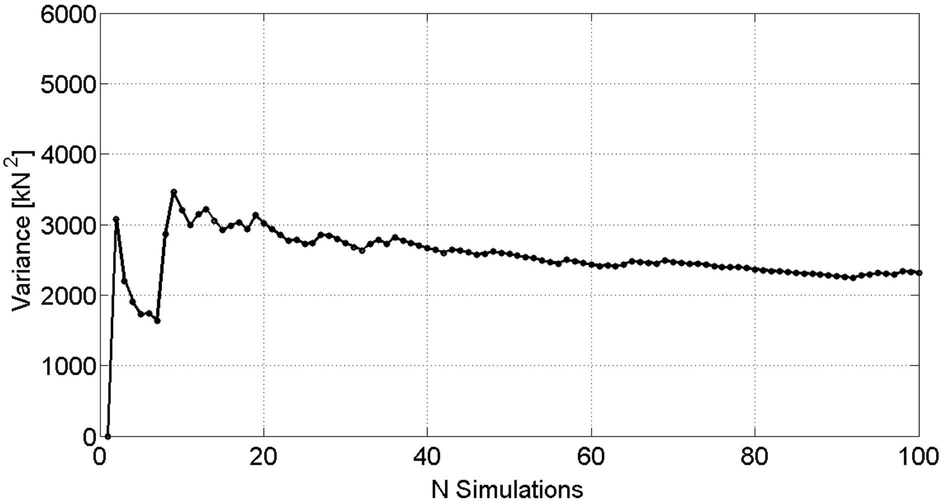

Figure 7.57: Convergence of the variance of the peak load for the heterogeneous models with $l_c = 1.2$ (top) and $l_c = 120$ (bottom).

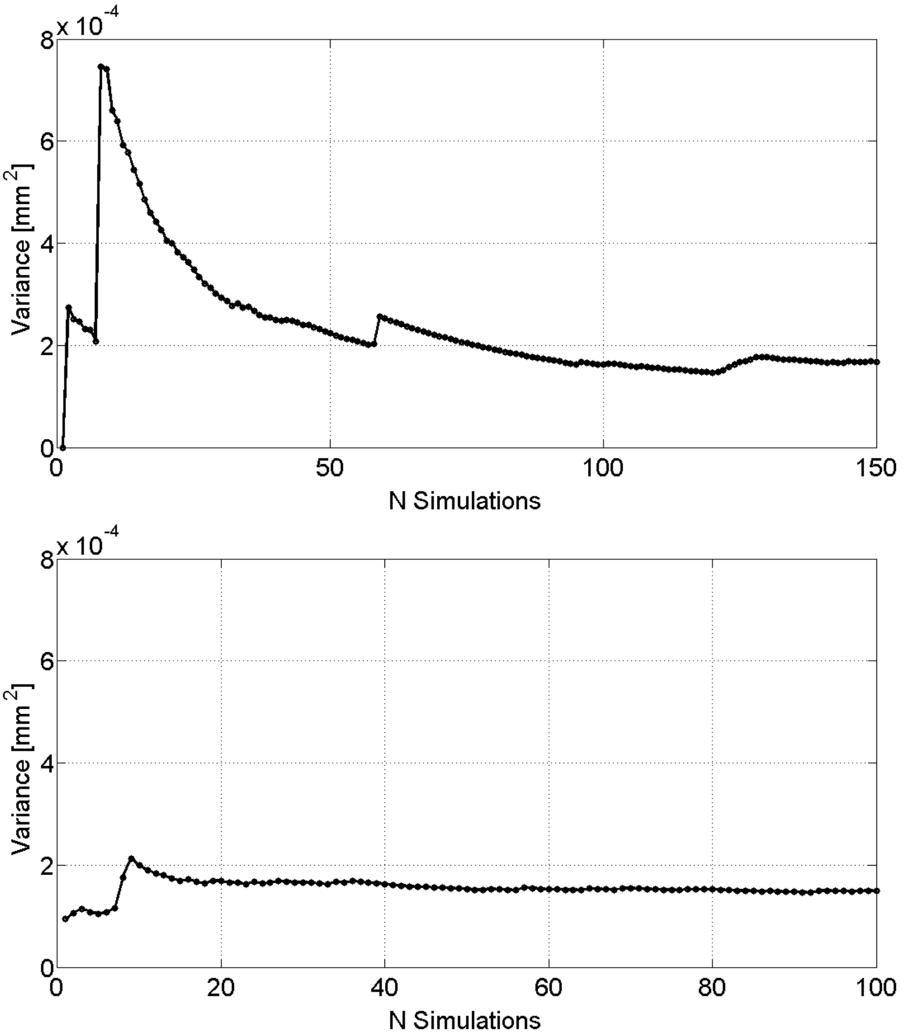

Figure 7.58: Convergence of the variance value of the displacements at the loading point for the heterogeneous models with $l_c = 1.2$ (top) and $l_c = 120$ (bottom) correlation.

Finally, also for this case study a summative table (Table 7.11) proving the effect of the dimensionality reduction on the computational cost needed for sampling has been included. If for the shale specimen the reduction in computational cost has been significative and for the dogbone specimen less important, for this example the difference is appreciable and effective, but the overall absolute time needed for dimensionality reduction is still high. The reduction in computational time reduces from 921.3 to 393.1 seconds for the generation of one single sample, which considering that convergence of results is achieved after 120 simulations, the overall reduction in computational cost is approximately 17 hours. This result is a significant improvement, but it should be noted that, however, for the reduced order

RF mesh the total time needed for generation of 120 samples is of approximately 13 hours. This shows that the technique needs further improvements.

Table 7.11: Reduction of computational time needed for sampling due to the application of MOR technique to the Four-Point bending shear beam example.

RF n. el	RF mesh size	MOR n. el	MOR mesh size	FE n. el	FE mesh size	Sampling time RF	Sampling time MOR
62288	3 mm	26834	5.8 mm	1256	40 mm	921.3 s	383.1 s

Chapter 8

Conclusions and future work

8.1 Discussion of the results

The research conducted and discussed in this thesis aimed to develop novel numerical and computational methodologies for modelling of crack propagation of heterogeneous materials. The main focus of this research has been in the development of a computationally efficient and reliable methodology able to realistically reproduce the failure of spatially varying (concrete) and layered (shale rocks) quasi-brittle materials.

The first part of this work was dedicated to the study and comparison of different methodologies for modelling of crack propagation. Two different numerical models have been analysed and compared: the first, which employes a phase field model for a smeared representation of fractures, and the second, which uses a discrete representation of cracks. Using three different examples, selected in order to highlight the capability of each of the two model in reproducing different failure modes, has been observed that both frameworks provided good results in terms of both prediction of crack paths and material resistance. Nevertheless, in order to make the model based on the smeared approach fully capable of reproducing mixed-mode crack opening conditions, a first implementation able to distinguish the mechanical responses between elements with positive and negative Jacobian, has been introduced. Thanks to this first implementation, to the computational cost and due to the capability of the method based on the smeared approach of automatically capturing the crack initiation point, it has been decided to execute the incorporation of heterogeneity on this numerical framework. However, it must be highlighted that this implementation, as the results showed, needs further improvements, as the main crack is identified, but some differences between experimental and numerical results are found.

After a review of the two most widely used approaches used for numerical modelling of heterogeneities (multiscale modelling and stochastic approach), it has been decided to develop a stochastic approach to estimate the values of mechanical properties able to incorporate the effect of material heterogeneity in the phase field model using probability functions. It has been also decided to develop a methodology based on a non-Gaussian Weibull distribution, as it has been proved to be the distribution that most accurately describes the heterogeneities of brittle and quasi-brittle materials. Both monovariate and bivariate distributions have been considered for this study: fracture energy G has been selected as the mechanical property with heterogeneous nature for the monovariate case, and modulus of elasticity E is also considered for the bivariate. The effect of correlation lengths has also been included in order to consider the material length scale. Monte Carlo Simulation method has been also used for the sample realisation and post-processing phases.

In order to reduce the computational effort related to the generation of samples for G and E, a non-linear Model Order Reduction technique has been also developed and applied. This methodology, which takes into account the heterogeneity spatial distribution, is capable of reproducing with very good accuracy an equivalent and dimensionally reduced representation of the original random field, improving therefore the computational efficiency of the overall algorithm.

The proposed methodologies have been applied to reproduce numerically the mechanical response of samples made of two different materials: shale rock and concrete. Also, different loading conditions have been tested. For shale rock, highly heterogeneous and anisotropic material, before applying the developed methodology, preliminary numerical analyses have been performed on five specimens tested experimentally with Brazilian disc tests. These analyses tried to reproduce the effect of different bedding directions and materials inclusion on the values of material resistance and on the crack patterns, by assigning different values of G to different layered subdomains modelled numerically.

The stochastic methodology has been then applied to one of the five samples available experimentally: the numerical results, obtained including a sensitivity analysis and therefore considering different values of standard deviation in input, showed an excellent agreement with the experimental measurements, and, after a comparison with results obtained using a Gaussian K-L approach for samples realisations, has been proved that Weibull distribution allows a relatively quick convergence of results. Furthermore, the dimensionality reduction technique allowed to reduce drastically the computational effort needed in sampling phase.

Two further strategies have been used to include more explicitly the material laminar nature: (i) different values for mechanical properties have been assigned to each layer of the numerical model and (ii) mechanical properties have been defined as random fields with a correlation length equal to the thickness of the layers of the numerical model. For the verification analysis different values of E, Poisson's ratio ν and G were given to each layer, and different bedding directions were also. Damage has been found to localise between the interface of different layers and crack patterns have shown tendency to move through the layers with lower toughness. The maximum value of resistance was obtained for horizontal layers, while the minimum was obtained for inclinations between 30 and 60 degrees.

The second and third examples are case studies which study the failure behaviour of concrete in mode-I failure and mixed-mode failure. For both cases, can be again observed that the application of the methodology developed in this research provides reliable and realistic results. The effect of different standard deviations and different correlations lengths has also been analysed and has been proved that for higher values of correlation length, convergence is achieved more quickly. Also, the dimensionality reduction technique allowed for these case studies to reduce the overall computational effort. However, it should be noticed that the reduction in computational cost seems to be more effective for materials with very fine constituents (shale rocks), while for materials such as concrete with larger size constituents this methodology would need to be further developed.

Some of the limitations highlighted in this thesis (especially in chapter 3) and recalled in this chapter can find their resolution and extension (which create potential development for possible future works) in methods such as XFEM and IGA. XFEM can be used in order not to restrict damage evolution and propagation only to the elements used to discretise the domain and to alleviate those issues related to insufficient mesh refinement. In fact, despite the mesh refinement technique included in this work works efficiently, the representation of crack can be improved. Observing the shape of the fracture obtained for the homogeneous model, in fact, it seems that, despite quite smooth, the crack pattern shows some mesh dependence that could potentially find its resolution with the use of XFEM. IGA can be useful in sense of accurateness of results and error minimisation: in fact, the use of k-refinement in addition to the classical h- and p- refinements, would provide results with lower values for error estimators. But in order to asses this aspect, it would be necessary to have values for residuals available pre- and post-application of B-splines shape functions typical of IGA.

The results discussed above have been obtained using a 2-dimensional numerical framework. However, in order to be able to extrapolate these findings in a three-

dimensional configuration a series of aspects should be considered:
- in terms of numerical modelling of crack propagation, it should be noted that, generally speaking, an increase in terms of computational cost would be recorded due to obvious reasons such as higher dimension of stiffness matrices and higher number of elements to be processed and refined when the crack propagation is identified;
- larger covariance matrix and sample vectors would also be identified, leading to a further increase in computational cost for both sampling phase and dimensionality-reduction phase;
- especially for examples similar to the last two, it must be identified an alternative method for dimensionality reduction in order to optimise its use and don't make it unfeasible from the computational point of view;
- the layered nature of materials should be properly taken into account by observing how bedding direction varies along the three principal directions.

8.2 Future work

The research conduced and reported in this thesis provides also a series of possible future work. The following work is therefore recommended.

1. The developed methodology can be applied for modelling of heterogeneities in the numerical framework for crack propagation based on the configurational force method; however, it must be considered that the configurational force method involves the motion of nodes forming the FE domain and, therefore, a strategy for the estimation of the random mechanical properties of each node with new positions must be included to keep the accuracy of the description of the random fields.

2. Interface element zones can be introduced to include the effect of thin and weak planes on shale rocks. However, this implementation requires either direct reduction for values of G and E for weak layers, or more sophisticated models, like the one developed by He and Afolagboye (2017), where more parameters can be considered to model accurately the real behaviour of weak layers.

3. The constitutive model of the phase field approach could be extended to include the anisotropic behaviour of transversely isotropic materials suck as shale rocks. This modification can be conducted on the deterministic numerical framework first and, successively, on the model implemented by the

stochastic approach.

4. The existing implemented framework for crack propagation on heterogeneous materials can be extended to multi-physics problems (e.g. hyrdofracture and thermofracture) to apply the developed methodology to a wider range of case studies such as fracking.

Appendix A

Codes

In this appendix the most important section of the code developed and implemented are provided with the support of additional comments.

A.1 Smeared approach: alternate problem resolution

In the next to subsections the main subroutines used for the resolution of the deformation and damage problems are provided. Please note that have been included those subroutines where the differentiation between tension and compression (described numerically in Chapter 3) has been implemented.

A.1.1 Deformation problem

```
% mu, lambda: lame' moduli
% k_eps:       regularisation parameter
% boundary:    boundary conditions
% p1: initial position FE nodes
% pFE: current position FE nodes
% edges: edges ID of FE domain
% trian: finite element ID
% def0: initial position FE nodes
% damage: values for damage parameter s

num_point=size(pFE,2);
force0=p1+def0;
J_index=0; num_el=size(trian,2);
stif_mat=zeros(16,num_el);
```

```
a_mat = zeros(2,1);  f_vec = zeros(2,1);
B_left=zeros(3,3,num_el);
identity=zeros(3,3);
Jacob=zeros(1,num_el);
Identity_mat=zeros(3,3,num_el);
st_el=zeros(2,2,2,2,num_el);
identity(1,1)=1; identity(2,2)=1; identity(3,3)=1;
for el=1:num_el
    Identity_mat(:,:,el)=identity;
end
f_col=[force0(1,:)';force0(2,:)'];
[defFx,defFy]=pdegrad(p1,trian,f_col);
F_mat=zeros(3,3,num_el);
F_mat(1,1,:)=defFx(1,:); F_mat(2,1,:)=defFx(2,:);
F_mat(1,2,:)=defFy(1,:); F_mat(2,2,:)=defFy(2,:);
F_mat(3,3,:)=1;
Jacob(:)=F_mat(1,1,:).*F_mat(2,2,:)-F_mat(2,1,:).*F_mat(1,2,:);
%%%%%%%%%%%%%%%%%%%%%%%%%%%%%%%%%%%%%%%
% thension-compression implementation %
%%%%%%%%%%%%%%%%%%%%%%%%%%%%%%%%%%%%%%%
J_index=find(Jacob<1);
damage_Jacob=damage; damage_Jacob(J_index)=1;
damage_coeff=damage_Jacob.^2+k_eps;
%%%%%%%%%%%%%%%%%%%%%%%%%%%%%%%%%%%%%%%
for el=1:num_el
    B_left(:,:,el)=F_mat(:,:,el)*F_mat(:,:,el)';
end
%this is where all the tensors are calculated
[C_stiff,TTens]=elast_tensor(mu,lambda,trian,B_left,Jacob,Identity_mat);
for i=1:num_el
    st_el(:,:,:,:,i)=damage_coeff(1,i).*C_stiff(:,:,:,:,i);
end
stif_mat = stiffness_arrangement(st_el);
% global stiffness matrix assembly
```

```
[K,M,FFE,Q,G,H,R]=assempde(boundary,pFE,edges,trian,stif_mat,a_mat,f_vec);
Tcauchy2=zeros(4,size(trian,2));
for i=1:num_el
    TCauchy(:,:,i)=damage_coeff(1,i).*(TTens(:,:,i));
end
Tcauchy2=vector_rearrangement1(TCauchy);
FFE=zeros(2,size(pFE,2));
for n_el=1:size(trian,2)
    for ip=1:3
        px(ip)=pFE(1,trian(ip,n_el));
        py(ip)=pFE(2,trian(ip,n_el));
        pt=[px;py];
    end
    Jdet=(-pt(1,1)+pt(1,2))*(-pt(2,1)+pt(2,3))-(-pt(1,1)+pt(1,3))*(-pt(2,1)+pt(2,2));
    Mat1=zeros(4,2,3);
    for ip=1:3
        Mat1(1,1,ip)=pt(2,mod(ip,3)+1)-pt(2,mod(ip+1,3)+1);
        Mat1(2,1,ip)=pt(1,mod(ip+1,3)+1)-pt(1,mod(ip,3)+1);
        Mat1(3,2,ip)=Mat1(1,1,ip);
        Mat1(4,2,ip)=Mat1(2,1,ip);
    end
    Mat1=Mat1.*Jdet^(-1);
    for ip=1:3
        f_m(:,ip)=(Mat1(:,:,ip)'*Tcauchy2(:,n_el))*(Jdet)/2;
    end
    for ip=1:3
        for a=1:2
            FFE(a,trian(ip,n_el))=FFE(a,trian(ip,n_el))+f_m(a,ip);
        end
    end
end
FFE=-[FFE(1,:),FFE(2,:)]';
delta=assempde(K,M,FFE,Q,G,H,R);
```

```
delta=[delta(1:num_point,1)';delta((num_point+1):2*num_point,1)'];
f_solution=def0+delta; % displacements
pFE=pFE+delta; % mesh pos update
```

A.1.2 Damage problem

```
% bcBoundary_s: bc for damage problem
% mu, lambda: lame' moduli
% gamma: fracture energy
% eps: epsilon (material length scale)
% node: FE nodes
% edg: FE edges ID
% triang: finite elements ID
% ux, uy: current displacements in x and y dir

num_el=size(triang,2);
displ=[ux;uy];
column_disp=[displ(1,:)';displ(2,:)'];
[Ux,Uy]=pdegrad(node,triang,column_disp);
Identity=zeros(3,3,num_el);
F=zeros(3,3,num_el);
Ud_mat=zeros(3,3,num_el);
Ud_mat(1,1,:)=Ux(1,:); Ud_mat(2,1,:)=Ux(2,:);
Ud_mat(1,2,:)=Uy(1,:); Ud_mat(2,2,:)=Uy(2,:);
for tr=1:num_el
    Identity(:,:,tr)=eye(3,3);
end
F=Identity+Ud_mat;
Jac=zeros(1,num_el);
Jac(:)=F(1,1,:).*F(2,2,:)-F(2,1,:).*F(1,2,:);

C_right=zeros(3,3,num_el);
Inv_c=zeros(1,num_el);
for tc=1:num_el
    C_right(:,:,tc)=F(:,:,tc)'*F(:,:,tc);
    Inv_c(tc)=trace(C_right(:,:,tc));
end
```

```
W1p=(0.5)*mu.*(Inv_c-3); W1m=W1p;
W2p=(0.5)*lambda.*log(Jac).^2-mu.*log(Jac); W2m=W2;
%%%%%%%%%%%%%%%%%%%%%%%%%%%%%%%%%%%%
% thension-compression implementation %
%%%%%%%%%%%%%%%%%%%%%%%%%%%%%%%%%%%%
Jacob_m=find(Jac<1); Jacom_p=find(Jac>=1);
W2p(Jacob_m)=0;
W1p(Jacob_m)=0;
W2m(Jacom_p)=0;
W1m(Jacom_p)=0;
%%%%%%%%%%%%%%%%%%%%%%%%%%%%%%%%%%%%
Wp=W1p+W2p; Wm=W1m+W2m;
a_mat=2*(Wp)./gamma + eps.^(-1);
c_mat=ones(1,num_el).*eps;
f_vec=ones(1,num_el)./(eps);
s_damage=assempde(bcBoundary_s,node,edg,triang,c_mat,a_mat,f_vec);
```

A.2 Material heterogeneity

In this section the main subroutines for modelling of heterogeneity by means of the Weibull distribution have been included, as well as the programme used for the RF mesh generation, dimensionality reduction and mapping from RF to FE mesh.

A.2.1 Non-Gaussian process: Weibull distribution

```
% p, t: FE nodes and elements ID and info
% nt: number of triangles/elements

cas3 = 1;  %%% 1 = Monovariate  2 = Bivariate
%%%%%%%%%%%%%%%%%%%%%%%%%%%%%%%%%%%%%%%%%%%%
if cas3 == 1
    mean(1,1) = 0;
    V(1,1) = 0.5;
    %Step1
    for i = 1:nt
    rand_valn(:,i) = random('logn',mean,V);
    end
```

```
    %Step2
    for i=1:nt
      for j=1:nt
        x1i=p(1,t(1,i)); x2i=p(1,t(2,i)); x3i=p(1,t(3,i));
        y1i=p(2,t(1,i)); y2i=p(2,t(2,i)); y3i=p(2,t(3,i));
        cxi=(x1i+x2i+x3i)/3; cyi=(y1i+y2i+y3i)/3;
        x1j=p(1,t(1,j)); x2j=p(1,t(2,j)); x3j=p(1,t(3,j));
        y1j=p(2,t(1,j)); y2j=p(2,t(2,j)); y3j=p(2,t(3,j));
        cxj=(x1j+x2j+x3j)/3; cyj=(y1j+y2j+y3j)/3;
        Cff(i,j)=(Sigma)^2*exp(-(3.14*sqrt((cxi-cxj)^2+...
            (cyi-cyj)^2))/(clength^2));
      end
    end
    C = chol(Cff);
    %Step3
    n = C'*rand_valn;
    %Step4
    param(1,:) = mle(n(1,:),'distribution','Weibull');
    scale1 = param(1,1);
    shape1 = param(1,2);
    %Step5
    arg_log1 = 0.5 .* (1-erf(n(1,:)/sqrt(2))) ;
    y_out(1,:) = scale1 .* (-log(arg_log1)).^(1/shape1);

elseif case3 == 2
    %Step1
    M(1,1) = 0;    V(1,1) = 0.5;
    M(2,1) = 0;    V(2,1) = 0.25;
    for i=1:nt
      for j=1:nt
        x1i=p(1,t(1,i)); x2i=p(1,t(2,i)); x3i=p(1,t(3,i));
        y1i=p(2,t(1,i)); y2i=p(2,t(2,i)); y3i=p(2,t(3,i));
        cxi=(x1i+x2i+x3i)/3; cyi=(y1i+y2i+y3i)/3;
        x1j=p(1,t(1,j)); x2j=p(1,t(2,j)); x3j=p(1,t(3,j));
        y1j=p(2,t(1,j)); y2j=p(2,t(2,j)); y3j=p(2,t(3,j));
        cxj=(x1j+x2j+x3j)/3; cyj=(y1j+y2j+y3j)/3;
        Cff(i,j)=(Sigma)^2*exp(-(3.14*sqrt((cxi-cxj)^2+...
```

```
            (cyi-cyj)^2))/(clength^2));
        end
    end
    C = chol(Cff);
    for i = 1:nt
      rand_valn(:,i) = random('norm',M,V);
    end
    n = C'*rand_valn;
    % define the 5 parame for Weibull Bivariate
    param(1,:) = mle(rand_valn(1,:),'distribution','Weibull');
    param(2,:) = mle(rand_valn(2,:),'distribution','Weibull');
    scale1 = param(1,1);
    scale2 = param(2,1);
    shape1 = param(1,2);
    shape2 = param(2,2);
    rho = 0.5;
    CorrMat = [sigma(1,1)^2 rho*sigma(1,1)*sigma(2,1);
           rho*sigma(2,1)*sigma(1,1) sigma(2,1)^2];
    for i = 1:nt
        norm_biv(:,i) = mvnrnd(M,CorrMat);
    end
    % trasform to Weibull
    arg_log1 = 0.5 .* (1-erf(norm_biv(1,:)/sqrt(2))) ;
    arg_log2 = 0.5 .* (1-erf(norm_biv(2,:)/sqrt(2))) ;
    y_out(1,:) = scale1 .* (-log(arg_log1)).^(1/shape1);
    y_out(2,:) = scale2 .* (-log(arg_log2)).^(1/shape2);
```

A.2.2 Model Order Reduction

```
% Generation RF mesh and MOR dimension
clear all

mesh_size1 = 2;
correlation_length = 10;

k_random_save1=[];          k_random_save2=[];
```

```
mu_random_save1=[];           mu_random_save2=[];
lambda_random_save1=[];       lambda_random_save2=[];
E_random_save1=[];            E_random_save2=[];
CorrMat1=[];                  CorrMat2=[];

[geom1_dual,ms1_dual]=geometry_creation(mesh_size1);
[p1_dual,e1_dual,t1_dual]=initmesh(geom1_dual,'Hmax',
    ms1_dual);

E=24.8; ni=0.18;
lambda_vett(1)=E*ni/((1+ni)*(1-2*ni));
mu_vett(1)=E/(2*(1+ni));
kfratt_vett(1)=2.5*10^(-5); % KN/mm
eps_vett(1)=1*10^(-1);
acont=1;
num_tri1=size(t1_dual,2);
%num_tri2=size(t2_dual,2);
disp('Creation of the random filed mesh...');
[k_random_save1,mu_random_save1,lambda_random_save1,
    E_random_save1,CorrMat1]=problem_dual(...
     mu_vett,lambda_vett,kfratt_vett,eps_vett,p1_dual,e1_dual
         ,t1_dual,acont,CorrMat1,...
     k_random_save1,mu_random_save1,lambda_random_save1,
         E_random_save1,num_tri1,correlation_length);
disp('RANDOM FILED MESH CREATED');
%ISOMAP
% Distance Matrix
pos = [p1_dual(1,:);p1_dual(2,:)];
IPisomap = pos' * pos;
DistMat = sqrt(bsxfun(@plus, diag(IPisomap), diag(IPisomap)
    ') - 2 * IPisomap);
k_val = 3;
fun_n = 'k_val';
n_dimmen = 7;
options.dims = 1:50;
[isoY, isoR, isoE] = Isomap_sub(DistMat, fun_n, n_dimmen,
    options);
```

A.2.3 Mapping RF-FE mesh

```
nt1=size(t1,2);
nt2=size(t2,2);
cent1=[]; cent2=[];
for i=1:nt1
    x1i=p1(1,t1(1,i)); x2i=p1(1,t1(2,i)); x3i=p1(1,t1(3,i));
    y1i=p1(2,t1(1,i)); y2i=p1(2,t1(2,i)); y3i=p1(2,t1(3,i));
    cent1(1,i)=(x1i+x2i+x3i)/3; cent1(2,i)=(y1i+y2i+y3i)/3;
end
for j=1:nt2
    x1j=p2(1,t2(1,j)); x2j=p2(1,t2(2,j)); x3j=p2(1,t2(3,j));
    y1j=p2(2,t2(1,j)); y2j=p2(2,t2(2,j)); y3j=p2(2,t2(3,j));
    cent2(1,j)=(x1j+x2j+x3j)/3; cent2(2,j)=(y1j+y2j+y3j)/3;
end
for j=1:nt2
    dist_sum=0;
    k_sum=0;
    for i=1:nt1
        dist = sqrt((cent1(1,i)-cent2(1,j))^2+(cent1(2,i)-
           cent2(2,j))^2);
        if dist<ms
            dist_sum = dist_sum + (1/dist);
            k_sum = k_sum + ks(1,i)*(1/dist);
        end
    end
    map_rand(1,j) = k_sum/dist_sum;
end
```

Bibliography

M. Abbas, B. Bohloli, N. Mondol, and L. Grande. Brazilian tensile strength test-post-failure behavior of jurassic and cretaceous shales from svalbard. In *77th EAGE Conference and Exhibition 2015*, 2015.

M. Aliha, M. Ayatollahi, D. Smith, and M. Pavier. Geometry and size effects on fracture trajectory in a limestone rock under mixed mode loading. *Engineering Fracture Mechanics*, 77(11):2200–2212, 2010.

H. Alkhateb, A. Al-Ostaz, and K. I. Alzebdeh. Developing a stochastic model to predict the strength and crack path of random composites. *Composites Part B: Engineering*, 40(1):7–16, 2009.

D. L. Allaix and V. I. Carbone. Discretization of 2d random fields: A genetic algorithm approach. *Engineering Structures*, 31(5):1111–1119, 2009.

L. Ambrosio and V. M. Tortorelli. *On the approximation of free discontinuity problems.* Scuola Normale Superiore, 1990.

H. Amor, J.-J. Marigo, and C. Maurini. Regularized formulation of the variational brittle fracture with unilateral contact: Numerical experiments. *Journal of the Mechanics and Physics of Solids*, 57(8):1209–1229, 2009.

P. Areias and T. Belytschko. Analysis of three-dimensional crack initiation and propagation using the extended finite element method. *International Journal for Numerical Methods in Engineering*, 63(5):760–788, 2005.

M. Arrea. *Mixed-mode crack propagation in mortar and concrete.* Cornell University, Jan., 1982.

I. Babuška. Homogenization and its application. mathematical and computational problems. In *Numerical Solution of Partial Differential Equations–III*, pages 89–116. Elsevier, 1976.

S. Balay, J. Brown, K. Buschelman, V. Eijkhout, W. Gropp, D. Kaushik, M. Knepley, L. C. McInnes, B. Smith, and H. Zhang. Petsc users manual revision 3.3. *Computer Science Division, Argonne National Laboratory, Argonne, IL*, 2012.

Z. P. Bazant and F.-B. Lin. Nonlocal smeared cracking model for concrete fracture. *Journal of Structural Engineering*, 114(11):2493–2510, 1988.

Z. P. Bazant and J. Planas. *Fracture and size effect in concrete and other quasibrittle materials*, volume 16. CRC press, 1997.

T. Belytschko, Y. Krongauz, D. Organ, M. Fleming, and P. Krysl. Meshless methods: an overview and recent developments. *Computer methods in applied mechanics and engineering*, 139(1-4):3–47, 1996.

J.-M. Berthelot and L. Fatmi. Statistical investigation of the fracture behaviour of inhomogeneous materials in tension and three-point bending. *Engineering fracture mechanics*, 71(11):1535–1556, 2004.

J.-M. Berthelot, B. Diouf, and P. Picart. Statistical three-dimensional investigation of the damage evolution in heterogeneous materials. *Engineering Fracture Mechanics*, 75(6):1431–1450, 2008.

G. Bhardwaj, I. Singh, and B. Mishra. Stochastic fatigue crack growth simulation of interfacial crack in bi-layered fgms using xiga. *Computer Methods in Applied Mechanics and Engineering*, 284:186–229, 2015.

P. Bhattacharya. Weibull distribution for estimating the parameters. In *Wind Energy Management*. InTech, 2011.

T. Bieler, P. Eisenlohr, F. Roters, D. Kumar, D. Mason, M. Crimp, and D. Raabe. The role of heterogeneous deformation on damage nucleation at grain boundaries in single phase metals. *International Journal of Plasticity*, 25(9):1655–1683, 2009.

C. Bobko and F.-J. Ulm. The nano-mechanical morphology of shale. *Mechanics of Materials*, 40(4):318–337, 2008.

J. Bonet and R. D. Wood. *Nonlinear continuum mechanics for finite element analysis*. Cambridge university press, 1997.

A. Borghi, P. Renard, L. Fournier, and F. Negro. Stochastic fracture generation accounting for the stratification orientation in a folded environment based on an implicit geological model. *Engineering Geology*, 187:135–142, 2015.

G. Bossi, L. Borgatti, G. Gottardi, and G. Marcato. The boolean stochastic generation method-bosg: A tool for the analysis of the error associated with the simplification of the stratigraphy in geotechnical models. *Engineering Geology*, 203:99–106, 2016.

P.-O. Bouchard. Damage and discrete crack propagation modelling: Some results and challenges for 2d and 3d configurations. In *ICF11-International Conference on Fracture*, pages 6–pages, 2005.

B. Bourdin, G. A. Francfort, and J.-J. Marigo. Numerical experiments in revisited brittle fracture. *Journal of the Mechanics and Physics of Solids*, 48(4):797–826, 2000.

B. Bourdin, J.-J. Marigo, C. Maurini, and P. Sicsic. Morphogenesis and propagation of complex cracks induced by thermal shocks. *Physical review letters*, 112(1): 014301, 2014.

R. Brighenti, A. Carpinteri, A. Spagnoli, and D. Scorza. Cracking behaviour of fibre-reinforced cementitious composites: A comparison between a continuous and a discrete computational approach. *Engineering Fracture Mechanics*, 103:103–114, 2013.

M. Brunet, S. Mguil, and P. Pol. Modelling of a roll-forming process with a combined 2d and 3d fem code. *Journal of Materials Processing Technology*, 80:213–219, 1998.

H. D. Bui. *Fracture mechanics: inverse problems and solutions*, volume 139. Springer Science & Business Media, 2007.

Y. Cai, L. Han, L. Tian, and L. Zhang. Meshless method based on shepard function and partition of unity for two-dimensional crack problems. *Engineering Analysis with Boundary Elements*, 65:126–135, 2016.

J. Carmeliet and H. Hens. Probabilistic nonlocal damage model for continua with random field properties. *Journal of engineering mechanics*, 120(10):2013–2027, 1994.

M. R. Chandler, P. G. Meredith, N. Brantut, and B. R. Crawford. Fracture toughness anisotropy in shale. *Journal of Geophysical Research: Solid Earth*, 121(3): 1706–1729, 2016.

Q. Chen, M. M. Nezhad, Q. Fisher, and H. Zhu. Multi-scale approach for modeling the transversely isotropic elastic properties of shale considering multi-inclusions and interfacial transition zone. *International Journal of Rock Mechanics and Mining Sciences*, 84:95–104, 2016.

Z. Chong, X. Li, P. Hou, Y. Wu, J. Zhang, T. Chen, and S. Liang. Numerical investigation of bedding plane parameters of transversely isotropic shale. *Rock Mechanics and Rock Engineering*, 50(5):1183–1204, 2017.

B. Crawford, N. DeDontney, B. Alramahi, et al. Numerical modeling of composite bilaminate materials as an analog for strength variation in anisotropic shale formations. In *ISRM Regional Symposium-EUROCK 2014*. International Society for Rock Mechanics, 2014.

R. de Borst, J. J. Remmers, A. Needleman, and M.-A. Abellan. Discrete vs smeared crack models for concrete fracture: bridging the gap. *International Journal for Numerical and Analytical Methods in Geomechanics*, 28(7-8):583–607, 2004.

G. Del Piero, G. Lancioni, and R. March. A variational model for fracture mechanics: numerical experiments. *Journal of the Mechanics and Physics of Solids*, 55(12): 2513–2537, 2007.

A. Der Kiureghian and J.-B. Ke. The stochastic finite element method in structural reliability. *Probabilistic Engineering Mechanics*, 3(2):83–91, 1988.

L. Devroye. Sample-based non-uniform random variate generation. In *Proceedings of the 18th conference on Winter simulation*, pages 260–265. ACM, 1986.

L. S. Dimas, T. Giesa, and M. J. Buehler. Coupled continuum and discrete analysis of random heterogeneous materials: elasticity and fracture. *Journal of the Mechanics and Physics of Solids*, 63:481–490, 2014.

L. S. Dimas, D. Veneziano, and M. J. Buehler. Strength and fracture toughness of heterogeneous blocks with joint lognormal modulus and failure strain. *Journal of the Mechanics and Physics of Solids*, 92:72–86, 2016.

D. Dipasquale, G. Sarego, M. Zaccariotto, and U. Galvanetto. Dependence of crack paths on the orientation of regular 2d peridynamic grids. *Engineering Fracture Mechanics*, 160:248–263, 2016.

V. Dokhani, M. Yu, and B. Bloys. A wellbore stability model for shale formations: Accounting for strength anisotropy and fluid induced instability. *Journal of Natural Gas Science and Engineering*, 32:174–184, 2016.

J. Dolbow and T. Belytschko. A finite element method for crack growth without remeshing. *International journal for numerical methods in engineering*, 46(1): 131–150, 1999.

T. Douillet-Grellier, R. Pramanik, K. Pan, A. Albaiz, B. Jones, H. Pourpak, J. Williams, et al. Mesh-free numerical simulation of pressure-driven fractures in brittle rocks. In *SPE Hydraulic Fracturing Technology Conference*. Society of Petroleum Engineers, 2016.

K. Duan and C. Kwok. Discrete element modeling of anisotropic rock under brazilian test conditions. *International Journal of Rock Mechanics and Mining Sciences*, 2015.

Q. Duan, J.-H. Song, T. Menouillard, and T. Belytschko. Element-local level set method for three-dimensional dynamic crack growth. *International Journal for Numerical Methods in Engineering*, 80(12):1520–1543, 2009.

R. Einsfeld, A. Elwi, T. Bittencourt, and L. Martha. Numerical simulation of fracturing in concrete structures using a combination of smeared and discrete approaches. *International Journal of Rock Mechanics and Mining Sciences*, 34 (3):189–e1, 1997.

I. Elishakoff and Y. Ren. *Finite element methods for structures with large stochastic variations*, volume 7. Oxford University Press on Demand, 2003.

F. Erdogan. Fracture mechanics. *International Journal of Solids and Structures*, 37(1â“2):171 – 183, 2000. ISSN 0020-7683. doi: http://dx.doi.org/10.1016/S0020-7683(99)00086-4. URL `http://www.sciencedirect.com/science/article/pii/S0020768399000864`.

H. D. Espinosa and P. D. Zavattieri. A grain level model for the study of failure initiation and evolution in polycrystalline brittle materials. part i: Theory and numerical implementation. *Mechanics of Materials*, 35(3):333–364, 2003a.

H. D. Espinosa and P. D. Zavattieri. A grain level model for the study of failure initiation and evolution in polycrystalline brittle materials. part ii: numerical examples. *Mechanics of Materials*, 35(3):365–394, 2003b.

C. L. Evans and R. F. Gariepy. Measure theory and fine properties of functions. *Studies in Advanced Mathematics". CRC Press. Boca Raton London New York Washington, DC*, 1992.

G. Falsone and N. Impollonia. A new approach for the stochastic analysis of finite element modelled structures with uncertain parameters. *Computer Methods in Applied Mechanics and Engineering*, 191(44):5067–5085, 2002.

A. Faraz, E. M. Saniga, and C. Heuchenne. Shewhart control charts for monitoring reliability with weibull lifetimes. *Quality and Reliability Engineering International*, 31(8):1565–1574, 2015.

G. A. Fenton. Error evaluation of three random-field generators. *Journal of engineering mechanics*, 120(12):2478–2497, 1994.

B. Figueiredo, C.-F. Tsang, J. Rutqvist, and A. Niemi. Study of hydraulic fracturing processes in shale formations with complex geological settings. *Journal of Petroleum Science and Engineering*, 152:361–374, 2017.

J. Fish and T. Belytschko. A first course in finite elements. 2007.

J. Fish and Q. Yu. Two-scale damage modeling of brittle composites. *Composites Science and Technology*, 61(15):2215–2222, 2001.

R. W. Floyd. Algorithm 97: shortest path. *Communications of the ACM*, 5(6):345, 1962.

G. A. Francfort and J.-J. Marigo. Revisiting brittle fracture as an energy minimization problem. *Journal of the Mechanics and Physics of Solids*, 46(8):1319–1342, 1998.

J.-W. Fu, X.-Z. Zhang, W.-S. Zhu, K. Chen, and J.-F. Guan. Simulating progressive failure in brittle jointed rock masses using a modified elastic-brittle model and the application. *Engineering Fracture Mechanics*, 178:212–230, 2017.

T. C. Gasser and G. A. Holzapfel. Modeling 3d crack propagation in unreinforced concrete using pufem. *Computer Methods in Applied Mechanics and Engineering*, 194(25-26):2859–2896, 2005.

T. C. Gasser and G. A. Holzapfel. 3d crack propagation in unreinforced concrete.: A two-step algorithm for tracking 3d crack paths. *Computer Methods in Applied Mechanics and Engineering*, 195(37):5198–5219, 2006.

M. G. Geers, V. G. Kouznetsova, and W. Brekelmans. Multi-scale computational homogenization: Trends and challenges. *Journal of computational and applied mathematics*, 234(7):2175–2182, 2010.

M. Georgioudakis, G. Stefanou, and M. Papadrakakis. Stochastic failure analysis of structures with softening materials. *Engineering Structures*, 61:13–21, 2014.

E. Gironacci, M. Mousavi Nezhad, M. Rezania, and G. Lancioni. A nonlocal probabilistic method for modelling of crack propagation. *International Journal of Mechanical Sciences*, Accepted. In press., 2017.

K. Glover. All optimal hankel-norm approximations of linear multivariable systems and their l,-error bounds. *International journal of control*, 39(6):1115–1193, 1984.

L. Gorjan and M. Ambrožič. Bend strength of alumina ceramics: A comparison of weibull statistics with other statistics based on very large experimental data set. *Journal of the European Ceramic Society*, 32(6):1221–1227, 2012.

A. A. Griffith. The phenomena of rupture and flow in solids. *Philosophical transactions of the royal society of london. Series A, containing papers of a mathematical or physical character*, 221:163–198, 1921.

U. Groh, H. Konietzky, K. Walter, and M. Herbst. Damage simulation of brittle heterogeneous materials at the grain size level. *Theoretical and Applied Fracture Mechanics*, 55(1):31–38, 2011.

Y.-L. Gui, H. H. Bui, J. Kodikara, Q.-B. Zhang, J. Zhao, and T. Rabczuk. Modelling the dynamic failure of brittle rocks using a hybrid continuum-discrete element method with a mixed-mode cohesive fracture model. *International Journal of Impact Engineering*, 87:146–155, 2016.

H. Guo, N. Aziz, and L. Schmidt. Rock fracture-toughness determination by the brazilian test. *Engineering Geology*, 33(3):177–188, 1993.

M. Gutiérrez and R. de Borst. Deterministic and stochastic analysis of size effects and damage evolution in quasi-brittle materials. *Archive of Applied Mechanics*, 69(9-10):655–676, 1999.

N. Guy, D. M. Seyedi, and F. Hild. A probabilistic nonlocal model for crack initiation and propagation in heterogeneous brittle materials. *International Journal for Numerical Methods in Engineering*, 90(8):1053–1072, 2012.

M. Haddad, K. Sepehrnoori, et al. Xfem-based czm for the simulation of 3d multiple-stage hydraulic fracturing in quasi-brittle shale formations. In *49th US Rock Mechanics/Geomechanics Symposium*. American Rock Mechanics Association, 2015.

A. Haldar and S. Mahadevan. *Probability, reliability, and statistical methods in engineering design.* John Wiley, 2000.

J. He and L. O. Afolagboye. Influence of layer orientation and interlayer bonding force on the mechanical behavior of shale under brazilian test conditions. *Acta Mechanica Sinica*, pages 1–10, 2017.

D. Hobbs. The tensile strength of rocks. In *International Journal of Rock Mechanics and Mining Sciences & Geomechanics Abstracts*, volume 1, pages 385IN17389–388IN18396. Elsevier, 1964.

R. M. Holt, E. Fjær, J. F. Stenebråten, and O.-M. Nes. Brittleness of shales: Relevance to borehole collapse and hydraulic fracturing. *Journal of Petroleum Science and Engineering*, 131:200–209, 2015.

P. Hou, F. Gao, Y. Ju, X. Liang, Z. Zhang, H. Cheng, and Y. Gao. Experimental investigation on the failure and acoustic emission characteristics of shale, sandstone and coal under gas fracturing. *Journal of Natural Gas Science and Engineering*, 35:211–223, 2016.

J. Hudson, E. Brown, and F. Rummel. The controlled failure of rock discs and rings loaded in diametral compression. In *International Journal of Rock Mechanics and Mining Sciences & Geomechanics Abstracts*, volume 9, pages 241IN1245–244IN4248. Elsevier, 1972.

C. E. Inglis. Stresses in a plate due to the presence of cracks and sharp corners. *Transactions of the institute of naval architects*, 55(219-241):193–198, 1913.

G. R. Irwin. Analysis of stresses and strains near the end of a crack traversing a plate. *J. appl. Mech.*, 1957.

ISRM. Suggested methods for determining tensile strength of rock materials. *International Journal of Rock Mechanics and Mining Sciences amp; Geomechanics Abstracts*, 15(3):99 – 103, 1978. ISSN 0148-9062. doi: https://doi.org/10.1016/0148-9062(78)90003-7. URL `http://www.sciencedirect.com/science/article/pii/0148906278900037`.

L. Jendele, J. Cervenka, V. Saouma, and R. Pukl. On the choice between discrete or smeared approach in practical structural fe analyses of concrete structures. In *Fourth International Conference on Analysis of Discontinuous Deformation Glasgow, Scotland UK*, 2001.

S. Jeong, K. Nakamura, S. Yoshioka, Y. Obara, and M. Kataoka. Fracture toughness of granite measured using micro to macro scale specimens. *Procedia engineering*, 191(5):761–767, 2017.

M. Jirásek and Z. P. Bažant. Particle model for quasibrittle fracture and application to sea ice. *Journal of engineering mechanics*, 121(9):1016–1025, 1995.

Ł. Kaczmarczyk, M. M. Nezhad, and C. Pearce. Three-dimensional brittle fracture: configurational-force-driven crack propagation. *International Journal for Numerical Methods in Engineering*, 97(7):531–550, 2014.

M. Kaliske, H. Dal, R. Fleischhauer, C. Jenkel, and C. Netzker. Characterization of fracture processes by continuum and discrete modelling. *Computational Mechanics*, 50(3):303–320, 2012.

A. Karamnejad, V. P. Nguyen, and L. J. Sluys. A multi-scale rate dependent crack model for quasi-brittle heterogeneous materials. *Engineering Fracture Mechanics*, 104:96–113, 2013.

V. L. Khasin. Stochastic model of crack propagation in brittle heterogeneous materials. *International Journal of Engineering Science*, 82:101–123, 2014.

H. Kim, J.-W. Cho, I. Song, and K.-B. Min. Anisotropy of elastic moduli, p-wave velocities, and thermal conductivities of asan gneiss, boryeong shale, and yeoncheon schist in korea. *Engineering Geology*, 147:68–77, 2012.

M. Kleiber and T. D. Hien. *The stochastic finite element method: basic perturbation technique and computer implementation*. Wiley, 1992.

J. F. Knott and D. Elliott. *Worked Examples in Fracture Mechanics: JF Knott, D. Elliott*. Institution of Metallurgists, 1979.

G. Lancioni and G. Royer-Carfagni. The variational approach to fracture mechanics. a practical application to the french panthéon in paris. *Journal of elasticity*, 95 (1-2):1–30, 2009.

G. M. Latha and A. Garaga. Elasto-plastic analysis of jointed rocks using discrete continuum and equivalent continuum approaches. *International Journal of Rock Mechanics and Mining Sciences*, 53:56–63, 2012.

H. Lauschmann. A stochastic model of fatigue crack growth in heterogeneous material. *Engineering fracture mechanics*, 26(5):707–728, 1987.

C.-C. Li and A. Der Kiureghian. Optimal discretization of random fields. *Journal of engineering mechanics*, 119(6):1136–1154, 1993.

D. Li and L. N. Y. Wong. The brazilian disc test for rock mechanics applications: review and new insights. *Rock mechanics and rock engineering*, 46(2):269–287, 2013.

H. Li, N. Chawla, and Y. Jiao. Reconstruction of heterogeneous materials via stochastic optimization of limited-angle x-ray tomographic projections. *Scripta Materialia*, 86:48–51, 2014.

J. Li and W. B. Salah. Numerical simulations on cracking process in ceramic specimens under thermal shock by using a non-local fracture model. *Procedia Materials Science*, 3:1492–1498, 2014.

T. Li, J.-J. Marigo, D. Guilbaud, and S. Potapov. Gradient damage modeling of brittle fracture in an explicit dynamics context. *International Journal for Numerical Methods in Engineering*, 108(11):1381–1405, 2016a.

Z. Li, X. Wang, H. Wang, and R. Y. Liang. Quantifying stratigraphic uncertainties by stochastic simulation techniques based on markov random field. *Engineering Geology*, 201:106–122, 2016b.

Z. Liang, C. Tang, H. Li, T. Xu, and Y. Zhang. Numerical simulation of 3-d failure process in heterogeneous rocks. *International Journal of Rock Mechanics and Mining Sciences*, 41:323–328, 2004.

H. Liu, M. Roquete, S. Kou, and P.-A. Lindqvist. Characterization of rock heterogeneity and numerical verification. *Engineering Geology*, 72(1):89–119, 2004.

O. Lloberas-Valls, D. Rixen, A. Simone, and L. Sluys. Multiscale domain decomposition analysis of quasi-brittle heterogeneous materials. *International Journal for Numerical Methods in Engineering*, 89(11):1337–1366, 2012.

E. Madenci, K. Colavito, and N. Phan. Peridynamics for unguided crack growth prediction under mixed-mode loading. *Engineering Fracture Mechanics*, 167:34–44, 2016.

B. Mahanta, A. Tripathy, V. Vishal, T. Singh, and P. Ranjith. Effects of strain rate on fracture toughness and energy release rate of gas shales. *Engineering Geology*, 2016.

W. L. Martinez and A. R. Martinez. *Computational statistics handbook with MATLAB*, volume 22. CRC press, 2007.

K. Matouš, M. G. Geers, V. G. Kouznetsova, and A. Gillman. A review of predictive nonlinear theories for multiscale modeling of heterogeneous materials. *Journal of Computational Physics*, 330:192–220, 2017.

S. May, R. de Borst, and J. Vignollet. Powell–sabin b-splines for smeared and discrete approaches to fracture in quasi-brittle materials. *Computer Methods in Applied Mechanics and Engineering*, 307:193–214, 2016.

B. McGinty. Fracture mechanics with detailed explanations and examples, July 2017. URL `http://www.fracturemechanics.org/ellipse.html`.

C. Miehe and C. Bayreuther. On multiscale fe analyses of heterogeneous structures: from homogenization to multigrid solvers. *International Journal for Numerical Methods in Engineering*, 71(10):1135–1180, 2007.

M. Mokhtari and A. N. Tutuncu. Impact of laminations and natural fractures on rock failure in brazilian experiments: A case study on green river and niobrara formations. *Journal of Natural Gas Science and Engineering*, 36:79–86, 2016.

B. Moore. Principal component analysis in linear systems: Controllability, observability, and model reduction. *IEEE transactions on automatic control*, 26(1): 17–32, 1981.

S. Morgan, H. Einstein, et al. The effect of bedding plane orientation on crack propagation and coalescence in shale. In *48th US Rock Mechanics/Geomechanics Symposium*. American Rock Mechanics Association, 2014.

J. Mosler and G. Meschke. Embedded crack vs. smeared crack models: a comparison of elementwise discontinuous crack path approaches with emphasis on mesh bias. *Computer Methods in Applied Mechanics and Engineering*, 193(30):3351–3375, 2004.

T. Most. *Stochastic crack growth simulation in reinforced concrete structures by means of coupled finite element and meshless methods*. PhD thesis, 2005.

M. Mousavi Nezhad, Q. Fisher, E. Gironacci, and M. Rezania. A nonlocal probabilistic method for modelling of crack propagation. *Rock Mechanics and Rock Engineering*, Accepted. In press., 2018.

S. H. Na, W. C. Sun, M. D. Ingraham, and H. Yoon. Effects of spatial heterogeneity and material anisotropy on the fracture pattern and macroscopic effective toughness of mancos shale in brazilian tests. *Journal of Geophysical Research: Solid Earth*, 2017.

B. Nguyen, H. Tran, C. Anitescu, X. Zhuang, and T. Rabczuk. An isogeometric symmetric galerkin boundary element method for two-dimensional crack problems. *Computer Methods in Applied Mechanics and Engineering*, 306:252–275, 2016a.

T. Nguyen, J. Yvonnet, Q.-Z. Zhu, M. Bornert, and C. Chateau. A phase field method to simulate crack nucleation and propagation in strongly heterogeneous materials from direct imaging of their microstructure. *Engineering Fracture Mechanics*, 139:18–39, 2015.

T. Nguyen, N. Quoc, and V. Nguyen. Meshfree approach for hydraulic fracture. *Engineering Geology*, 2016b.

T. T. Nguyen, J. Yvonnet, M. Bornert, and C. Chateau. Initiation and propagation of complex 3d networks of cracks in heterogeneous quasi-brittle materials: Direct comparison between in situ testing-microct experiments and phase field simulations. *Journal of the Mechanics and Physics of Solids*, 95:320–350, 2016c.

T.-T. Nguyen, J. Yvonnet, Q.-Z. Zhu, M. Bornert, and C. Chateau. A phase-field method for computational modeling of interfacial damage interacting with crack propagation in realistic microstructures obtained by microtomography. *Computer Methods in Applied Mechanics and Engineering*, 312:567–595, 2016d.

V. P. Nguyen, O. Lloberas-Valls, M. Stroeven, and L. J. Sluys. Homogenization-based multiscale crack modelling: from micro-diffusive damage to macro-cracks. *Computer Methods in Applied Mechanics and Engineering*, 200(9):1220–1236, 2011a.

V. P. Nguyen, M. Stroeven, and L. J. Sluys. Multiscale continuous and discontinuous modeling of heterogeneous materials: a review on recent developments. *Journal of Multiscale Modelling*, 3(04):229–270, 2011b.

V. P. Nguyen, O. Lloberas-Valls, M. Stroeven, and L. J. Sluys. Computational homogenization for multiscale crack modeling. implementational and computational aspects. *International Journal for Numerical Methods in Engineering*, 89 (2):192–226, 2012a.

V. P. Nguyen, M. Stroeven, and L. J. Sluys. An enhanced continuous–discontinuous multiscale method for modeling mode-i cohesive failure in random heterogeneous quasi-brittle materials. *Engineering Fracture Mechanics*, 79:78–102, 2012b.

K. Noghabai. Discrete versus smeared versus element-embedded crack models on ring problem. *Journal of engineering mechanics*, 125(3):307–315, 1999.

S. P. Oliveira. Spectral element approximation of fredholm integral eigenvalue problems. *Blucher Mechanical Engineering Proceedings*, 1(1):3358–3363, 2012.

D. Pardo, C. Torres-Verdín, and M. Paszynski. Simulations of 3d dc borehole resistivity measurements with a goal-oriented hp finite-element method. part ii: through-casing resistivity instruments. *Computational Geosciences*, 12(1):83–89, 2008.

D. Pathak, H. Gharti, A. Singh, and A. Hiratsuka. Stochastic modeling of progressive failure in heterogeneous soil slope. *Geotechnical and Geological Engineering*, 26(2):113–120, 2008.

R. Patil, B. Mishra, and I. Singh. A new multiscale xfem for the elastic properties evaluation of heterogeneous materials. *International Journal of Mechanical Sciences*, 122:277–287, 2017.

S. Patinet, L. Alzate, E. Barthel, D. Dalmas, D. Vandembroucq, and V. Lazarus. Finite size effects on crack front pinning at heterogeneous planar interfaces: Experimental, finite elements and perturbation approaches. *Journal of the Mechanics and Physics of Solids*, 61(2):311–324, 2013.

P. M. Pawar. On the behavior of thin walled composite beams with stochastic properties under matrix cracking damage. *Thin-Walled Structures*, 49(9):1123–1131, 2011.

N. Pindra, V. Lazarus, and J.-B. Leblond. Geometrical disorder of the fronts of a tunnel-crack propagating in shear in some heterogeneous medium. *Journal of the Mechanics and Physics of Solids*, 58(3):281–299, 2010.

D. Pisarenko and N. Gland. Modeling of scale effects of damage in cemented granular rocks. *Physics and Chemistry of the Earth, Part A: Solid Earth and Geodesy*, 26 (1-2):83–88, 2001.

R. Popescu, G. Deodatis, and J. Prevost. Simulation of non-gaussian stochastic fields with applications to soil liquefaction: two case studies. In *Proceedings of the 12th ASCE Engineering Mechanics Speciality Conference, Reston, Va*, 1998.

M. Prechtel, P. L. Ronda, R. Janisch, A. Hartmaier, G. Leugering, P. Steinmann, and M. Stingl. Simulation of fracture in heterogeneous elastic materials with cohesive zone models. *International Journal of Fracture*, 168(1):15–29, 2011.

F. Putar, J. Sorić, T. Lesičar, and Z. Tonković. Damage modeling employing strain gradient continuum theory. *International Journal of Solids and Structures*, 120: 171–185, 2017.

Y. Rashid. Ultimate strength analysis of prestressed concrete pressure vessels. *Nuclear engineering and design*, 7(4):334–344, 1968.

C. Y. Rena, G. Ruiz, and E. W. Chaves. A comparative study between discrete and continuum models to simulate concrete fracture. *Engineering Fracture Mechanics*, 75(1):117–127, 2008.

C. L. Richardson, J. Hegemann, E. Sifakis, J. Hellrung, and J. M. Teran. An xfem method for modeling geometrically elaborate crack propagation in brittle materials. *International Journal for Numerical Methods in Engineering*, 88(10): 1042–1065, 2011.

A. Rinaldi. Bottom-up modeling of damage in heterogeneous quasi-brittle solids. *Continuum Mechanics and Thermodynamics*, pages 1–15, 2013.

F. Rong, H. Wang, M. Xia, F. Ke, and Y. Bai. Catastrophic rupture induced damage coalescence in heterogeneous brittle media. *pure and applied geophysics*, 163(9): 1847–1865, 2006.

M. Sahimi. *Flow and transport in porous media and fractured rock: from classical methods to modern approaches.* John Wiley & Sons, 2011.

V. Saouma and A. Ingraffea. Fracture mechanics analysis of discrete cracking. In *Proceedings of IABSE Colloquium on Advanced Mechanics of Reinforced Concrete, Delft, the Netherlands*, pages 413–436, 1981.

J. Schicker and M. Pfuff. Statistical modelling of fracture in quasi-brittle materials. *Advanced Engineering Materials*, 8(5):406–410, 2006.

W. Schilders. Introduction to model order reduction. *Model order reduction: theory, research aspects and applications*, pages 3–32, 2008.

R. Sencu, Z. Yang, and Y. Wang. An adaptive stochastic multi-scale method for cohesive fracture modelling of quasi-brittle heterogeneous materials under uniaxial tension. *Engineering Fracture Mechanics*, 163:499–522, 2016.

S. Shang and G. J. Yun. Stochastic finite element with material uncertainties: Implementation in a general purpose simulation program. *Finite Elements in Analysis and Design*, 64:65–78, 2013.

M. Shinozuka. Monte carlo solution of structural dynamics. *Computers & Structures*, 2(5-6):855–874, 1972.

M. Shinozuka and G. Deodatis. Simulation of stochastic processes by spectral representation. *Applied Mechanics Reviews*, 44(4):191–204, 1991.

V. Shushakova, E. R. Fuller, and S. Siegesmund. Microcracking in calcite and dolomite marble: microstructural influences and effects on properties. *Environmental earth sciences*, 69(4):1263–1279, 2013.

S. A. Silling, M. Zimmermann, and R. Abeyaratne. Deformation of a peridynamic bar. *Journal of Elasticity*, 73(1-3):173–190, 2003.

L. Sirovich. Turbulence and the dynamics of coherent structures. i. coherent structures. *Quarterly of applied mathematics*, 45(3):561–571, 1987.

P. Sparks and C. Oskay. The method of failure paths for reduced-order computational homogenization. *International Journal for Multiscale Computational Engineering*, 14(5), 2016.

G. Stefanou. The stochastic finite element method: past, present and future. *Computer Methods in Applied Mechanics and Engineering*, 198(9):1031–1051, 2009.

G. Stefanou and M. Papadrakakis. Stochastic finite element analysis of shells with combined random material and geometric properties. *Computer Methods in Applied Mechanics and Engineering*, 193(1):139–160, 2004.

C. Steinke, K. Özenç, G. Chinaryan, and M. Kaliske. A comparative study of the r-adaptive material force approach and the phase-field method in dynamic fracture. *International Journal of Fracture*, 201(1):97–118, 2016.

B. Sudret and A. Der Kiureghian. *Stochastic finite element methods and reliability: a state-of-the-art report.* Department of Civil and Environmental Engineering, University of California Berkeley, CA, 2000.

B. Sun and Z. Li. Adaptive image-based method for integrated multi-scale modeling of damage evolution in heterogeneous concrete. *Computers & Structures*, 152: 66–81, 2015.

K. Sun, S. Zhang, and L. Xin. Impacts of bedding directions of shale gas reservoirs on hydraulically induced crack propagation. *Natural Gas Industry B*, 3(2):139–145, 2016.

J. L. Swedlow, M. L. Williams, and W.-H. Yang. Elasto-plastic stresses and strains in cracked plates(elasto-plastic stresses and strains in cracked plates analized by numerical method, noting stress singularities and stress-strain fields). In *INTERNATIONAL CONFERENCE ON FRACTURE, 1 ST, SENDAI, JAPAN*, pages 259–282, 1966.

T. J. Tautges, C. Ernst, C. Stimpson, R. J. Meyers, and K. Merkley. Moab: a mesh-oriented database. Technical report, Sandia National Laboratories, 2004.

J. B. Tenenbaum, V. De Silva, and J. C. Langford. A global geometric framework for nonlinear dimensionality reduction. *science*, 290(5500):2319–2323, 2000.

N. T. Thomopoulos. *Essentials of Monte Carlo simulation: Statistical methods for building simulation models*. Springer Science & Business Media, 2012.

V. Tomar and M. Zhou. Deterministic and stochastic analyses of fracture processes in a brittle microstructure system. *Engineering fracture mechanics*, 72(12):1920–1941, 2005.

M. R. A. Van Vliet. Size effect in tensile fracture of concrete and rock. 2000.

K. S. Vemaganti and J. T. Oden. Estimation of local modeling error and goal-oriented adaptive modeling of heterogeneous materials: Part ii: a computational environment for adaptive modeling of heterogeneous elastic solids. *Computer Methods in Applied Mechanics and Engineering*, 190(46):6089–6124, 2001.

Y. B. Veytskin, V. K. Tammina, C. P. Bobko, P. G. Hartley, M. B. Clennell, D. N. Dewhurst, and R. R. Dagastine. Micromechanical characterization of shales through nanoindentation and energy dispersive x-ray spectrometry. *Geomechanics for Energy and the Environment*, 9:21–35, 2017.

D. Villanueva, A. Feijóo, and J. L. Pazos. Multivariate weibull distribution for wind speed and wind power behavior assessment. *Resources*, 2(3):370–384, 2013.

M. Vořechovskỳ. Interplay of size effects in concrete specimens under tension studied via computational stochastic fracture mechanics. *International Journal of Solids and Structures*, 44(9):2715–2731, 2007.

K. A. Vu and M. G. Stewart. Predicting the likelihood and extent of reinforced concrete corrosion-induced cracking. *Journal of structural engineering*, 131(11): 1681–1689, 2005.

J. Wang, L. Xie, H. Xie, L. Ren, B. He, C. Li, Z. Yang, and C. Gao. Effect of layer orientation on acoustic emission characteristics of anisotropic shale in brazilian tests. *Journal of Natural Gas Science and Engineering*, 36:1120–1129, 2016.

L. Wang. *Karhunen-Loeve expansions and their applications.* PhD thesis, London School of Economics and Political Science (United Kingdom), 2008.

S. Wang, S. Sloan, D. Sheng, and C. Tang. Numerical analysis of the failure process around a circular opening in rock. *Computers and Geotechnics*, 39:8–16, 2012.

E. Weinan, B. Engquist, X. Li, W. Ren, and E. Vanden-Eijnden. Heterogeneous multiscale methods: a review. *Commun. Comput. Phys*, 2(3):367–450, 2007.

K. Wieghardt. Über das spalten und zerreißen elastischer körper. *Z. Mathematik und Physik*, 55(2):60–103, 1907.

B. J. Winkler. *Traglastuntersuchungen von unbewehrten und bewehrten Betonstrukturen auf der Grundlage eines Objektiven Werkstoffgesetze.* PhD thesis, University of Innsbruck, Austria, 2001.

Z. Yang and X. F. Xu. A heterogeneous cohesive model for quasi-brittle materials considering spatially varying random fracture properties. *Computer methods in applied mechanics and engineering*, 197(45):4027–4039, 2008.

Z. Yang, X. Su, J. Chen, and G. Liu. Monte carlo simulation of complex cohesive fracture in random heterogeneous quasi-brittle materials. *International journal of Solids and Structures*, 46(17):3222–3234, 2009.

X. Zeng and Y. Wei. Crack deflection in brittle media with heterogeneous interfaces and its application in shale fracking. *Journal of the Mechanics and Physics of Solids*, 2017.

T. Zhang, Y. Du, T. Huang, J. Yang, and X. Li. Stochastic simulation of patterns using isomap for dimensionality reduction of training images. *Computers & Geosciences*, 79:82–93, 2015.

J. Zhong, L. Shengxin, M. Yinsheng, Y. Chengming, L. Chenglin, L. Zongxing, L. Xuan, and L. Yong. Macro-fracture mode and micro-fracture mechanism of shale. *Petroleum Exploration and Development*, 42(2):269–276, 2015.

F. Zhou and J.-F. Molinari. Stochastic fracture of ceramics under dynamic tensile loading. *International journal of solids and structures*, 41(22):6573–6596, 2004.

J. Zhou, L. Zhang, Z. Pan, and Z. Han. Numerical investigation of fluid-driven near-borehole fracture propagation in laminated reservoir rock using pfc 2d. *Journal of Natural Gas Science and Engineering*, 36:719–733, 2016.

X. Zhou, J. Bi, and Q. Qian. Numerical simulation of crack growth and coalescence in rock-like materials containing multiple pre-existing flaws. *Rock Mechanics and Rock Engineering*, 48(3):1097–1114, 2015.

X.-P. Zhou and J. Bi. 3d numerical study on the growth and coalescence of pre-existing flaws in rocklike materials subjected to uniaxial compression. *International Journal of Geomechanics*, 16(4):04015096, 2016.